Effects of Environmental Conditions on Estimating the Long-Term Performance of a Cementitious Waste Form for the Immobilization of Nuclear Waste

By

Peng Zhang

Dissertation

Submitted to the Faculty of the

Graduate School of Vanderbilt University

in partial fulfillment of the requirements

for the degree of

DOCTOR OF PHILOSOPHY

in

Environmental Engineering

May, 14, 2021

Nashville, Tennessee

Approved:

David S. Kosson, Ph.D.

Kevin G. Brown, Ph.D.

Florence Sanchez, Ph.D.

John C. Ayers, Ph.D.

Hans van der Sloot, Ph.D.

Johannes C.L. Meeussen, Ph.D.

ACKNOWLEDGEMENTS

This work would not have been possible without the support of my advisors, Dr. David Kosson and Dr. Kevin Brown. Thank you for your advice, guidance, and encouragements along the way. I also must thank my entire committee for their time and valuable suggestions.

I am grateful to all of those with whom I have had the pleasure to work with over the years at Vanderbilt University. Thank you, Dr. Janelle Lewis, for mentoring me during my early years in the research group. I also must thank Dr. Andrew Garrabrants, Rossane DeLapp, Dr. Zhiliang Chen, Rich Teising, Dr. Lesa Brown, and many other members of the research group for providing me extensive technical supports. I would also like to thank Darlene Weaver and all other Civil & Environmental Engineering staff for their help with all types of administrative tasks. Finally, I would like to thank all my friends at Vanderbilt who made this place feel like home to me.

I must also acknowledge the financial support from the U. S. Department of Energy, under Cooperative Agreement Number DE-FC01-06EW07053 entitled "The Consortium for Risk Evaluation with Stakeholder Participation III" awarded to Vanderbilt University, David S. Kosson, principal investigator.

Most importantly, my deep and sincere gratitude to my family for their continuous and unparalleled love, help and support. I am forever indebted to my parents for giving me the opportunities and experiences that have made me who I am.

Disclaimer: This document was prepared as an account of work sponsored by an Agency of the United States Government. Neither the United States Government nor any agency thereof, nor any of their employees, makes any warranty, express or implied, or assumes any legal liability or responsibility for the accuracy, completeness, or usefulness of any information, apparatus, product, or process disclosed, or represents that its use would not infringe privately owned rights. Reference herein to any specific commercial product, process, or service by trade name, trademark, manufacturer, or otherwise does not necessarily constitute or imply its endorsement, recommendation, or favoring by the United States Government or any agency thereof. The opinions, findings, conclusions, or recommendations expressed herein are those of the authors and do not necessarily represent the views of the Department of Energy.

TABLE OF CONTENTS

Page

LIST OF TABLES

Table Page

LIST OF FIGURES

Figure Page

1. INTRODUCTION

1.1 Motivation

Ever since the utilization of nuclear technology began in the 1940s, the safe disposal of nuclear wastes has been a challenge. Each year, around 2000 to 2300 metric tons of used nuclear fuel is generated from the nuclear industry according to the Nuclear Energy Institute. In the United States, nuclear waste is also a legacy from the nuclear weapons production activities beginning with the Manhattan Project. Currently at DOE Hanford Site, which is the most challenging clean-up task in the DOE's nuclear complex, 56 million gallons of radioactive wastes generated from plutonium separation and other related processes are stored in 177 large, underground tanks awaiting treatment and disposal [1,2]. The stored radioactive and heterogeneous wastes are planned to be separated into a higher activity, lower volume fraction and a lower activity, higher volume fraction (denoted LAW) streams. The expected LAW contains less than 10% of the total radioactivity of the Hanford waste but is more than 90% of the volume [3]. Portions of high salt content radioactive tank waste and secondary liquid LAW are being considered for treatment with a mixture of fly ash, blast furnace slag (BFS), and ordinary Portland cement to produce Cast Stone as a waste form followed by near surface disposal [4–6]. BFS serves as a cementitious and pozzolanic binder as well as a reducing agent for the radioactive technetium-99 (^{99}Tc) by reducing the soluble form Tc(VII) to less soluble Tc(IV). A similar formulation is used in the saltstone material, which is a waste form currently being used for LAW disposal at the Savannah River Site Saltstone Disposal Facility (SDF) [7].

During the regulatorily-required service life of 1000 years for near-surface disposal [8], the waste forms are subject to aging processes from the surrounding environment, which impact the physical and chemical properties of the material and potentially adversely affect the retention of radionuclides and chemical contaminants [9–12]. For example, waste forms containing LAW are intended for disposal in engineered facilities with shallow land burial. To minimize the interaction of the waste form with the environment, especially through surface water and groundwater, near surface disposal facilities are often located in semi-arid or arid environments. The dry surrounding atmosphere can cause loss of moisture in the initially saturated porous waste form, impacting the waste form aging and transport of the constituents from within the material. Depending on the disposal scenario, the waste form is subject to multiple environmental aging processes such as carbonation, oxidation, sulfate attack, chloride penetration, and leaching [13–16]. In the case of near surface disposal, carbonation and oxidation along with leaching attracts special attention

because of the availability of CO_2, O_2, and water (constantly or intermittently) in the surrounding environment. Correlation has been observed between drying and carbonation in multiple experiments despite the lack of consensus on the relationship [17–21]. In addition to drying, varying CO_2 content in the surrounding environment due to potential accumulation in soil gas also raises uncertainty in estimating the carbonation rate and extent [22,23] over extended time intervals. The impact of aging on the long-term performance of the waste form and potential risks to the environment and human health have only been evaluated using what are considered bounding conditions that result in biased results that can have many orders-of-magnitude over-estimation of contaminant release [24]. These bounding results constrain effective and efficient waste management, also substantially increasing disposal costs.

While the mechanisms of carbonation in ordinary Portland cement (OPC) pastes and concretes are relatively well understood [25–28] and have been studied in some blended cement systems containing fly ash (FA) or blast furnace slag (BFS) [15,18,29,30], carbonation rarely has been studied for the Cast Stone type of material that contains high fractions of FA and BFS but very limited OPC [31,32], which yields a lower Ca/Si ratio in the solid matrix compared to OPC or common blended cement systems. In addition, the high salt content and the radioactive isotopes in the waste stream further increase the complexity of the material's mineralogy and pore water chemistry. While cementitious materials with high salt content have become a common application for waste disposal and construction [6,33–36], existing drying studies on cementitious materials have neglected the effects of salt pore solution on the capillary force and water activity that drives the moisture diffusion.

Assessment on the performance of the Cast Stone waste form is primarily based on leaching tests conducted on freshly prepared material (e.g., after 28 days of curing). Without the consideration of aging, Cast Stone has been found viable for the solidification of Hanford secondary liquid waste primarily in that the release of ^{99}Tc from the waste form through leaching testing is significantly lower than the regulatory threshold [37]. However, carbonation impacts the leaching of the constituents of potential concerns (COPCs) because it changes the material mineralogy, which reduces the pH of the pore water and alters pore structures [10,11,13,38–40]. The coupled impact of drying and carbonation on leaching from a cementitious material has rarely been studied [10,11] but is crucial for evaluating the retention ability for the COPCs in Cast Stone and other similar waste forms during field disposal scenarios.

This dissertation investigated the effects of environmental conditions that are expected in the field on carbonation in the Cast Stone waste form and evaluated the impact of carbonation in different environmental conditions on the leaching behavior of Cast Stone. Specific environmental factors considered include environmental relative humidity and CO_2 concentration. Using a combination of aging experiments, extensive material characterization, and geochemical speciation and reactive transport modeling, the

individual and coupled effects of drying and carbonation on water saturation, microstructure, chemical distribution, and leaching of constituents of potential concern (COPCs) were evaluated (Figure 1.1). A moisture transport model was developed to predict drying in Cast Stone as a function of environmental relative humidity considering the evolution of capillary force and salt solution water activity. Geochemical speciation coupled with reactive transport models were used to simulate leaching tests and gain insights into the impacts of drying and carbonation on the leaching of major constituents and COPCs. The reactive transport model provides a tool for predicting the long-term performance of the waste form. This study also informs the understanding of carbonation in alkali-activated materials due to the similarity in the composition with Cast Stone. Recent studies focus on using alkali-activated materials, which contains high volume of supplemental cementitious materials and an alkaline solution as a sustainable alternative to Portland cement for construction and other purposes [35,36,41]. The durability of alkali activated materials can be negatively impacted by their vulnerability to aging processes such as carbonation[31].

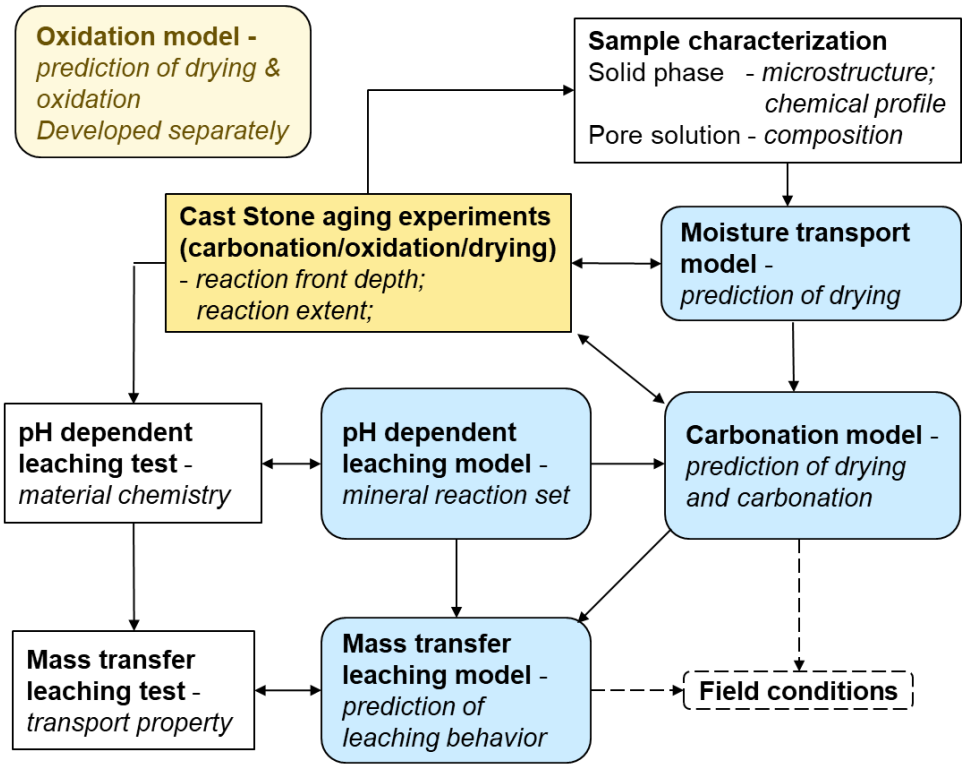

Figure 1.1 Framework of dissertation research

1.2 Research hypothesis, objectives and approach

The central hypothesis of this research is that drying and carbonation processes during aging of Cast Stone increase the rate of mass transport during leaching through a combination of physical and chemical changes to the microstructure of the Cast Stone material.

The overall objective of this research has been to quantify and develop models to estimate the impact of environmental conditions including relative humidity and CO_2 concentration on carbonation and leaching behavior from the Cast Stone waste form. A parallel related effort has been underway to examine the rates and impacts of oxidation, and the combined effects of drying, carbonation, and oxidation on COPC leaching.

The specific objectives of the research presented in this dissertation have been to:

1. Experimentally measure the change in relative saturation in Cast Stone as a function of external relative humidity and develop a moisture transport model that accounts for the effect of the salt solution on capillary forces and solution water activity.
2. Determine the rate and extent of carbonation as a function of environmental CO_2 concentration and environmental relative humidity.
3. Assess the impact of carbonation under different CO_2 concentrations on pH dependent leaching and diffusion-controlled mass transport leaching of major and trace constituents from Cast Stone and understand the underlying mechanisms through calibration and coupled use of geochemical speciation and reactive transport models.
4. Assess the coupled impact of drying and carbonation on diffusion-controlled leaching of major and trace constituents and through use of a reactive transport model to verify assumptions on the controlling mechanism.

The general approach for the research was to begin with an experimental investigation on the Cast Stone material subject to aging under various environmental conditions, followed by the development of a series of numerical, geochemical speciation and reactive transport models of the experimental cases, based on theories and data obtained from experimental results. Aging experiments were designed to independently evaluate drying as a function of relative humidity, carbonation as a function of CO_2 concentration, and oxidation, as well as their coupled effects. Granular and monolithic Cast Stone samples were aged in environmental conditions with different relative humidity (RH) conditions and CO_2 concentrations for various periods of time (Figure 1.2). The effects of oxidation on Cast Stone were examined as part of another study, and part of the results are provided in Appendix A.

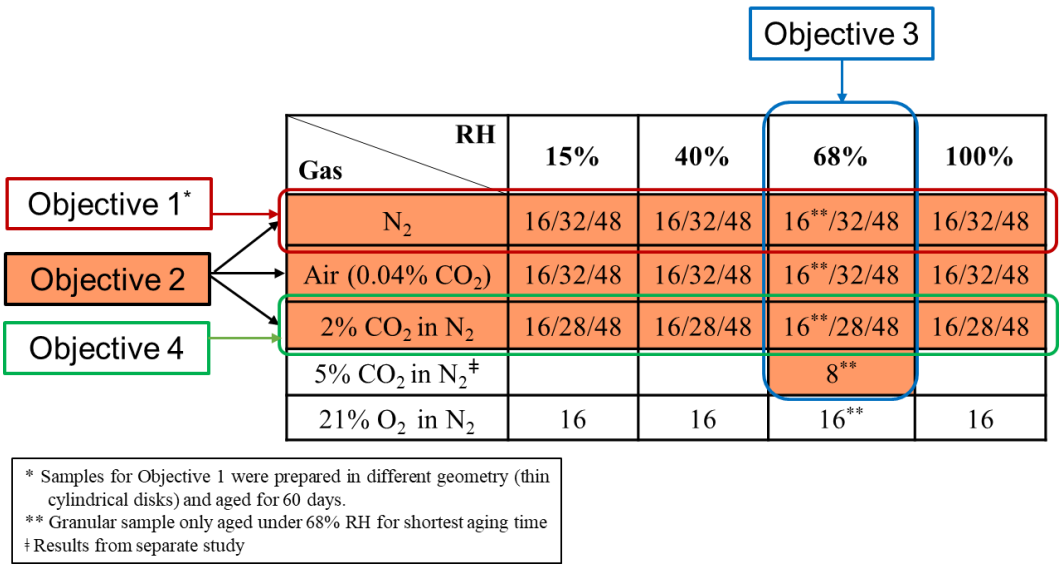

Figure 1.2 Design of Cast Stone aging experiments for each research objective.

*Values in the table indicate the aging times (in weeks) of samples in each aging condition. (ǂ) separate study performed by [42].

Drying of the Cast Stone material was studied by analyzing the 1) saturation profile as function of time and 2) redistribution of constituents. Carbonation in the material was investigated by analyzing 1) ingress rate and reaction extent, 2) physical and chemical evolution, and 3) leaching behavior using pH dependent batch leaching and monolith diffusion leaching tests. The relationships between drying, CO_2 content, and carbonation were investigated. Geochemical speciation and reactive transport models were developed to simulate the carbonation and leaching of Cast Stone under specific conditions representative of the experimental conditions.

1.3 Structure of the dissertation

This dissertation is organized into six Chapters. In Chapter 2, a water transport model coupling capillary liquid flow with vapor diffusion is introduced that describes the drying process measured for the Cast Stone waste form. The vapor-liquid equilibrium formulation as the driving force for vapor diffusion accounts for the evolution of capillary force and water activity induced by salt pore solution condensation. In Chapter 3, the impact of environmental CO_2 concentration and RH on the carbonation of Cast Stone is assessed by evaluating the penetration rate, carbonate content, hydroxide flux from diffusion-controlled leaching, water saturation profile, and redistribution of highly soluble constituents. A conceptual model for coupled drying and carbonation is introduced and the relationships between the two aging mechanisms are discussed. In

Chapter 4, the effect of carbonation on leaching of major and trace constituents from the Cast Stone is discussed based on results from experiments and simulations. Liquid-solid partitioning (LSP) and chemical speciation of the constituents were analyzed using pH dependent leaching and geochemical speciation modeling. Diffusive transport of the constituents in the Cast Stone was evaluated using diffusion-controlled mass transport leaching tests and reactive transport modeling using the geochemical speciation model derived from pH dependent leaching. Chapter 5 discusses the coupled drying and carbonation effects on mass transport leaching behavior from Cast Stone. Carbonation front depth in the material estimated from the reactive transport modeling of carbonation ingress and from leaching is compared with experimental measurements to inform the estimation of uncertainties in future modeling work.

2. DRYING MODEL OF A HIGH SALT CONTENT CEMENTITIOUS WASTE FORM: EFFECT OF CAPILLARY FORCES AND SALT SOLUTION

Abstract

A water transport model coupling capillary liquid flow with vapor diffusion is developed to describe the drying process for a cementitious waste form with high salinity pore water. Vapor-liquid equilibrium is formulated as the driving force for vapor diffusion and the model accounts for pore capillary and high salinity effects on water thermodynamic activity. Pore filling and pore water surface tension as a function of pore size distribution and water saturation have been quantified for the material. Geochemical speciation modeling is used to simulate pore water activity as a function of composition over the range of saturation. The theoretical relationship between relative humidity and water saturation generally agrees with experimental measurement, and the developed model can predict drying rates under various external relative humidity conditions. The model was developed to be incorporated into reactive transport models considering the effects of drying such as salt redistribution and efflorescence.

2.1. Introduction

Predicting moisture distribution and transport is important for estimating durability and constituent transport for cementitious materials. Depletion of moisture can lead to shrinkage cracking and facilitates diffusive ingress of reactive gases (e.g., CO_2, O_2) from the surrounding environment [43]. For example, carbonation of cementitious materials can progress faster and further into the material under unsaturated conditions. Morandeau, et al. [29,44] found that carbonation in materials with fly ash replacement is more sensitive to drying than that in OPC-based materials, as the former materials contain coarser capillary pores. However, some researchers found insufficient moisture within a material can restrict carbonation reactions [17,19,45].

Moisture transport occurs as a result of the thermodynamic imbalance between the core of the material and the surrounding environment. Hydraulic pressure gradients lead to the capillary movement of liquid water, and the gradient in relative humidity (RH) drives diffusion of water vapor. Capillary water flow transports dissolved ionic constituents [46], while vapor diffusion does not. This difference makes it important to distinguish between both mechanisms of water transport when considering mass transport of material constituents such as salts and hazardous species. Although liquid phase ionic diffusion can relax internal concentration gradients (albeit at a slower rate than capillary flow), some salts can crystallize in the pores

near the surface of the material when chemical supersaturation is reached via evaporation [47–50]. One of the consequences is efflorescence, which is a common issue with building materials and some geologic materials, especially for those materials with high salt content in the pore solution [41,51–54].

High salt content is found in many types of cementitious waste forms and construction materials. Cementitious waste forms have been used to solidify concentrated liquid waste such as landfill leachate and radioactive waste to immobilize constituents of concerns [33,55–58]. For example, a cementitious waste form referred to as Cast Stone is being investigated as a treatment method for near-surface disposal of low-activity nuclear waste and secondary waste with high salt content generated at the U.S. DOE Hanford Site (Richland, Washington) [58]. A similar waste form named saltstone has been used for low-activity nuclear waste disposal at the DOE Savannah River Site (Aiken, South Carolina) [57]. The semi-arid environment at the Hanford Site raises concerns about drying effects on waste form performance [24]. Recent studies also focus on using alkali-activated materials as an alternative to Portland cement for construction and other purposes [35,36,41]. The high alkali content in these materials has been found more likely to produce salt-redistribution and efflorescence during drying [41]. Therefore, a moisture transport model is not only important for predicting the moisture profile within the cementitious material but also for predicting the redistribution of pore solution components as a response to capillary flow and drying.

Numerous efforts have focused on modeling moisture transport in cementitious materials. The most common modeling practice uses a non-linear, diffusion-type equation with the water diffusivity being a function of water saturation [46,59–66]. The functional relationship between diffusivity and saturation is usually derived empirically by a water vapor sorption isotherm (WVSI) from a water desorption (drying) experiment. Although models have been successful in predicting moisture loss from materials of interest, most of these models lack the basis for quantifying the transport of dissolved ions and predicting redistribution of constituents within the material during drying because they do not distinguish mechanisms between capillary water flow and water vapor diffusion. Samson et al. [66] and Johannesson et al. [67] have adopted models distinguishing vapor phase from liquid phase transport, but both use empirically derived water diffusivity for vapor diffusion. Since the physical and chemical properties of materials may change during aging, empirical models derived from the measurement of the initial material could mis-predict the drying of the material over the long-term.

To distinguish the transport of liquid water and water vapor, it is necessary to use different sub-models to account for each mechanism. Liquid flow driven by the hydraulic head gradient is described by the well-established Richards equation [68]. Vapor diffusion is driven by the gradient in water vapor pressure. Theoretically, the vapor pressure in the pore is governed by Kelvin's equation, which includes effects of surface tension, contact angle, pore size, and vapor pressure of the pore solution [52,69–73]. Study shows

that there can be large differences in the drying characteristics of OPC-based materials and materials containing supplementary cementitious materials (fly ash, slag, etc.) due to the different pore structure characteristics [70]. Furthermore, as a result of high salinity in the pore solution and the increase in pore solution chemical saturation as drying progresses, the effect of salt solutions on the surface tension and water activity becomes significant in cementitious materials with high salt content [52,53,72,73]. Estimation of vapor liquid equilibrium based on theoretical calculation is therefore important for simulating drying in high salt cementitious materials.

The objective of this study was to develop a model that mechanistically accounts for both capillary liquid and vapor phase water transport in the Cast Stone waste form during drying. Hydraulic and pore water properties of the material were experimentally characterized or were estimated using a geochemical speciation model and then used to derive the relative humidity (equivalent to water thermodynamic activity) as a function of water saturation based on Kelvin's equation. The measured pore size distribution of the material was used to relate water saturation to maximum water-filled pore size. The impact of a high ionic strength salt solution and capillary forces within cement pores on vapor-liquid partitioning has been quantified. Subsequently, two sub-models have been derived to account for moisture transport by liquid capillary transport and by vapor phase diffusion using the basic relationships of hydrology and diffusion, and then these sub-models have been coupled using a four-stage conceptual model to describe the drying process. Drying experiments were conducted to provide key model parameters (surface mass transfer rate, gas phase tortuosity, etc.) and to compare with modeling results. Finally, the relative contributions of each mechanism (liquid or vapor transport) to water flux during the drying process has been evaluated.

2.2 Material and experimental methods

2.2.1 Material preparation and characterization

The Cast Stone cementitious binder is a mixture of class F fly ash (FAF), blast furnace slag (BFS), and Type I/II ordinary Portland cement. The binder is mixed with a salt waste solution containing 5M sodium [74] at a water to binder ratio of 0.48. Cast Stone samples were cured at 25 °C and 100% RH under nitrogen for 90 days to allow complete hydration and full initial saturation, while minimizing carbonation and oxidation. The material preparation procedure follows that described by Lockrem [4].

The bulk porosity of Cast Stone was derived from the skeletal density measured by nitrogen pycnometry using a Micromeritics AccuPyc II 1340 pycnometer (Micromeritics Instrument Corp, Norcross, Georgia).

Prior to measurement, samples of Cast Stone were oven-dried at 60 °C under vacuum for 24 hours. The composition of Cast Stone and the dry bulk density, skeletal density, and porosity are shown in Table 2.1.

Table 2.1 Composition and physical properties of Cast Stone.

Component (wt %)	OPC	FAF	BFS	Salt waste solution	Dry bulk density (g/cm^3)	Skeletal density (g/cm^3)	Porosity* (cm^3/cm^3)
	4.8	27	28.2	40	1.40	2.40	0.41

*Porosity = 1-dry bulk density/skeletal density.

The pore size distribution in Cast Stone was characterized by a combination of nitrogen adsorption/desorption (N_2 sorption) and mercury intrusion porosimetry (MIP) to account for the difference in the optimum measurement range of the test methods [75–78]. Mercury intrusion has been found to cause damage to pore structure when high pressure is applied to measure small pore size [78]. Meanwhile, the application range of the calculation model to N_2 sorption data is in the mesopore to micropore range, because coarser pore sizes (>50 nm) are assumed to remain empty during N_2 sorption [79]. Mesopore structure was determined by N_2 sorption conducted at 77.2 K using a Micromeritics 2020 Accelerated Surface Area and Porosimetry System. The pore size distribution between 1.7 and 30 nm diameter was derived assuming cylindrical pores using the Barrett, Joyner, and Halenda (BJH) model [76]. Macroscale pore structure to a minimum pore diameter of 3 nm was determined by MIP using a Micromertics AutoPore V9600 porosimeter up to a maximum pressure of 430 MPa.

2.2.2 Pore water extraction and properties

The pore water of the Cast Stone material was approximated by conducting an up-flow column percolation experiment with deionized water flowing through a packed bed of crushed Cast Stone material. Eluate water volume was up to a liquid-to-solid ratio of 0.31 mL/g-dry, which approximates one pore volume exchange. The concentrations of constituents in the extract were analyzed with inductively couple plasma-optical emission spectrometry (ICP-OES, Agilent Technologies, Santa Clara, CA) following EPA Method 6010D [80]. The concentrations of anions were analyzed with ion chromatography (IC, Metrohm USA, Riverview, FL) following EPA Method 9056A [81]. Electrical conductivity, pH, and density of the extract also were measured.

The composition and properties of the pore water are listed in Table 2.2. The concentrations of nitrate and nitrite anions have been corrected to charge balance the solution. The ionic strength was estimated from the measured cation and anion concentrations. Equilibrium relative humidity was measured above the extracted pore water surface to estimate the water activity of the pore solution. Relative humidity is a measure of water activity in the vapor phase, and at vapor-liquid equilibrium, a direct measure of water activity in solution. Notably, the pore water contained high sodium content that can potentially precipitate in the form of sodium nitrate, sodium nitrite, and sodium sulfate as the material dries, as shown by geochemical speciation modeling results in section 2.5.1.

Table 2.2 Chemical composition and properties of Cast Stone pore water.

Constituents	Al	Ca	Cr	K	Na	Si	SO_4^{2-}	NO_3^-	NO_2^-	CO_3^{2-}
(mol/L)	0.0026	0.0015	0.0011	0.161	2.61	0.0049	0.22	1.13	0.409	0.25

Properties	Density (g/cm^3)	Ionic strength (mol/L)	Water activity	pH
	1.14	3.3	0.95	12.98

2.2.3 Sample drying in controlled environments

Hydrated samples of Cast Stone were cut into thin cylindrical disks (25.8 mm d×10 mm h) and were first equilibrated at 100% RH for approximately 7 days until a consistent mass (weight difference less than 0.5%) was achieved for three consecutive daily measurements. Samples were saturated by vapor equilibration rather than immersion in water because the Cast Stone matrix can be damaged when contacting with water, which is likely due to the dissolution of soluble salts [82]. Saturated samples were then transferred into sealed containers for drying in lower RH environments. The RH in the sealed containers were maintained at 11%, 33%, and 68% using saturated salt solutions of lithium chloride, magnesium chloride, and sodium nitrite, respectively [83] with samples placed 1 cm above the solution. The mass of each sample was measured at the end of the first 48 hours and then monitored every seven days, until two successive measurements of mass show a decrease of less than 0.02% (approximately 58 days in total).

To measure the relative humidity of the saturated material, size reduced granular material (2 mm diameter) was mixed with a small amount of water to fill the pore spaces. The relative humidity at equilibrium over the mixture in the container was measured.

Chemically bound water in samples equilibrated under each drying condition was measured using thermogravimetric analysis coupled with mass spectroscopy (TGA-MS) following the method described in Maruyama et al. [84]. TGA was carried out using a TA Instruments Q600 SDT analyzer (New Castle, Delaware, USA) under nitrogen gas flow. Approximately 25 mg of powdered sample was initially equilibrated at a temperature of 105°C until constant weight was reached to remove evaporable water prior to heating to 500°C at a rate of 10.0°C/min [84]. Chemically bound water was estimated by sample mass loss between 105°C and 400°C following the reported dehydration temperature range for C-S-H [31,85]. Mass spectroscopy was used to confirm water as the gaseous decomposition product under the above temperature range. Example of TGA data analysis is shown in (Figure B3).

2.3. Modeling approach

2.3.1 Theory of drying from cementitious material

2.3.1.1 Conceptual model

The drying process is based on a four-stage conceptual drying model that considers different controlling mechanisms at each stage (Figure 2.1) as proposed by Garrabrants and Kosson [63]. Each position in the material undergoes up to four drying stages throughout the drying process, characterized by declining water saturation *S*. Water saturation is defined as the volume fraction of water in pore space. The initially water saturated sample at $x=l/2$ (where l is the thickness of the sample) is exposed to air (Stage 0; initial condition). With environmental relative humidity lower than the water activity, water molecules evaporate from the sample surface to the air. After drying begins, there exists a continuous liquid phase in the material with the vapor phase discontinuous (Stage I). Hence, water transport is dominated by the liquid capillary flow and the distribution of water saturation within the material remains relatively constant with location. As water saturation decreases below the capillary saturation (Stage II), where a continuous vapor phase forms, an internal pressure gradient of water vapor is introduced. The moisture transport consists of both vapor diffusion and liquid capillary flow. Finally, when water saturation is further reduced to less than insular saturation (Stage III), where the liquid phase is discontinuous, liquid capillary flow is restricted and the moisture transport is controlled by vapor diffusion. Throughout the whole process, local vapor-liquid equilibrium is assumed. The setting of all the model parameters is discussed in section 2.3.3.

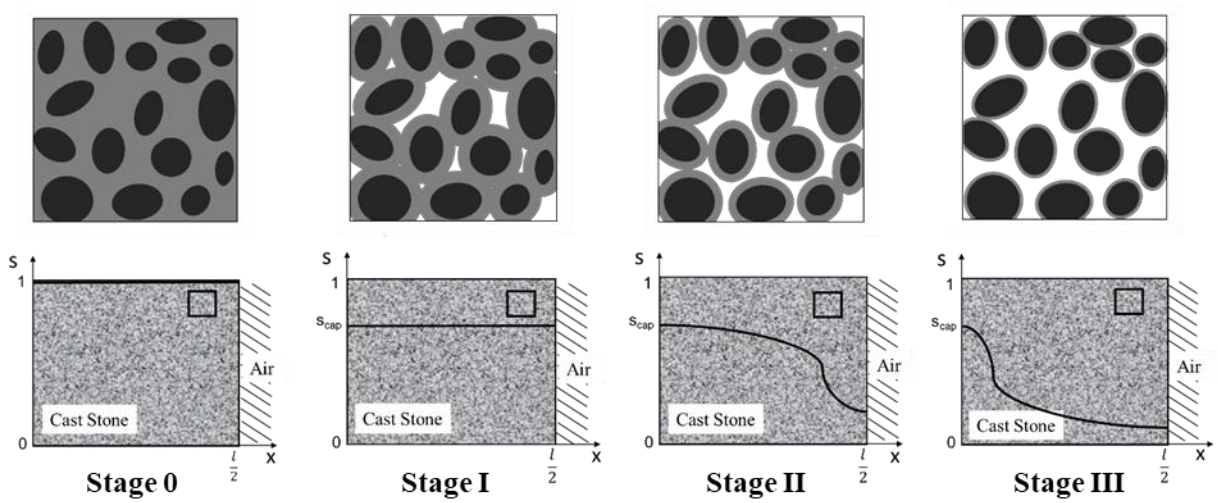

Figure 2.1 Conceptual model of the drying process following Garrabrants and Kosson [63]. Stage 0-I: liquid transport controlled; Stage I-II: liquid and vapor transport; Stage II-III: vapor transport controlled. Plots in the lower row indicate the saturation profile at the specific stage.

2.3.1.2 Vapor-liquid equilibrium in capillary pores

In a curved vapor-liquid surface, at equilibrium, water vapor pressure P is described by Kelvin's equation [69]:

$$RT \ln \frac{P}{P^*} = 2\sigma \frac{V_{m,l}}{r} \tag{2-1}$$

where P^* is saturated water vapor pressure, σ is surface tension, r is curvature radius of the pore water surface that is also considered the pore radius, R is the universal gas constant, T is temperature, and $V_{m,l}$ is molar volume of water vapor. As relative humidity H is defined as H=P/P_0, where P_0 is vapor pressure of pure water, and water activity of pore solution H_{sol} is defined as $H_{sol} = P^*/P_0$, water vapor pressure is related to the relative humidity and water activity of pore solution in the following form:

$$\frac{P}{P^*} = \frac{\frac{P}{P_0}}{\frac{P^*}{P_0}} = H/H_{sol} \tag{2-2}$$

Substituting Eq. 2-2 into Eq. 2-1 and rearranging yields an expression for pore water relative humidity H:

$$H = exp\left(-\frac{2V_{m,l}}{RT}\frac{\sigma}{r}\right) \times H_{sol} \quad (2\text{-}3)$$

In Eq. 2-3, the molar volume of pore solution $V_{m,l}$ was assumed constant with ionic strength. Pore size radius r, surface tension σ, and water activity of the pore solution H_{sol}, were determined from experimental measurements or model simulation, and their functional relationships with water saturation and pore solution composition were determined.

2.3.1.3 Water activity and surface tension as functions of pore solution composition

Water activity of the pore solution as a function of solution composition was derived by simulating the drying process of pore solution under equilibrium with the solid phases of Cast Stone. The geochemical speciation modeling software PHREEQC (version3.2.12, United States Geological Survey [86]) was used to determine water activity as a function of composition and liquid-solid equilibrium at different drying states. The mineral assemblage [87–89] and its derivation, and aqueous composition of the initial reaction system are given in Appendix B-I, Table B2 and Table B3, respectively. The mineral assemblage of the material was developed based on the geochemical speciation modeling results of the solubility of major constituents (Na, Ca, Si, Al, S, K, N, and C) compared to experimental measurements [90]. In the simulation, water is removed from the system step by step and liquid-solid equilibrium is solved for at the end of each step. Because of the high ionic strength of the salt solution (I>3.3 M), the Pitzer thermodynamic model [91,92] with ion interaction parameters for major solution constituents was selected to calculate activity of solution species. Interaction parameters for NO_3^-, $Al(OH)_4^-$, and $H_2SiO_4^{2-}$ ions that were not in the original PHREEQC Pitzer database [92] were collected from literature (Table B4). Water activity was computed from the osmotic coefficient, which was derived from Pitzer parameters, as described by Eq. 2-1 and 2-25 in Plummer, et al. [92].

A functional relationship was derived between the simulated water activity of pore solution H_{sol} and pore solution concentration factor F, where F is equal to 1 at the reference state of the initial pore water concentration at water saturation of the material ($S=1$). F decreases proportionately from 1 to 0 as the pore solution is concentrated by evaporation and F increases proportionately as pore water is diluted, such as for experiments. In the pore solution, F is assumed equal to S in pore matrix. The H_{sol} *as a* function of F is fit using a three-parameter exponential function regressed to point value estimates of H_{sol} from PHREEQC calculations at different values of F:

$$\widehat{H_{sol}} = a + b \cdot exp(c \cdot F) \quad (2\text{-}4)$$

Surface tension as a function of pore solution concentration factor F was derived assuming the major electrolyte component in pore solution is $NaNO_3$, with the $NaNO_3$ concentration increasing from the initial condition due to evaporation. Surface tension of a sodium nitrate solution (1-12.2 mol/L) from Washburn, et al. [93] was used (Table B1). A four-parameter bi-exponential function was used to fit the ratio between solution surface tension σ and pure water surface tension σ_0 to pore solution concentration factor:

$$\widehat{\left(\frac{\sigma}{\sigma_0}\right)} = \; d \cdot exp(-e \cdot F) + f \cdot exp(-g \cdot F) \tag{2-5}$$

2.3.1.4 Vapor diffusion

Vapor diffusion is driven by the water vapor pressure gradient and is assumed to follow Fick's first law of diffusion. The diffusion equation was derived starting from the mass balance of water vapor:

$$\frac{\partial \rho_v}{\partial t} = -\frac{\partial j_v}{\partial z} \tag{2-6}$$

where ρ_v is the partial density of water vapor, j_v is the water vapor flux, t is time, and z is the distance from outer boundary. The equation of state for ideal gases is:

$$\rho_v = \frac{P}{R_V T} \tag{2-7}$$

where R_v is ideal gas constant for water vapor. According to Fick's first law, the flux of substance is proportional to its concentration gradient:

$$j_v = -\frac{\partial \rho_v}{\partial z} = -D_{0,G}\frac{\partial (P/R_V T)}{\partial z} = -D_{0,G}\frac{1}{R_V T}\frac{\partial P}{\partial z} \tag{2-8}$$

where $D_{0,G}$ is the free diffusivity of water vapor in air. $D_{0,G}$ is replaced by an expression for the effective diffusivity $D_{e,G}$ to account for the varying cross-sectional area within the pore as water saturation changes. The effective diffusivity is a function of porosity ε, gas phase tortuosity τ_G, and water saturation based on the relationship derived by Millington and Quirk [94,95]:

$$D_{e,G} = \frac{D_{0,G}}{{\tau_G}^2}(1-S)^{10/3} \cdot \varepsilon^{4/3} \tag{2-9}$$

Substituting Eq. 2-7 and Eq. 2-8 into both sides of Eq. 2-6:

$$\frac{1}{R_V T}\frac{\partial P}{\partial t} = \frac{1}{R_V T} \cdot \frac{\partial}{\partial z}\left(D_{e,G}\frac{\partial P}{\partial z}\right) \tag{2-10}$$

Since $P=H \cdot P_0$, then:

$$\frac{P_0}{R_V T}\frac{\partial H}{\partial t} = \frac{P_0}{R_V T}\cdot\frac{\partial}{\partial z}\left(D_{e,G}\frac{\partial H}{\partial z}\right) \tag{2-11}$$

Therefore, Eq. 2-6 can be simplified to

$$\frac{\partial H}{\partial t} = \frac{\partial}{\partial z}\left(D_{e,G}\frac{\partial H}{\partial z}\right) \tag{2-12}$$

In Eq. 2-12, vapor diffusion is driven by the gradient of relative humidity H, where H is defined as in Eq. 2-3 and effective diffusivity $D_{e,G}$ is defined as in Eq. 2-9. At the outer boundary, where the sample surface is in contact with air, the water transport is driven by an evaporation process within the interfacial layer. The evaporation mass transfer is driven by the relative humidity gradient at the surface [60]:

$$j|_{surf} = -D_{0,G}\frac{P_0 M}{RT}\cdot\frac{H_{amb} - H_{surf}}{\delta} = \eta\left(H_{amb} - H_{surf}\right) \tag{2-13}$$

where M is molar mass of water, δ is the thickness of interfacial layer, and H_{amb} and H_{surf} are environmental relative humidity and relative humidity at the material surface, respectively. The mass transfer coefficient η can be determined through experiment (Eq. 2-28) [96]. At the inner boundary, no flux is assumed:

$$j|_{center} = 0 \tag{2-14}$$

2.3.1.5 Liquid capillary flow

The Richards equation [68] describes liquid transport in unsaturated porous media, which is driven by the hydraulic pressure gradient:

$$\frac{\partial\theta}{\partial t} = \frac{\partial}{\partial z}\left[K[\theta]\left(\frac{\partial\varphi}{\partial z} + 1\right)\right] \tag{2-15}$$

where θ is the moisture content, φ is hydraulic pressure head, and K is the hydraulic conductivity that changes as a function of moisture content. For the case considered here, gravity is negligible compared to the capillary force and so the term +1 is omitted. The hydraulic pressure head is related to water saturation with an analytical function as defined by van Genuchten [97]:

$$\mathrm{S}_e = \frac{1}{[1 + (\alpha\varphi)^n]^m} \tag{2-16}$$

where, α, m, and n are the van Genuchten parameters and were determined through laboratory testing [98]. The effective water saturation S_e is defined as:

$$S_e = \frac{\theta - \theta_r}{\theta_s - \theta_r} \tag{2-17}$$

where θ is the moisture content per unit volume of bulk material. θ_s and θ_r represent the saturated and residual moisture content, respectively. Therefore:

$$\varphi = -\frac{1}{\alpha}\left[\left(\frac{\theta-\theta_r}{\theta_s-\theta_r}\right)^{-1/m}-1\right]^{1/n} \tag{2-18}$$

The hydraulic pressure head can also be theoretically derived from surface tension and pore radius by the Young-Laplace equation [78]. Hydraulic conductivity is related to saturation as defined by the Mualem-van Genuchten type function:

$$\mathrm{K}[\theta] = K_{sat}{S_e}^{L}\left[1-\left(1-{S_e}^{1/m}\right)^{m}\right]^{2} \tag{2-19}$$

where L is an empirical pore-connectivity parameter and assumed to be 0.5 [98].

2.3.1.6 Integration of sub-models

Vapor diffusion and liquid flow control different drying stages following the conceptual model used in this research (Figure 2.1). Assuming coupled transport mechanisms, the flux of the water mass from each of the two mechanisms are added together. The equations that follow describe the methodology of the combination.

Multiply both sides of Eq. 2-6 by unit total volume V gives the change of water vapor mass m_v:

$$\frac{\partial m_v}{\partial t} = -\frac{\partial j_v}{\partial z}\cdot V \tag{2-20}$$

Replace j_v with Eq. 2-8 and $P=H\cdot P_0$:

$$\frac{\partial m_v}{\partial t} = \frac{\partial}{\partial z}\left(\frac{P_0}{R_V T}\cdot D_{e,G}\cdot V\cdot\frac{\partial H}{\partial z}\right) \tag{2-21}$$

Represent $\frac{\partial H}{\partial z}$ with:

$$\frac{\partial H}{\partial z} = \frac{\partial H}{\partial S}\frac{\partial S}{\partial z} \tag{2-22}$$

For liquid flow, multiply both sides of Eq. 2-15 with the total volume and water density ρ_l to give the change of water vapor mass m_l:

$$\frac{\partial m_l}{\partial t} = \frac{\partial}{\partial z}\left(V\cdot\rho_l\cdot K[\theta]\cdot\frac{\partial\varphi}{\partial z}\right) \tag{2-23}$$

Represent $\frac{\partial \varphi}{\partial z}$ with:

$$\frac{\partial \varphi}{\partial z} = \frac{\partial \varphi}{\partial S}\frac{\partial S}{\partial z} \tag{2-24}$$

Define the equivalent diffusivity of vapor $D_{v,eq}$ and liquid $D_{l,eq}$ as functions of water saturation (S) based on Eq. 2-9, Eq. 2-21, and Eq. 2-23:

$$D_{v,eq}[S] = \frac{P_0}{R_V T} \cdot \frac{D_{0,G}}{{\tau_G}^2} \cdot (1-S)^{10/3} \cdot \varepsilon^{4/3} \frac{\partial H}{\partial S} \tag{2-25}$$

$$D_{l,eq}[S] = \rho_l \cdot K[\theta] \cdot \frac{\partial \varphi}{\partial S} \tag{2-26}$$

Adding Eq. 2-25 to Eq. 2-26, the flux of water m_v is sum of the mass change of liquid and vapor:

$$\frac{\partial m_w}{\partial t} = \frac{\partial m_v}{\partial t} + \frac{\partial m_l}{\partial t} = \left(\frac{\partial}{\partial z}\left(D_{v,eq}[S] \frac{\partial S}{\partial z} \right) + \frac{\partial}{\partial z}\left(D_{l,eq}[S] \frac{\partial S}{\partial z} \right) \right) V \tag{2-27}$$

The values of $D_{v,eq}$ and $D_{l,eq}$ as functions of S are presented in section 2.5.3 and the contributions of liquid flow and vapor diffusion as a function of water saturation to drying at different external RH are compared.

2.3.2 Numerical methods

A one-dimensional (1-D) drying case is studied using a finite volume method to solve for the 1-D vapor diffusion and Richards equations. A Neumann boundary condition is set up based on the evaporation equation (Eq. 2-13). To make the water transport solution easily coupled with the more general reactive transport model including salt transport and geochemical speciation, the geochemical speciation and mass transport solver ORCHESTRA is used [99]. In the ORCHESTRA model set-up, the diffusion and advection modules are used, in combination with user defined modules containing the water activity expressions (Eq. 2-3-Eq. 2-5) and hydraulic property expressions (Eq. 2-18 and Eq. 2-19) to calculate the different fluxes describing water transport. A stable solution requires a relatively small spatial step Δx and time step Δt because of the strong nonlinearities of $D_{v,eq}$ and $D_{l,eq}$. The stability of the solution was checked by successively decreasing Δx and adjusting Δt according to the von Neumann stability criteria (Crank, Eq. 8.50) [100] until the two solutions converged.

2.3.3 Model parameterization

The simulation was performed for the drying experiment, where room temperature and ambient air pressure are used. One-dimensional drying was assumed at the top and bottom surfaces of the cylindrical disk sample

(25.8 mm d×10mm h). Porosity and pore size distribution data were obtained from nitrogen pycnometry, nitrogen sorption and MIP (section 2.2.1).

The set of van Genuchten parameters for Cast Stone used in Eq. 2-16 were obtained from the water retention test (ASTM D6836-02) that was performed on a cementitious waste form with a composition similar to Cast Stone [98]. Saturated hydraulic conductivity K_{sat} in Eq. 2-15 is calibrated against the 68% RH drying curve within the first 9 days, where water saturation in this period is greater than or close to capillary saturation and the drying is solely controlled by liquid water capillary flow.

The mass transfer coefficient η (Eq. 2-13) was calculated from the moisture loss in the first 48 hours of drying in 68% RH:

$$\eta = \frac{m_0 - m_{48h}}{(H_{surf} - H_{amb})At} \tag{2-28}$$

where A is the surface area. The gas phase tortuosity τ_G (Eq. 2-9) was calibrated against the 11% RH drying curve at time greater than 9 days, where water saturation during this stage is much less than capillary saturation; therefore, drying is controlled by gas phase diffusion. Key parameters of the model are listed in Table 2.3.

Table 2.3 Key parameters for drying model.

	Parameter	Value	Reference
ε	Porosity	0.41	Experiment
$D_{0,G}$	Free water diffusivity in air (m^2/s)	2.49×10^{-5}	[101]
K_{sat}	Saturated hydraulic conductivity (m/s)	2.1×10^{-11}	Calibrated
$\boldsymbol{\tau_G}$	Gas phase tortuosity (-)	20	Calibrated
η	Mass transfer coefficient ($kg/m^2/s$)	1.03×10^{-5}	Experiment
α	van Genuchten parameter (m^{-1})	1.008×10^{-3}	[98]
n	van Genuchten parameter (-)	1.671	[98]
λ	van Genuchten parameter (-)	0.5	[98]
θ_s	van Genuchten parameter (-)	0.41	Equivalent to porosity
θ_r	van Genuchten parameter (-)	0.012	Calculated*

* When the ratio between equivalent diffusivity of liquid $D_{l,eq}$ and equivalent diffusivity of vapor $D_{v,eq}$ equals 1/10 (see Figure 2.10), the corresponding moisture content is determined as the residual moisture content (θ_r) and the corresponding water saturation is defined as insular saturation. When moisture content is lower than θ_r, liquid phase transport (Richards Equation) is not effective.

2.3.4 Model verification

An independent case of 1-D drying in a cementitious material modeled using ORCHESTRA was compared to a known analytical solution [61] scripted in MATLAB, to assure the accuracy and correctness of the numerical calculations in ORCHESTRA. Model prediction agreed well with the analytical solution as shown in Figure B1.

2.4. Results

2.4.1 Pore size radius as a function of water saturation

The combination of the intrusion volume by MIP in the pore diameter range of 30-340 nm and the pore volume by N_2 sorption calculated with the BJH model in the pore diameter range of 1.7-30 nm is considered as the total pore volume. Assuming drying in the pores occurs progressively from the largest pores to the smaller pores without hysteresis, water saturation was calculated as the fractional cumulative volume at the corresponding pore radius (cumulative volume between 1.7 nm and the respective pore radius divided by total pore volume; Figure 2.2). A second-degree polynomial is used to fit the data with good correlation (R^2>0.99) over saturation range from 0.03 to 0.90. At the high saturation range (S>0.9), where the unfilled pore size is relatively large, drying is not controlled by vapor diffusion (Section 2.3.1) and the effect of capillary pore size is negligible. Therefore, the pore radius in this saturation range is excluded in the fitting of the function.

The pore radius can be impacted by the salt deposition during drying, especially for pore water with high salt content. The pore size characterizations in this study were performed on pre-dried material, but more detailed characterization or simulation is needed to account for the dynamic evolution of salt deposition during the drying and its impact on pore structure. However, compared to single drying cycle, it was found that repeated imbibition-drying cycles have larger impacts on the pore structure that might induce internal stress on porous matrix [47]. This effect was not considered in the current study that focused on a single drying process.

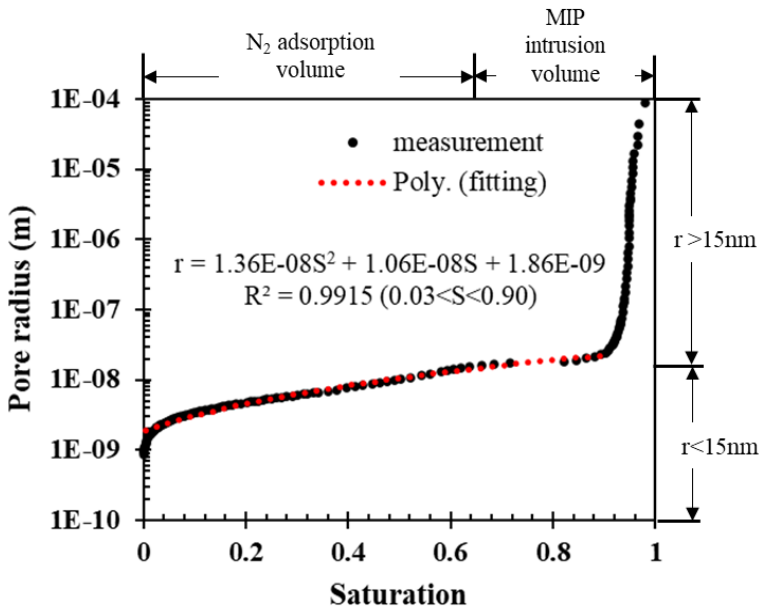

Figure 2.2 Representative pore radius as a function of water saturation of Cast Stone.

2.4.2 Surface tension and water activity as a function of pore solution composition

The surface tension σ of the pore water as a function of pore solution concentration factor F was based on the surface tension data of $NaNO_3$ solution from Washburn, et al. [93] (Figure 2.3).

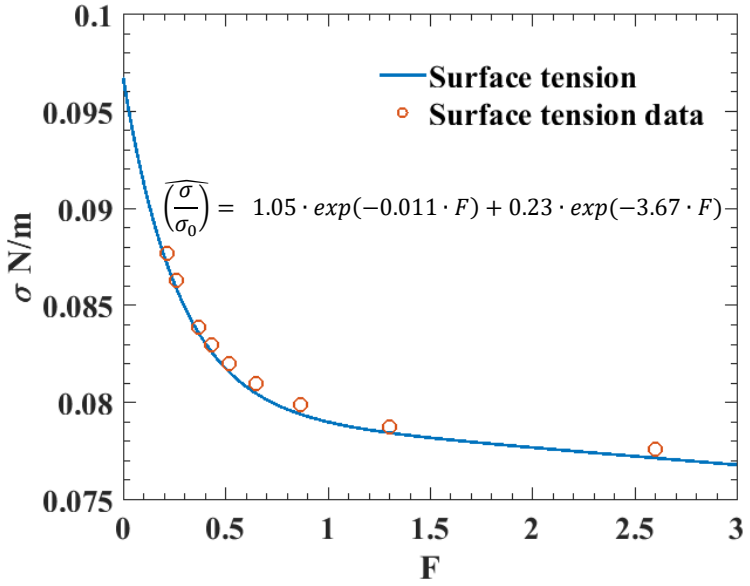

Figure 2.3 Surface tension of $NaNO_3$ solution as a function of pore solution concentration factor [93].

The PHREEQC simulation of the water activity of the pore solution as a function of pore solution concentration factor is shown in Figure 2.4. The result is compared with the water activity calculated from Raoult's law, which applies for an ideal solution. Other solution properties (ionic strength, pH, activity coefficient, concentrations of major constituents, and saturation indexes of minerals) as a function of drying are shown in Figure 2.5.

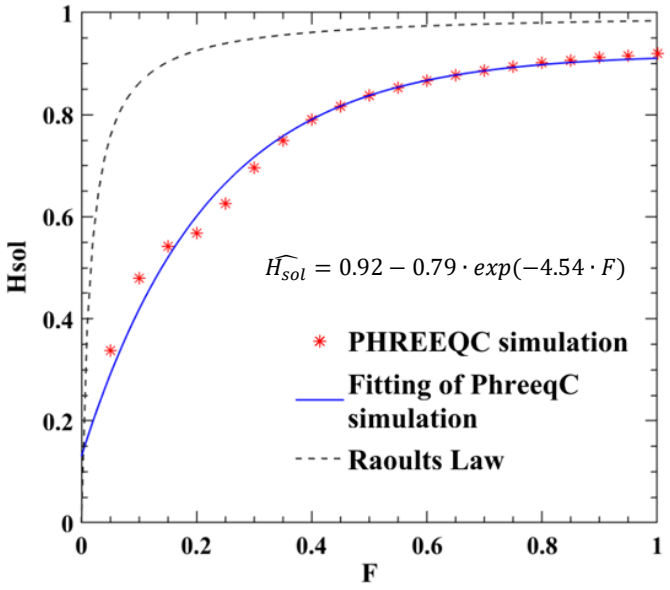

Figure 2.4 Water activity of pore solution as a function of pore solution concentration factor.

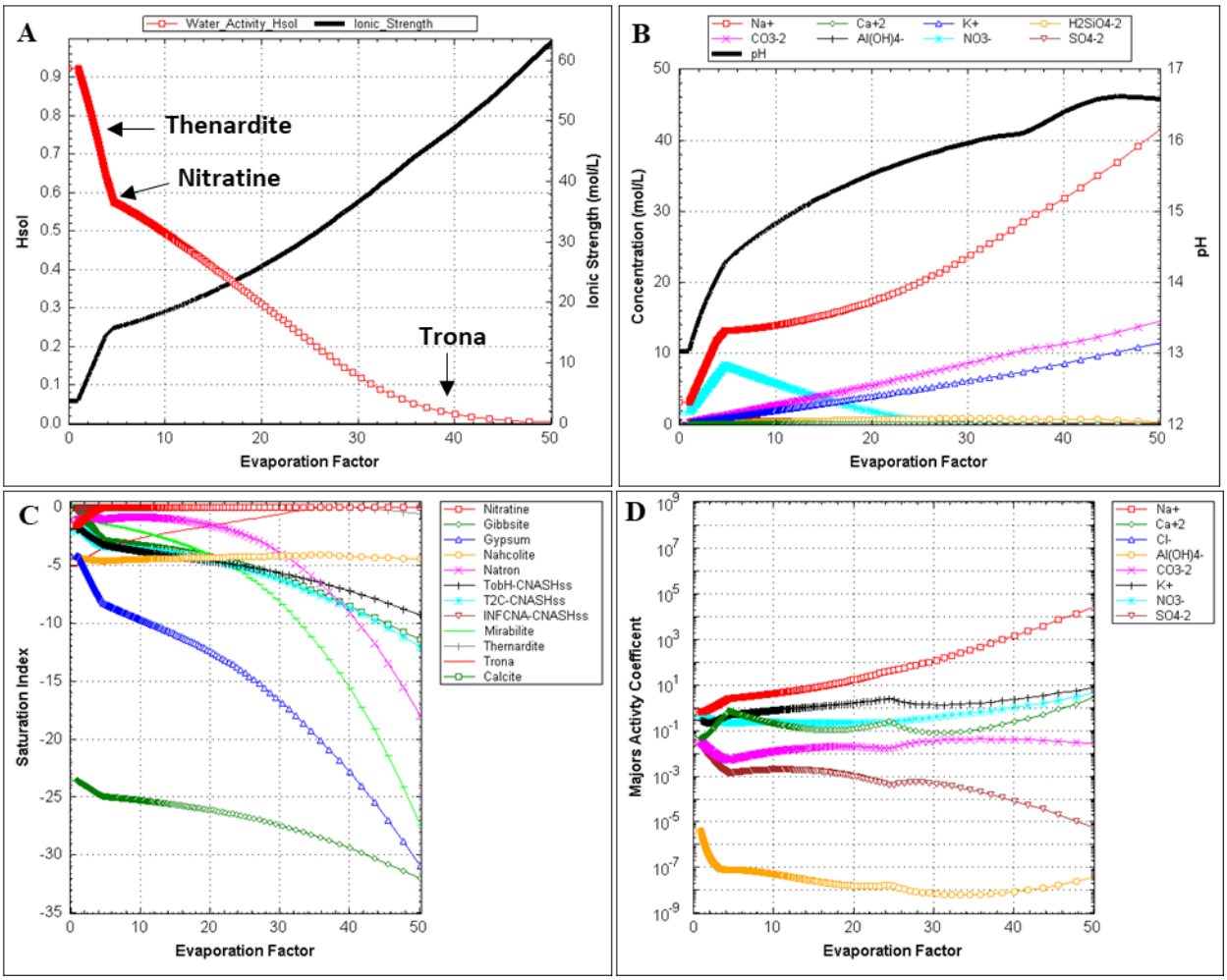

Figure 2.5 Solution properties as a function of evaporation factor* from PHREEQC simulation: A. Water activity and ionic strength; B. pH and concentrations of major species; C. saturation indexes of minerals**; D. activity coefficients of major ions.

*Evaporation factor: ratio of the volume of the initial solution to the volume of the final solution (=1/S). **Saturation index: SI = log(IAP/K_{eq}). IAP: ion activity product; K_{eq} equilibrium constant. SI>0: supersaturated; SI =0 saturated; SI <0 under saturated

2.4.3 Water saturation as a function of relative humidity

The measured water saturation of Cast Stone samples as a function of relative humidity under equilibrium is shown in Figure 2.6. Capillary saturation was determined by extrapolating the RH-S function from RH≤68 to the relative humidity over saturated material (indicated by the dashed line).

With water activity and surface tension as functions of pore solution concentration factor *F*, and pore radius as a function of water saturation *S* derived for Cast Stone material, and assuming *F* is equal to *S* in pore matrix, the theoretical relationship between relative humidity and saturation in Cast Stone as governed by

Kelvin's equation (Eq. 2-3) was derived (Figure 2.6). Calculation from Kelvin's equation generally fits the measurement, with slight underestimation of saturation within RH range of 0.1-0.8. The deviation is likely due to the hysteresis behavior of the material in the water sorption cycle [43,65,68,77]. Hysteresis in water sorption refers to the different equilibrium RH-S relationships measured in a material during its wetting versus its drying process. Factors such as pore connectivity (inkbottle effect) and a different shape of the liquid-vapor interface can result in hysteresis, but these differences are not considered in this model. Semi-empirical models exist that capture the effect of hysteresis through the measurement of the water adsorption/desorption isotherm [102]. Experimental studies by Baroghel-bouny [43,77] have shown that the hysteresis effects in cement pastes and concretes are most significant in the mid-RH range.

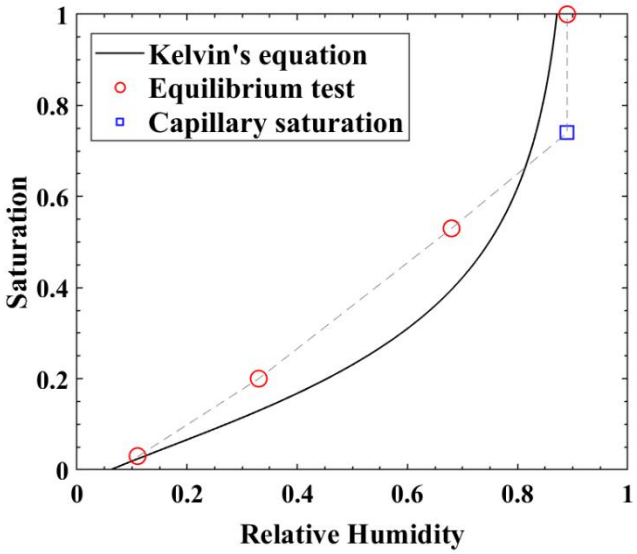

Figure 2.6 Water saturation as a function of relative humidity from measurement and Kelvin's equation.

2.4.4 Drying rate and experimental validation

The simulation results of water saturation as a function of drying time under 11%, 33%, and 68% RH are compared to experimental data in Figure 2.7. The simulation predictions and data generally agree, but the model slightly underestimates the initial drying rate, where capillary flow dominates. This underestimation can be explained by the deviation observed in Figure 2.6, where the measured water saturation value and the theoretical water saturation value differ most in the intermediate RH range.

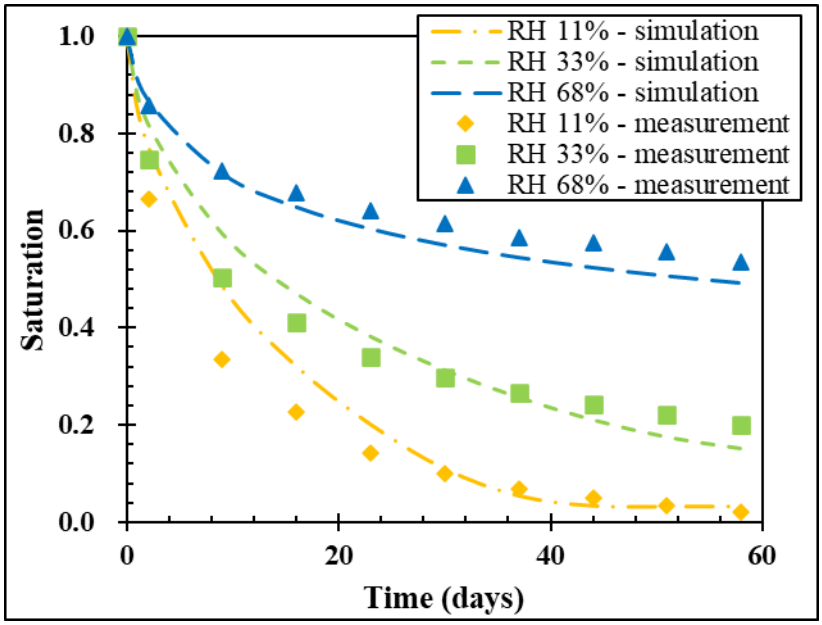

Figure 2.7 Experimental results and model predictions of water saturation as a function of time.

2.5. Discussion

2.5.1 Water activity of pore solution during drying

The water activity of Cast Stone pore solution is 0.92 from the PHREEQC geochemical speciation simulation incorporating the Pitzer activity model (Figure 2.4). The high concentration of dissolved sodium salts introduces strong interactions between molecules in solution that precludes the assumption of an ideal solution. Therefore, the water activity of pore solution from the Pitzer model deviates from the Raoult's law prediction.

The validity of thermodynamic calculations including the solid phases and initial pore solution composition is important for the accuracy of water activity calculation. As a reference, the simulated molar ratio of H_2O/(Si+Al) of CNASH_ss phases as a function of saturation are shown in Figure 2.8. The simulated results of both H_2O/(Si+Al) and Ca/Si are reasonable compared with the reported value range for saturated alkali-activated material (H_2O/Si $\approx$ 1, Ca/Si between 0.7-1.2, Figure B4) [103]. As a verification, thermogravimetric analysis coupled with mass spectroscopy (TGA-MS) was run on samples equilibrated to 11%, 33%, 68%, and 100% RH environments to analyze the content of chemically bound water (Figure 2.8). The measured relationship between chemically bound water and saturation resembles the relationship

between H_2O/(Si+Al) to saturation from simulation, indicating a reasonable representation of the chemical properties of the material under drying by the model.

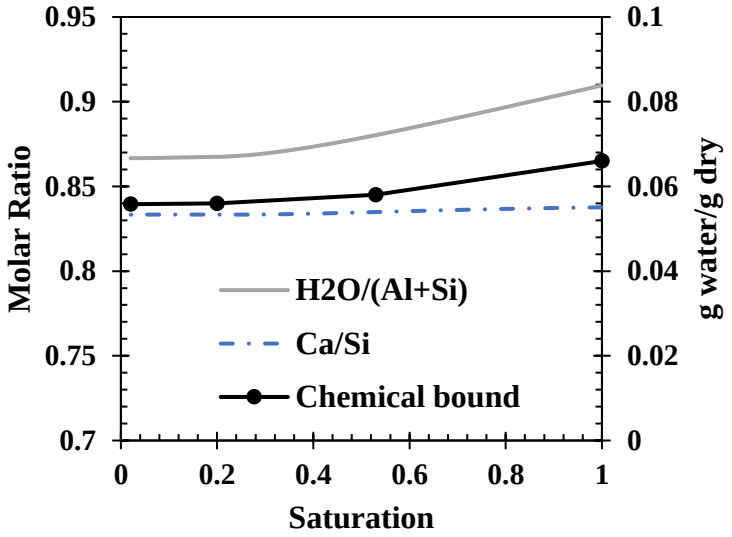

Figure 2.8 Molar ratio of H_2O/(Si+Al) and Ca/Si of CNASH solid solution in simulated system (left axis) and chemical bound water in Cast Stone material as measured from TGA-MS (right axis).

As water is removed from solution by evaporation, the ionic strength increases and water activity decreases. Three inflection points on the water activity curve (Figure 2.5A) correspond to the precipitation of thenardite (Na_2SO_4; H_{sol} = 0.65), nitratine ($NaNO_3$; H_{sol} = 0.57), and trona ($Na_3H(CO_3)_2 \cdot 2H_2O$; H_{sol} = 0.04; Figure 2.5C). The formation of two mineral phases with high numbers of waters of hydration (mirabilite ($Na_2SO_4 \cdot 10H_2O$) and natron ($Na_2CO_3 \cdot 10H_2O$)) is less favorable as drying progresses. Among the three end members used to describe the CNASH solid solution in Cast Stone, TobH-CNASHss (CaO:H_2O=1:2.5) has the highest amount of water of hydration and its relative amount in solid solution decreases from the beginning of drying. The relative amount of T2C-CNASHss (CaO:H_2O=1:1.7) initially increases followed by a decrease at an evaporation factor of 10; INFCNA-CNASHss that has the least amount of water of hydration (CaO:H_2O =1:1.3) is the most thermodynamically favored end member during drying.

The solubility of minerals is also dependent on the ionic strength in the solution. For both Na^+ and Ca^{2+}, the activity coefficient increases as ionic strength increases (Figure 2.5D). The increase in activity coefficient leads to a decrease in solubility of related salts because the activities of ions are increased, while the equilibrium constant remains unchanged. This result is different from a solution with low ionic strength, in which the presence of other salts (which increase the ionic strength of solution) would increase the

solubility of the oversaturated salt, because the activity coefficient generally decreases with increasing ionic strength at low ionic strengths [91].

2.5.2 Effect of capillary force and salt solution on relative humidity

The effects of capillary forces, which reflect surface tension and pore radius, in addition to pore solution water activity H_{sol}, which reflects ionic composition, control internal relative humidity H and both factors need to be considered when deriving the relationship between relative humidity and water saturation for a material (Figure 2.9). Two factors contributed to the declining internal relative humidity as saturation decreases: (i) decreasing pore size as pore water is removed and (ii) increasing surface tension and ionic strength as pore solution is concentrated by evaporation. The impact of surface tension of the salt solution was evaluated by reproducing the calculation of H from Kelvin's equation assuming constant surface tension as that of pure water (Figure 2.9, dashed line). The effect of pore solution water activity is shown by reproducing the calculation assuming pure water for both surface tension and pore solution activity (effect of pore radius only; dotted line). It can be seen that pore radius and the pore solution water activity significantly reduce the internal relative humidity and the impact is more significant when saturation is lower. Comparatively, surface tension of the pore solution plays a negligible role on controlling the internal relative humidity.

Pore size distribution of a cementitious material is dependent on the composition of dry binders, activating solution, and curing condition and can be characterized for specific materials. It needs to be noted that, studies have suggested that there might exist an adsorbed liquid-like layer (ALLL) between the pore wall and empty pore space before capillary condensation commences, with the thickness of the ALLL varying as a function of RH [78]. However, characterization of a pore size distribution is mostly frequently performed on a pre-dried specimen with a fixed thickness of ALLL. Therefore, the characterization might yield a larger pore radius than the actual capillary pore radius governing the vapor liquid equilibrium used in Kelvin's equation and needs to be evaluated for specific materials. In this study, sensitivity analysis indicated that the thickness of the ALLL has a minimal impact on the vapor-liquid equilibrium in Cast Stone (Figure B2) and, therefore, was not included in the model.

The change of surface tension of pore solution with drying depends on solution composition. Surface tension data are available for a series of salt solutions [93] but might also be derived by calculating surface excess and surface phase composition for the electrolyte solution [104,105]. For strong aqueous electrolytes such as $NaNO_3$, surface tension is greater than that in pure water and increases with concentration, which

thereby decrease the internal relative humidity as drying progresses (Eq. 2-3). Studies on C-S-H phases found that the increase of surface tension of pore solution during drying alters the organization of C-S-H sheets, and there is exchange of gel-pore water with interlayer water in the early stage of drying. Both factors cause the micropore structure change in Portland cement material during drying and has been mechanistically studied [106,107]. Drying shrinkage is also likely to occur to C-N-A-S-H phases in Cast Stone. In general, existing studies on alkali-activated materials showed that the alkali-activated slag might suffer greater drying shrinkage compared to OPC [108]. The addition of fly ash and a high concentration of NaOH solution both mitigate the shrinkage, due to their effects on coarsening pore structure and reducing surface tension of pore solution, respectively [108,109]. Some studies [110,111] found that alkali-activated fly ash paste is less sensitive to drying in terms of pore structure compared to OPC. The mechanism of the phase rearrangement and microstructural evolution under drying for Cast Stone needs to be further studied. However, the model presented allows dynamic pore structure as a function of drying to be independently input and used for calculation.

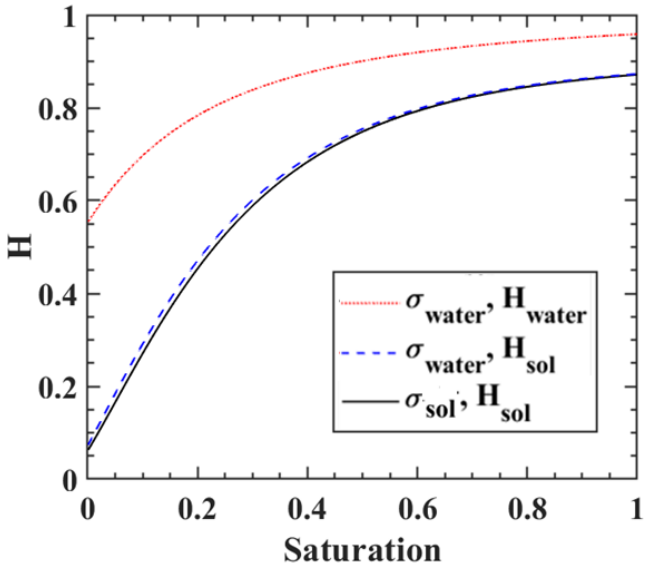

Figure 2.9 Effect of pore size, pore solution water activity and surface tension of pore solution on the internal relative humidity as a function of water saturation. (σ: surface tension; H: water activity of solution; subscript "water" indicates property of pure water, subscript "sol" indicates property of cast stone pore solution)

2.5.3 Vapor diffusion and liquid flow

The developed transport model enables separating vapor diffusion and capillary liquid flow, which is necessary for calculating redistribution of dissolved constituents during drying. Equivalent diffusivity of

vapor $D_{v,eq}$ and liquid $D_{l,eq}$ as a function of water saturation calculated based on Eq. 2-25 and Eq. 2-26 are shown in Figure 2.10. From the figure, capillary liquid flow (diffusivity) is greater than the water vapor diffusivity through the entire saturation range until saturation drops to below 0.07, and the corresponding environmental RH is 20%. As environmental RH decreases below 20%, the vapor diffusivity is greater than liquid water diffusivity. Since vapor transport does not transport dissolved constituents, prior water transport models, which do not separate vapor transport, would significantly overestimate the transport of ions under drier conditions. Both vapor diffusion and capillary liquid flow are dependent on the pore structure of the material [70,71,112], and the vapor diffusion is also dependent on the salt solution properties. Therefore, equivalent diffusivities of each mechanism need to be evaluated for specific materials.

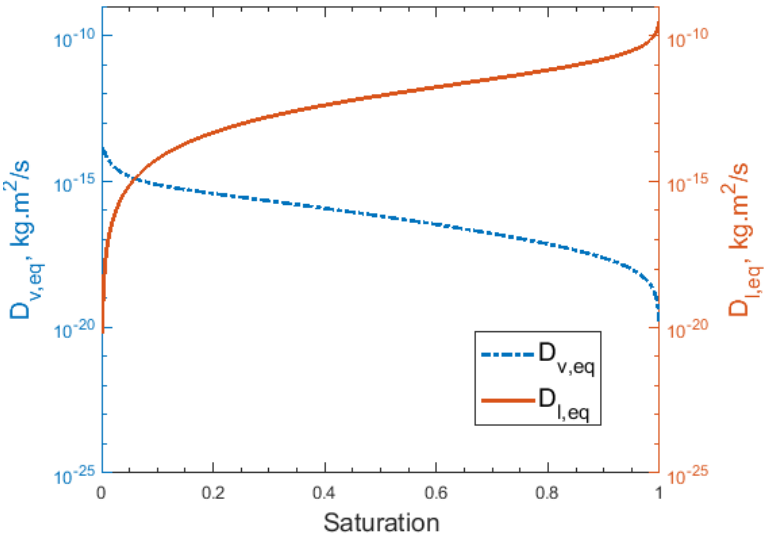

Figure 2.10 Equivalent diffusivity of water vapor $D_{v,eq}$ and liquid water $D_{l,eq}$ as functions of water saturation. Equivalent diffusivity as described in Eq. 2-25 and Eq. 2-26.

Drying is simulated by individual mechanisms (i.e., vapor diffusion and capillary flow) to compare the contribution of each mechanism to drying (Figure 2.11). For drying at external 11% and 33% RH, the hybrid model that includes both mechanisms best reproduces the measurements. Since vapor diffusion is driven by the gradient of water activity from the environment to the interior of the material, under low humidity environment (11% RH and later stage of drying in 33% RH), vapor diffusion dominates the water transport. Whereas in 68% RH, vapor diffusion is restricted due to the consistently high water saturation (Figure 2.6) and because vapor diffusion does not significantly contribute to water transport before capillary saturation is reached, drying is dominated by capillary liquid flow. The predictions of drying at external 68% RH are almost identical from the liquid flow and hybrid model. Therefore, the proposed model is most

useful for predicting the drying of cementitious materials in arid areas, where it provides the advantage of separating capillary flow and vapor diffusion.

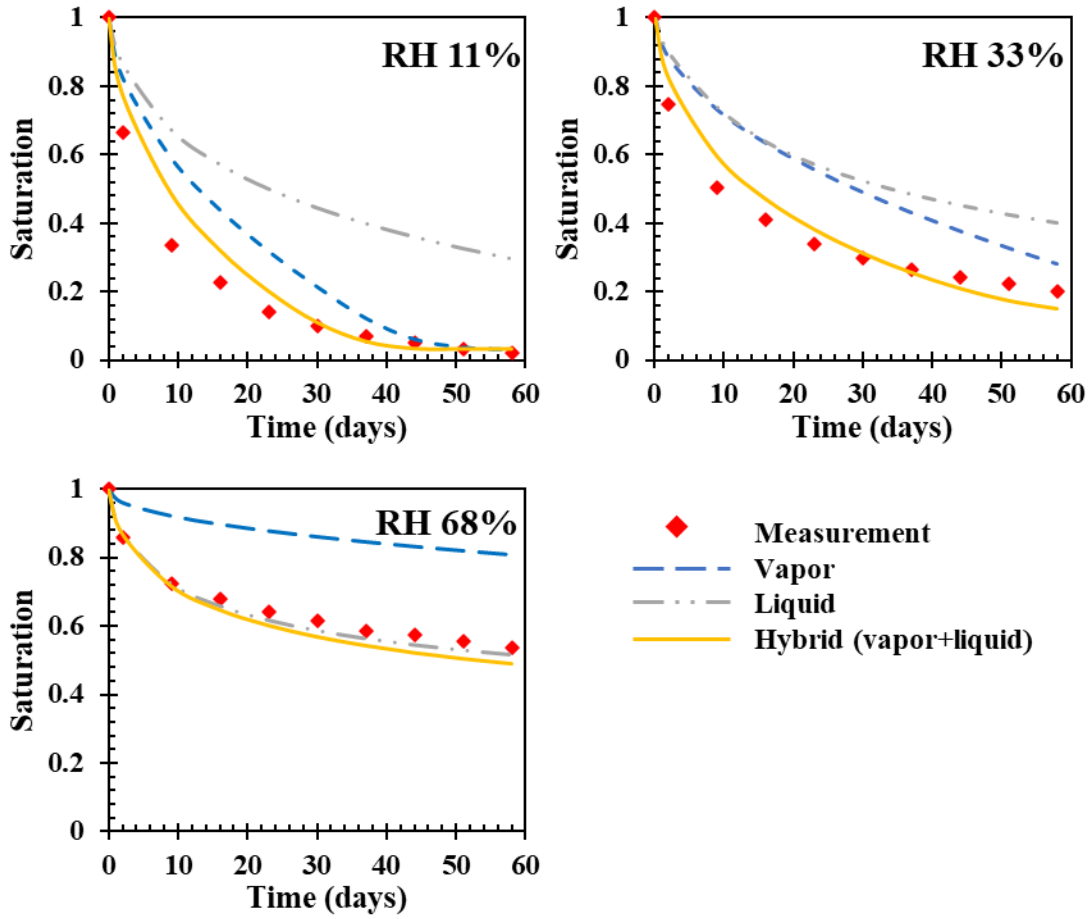

Figure 2.11 Contribution of capillary flow (Eq. 2-15) and vapor diffusion (Eq. 2-6) in different external relative humidity conditions.

2.6. Conclusions

The modeling approach described in this paper differs from previous studies in that the properties of the high-salt pore solution (surface tension and saturated relative humidity) and pore size are expressed as a function of water saturation and the model considers the combined effects of liquid flow based on Richards equation and vapor diffusion. The structure of the model makes the prediction of capillary transport of salt constituents during drying feasible. The modeling results of pore saturation as a function of time compared favorably with verification drying experiments on slices of Cast Stone material. Ongoing studies now focus on modeling the salt redistribution and carbonation during drying of Cast Stone in reactive environments.

To improve the accuracy of the model, microstructural properties of the material such as pore connectivity and microstructural evolution under drying need to be considered.

This study highlights the importance of experimental parameterization of pore structure and pore water properties on the modeling process to provide an improved model for the description of moisture transport from materials with highly saline pore solutions. Although pore salinity is not likely to be as important in traditional cementitious materials, it is expected that the same approach would provide an improved model of moisture movement through other cement-based materials.

3. THE ROLE OF ENVIRONMENTAL CONDITIONS ON THE CARBONATION OF AN ALKALI-ACTIVATED CEMENTITIOUS WASTE FORM

Abstract

Cast Stone is a cementitious wasteform being considered for the solidification of low activity waste at the DOE Hanford Site. Under near-surface disposal conditions in a semi-arid environment, Cast Stone is subject to drying and carbonation that may impact retention of waste constituents. This study investigates the effects of environmental CO_2 concentration and relative humidity (RH) on the carbonation of Cast Stone. The rate of carbonation front ingress and the extent of carbonation reaction were characterized for samples aged up to 48 weeks at three RH levels and two CO_2 concentrations. While the 68% RH environment allowed the greatest reaction extent, the 15% RH environment yielded the deepest carbonation front ingress. At 68% RH, there was a linear relationship between the ingress rate and CO_2 concentration. Carbonation reactions increased the drying rate of Cast Stone. Redistribution of sodium toward the wetting front was observed under drying and carbonation conditions.

3.1 Introduction

Cementitious materials have been developed and applied for the treatment and disposal of nuclear waste globally [113,114]. At the U.S. DOE Hanford Site (Richland, Washington), Cast Stone, a cementitious blended material composed of Class F fly ash (FAF, 45 wt%), blast furnace slag (BFS, 47 wt%), ordinary Portland cement (OPC, 8 wt%), and a high dissolved salt content liquid low activity waste (LAW) simulant [74] has been developed for potential immobilization of constituents of potential concern (COPCs) from the low-activity waste (LAW) and secondary waste effluents from the Waste Treatment and Immobilization Plant (WTP) [6,115]. The WTP effluent has a high sodium alkali content (2.8-4.3 mol/L NaOH) which favors the activation of the fly ash and slag [74], while the alkali conditions in the cured material tends to stabilize COPCs as hydroxides [90]. Cast Stone materials are expected to be placed in the near-surface Integrated Disposal Facility (IDF) in the highland desert environment of the Hanford Reservation.

During its life cycle, Cast Stone can be affected by several aging mechanisms that can alter the chemical and physical properties of the material and, potentially, change the retention of COPCs. One such aging mechanism is carbonation, or the reaction of alkaline media with CO_2 from the contacting atmosphere. In a partially water-saturated porous media, the carbonation reaction occurs within pore water in the cementitious waste form. The reaction occurs mainly through the following processes [25]: the mass

transport of CO_2 from the environment into the gas-filled pore space; dissolution of CO_2 into the pore solution (Eq. 3-1) to form CO_3^{2-} and HCO_3^- (Eqs. 3-2 and 3-3); and reaction of dissolved (bi)carbonate with hydroxide ions and dissolved species, such as calcium and magnesium, to form water and carbonate precipitates (Eq. 3-4 shown for divalent species) [31]. The result of the carbonation reaction is a depletion of hydroxide ions and generation of water.

$$CO_2 + H_2O \Leftrightarrow H_2CO_3 \quad (3\text{-}1)$$

$$H_2CO_3 \Leftrightarrow H^+ + HCO_3^- \quad (3\text{-}2)$$

$$HCO_3^- \Leftrightarrow H^+ + CO_3^{2-} \quad (3\text{-}3)$$

$$X^{+2} + 2OH^- + CO_3^{2-} + 2H^+ \Leftrightarrow XCO_3(s) + 2H_2O \quad (3\text{-}4)$$

The reaction in Eq. 3-4 reduces hydroxide ions in the pore solution, resulting in a local decrease in pH. In response to the decrease in dissolved species in the pore water, solid phase hydroxides (e.g., portlandite) dissolve to replace the hydroxide ions in the pore water (Eq. 3-5), and as portlandite being depleted, calcium-silicate-hydrates (C-S-H) decalcify to portlandite and lower calcium C-S-H (Eq. 3-6) [13,17,26,116].

$$Ca(OH)_{2(s)} \rightarrow Ca^{+2} + 2(OH^-) \quad (3\text{-}5)$$

$$x\text{CaO}\cdot\text{SiO}_2\cdot n\text{H}_2\text{O}_{(s)} + y\text{H}_2\text{O} \rightarrow (x\text{-}y)\text{CaO}\cdot\text{SiO}_2\cdot n\text{H}_2\text{O}_{(s)} + y\text{Ca(OH)}_{2(s)} \quad (3\text{-}6)$$

The reduction in pH and buffering capacity of the matrix leads to changes in the solubility and the leaching behavior of COPCs [10,39,40]. Meanwhile, the physical and mass transport properties are also subject to changes due to the formation and redistribution of new solid phases with differing molar volumes during carbonation [40,117,118].

The rate and extent of carbonation of a cementitious material depends on many environmental factors such as CO_2 concentration and relative humidity (RH) in the environment [18,119,120], which vary in the surrounding environment at a disposal site. For example, CO_2 concentration in the contacting environment of the planned Hanford IDF may range from atmospheric level (0.03%-0.04%) to greater than 2%, depending on the depth, temperature, and microbial abundance in the covering layer [121]. Meanwhile, to minimize the interaction of the waste form with the environment through surface water and groundwater, near surface disposal facilities are often located in arid or semi-arid environments; however, large variations in RH may be expected [24]. The annual infiltration rate for the IDF is 0.9 mm/yr., and the lowest monthly relative humidity recorded reaches 21.9% [24].

Carbonation processes in cementitious materials can be different under natural and accelerated aging conditions, due to factors such as the reactive capacity with CO_2 in the material (e.g., OH^- alkalinity) and different pH in pore solution that generates different reaction products [31,120]. The carbonation ingress rate under higher CO_2 concentration than the atmospheric level has been reported to deviate from the rate implied by uniform Fickian diffusion, partly due to the change in the physical properties of the carbonated material over time [30]. This result raises caution when extrapolating the results from accelerated testing under elevated CO_2 concentration (>0.5%) [120] to carbonation under natural conditions (0.04%).

Many studies have investigated the relationship between environmental RH and carbonation in hydrated cement and concrete materials and have commonly found that the carbonation reaction reaches a maximum ingress rate under intermediate RH (50-65%) [19–21,120]. In some of those studies, samples were weighed before and after aging to indicate the overall CO_2 uptake after excluding the moisture loss from drying, and carbonation depth was measured to derive the ingress rate. However, such methods were not capable of capturing the extent of the carbonation reaction (i.e., depletion of hydroxide) in aged samples, which was unlikely uniform across the depth and could vary as functions of distance from the exposure surface and environmental RH [40].

The low OPC content and high alkali solution in the Cast Stone formulation makes the material more similar to alkali-activated materials, which have received extensive attention in recent studies as a sustainable alternative to OPC [35,36]. Like alkali-activated materials, Cast Stone has been found to contain a limited amount of portlandite in the crystalline phases but has high amorphous phase content as indicated by XRD, ranging from 63%-88% [122–124]. The main hydration product in Cast Stone is likely calcium (alkali) aluminosilicate hydrate (C–(N–)A–S–H) gel, which has been identified in many alkali-activated cement systems [31,103]. Compared to the calcium (alumino) silicate hydrate (C–(A–)S–H) gel typically formed in hydrated OPC, C–(N–)A–S–H contains relatively less calcium and more aluminum with alkali (sodium) replacement [31,125]. The high amorphous content of the material challenges the characterization of the mineral phases in the material, which can be resolved with additional tools such as geochemical modeling [90].

Under carbonation, the chemical and physical behavior in alkali-activated materials is not fully understood and can be different from OPC-based systems [18,126]. Without the presence of portlandite as a pH buffer, dissolved (bi)carbonate directly reacts with the C–(N–)A–S–H phase, which causes decalcification (Eq. 3-7) and dealumination reactions (Eq. 3-8) and resulting in silicate polymerization and precipitation of calcium and alkali carbonates [31,127,128].

$$(\equiv Si{-}O{-}Ca{-}O{-}Si \equiv) + (H_2CO_3) \rightarrow 2(\equiv Si{-}OH) + (CaCO_3) \quad (3\text{-}7)$$

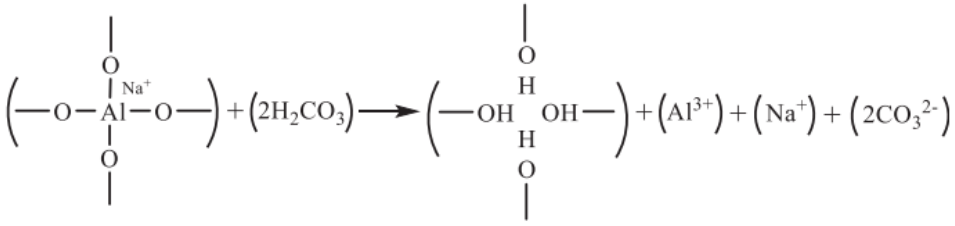

(3-8)

The polymerization and precipitation can significantly alter the physical property of the material. Dutzer et al. [129] observed greater porosity reduction after carbonation in OPC paste compared with a blended system of OPC, FA, and slag. Meanwhile, extensive micro-cracking was observed in the blended system after carbonation, but cracking was observed to a more limited extent for OPC pastes. Both decreased porosity and increased microcracking can alter the mass transport properties of the material. In addition, a higher carbonation rate has been found for the alkali-activated slag mortar, and OPC with fly ash replacement, compared with Portland cement mortars [31,40,130]. As a result, different effects of RH and CO_2 partial pressure on carbonation from what is observed in cement paste and concrete may be expected in Cast Stone. Current assessments on the performance of the Cast Stone have not considered the potential impact of carbonation and the variation in environmental conditions at the disposal site, which may lead to biased estimation on its retention ability for COPCs [37]. An understanding of carbonation impacts on the performance of Cast Stone waste forms through evaluating the rate of ingress and the extent of reaction is important to improve the long-term prediction of COPC retention during the materials service life.

This study provides an experimental investigation of the effect of CO_2 concentration and environmental RH on carbonation in Cast Stone. The ingress rate of the carbonation front and the extent of carbonation is evaluated for samples aged under different environmental conditions with several CO_2 concentrations and RH levels. The extent of carbonation reaction as a function of depth in aged samples was estimated using a 1-D leaching test. In the leaching test, the exposure surface during the aging process is in contact with tank water, leading to diffusion-controlled mass transfer from Cast Stone to tank water. The hydroxide flux from leaching provides an indication of the hydroxide profile in the aged Cast Stone. Porosity analysis was carried out to study the microstructural change of the sample under carbonation, and the moisture loss in the material was monitored to understand the interaction between carbonation and drying. A conceptual model describing the coupled process of drying and carbonation is presented, and dimensional analysis is used to investigate the controlling factor in the carbonation process in Cast Stone as a function of environmental conditions (CO_2 concentration and environmental RH). Finally, the potential migration of

sodium during aging was studied using scanning electron microscopy/energy dispersive x-ray spectroscopy (SEM-EDS).

3.2 Experimental Methods

3.2.1 Material and sample preparation

A Cast Stone waste form was prepared following the mixing procedure of Lockrem [4] using a dry blend of components including OPC, FAF, and Grade 100 BFS at a weight ratio of 8:45:47. OPC and FAF were obtained from concrete vendors, and the BFS was provided by the Pacific Northwest National Laboratory. The oxide compositions of the individual materials are provided in Table C1.

A liquid waste simulant, representing a 5.9 M Na WTP effluent, was prepared using a recipe based on anticipated LAW composition [74] shown in Table 3.1.

Table 3.1 Composition of secondary waste simulant.

	Na^+	**Cl^-**	**F^-**	**SO_4^{2-}**	**PO_4^{3-}**	**CO_3^{2-}**	**NO_2^-**	**Al^{3+}**	**OH^-**	**K^+**	**NO_3^-**	**CrO_4^{2-}**
Concentration (mol/L)	5.86	0.05	0.04	0.1	0.06	0.31	0.63	0.34	3.12	0.04	1.81	0.13

The dry blend was mixed with waste simulant at a water-to-binder ratio (not including solutes) of 0.48 and the mixture cast into 25-mm diameter by 110-mm height cylindrical molds. After setting for 72 hours, samples were demolded and cured for 90 days at 25 °C and 100% RH in an environmental chamber filled with N_2. After curing, some of the monoliths were particle size reduced to 85 wt% less than 2 mm by crushing under nitrogen to allow for more surface area and more complete carbonation during aging. The remaining monoliths were coated with impermeable epoxy and potted into cylindrical molds. Approximately 5 mm was cut off of one end of each sample to create a fresh surface for environmental exposure, forcing a 1-D ingress by diffusion of the reactive gas (CO_2) into the sample.

3.2.2 Sample aging

Monolithic samples were aged at room temperature (21±2°C) under four different CO_2 and O_2 environments (i.e., 100% nitrogen, air at 21% O_2 and 0.04% CO_2 (v/v), 2% CO_2 (v/v) in nitrogen, and 5% CO_2 (v/v) in nitrogen) and four RH (i.e., 15, 40, 68, and 100% RH). Material ID structure, aging conditions, and specific aging times are summarized in Table 3.2. Granular samples were aged for 16 weeks under the same gaseous

atmospheres but only under 68% RH. All samples were aged in well-sealed chambers with continuous gas exchange allowing for four volumetric turnovers per day. The environments were humidified by passing in-flowing gas through bubblers to generate the desired humidity levels, and the RH in each chamber was measured every two weeks. All samples were pre-conditioned under nitrogen at the specified RH for 60 days prior to aging in the inert or reactive environment; however, drying continued during aging. The changes in sample mass before and after pre-conditioning are shown in Table C2.

Table 3.2 Aging times (weeks) of monolithic samples and aging conditions.

		Environmental RH			
Material ID	**Atmosphere**	15%	40%	68%	100%
CS-N(*RH*)-*wks*	100% N_2	16, 32, 48	16, 32, 48	16, 32, 48	16, 32, 48
CS-A(*RH*)-*wks*	Air (0.04% CO_2)	16, 32, 48	16, 32, 48	16, 32, 48	16, 32, 48
CS-2C(*RH*)-*wks*	2% CO_2 in N_2	16, 28, 48	16, 28, 48	16, 28, 48	16, 28, 48
CS-N68-8w**	100%N_2	-	-	8	-
CS-5C68-8w**	5% CO_2 in N_2	-	-	8	-

*Sample coding scheme: CS-aging condition (gas + RH)-aging times. For gas: N, A, 2C and 5C refer to nitrogen, air, 2% CO_2 in nitrogen and 5% CO_2 in nitrogen. For example, CS-2C68-48w refers to Cast Stone aged in 2% CO_2 in N_2 at 68% RH for 48 weeks.

**Initial screening study from [32].

3.2.3 Sample analysis

3.2.3.1 Carbonation depth

The depth of carbonation front penetration into aged Cast Stone samples was estimated by pH change using phenolphthalein [130]. A cross-section of the monolithic samples, created by cutting the sample longitudinally, was sprayed with a solution of 1% phenolphthalein in ethanol. Phenolphthalein appears colorless when pH is less than around 8.3 and turns fuchsia at pH above 10. The distance from the material surface to the pH 10 color indicator was measured in millimeters with a steel ruler. To avoid edge effects, the shallowest depth of color change was considered the carbonation front depth for the sample.

3.2.3.2 Extent of carbonation reaction

For granular samples, the extent of carbonation reaction was estimated by total inorganic carbon (TIC) content and alkalinity of the material. TIC analysis was performed using a Shimadzu model TOC-V CPH/CPN combined with an SSM-5000A solid sample unit. For each 20-mg solid sample, 500 µL of

concentrated phosphoric acid was added to evolve CO_2. The TIC of aged samples was indicative of the carbonates generated by the carbonation reaction. The alkalinity of the material was determined from the acid-base titration curve derived from the parallel batch extractions following EPA Method 1313 [131]. From the alkalinity curve, the total alkalinity was estimated as the amount of the acid (mol H^+/kg-dry) required reduce the pH of the Method 1313 extraction from the natural pH[1] in reagent water to an end-point pH of 4.5 [132]. The hydroxide alkalinity was determined by the amount of acid required to reduce the extraction pH to 8.3 and carbonate alkalinity was the difference of the total and hydroxide alkalinity [132]. An illustration of alkalinity based on a titration curve is presented in Figure C1.

For monolith samples, the extent of the carbonation reaction (i.e., the reduction in hydroxide content) was estimated as a function of depth from the exposure surface using the results of a 1-D leaching test following EPA Method 1315 [133]. The exposure surface of the monolithic sample was contacted with de-oxygenated (nitrogen bubbled) reagent water at a liquid-surface-area ratio of 10 mL/cm^2 of surface area in a sealed container with minimal headspace. The leaching solution was refreshed at 0.08, 1, 2, 7, 14, 28, 42, 49, 63, 91, and 105 days of leaching. The pH of the collected eluate was measured to calculate the flux of hydroxide ions released during each leaching interval. A higher flux of hydroxide indicates that less hydroxide is consumed by the carbonation reaction.

3.2.3.3 Porosity analysis

The bulk porosity of the samples was derived from the skeletal density (ρ_s) measured by nitrogen pycnometry using a Micromeritics AccuPyc II 1340 pycnometer (Micromeritics Instrument Corp, Norcross, Georgia). Prior to measurement, samples of Cast Stone were oven-dried for 24 hours at 60 °C under vacuum so that the dry bulk density (ρ_d) could be measured. The porosity (ε) was determined as shown in Eq. 3-9:

$$\varepsilon = 1 - \frac{\rho_d}{\rho_s} \tag{3-9}$$

Porosity as a function of depth from the exposure surface was determined from backscattered electron image using the method introduced in [134]. Backscattered electron image is collected on the longitudinal cross-section of aged monolithic samples by scanning election microscopy (SEM). Scans were performed using a FEI Quanta 650 environmental scanning electron microscope (ESEM) equipped with a Schottky

[1] In Method 1313, the natural pH is defined as the pH of a reagent water extraction at a liquid-to-solid ratio of 10 mL/g-dry without acid or base addition.

field emission gun and gaseous analytical detector. Operating conditions in the environmental SEM mode were 130 Pa, 10kV accelerating voltage, 10.0-mm working distance and a spot size level of 3.5.

3.2.3.4 Moisture loss

The masses of monolithic samples were recorded before and after aging to estimate the loss of moisture during combined carbonation and drying.

3.2.3.5 Water saturation

Also, at selected aging intervals, monolith samples were cut into slices with approximately 6-mm thickness to determine the water saturation of the material as a function of distance from the exposure surface. Water saturation (S) is defined as the fractional volume of water in the pore space as determined by the mass of the saturated sample (m_{sat}), the mass of the sample oven-dried at 60 °C (m_{dry}), and the mass of the sample after aging (m_t) as shown in Eq. 3-10 [132].

$$S = \frac{m_{sat} - m_{dry}}{m_t - m_{dry}} \tag{3-10}$$

3.2.3.6 Distribution of sodium

The migration of sodium in monolithic samples during aging was investigated by scanning election microscopy-energy dispersive spectrometry (SEM-EDS) analysis of a longitudinal cross-section of samples impregnated with epoxy. The operating parameters of the instrument are described in section 3.2.3.3. Chemical information for EDS analysis was collected using an Oxford Instruments EDS and analyzed with Oxford's Aztec software (Oxford Instruments, Abingdon, Oxfordshire, UK). EDS maps were taken using a resolution of 256 (1 μm/pixel), 400 EDS frames per site, 100 μs pixel dwell time, and processing time level of 5 for signal noise reduction. An EDS mapping area of 0.3-mm width by 1-mm depth from the exposure surface was collected for each sample and analyzed quantitatively for a set of chemicals of interest. In carbonated samples, an additional EDS map was taken at the carbonation front at the depth indicated by the phenolphthalein test.

3.3 Results and Discussion

3.3.1 Effect of CO_2 concentration

3.3.1.1 Extent of reaction

Figure 3.1 presents TIC, natural pH, and alkalinity of granular Cast Stone samples aged for 16 weeks under different CO_2 concentrations and at 68% RH. The Cast Stone material aged without carbonation or (CS-N68-16w and CS-N68-8w) has similar natural pH (12.8 average) to that of OPC (12.7) reported in Branch et al. [40]. On average, 50% of the total alkalinity may be attributed to the hydroxide alkalinity, which is consistent with the addition of the highly alkaline waste simulant. Although the remainder of the total alkalinity is attributed to carbonate alkalinity, the TIC is very low (0.15 wt% carbon).

As the concentration of CO_2 in the environment increases, a greater extent of carbonation reaction was observed by a general increase in TIC content and a decrease in the natural pH of the material. After carbonation, hydroxide alkalinity of the material decreased and was almost completely consumed under 2% and 5% CO_2 conditions. Meanwhile, carbonate alkalinity increased as CO_2 concentration increased. Despite a significantly higher TIC content in the material carbonated in air (2.2 wt% carbon), the reduction in natural pH (12.1) and hydroxide alkalinity (2.2 meq/g-dry) was comparatively small. These observations agree with the simulation results from another study [31], which showed the pore solution in alkali-activated materials with Na concentration above 1 mol/kg to be constantly greater than pH 12 under atmospheric carbonation. The buffering of natural pH can be attributed to two factors – the significant amount of alkali ions provided by the Cast Stone liquid waste simulant [126] and the abundance of relatively high-Ca silicate phases in uncarbonated material that release calcium hydroxides upon consumption of hydroxides [26].

However, as the material is carbonated to a certain extent, carbonate speciation in the pore solution is strongly dependent on CO_2 partial pressure. For example, Bernal et al. [31] identified natron (Na_2CO_3) as being stable in alkali-activated binders under 0.04% CO_2, and nahcolite ($NaHCO_3$) as being stable under 1% CO_2. As a result, the natural pH of the material decreases as the CO_2 content increases in the atmosphere, and a large pH decrease is observed from ambient CO_2 to 2% CO_2, while the difference in TIC content is relatively small.

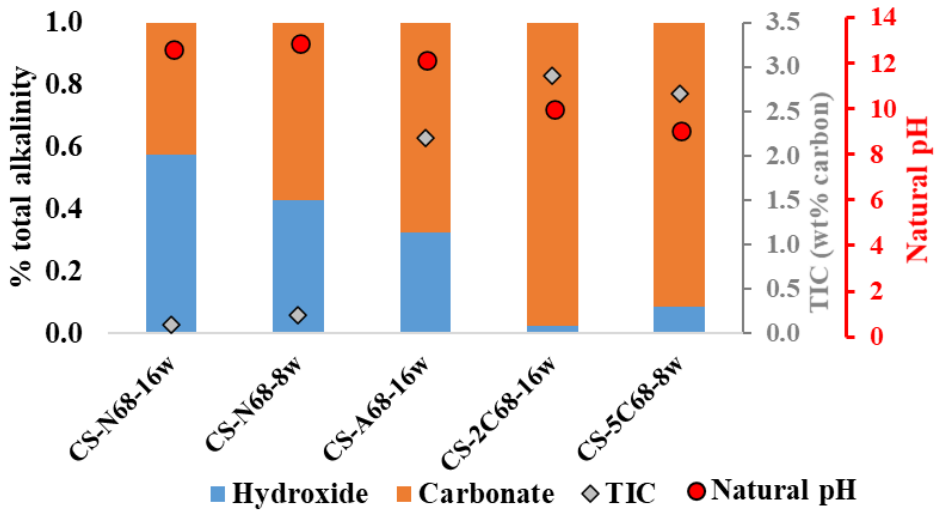

Figure 3.1 Alkalinity (hydroxide and carbonate), total inorganic carbon (TIC) content, and natural pH of Cast Stone samples as a function of CO_2 concentration at 68% RH.

Figure 3.2 compares the flux of hydroxide released from the material carbonated under various CO_2 concentrations (where the data are provided in Table C3). The magnitude of the hydroxide flux and time-dependence of the release of hydroxide from the material are indicative of the combined effect of the extent of carbonation reaction at a given depth (i.e., consumption of hydroxide ions) and the ingress depth of the carbonation front into the sample. In the figure, the hydroxide flux for the uncarbonated sample (CS-N68-16w) shows a monotonic decrease in hydroxide flux consistent with diffusion-controlled release. The lowest hydroxide flux occurs for the sample aged at 5% CO_2 for 8 weeks (CS-5C68-8w) at up to 4 orders-of-magnitude lower over the leaching time than the uncarbonated sample. The decrease in hydroxide flux is due to hydroxide being consumed by the carbonation reaction. The sample aged in 2% CO_2 for 16 weeks (CS-2C68-16w) – twice as long as the 5% CO_2 sample – shows an initial hydroxide flux (leaching time < 1 day) significantly higher than that in the more carbonated sample. In general, the initial flux of hydroxide decreases with increasing CO_2 concentration with CS-N68-16w > CS-A68-16w > CS-2C68-16w > CS-5C68-8w, indicating that more hydroxide is consumed during aging at higher CO_2 concentrations. The decrease in the initial flux of hydroxide during leaching is consistent the reduced hydroxide alkalinity with increasing CO_2 concentration observed in the granular samples.

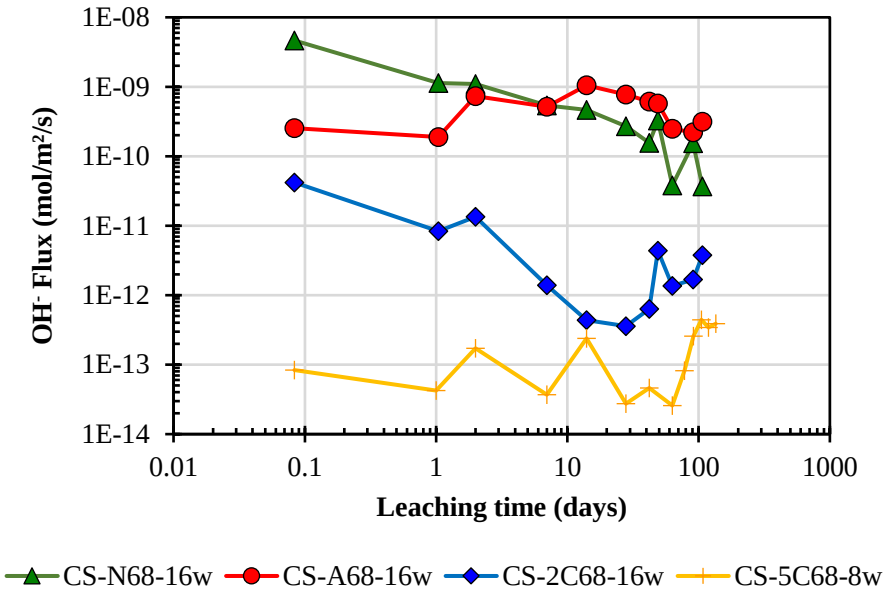

Figure 3.2 Flux of hydroxide from 1-D leaching tests of samples aged under various CO_2 concentration conditions and 68% RH.

3.3.1.2 *Carbonation rate*

After 16 weeks of aging, the depth of the carbonation reaction measured by phenolphthalein follows a linear relationship with CO_2 concentration with good degree of fit (Figure 3.3). This observation indicates that the carbonation reaction is proportional to the CO_2 concentration (i.e., a Fickian diffusion relationship between the carbonation depth and CO_2 concentration), suggesting the CO_2 concentration gradient as a driving force for mass transport and gas phase diffusion of CO_2 into the matrix is the rate-limiting process for carbonation. Thus, it can be inferred that the dissolution of CO_2 into the pore water and the reaction of dissolved CO_2 with pore water ions are rapid and also driven by the CO_2 concentration gradient between gaseous phase and liquid phase in pores (see Section 3.3).

When compared to the carbonation of OPC and concretes [25,135], Figure 3.3 shows that the rate of the carbonation front ingress (mm/yr) is much faster in Cast Stone, which is in agreement with studies on blended materials [26,126]. The lower total alkalinity of Cast Stone compared with OPC reduces the resistance of the material to carbonation [40]. Meanwhile, the replacement of fly ash and blast furnace slag was found to coarsen the porous structure, which facilitates the transport of CO_2 in the material [29].

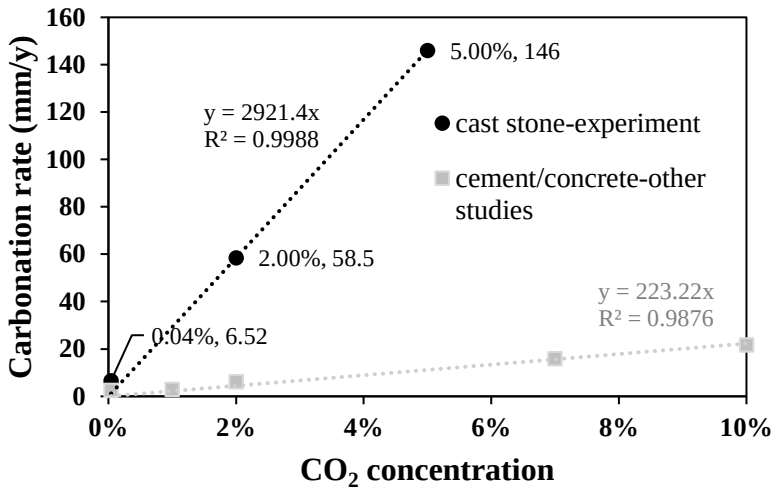

Figure 3.3 Carbonation rate as a function of CO_2 concentration for Cast Stone aged in air at 68% relative humidity. Carbonation of cement paste and concrete (water-to-binder of 0.45-0.5) at 60-70% RH from other studies [25,135] shown in gray.

3.3.2 Effect of environmental RH

3.3.2.1 Carbonation rate

The effects of environmental RH on the rate of carbonation front ingress in air and 2% CO_2 concentrations are shown in Figure 3.4. A comparison of carbonation in air with that in 2% CO_2 shows that the relationship between carbonation front depth with the square root of time differs with CO_2 concentration. Carbonation depth at 2% CO_2 appears to be proportional to $\sqrt{t}$, whereas, it is better represented by a power relationship with $\sqrt{t}$ under atmospheric carbonations. The measurement of the carbonation front using phenolphthalein test can underestimate the depth [136,137], and the uncertainty depends on the CO_2 concentration, aging time, and relative humidity. Under both CO_2 concentrations, the carbonation front ingress rate in Cast Stone increases as environmental RH decreases, and the RH effect is stronger under the accelerating condition. At low RH, a greater portion of the pore space is filled with gas, which decreases resistance to gas phase diffusion. The increase in the carbonation rate at lower RH supports the previous observation that the carbonation in Cast Stone is likely controlled by the gas phase diffusion; however, the difference between the carbonation rate under 15% RH and 40% RH is relatively small. In a previous study [138], the relative pore saturation at equilibrium with environmental RH for the Cast Stone material was found to be linearly proportional to RH. Therefore, it is reasonable to infer that, at low RH, the dissolution of CO_2 is restricted by the limited gas-liquid interface that may additionally control the carbonation rate. Thus, the carbonation

rate at low RH is governed by both the rate of CO_2 diffusion through air-filled pores and its rate of dissolution into pore water film.

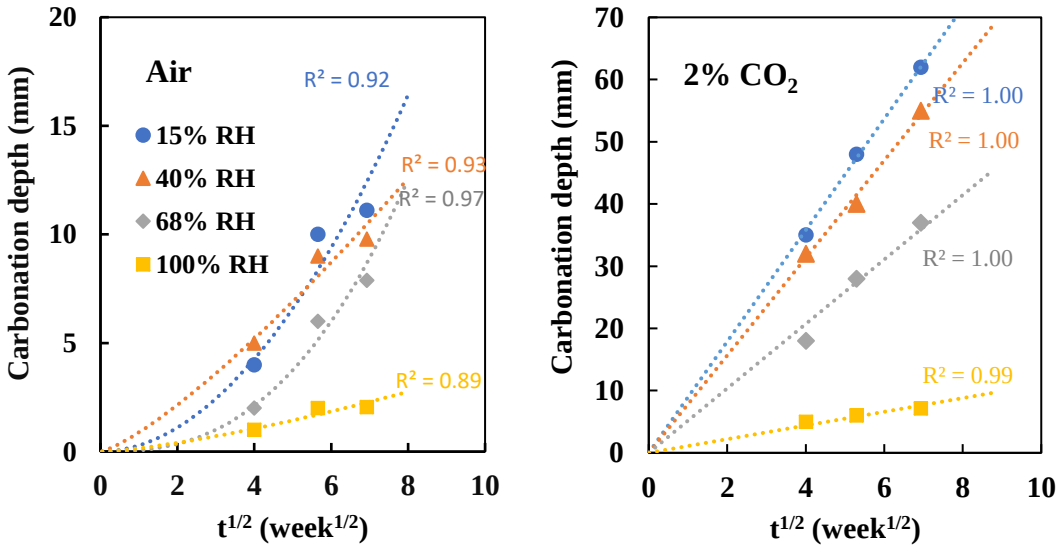

Figure 3.4 Carbonation front depth in Cast Stone as a function of root time in air (left) and 2% CO_2 atmosphere (right) as a function of relative humidity along with second order polynomial and linear fits, respectively (note that vertical axes scales are not equal).

Several studies on cementitious materials have found a close to linear relationship between carbonation front depth and square root of aging time ($\sqrt{t}$) for various RH conditions [17,18,126] as shown in Eq. 3-11.

$$x = A\sqrt{t} \tag{3-11}$$

This linear relationship is consistent with a process controlled by Fickian diffusion. Papadakis et al. [17] reported the proportionality coefficient (A) to be a factor of the square root of CO_2 concentration, the square root of diffusivity of CO_2, and the inverse square root of the total content of the readily carbonated phases in the system. Although it has been noted that maximum carbonation depth is observed at mid-range RH [19–21,120], the RH of the aging environment is not explicitly a factor in the proportionality coefficient. However, the impact of RH on the carbonation rate in Cast Stone appears to be different from that in cement and concrete materials.

In Figure 3.5, the proportionality constant following Eq. 3-11 is compared as a function of RH for Cast Stone (black data) and cementitious materials (gray data). The studies on cementitious materials [17,21] indicate a maximum proportionality coefficient at an RH of approximately 55%, which is consistent with the parabolic shape described by several studies [17,20,21,120]. However, the proportionality coefficient

shows a monotonic decay consistent with CO_2 diffusion controlling the carbonation depth. Initially, the monotonic behavior may be explained by the different water retention ability of the two materials in that Cast Stone has a coarser, open porous structure [138] and, therefore, is more susceptible to drying under an intermediate RH than cement paste.

In addition, the water generated during the carbonation reaction in Cast Stone and cementitious materials depends on the stoichiometry of the primary phases reacted and the extent of these reactions [11,19]. In OPC systems, carbonation is characterized initially by the dissolution of portlandite, where each mole of calcite formed consumes one mole of CO_2 and generates one mole of water. However, in Cast Stone, there is little to no portlandite in the system and the amount of water generated per unit consumption of CO_2 is related to the consumption and production of a more complex mineralogy (Table 3.3).

Table 3.3 shows the mineral composition of carbonated and uncarbonated materials in Cast Stone as derived from geochemical modeling of pH-dependent leaching data following EPA Method 1313 [90] using the LeachXS^{TM}-ORCHESTRA platform [99,139]. Only those mineral phases found at greater than 0.01 mol/kg in either carbonated or uncarbonated material at liquid-to-solid ratio of 1 mL/g-dry are included in the table. Detailed derivation of mineral compositions is provided in Appendix C-I. For each mineral in Table 3.3, the increase in CO_2 reacted and water generated as a result of carbonation are calculated. The net differences in CO_2 and water indicate that 1.3 moles of water are produced for each mole of CO_2 reacted. Thus, the extra water generated per mole of CO_2 reacted may facilitate carbonation in Cast Stone materials at lower environmental RH and lead to an increase in the proportionality coefficient at low RH. For cementitious materials, the amount of water generated may be too little to support the carbonation reaction at low RH due to lower moisture conditions.

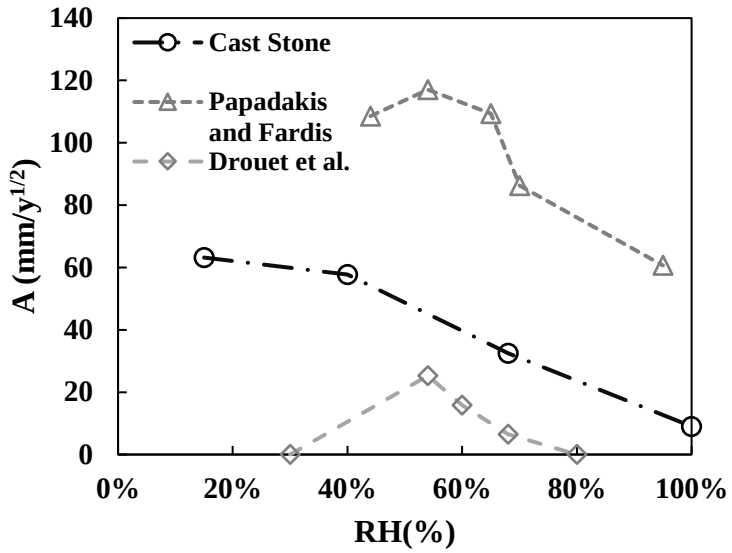

Figure 3.5 Carbonation rate coefficient *A* for Cast Stone (under 2% CO_2) and OPC paste material (water to binder ratio of 0.6 in Papadakis et al. [17] and 0.4 in Drouet et al.[21]) as a function of environmental RH (lines are only for indication).

Table 3.3 Composition and molar volume of mineral phases reacted and produced under carbonation and the associated amount of consumed CO_2 and H_2O generated by reaction.

Minerals	**ORCHESTRA Mineral ID**	**Formation Reactions**	**Amount in CS-N (mol/kg)**	**Amount in CS-C (mol/kg)**	**CO_2 consumed (ΔCO_2, mol/kg)**	**H_2O formed (ΔH_2O $_{reaction}$, mol/kg)**	**Molar Volume (cm^3/mol)**	**ΔVolume (cm^3/kg)**
Wairakite [88]	Wairakite	$2Al[OH]_4^- + Ca^{2+} + 8H^+ + 4\ H_2SiO_4^{2-} \rightarrow$ Wairakite $+18H_2O$	0.00	0.11	-	1.89	116.53	12.2
CNASH solid solutions [87,103]	CEM18_TobH	1.5CEM18_CNASH_ss $+ Ca^{2+} + H^+ + 0.5H_2O + 1.5\ H_2SiO_4^{2-} \rightarrow$ CEM18_TobH_CNASHss	0.77	0.00	-	-0.38	85.68	-85.0
	CEM18_T2C	CEM18_CNASH_ss $+ 1.5Ca^{2+} + 2H_2O + H_2SiO_4^{2-} \rightarrow$ CEM18_T2C_CNASHss $+ H^+$	0.21	0.00	-	-0.41		
	CEM18_INFCNA	$0.31Al[OH]_4^-$ + CEM18_CNASH_ss $+ Ca^{2+} + 1.19\ H_2SiO_4^{2-} + 0.69\ Na^+ \rightarrow$ CEM18_INFCNA $+ 0.5H_2O$	0.10	0.00	-	0.05		
Calcite [87]	CEM18_Cal	$CO_3^{2-} + Ca^{2+} \rightarrow$ CEM18_Cal	0.55	1.12	0.58	0.00	36.90	21.2
Dolomite[87]	Dolomite	$2CO_3^{2-} + Ca^{2+} + Mg^{2+} \rightarrow$ Dolomite	0.00	0.10	0.19	0.00	64.79	6.2
Brucite [87]	CEM18_Brc	$2H_2O + Mg^{2+} \rightarrow$ CEM18_Brc $+ 2H^+$	0.22	0.11	-	-0.21	24.27	-2.6
Amorphous Silica [87]	CEM18_Amor_Si	$2H^+ + H_2SiO_4^{2-} \rightarrow$ CEM18_Amor_Sl $+ 2H_2O$	0.00	0.03	-	0.06	27.31	0.9
Diaspore [87]	Diaspore	$Al[OH]_4^- + H^+ \rightarrow$ Diaspore $+ 2H_2O$	0.00	0.06	-	0.12	16.47	1.0
				TOTAL	0.77	1.00		-47.77
			mol H_2O/mol CO_2		1.30			

*Wairakite: $Ca_8Al_{16}Si_{32}O_{96}\cdot 16H_2O$; CEM18_TobH: $2CaO\cdot 3SiO_2\cdot 5H_2O$; CEM18_T2C: $3CaO\cdot 2SiO_2\cdot 5H_2O$; CEM18_INFCNA: $16CaO\cdot 5.5Na_2O\cdot 2.5Al_2O_3\cdot 19SiO_2\cdot 21H_2O$; Calcite: $CaCO_3$; Dolomite: $CaMg(CO_3)_2$; Brucite: $Mg(OH)_2$; Amorphous Silica: SiO_2; Diaspore: α-AlO(OH).

3.3.2.2 Drying under carbonation

To clarify the effects of RH on carbonation ingress rate, the microstructure and water saturation of the material were evaluated to understand the change in mass transport properties during carbonation. The porosity of uncarbonated (CS-N68) and carbonated (CS-2C68) Cast Stone measured by N_2 pycnometry are 0.39 and 0.45, respectively. The porosity profile across the carbonation front boundary determined from backscattered image (Figure 3.6) also showed relatively higher porosity in the carbonated region of the sample. Both of the observations indicated an increase in porosity after carbonation.

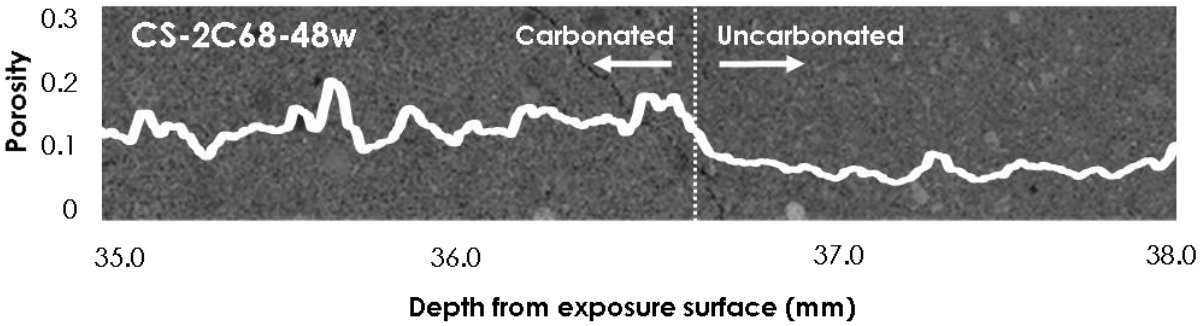

Figure 3.6 Porosity as a function of depth from the exposure surface near the carbonation front of CS-2C68-48w overlaid on the corresponding backscattered electron image (dashed line indicate the carbonation front from the phenolphthalein test).

The increase in porosity with carbonation is supported by the decrease in molar volume of the solid phases after carbonation compared to the uncarbonated material (Table 3.3). For each kilogram of material reacted, the volume of the minerals decreased by 47.7 cm^3, contributing to approximately 15% pore volume increase. Conversely, carbonation of cementitious materials is typically observed to decrease porosity after carbonation due to an increase in molar volume of reaction products [26,129]. Meanwhile, microcracking was found at the surface of the carbonated Cast Stone samples, which may contribute to the increase in effective gas phase diffusivity after carbonation by decreasing the physical resistance to diffusion.

3.3.2.2.1 Changes in mass

The changes in sample mass during aging in N_2 and 2% CO_2 are compared in Table 3.4. The mass of sample after equilibration to respective RH in N_2 and before aging was considered as the initial mass. Although the change in mass for samples stored under 100% N_2 is solely due to drying, the mass change in carbonated samples can be attributed to multiple factors, including CO_2 uptake (ΔCO_2), the loss of initial pore water from drying (ΔH_2O_{drying}), and loss of H_2O generated by the carbonation reaction ($\Delta H_2O_{reaction}$, Eq. 3-12):

$$Mass\ change = \Delta CO_2 + \Delta H_2O_{reaction} + \Delta H_2O_{drying} \quad (3\text{-}12)$$

Carbonated samples aged under 100% RH gained mass from ingress and reaction of gaseous CO_2. Under environmental conditions that promote drying (15%, 40%, and 68% RH), the decrease in mass was greater in carbonated samples than in uncarbonated samples, despite the reaction of CO_2 which would increase sample mass. Based on the measured carbonation depth (Figure 3.4), and the amount of CO_2 uptake and the water generated by reaction per gram of material as indicated in Table 3.3, the CO_2 gain and H_2O generated was estimated for each sample (Table 3.4). The contribution of pore water loss from drying in each sample was calculated using Eq. 3-12. The results show that carbonation increased the rate of pore water loss in the sample, and the greatest increase was under 68% RH, where the mass loss under carbonation was 4.3 times greater than that without carbonation.

Table 3.4 Change in mass of samples during aging under 100% N_2 and 2% CO_2 for 48 weeks due to CO_2 gain, water generation from carbonation reaction, and water loss from drying.

Aging Time	RH	Mass Change (g)		ΔCO_2 (g)	$\Delta H_2O_{reaction}$ (g)	ΔH_2O_{drying} (g)	
		CS-N	CS-C	CS-C	CS-C	CS-N	CS-C
48w	15%	-3.58	-7.09	2.65	-1.41	-3.58	-8.33
	40%	-2.43	-6.30	2.35	-1.25	-2.43	-7.40
	68%	-0.92	-3.34	1.58	-0.84	-0.92	-4.08
	100%	0.39	0.92	0.30	-0.16	0.39	0.78

* Mass changes were measured from the aging experiment. ΔCO_2 and $\Delta H_2O_{reaction}$ refers to the amount of CO_2 uptake and water generated from carbonation reactions and were estimated from simulation (Table 3.3). ΔH_2O_{drying} refers the pore water loss from drying as calculated from Eq. 3-12.

3.3.2.2.2 Moisture distribution

The moisture distribution in discrete slices of samples aged in N_2, air, and 2% CO_2 are compared in Figure 3.7 (where a full set of figures is provided in Figure C2). Drying front ingress was defined by a discrete slice saturation less than 0.78. Compared to uncarbonated samples, the drying front for carbonated samples aged both under 2% CO_2 and air progressed further into the sample under the same RH condition. The drying front ingress is more significant under the 2% CO_2 condition, with more than twice the drying front penetration than in uncarbonated samples.

However, in the region subject to drying, the moisture content gradient is significantly larger in the samples aged in air than in the samples aged under 2% CO_2. The moisture profile under 2% CO_2 is impacted by the more significant change in pore structure (increase porosity and cracking) due to changes in molar volume from reactants to products during the carbonation reaction and the generation of water from the carbonation

reaction itself. Higher porosity and cracking accelerate the ingress of CO_2 into the matrix which, in turn, increases the extent of the carbonation reaction and generates more water. This self-generation of water allows the carbonation reaction to proceed under low RH conditions and increases the relative saturation in the drying region of the material. Figure 3.7 clearly shows a relatively greater amount of water remaining in the dried region (saturation around 0.5) of the 2% CO_2 material, which allowed continuous dissolution of CO_2 and allowed the carbonation reaction to proceed even at 15% RH in the external environment. In contrast, samples aged in air experience less carbonation, less microstructural change, less enhance carbonation leading to lower relative saturation in the drying region. As a result, the depth of the carbonation reaction was limited to a 10-mm depth for air-aged samples versus approximately 60-mm for samples aged in 2% CO_2. These observations support the non-linear relationship observed between carbonation depth (X) and square root of time ($\sqrt{t}$) for samples aged in air at low RH (Figure 3.4) because the carbonation front under these conditions was dependent on the dissolution of CO_2 into a limited liquid film.

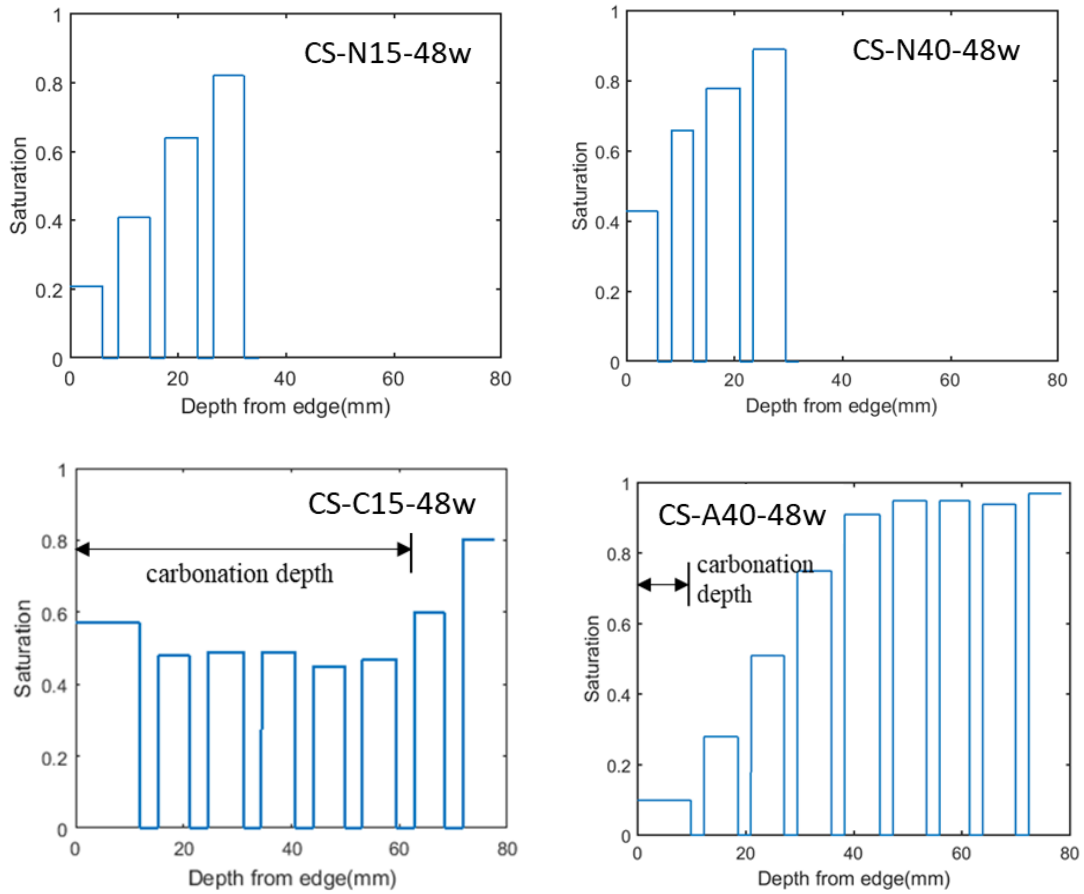

Figure 3.7 Saturation profile measured from discrete 6-mm slices cut from Cast Stone samples aged for 48 weeks (N15: nitrogen and 15% RH; N40: nitrogen and 40% RH; C15: 2% CO_2 and 15% RH; A40: air, 40% RH).

3.3.2.3 Extent of reaction

The environmental RH also impacts the extent of the carbonation reaction as evaluated by the flux of OH- from the EPA Method 1315 leaching test (Figure 3.8 with data in Table C5), in which the hydroxide flux from leaching of samples aged in N_2, air, and 2% CO_2 are compared. The impact of RH was different for carbonation in air and 2% CO_2. For samples aged in air, samples aged under 40% and 68% RH both have the greatest extent of carbonation at the exposure surface, as indicated by the lower initial hydroxide flux compared with the 15% and 100% RH. The relatively low CO_2 concentration and slower gas phase diffusion of CO_2 contributed to the limited extent of reaction. Samples aged in 15% RH had the lowest extent of carbonation at the sample surface, with hydroxide flux even greater than from samples aged in 100% RH. Under 15% RH, rapid gas phase diffusion occurs within the material and the reaction most likely occurs near the receding drying front, while insufficient moisture is present in the dried zone for carbonation to proceed.

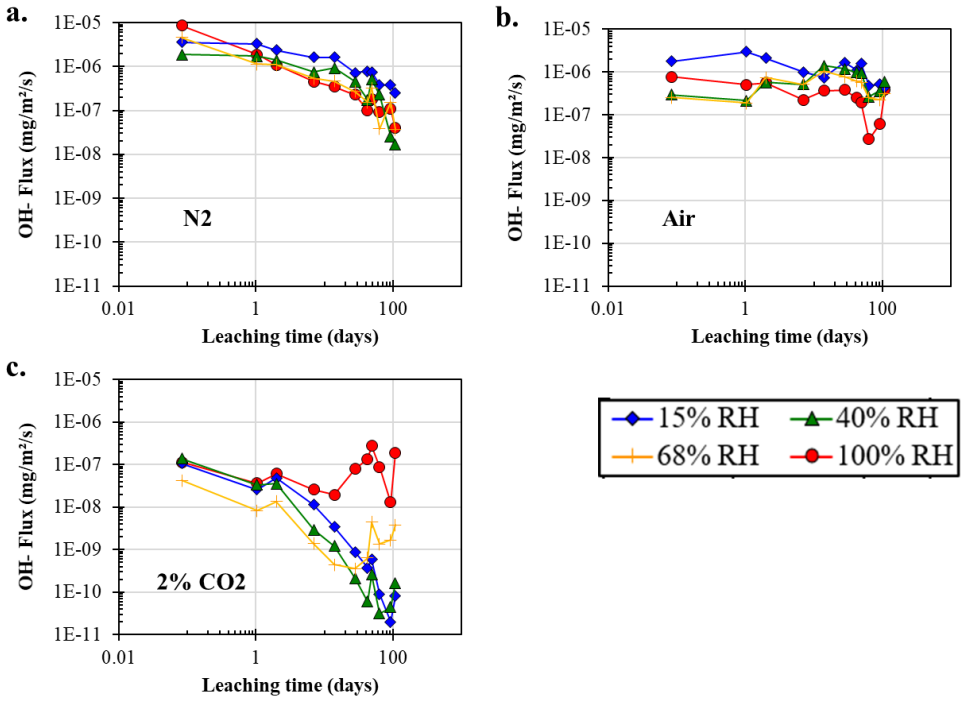

Figure 3.8 Flux of hydroxide from 1-D leaching test for samples aged for 16 weeks under a. nitrogen, b. air, and c. 2% CO_2 at various RH.

For samples aged under 2% CO_2, the greater driving force for CO_2 to dissolve and react in water film leads to a much greater extent of reaction and greater ingress of the carbonation front compared to samples aged in air, as indicated by the lower hydroxide fluxes and the longer leaching times with suppressed hydroxide

fluxes (Figure 3.8c). Samples aged under different RH presented different histories of hydroxide flux. For all RH conditions, the hydroxide flux decreased with leaching time at initial leaching, and the flux started to increase steadily at 91, 63, 28, and 14 days of leaching for 15%, 40%, 68%, 100% RH, respectively. As suggested from the trend of carbonation front depth in these samples, the longer leaching time when the inflection point occurs at lower RH can be related to the higher carbonation front ingress into the sample. Samples aged under 68% RH had lesser hydroxide flux in the early leaching period (< 14 days) compared with the others, suggesting a much greater extent of reaction under 68% RH (in the region near the exposure surface). This observation is consistent with the theory discussed above, that the presence of liquid phases in the pore spaces were favorable for the dissolution of CO_2 and carbonation reaction. For the samples aged in lower RH (i.e., 15% and 40%), the reaction extent was comparatively less, despite the fact that the carbonation front ingress was greater.

3.3.3 Conceptual model

The coupled processes of carbonation and drying in monolith Cast Stone is conceptualized in Figure 3.9. Transport occurs for water and CO_2 in both liquid and gas phases. Gaseous CO_2 diffuses through gas filled pore spaces and dissolves in pore solution through interphase mass transfer, forming HCO_3^-, and CO_3^{2-} (Eqs. 3-1 to 3.3), which then reacts with the dissolved species and releases water (Figure 3.9a). The gas phase diffusion of CO_2 is facilitated as drying proceeds in the material and the gas phase becomes continuous (Figure 3.9b). The gaseous diffusion is further facilitated when the porosity is increased and microcracking is formed in the carbonated material. Assuming the reaction rate between CO_2 and cement matrix is relatively fast and the transport of CO_2 in the liquid phase is negligible compared to the rate of reaction, the carbonation process in the material is mostly controlled by the gaseous diffusion along x-axis and mass transfer of CO_2 orthogonally along the y-axis (Figure 3.9c). On the whole, the carbonation conceptual model in Cast Stone differs from OPC in two aspects: 1) porosity increases and cracking forms in Cast Stone compared to decreased porosity for OPC; 2) greater water generation from carbonation in Cast Stone than for OPC.

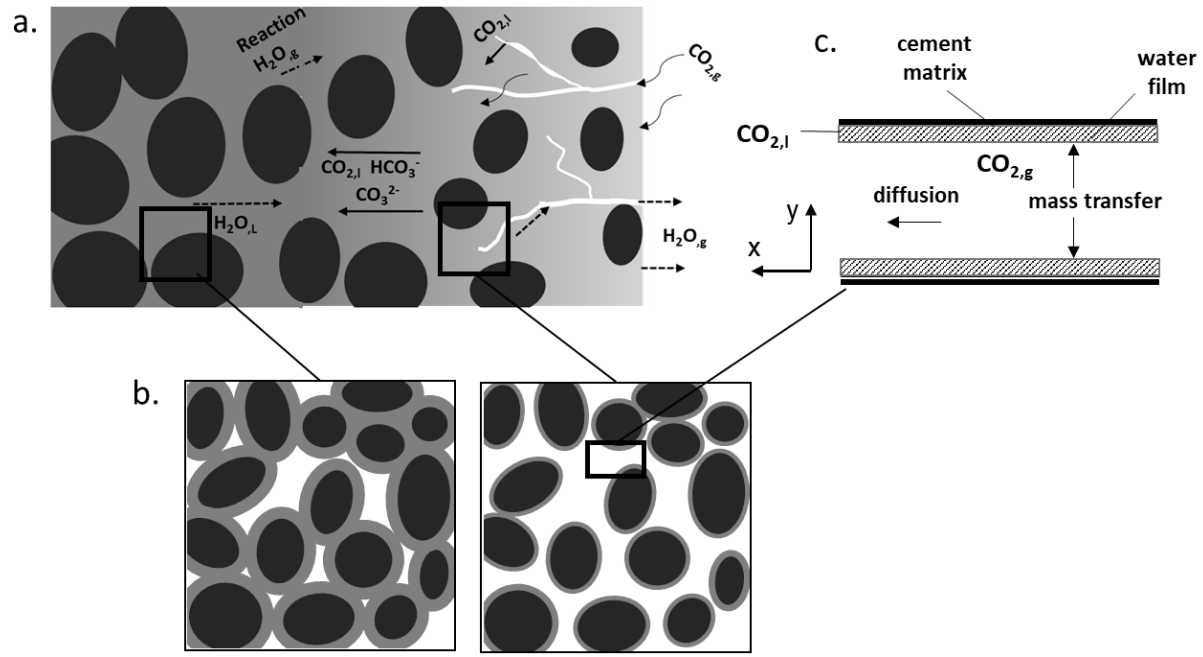

Figure 3.9 Conceptual model of carbonation and drying process in Cast Stone: a. transport of species in the porous structure; b. moisture distribution in pore structure with different extent of drying; and c. mass transport of CO_2 in the pores.

Transport of CO_2 in gas along the x-axis through diffusion can be represented in the following form with CO_2 concentration *(C_G)* gradient as the driving force:

$$\frac{\partial C_G}{\partial t} = \frac{\partial}{\partial x} D^{eff}_{CO_2\,(G)} \frac{\partial C_G}{\partial x} \tag{3-13}$$

where *t* is time and *x* is distance from the surface. The effective diffusivity of CO_2 in gas ($D^{eff}_{CO_2\,(G)}$) is a function of saturation and porosity and is defined by [46,95]:

$$D^{eff}_{CO_2\,(G)} = \frac{D_{0,G}}{{\tau_G}^2}(1-S)^{10/3}\varepsilon^{4/3} \tag{3-14}$$

where $D_{0,G}$ is the free diffusivity of CO_2 in air; τ_G is the gas phase tortuosity factor; *S* is saturation and ε is porosity. Porosity, saturation and tortuosity factors change with drying and carbonation (Figure 3.6). Meanwhile, mass transfer of CO_2 from gas to liquid phase is driven by the difference in CO_2 concentration and the mass transfer rate ($\boldsymbol{r_{CO_2\,(G)}}$) in porous medium can be defined as [140]:

$$r_{CO_2\,(G)} = ka(k_H C_G - C_L) = \frac{\partial C_G}{\partial t} \tag{3-15}$$

where k is the mass transfer coefficient (m/s), a is the effective specific interfacial area (m^{-1}), k_H is Henry's constant of CO_2 in water, and C_L is the CO_2 concentration in liquid. A non-dimensional parameter Sherwood number (Sh) can be used to evaluate the relative effect of mass transfer rate and diffusion [140,141]:

$$Sh = \frac{kd_{50}}{D^{eff}_{CO_2\,(G)}} \tag{3-16}$$

where d_{50} is the mean pore diameter at the specific saturation degree, which can be derived from the pore size distribution, assuming drying occurs progressively from larger pores to the smaller pores (details are provided in Appendix C-II). The value of k has been reported within the range of 10^{-5} to 10^{-4} m/s [142–144], and the value provided by Jeong et al. from simulation of CO_2 transport in cement mortar (5×10^{-5} m/s) [142] was used to determine the Sherwood number as a function of saturation.

Figure 3.10 shows how the value of the Sherwood number (Sh) decreases with decreasing saturation. The Sh value is 1 at 100% RH and decreases as the relative rate of gaseous diffusion increases and/or the rate of mass transfer decreases toward Sh = 0.7. For the three drying conditions used in the experiment (i.e., 68%, 40% and 15% RH), gas diffusion is relatively more rapid than mass transfer (Sh < 1). The mass transfer rate is additionally affected by the liquid-vapor interface, which decreases with drying. Dissolution of CO_2 into the liquid phase is assumed to be required for the carbonation reaction to proceed. Therefore, the extent of carbonation reaction is relatively low under lower RH conditions (Figure 3.8), as the reactant and reaction media are limited. This observation additionally suggests that the linear relationships observed between carbonation depth and $\sqrt{t}$ under 2% CO_2 (Figure 3.4) do not necessarily imply a diffusion-controlled carbonation process. Instead, the linear relationship is a coupled effect of the increase in gaseous diffusion pathway in the carbonated material and the limited CO_2 dissolution in the dried zone (i.e., the carbonation reaction occurs primarily at the drying front). Meanwhile, both the gaseous diffusion along x-axis and mass transfer along y-axis are proportional to the concentration of CO_2 in gas (Eq. 3-13 and Eq. 3-14). This explains the previous observations that carbonation rate is proportional to the CO_2 concentration (Figure 3.3) and the reaction extent increases as CO_2 concentration increases (Figure 3.1 and Figure 3.2).

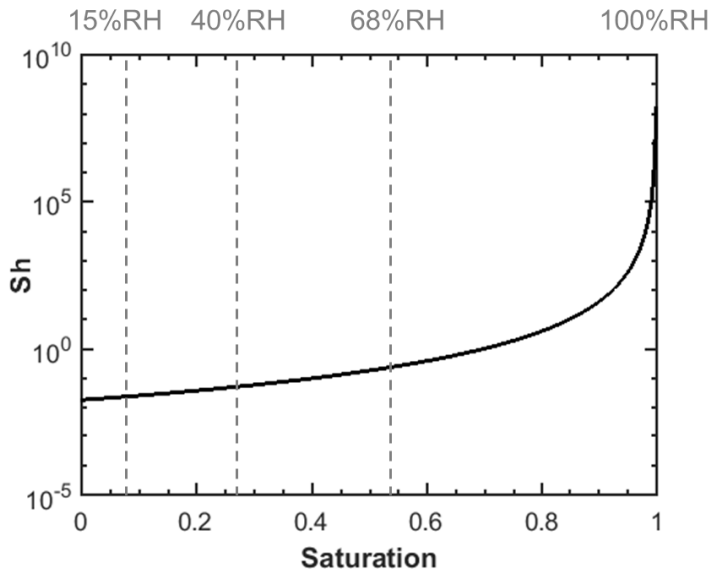

Figure 3.10 Sherwood number (*Sh*) as a function of relative saturation (where each dashed line shows the equilibrium saturation with indicated RH).

3.3.4 Migration of sodium

Alkalis, mainly sodium due to the high content and solubility, are mobile in alkali-activated materials under leaching conditions and during curing under high RH conditions [126,145]. During aging in low RH conditions, capillary water moves from the interior of the material toward the exposure surface in response to the hydraulic head gradient. Since carbonation accelerates drying, the capillary movement is also dependent on aging conditions. The effect of water movement on alkali distribution in Cast Stone was studied on samples with and without carbonation under 68% RH (i.e., the condition where the greatest extent of carbonation reaction and increase of drying was observed) through SEM-EDS mapping (Figure 3.11).

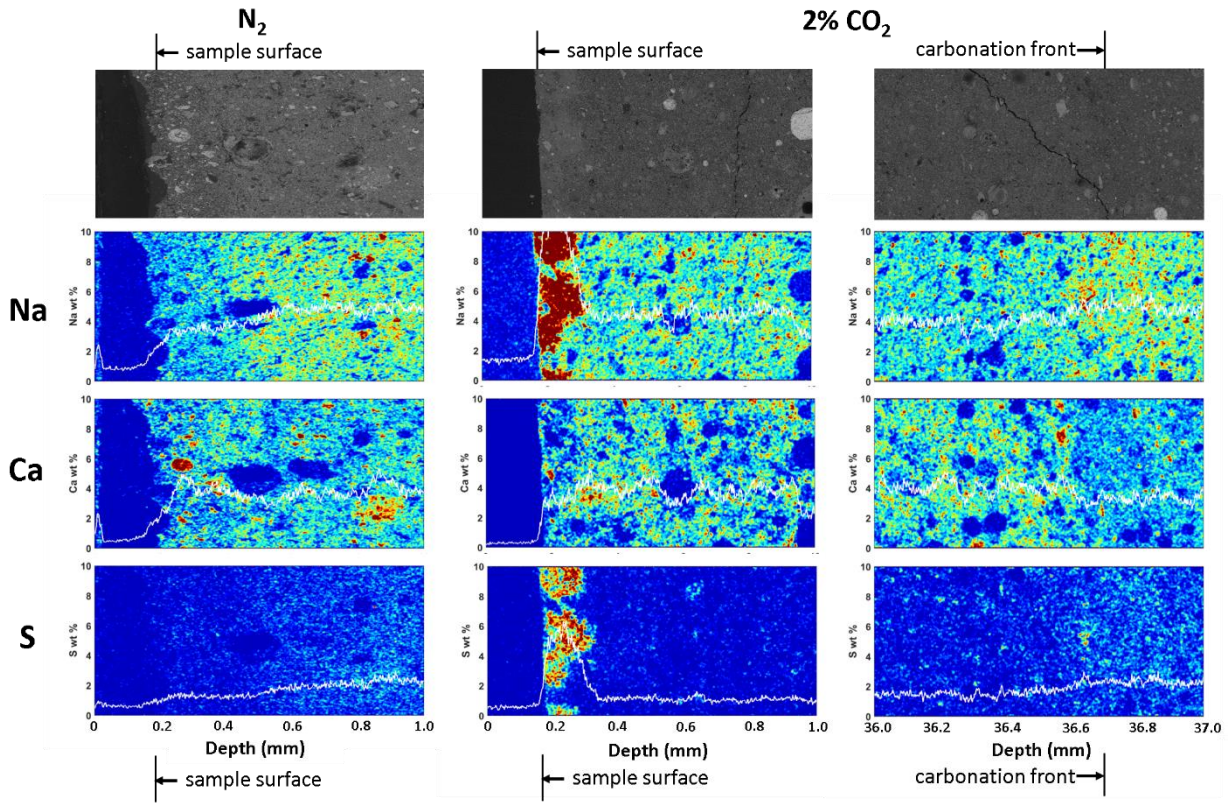

Figure 3.11 SEM-EDS maps of selected elements and backscattered electron images at the exposure surface and carbonation front of a sample aged in N_2 and 2% CO_2, 68% RH for 48 weeks.

In the uncarbonated sample, sodium appears to be evenly distributed across the measured depth, with slightly lower content near the exposure surface. At the exposure surface of the carbonated sample, there is clearly an accumulation of sodium with a thickness of 0.05-0.2 mm, and the charge is complemented by the sulfur species, in the form of SO_4^{2-}. At the carbonation front, higher sodium and sulfur contents are measured in the uncarbonated region compared with the carbonated region. The sodium content in the uncarbonated region is approximately the same as in the uncarbonated sample. These results indicate that sodium in the carbonated region moves toward the sample surface during aging and precipitates in the form of Na_2SO_4 due to the capillary water movement. Alkali movement also has been observed in another study on alkali-activated slag, in which efflorescence appears at the sample surface under 55% RH ambient environment [126]. The fact that sodium accumulation is only found in the carbonated material but not in uncarbonated material can be explained by the previous finding that the water movement is much more aggressive during carbonation, especially under 68% RH (Table 3.4), and the greater solubility of NaOH.

Calcium migration is observed to have a complementary effect on sodium. Generally, there is relatively less calcium content in the region where sodium content is greater. However, since calcium is much less

soluble in the pore solution and mostly bound in the cement matrix, the likelihood of observing strong migration of calcium to the same extent as sodium during aging is low.

3.4 Conclusions

This study shows the effect of environmental conditions on carbonation in the Cast Stone waste form, a cementitious material with similar properties to alkali-activated fly ash and slag systems. Specific environmental factors considered are CO_2 concentration and the relative humidity in the surrounding environment. Experimental studies were carried out and the key conclusions from the study are:

1) The carbonation rate in Cast Stone is much greater than that observed in OPC-based paste and concrete due to the lower alkalinity and coarser pore structure formed in Cast Stone as well as the evolution of the microstructure (i.e., porosity increase and microcracking) during carbonation.
2) Carbonation rate in Cast Stone is proportional to the CO_2 concentration when aged at 68% RH, and the reaction extent increases with increasing CO_2 concentration. These validated that CO_2 concentration gradient is the driving force for diffusion and dissolution of CO_2 in Cast Stone.
3) The ingress rate of the carbonation front in Cast Stone is higher under lower RH in both air and 2% CO_2 conditions. This result is different from OPC-based paste and concrete materials, which exhibit the greatest rate and extent of carbonation at 50-65% RH. Lower water retention ability, higher amount of water generation under carbonation, and increased diffusion pathway during carbonation are identified in Cast Stone versus in cement and concretes, which contribute to the increased carbonation ingress in Cast Stone under dry conditions. The effect of RH is more significant on carbonation rate at 2% CO_2 than in air.
4) The extent of carbonation reaction behind the carbonation front is most extensive at 68% RH for both natural and accelerated carbonation conditions. Under dry conditions (15% and 40% RH), low moisture content and limited liquid-gas interfacial area restricted the dissolution of CO_2.
5) Sodium and sulfate migrated toward the exposure surface during carbonation under 68% RH, which is consistent with capillary water movement and surface precipitation.

4. IMPACT OF CARBONATION ON LEACHING OF CONSTITUENTS IN CAST STONE WASTE FORM

Abstract

The effect of carbonation on the leaching of major and trace constituents from the Cast Stone waste form was studied through the combination of leaching experiments and simulations. Liquid-solid partitioning (LSP) and chemical speciation of the constituents was analyzed using pH dependent leaching and geochemical speciation modeling. Diffusive transport of the constituents in the waste form was evaluated using diffusion-controlled mass transport leaching tests and reactive transport modeling using the geochemical speciation model derived from pH dependent leaching. Comparisons among Cast Stone materials aged under nitrogen, air, and 2% CO_2 showed that carbonation impacts both solubility and diffusivity of major and trace constituents. For Cr, which was one constituent of potential concern and redox-sensitive species, carbonation under 2% CO_2 reduced the diffusion-controlled leaching by two orders of magnitude. The LSP of Cr was strongly dependent on the pH and pe state in the system.

4.1 Introduction

Cementitious materials have been developed and used as a cost effective option for the immobilization of nuclear wastes globally due to their potential in incorporating radionuclides and stabilizing the waste [113,146,147]. At the Hanford Site in southeastern Washington State, a portion of low activity waste streams is being considered to be disposed as Cast Stone, which is a cementitious waste form produced from Portland cement, fly ash, blast furnace slag, and liquid low activity waste. Depending on the source of the waste stream, waste feed contains high concentrations of dissolved salts (mostly sodium salts of nitrate, hydroxide, chloride, fluoride, and sulfate); various amounts of radionuclides (notably ^{99}Tc and ^{129}I); RCRA metals (including chromium); and other constituents of potential concern (COPCs) [1,58,122,148]. The high pH and reducing environment within Cast Stone provides favorable conditions for the immobilization of COPCs. Through several testing programs, cementitious waste forms for the Hanford Site secondary liquid waste have measured releases of COPCs (e.g., ^{99}Tc and Cr) from the waste form lower than regulatory thresholds [58,115,122].

However, because decay of these radionuclides (e.g., ^{99}Tc, ^{129}I) takes a long time from a human perspective, the long-term performance of the waste form and the resulting leaching behavior of COPCs need to be carefully studied. Through the service life of the waste form, exposure to a reactive atmosphere can alter

the properties of the waste form due to carbonation and oxidation reactions with the cement matrix. Oxidation affects the solubilities of redox sensitive constituents in Cast Stone; oxidation effects have been studied in detail [90]. The solubilities of constituents can also be affected by carbonation, which decreases the internal pH of the waste form and introduces carbonates to its pore solution [38–40]. Meanwhile, as discussed in Chapter 3, carbonation also alters the pore structure of Cast Stone, which increases the transport rate for dissolved and gaseous components within the material. Therefore, extensive experiments and modeling studies were conducted on Cast Stone materials to fully understand changes to their physical and chemical properties under carbonation and to evaluate the potential impact to the environment.

One of the most relevant methods to estimate the retention ability of a waste form and provide data to evaluate its environmental impact is through leaching tests, in which the waste form is placed in contact with an extracting solution and releases of constituents are measured. The liquid-solid partitioning of constituents in the material can be derived from leaching under near chemical equilibrium conditions. Since the solubilities of constituents can be highly dependent on the solution pH, it is necessary to carry out leaching under a wide pH range [149]. In addition to the constituents' solubilities, the effect of transport properties within the waste form on the releases of constituents can be estimated through physical testing and diffusion-controlled mass transport leaching tests.

The effect of carbonation on leaching from Portland cement-based materials has been demonstrated in many studies [10,13,16,40,149]. However, Cast Stone, which contains high amounts of blast furnace slag and fly ash, a limited amount of Portland cement, and a high salt content alkaline solution yielded a very different chemical composition after hydration compared with Portland cement. Specifically, a lower Ca/(Si+Al) ratio is expected in the phases that control the dissolution of Ca, and a much higher Na concentration can be found in the pore solution [150]. The resulting carbonation products in Cast Stone are likely to be different from the products observed in Portland cement [151], leading to different solubilities of constituents. To date, no experimental study has been carried out to evaluate the effects of carbonation on leaching from Cast Stone, though it is an essential step for predicting long term performance of the waste form.

In this study, pH dependent leaching and diffusion-controlled leaching were carried out on Cast Stone materials aged under environmental conditions with and without CO_2 to evaluate the impact of carbonation on the release of constituents. To understand the effects of carbonation on mineral evolution in Cast Stone, geochemical speciation modeling was used to evaluate the chemical speciation that controls the experimentally measured liquid-solid partitioning of constituents. Major and trace constituents, including carbonation- and redox-sensitive constituents in the waste form, were selected as the focus in this study. Mineral phases and solid solutions identified in this study and a previous study of Cast Stone [90] were

incorporated into the reactive transport models used to simulate diffusion-controlled leaching. Key physical and chemical parameters were calibrated from constituent diffusion-controlled leaching. Reactive transport modeling allows extrapolating lab test results to long-term field leaching.

4.2 Material and Methods

4.2.1 Aging experiment

Cast Stone samples were prepared following the formulation and method introduced in 3.2.1. Waste simulant was prepared using a recipe based on the anticipated Hanford Site low activity waste (LAW) composition [74]. Chromium was added in the form of Na_2CrO_4 to achieve 0.2 wt% loading. Cr is a redox-sensitive constituent that possesses lower solubility as Cr(III) than as Cr(VI) and, therefore, can serve as a redox indicator. Cr also is a major RCRA metal component of LAW [37]. Cast Stone samples in granular form and monolithic form were transferred into an aging environment after hydration under N_2 and 100% RH for 90 days, and pre-conditioning under N_2 and 68% RH for 60 days. Granular samples were then aged under nitrogen (0% CO_2; CS-N); air (0.04% CO_2 and 21% O_2; CS-A); 2% CO_2 (v/v in nitrogen; CS-C); and 68% RH for 16 weeks. Monolithic samples were aged under 68% RH for 48 weeks in nitrogen (CS-N-48w); air (CS-A-48w); and 2% CO_2 (CS-C-48w). The detailed aging method is described in section 3.2.2. It is assumed that during the hydration and aging periods, the reduction capacity (mostly contributed by reduced sulfur in the blast furnace slag) in Cast Stone reduces the doped Cr(VI) into Cr(III), which lowers the solubility of Cr. Studies on saltstone material which used a similar binder composition as Cast Stone showed that the saltstone was able to reduce the doped 0.1 wt% Cr(VI) after 21-37 days of curing [152,153]. The reduction capacity measured from the cured saltstone was between 605-849 μeq e^-/g, which is much greater than the amount of reduction capacity required to completely reduce the 0.2 wt% Cr(VI) to Cr(III) in the Cast Stone system (115.4 μeq e^-/g). Therefore, it is reasonable to assume that the Cr(VI) doped in Cast Stone is completely reduced after 90 days of hydration. During the aging period, the O_2 in the aging environment (e.g., air) diffuses into the material potentially reacting with the reduced Cr in CS-A, increasing the solubility of Cr [152].

4.2.2 Total content

The total contents of chemical constituents in the granular Cast Stone (CS-N) samples after aging were analyzed using lithium metaborate ($LiBO_2$) fusion [154]. Powdered samples were dried at 105°C, and 250 mg of samples were mixed with 600 mg of $LiBO_2$. The samples were heated at 1100°C for 10 min and then

well mixed with 50 ml of preheated 1 mol/L nitric acid. The resulting solution was analyzed by inductively coupled plasma-optical emission spectrometry (ICP-OES) using EPA Method 6010D [80] and inductively coupled plasma-mass spectrometry (ICP-MS) using EPA Method 6020B [155] for the concentrations of constituents. Due to the volatile nature of most of the anion constituents under fusion, total contents of anions that are volatile under high temperature (Cl, F, NO_3, Br, SO_4) were calculated from the composition of the waste simulant used in the formulations.

Thermogravimetric analysis (TGA) was used to estimate the mass fraction of carbonation products [85,151]. TGA was analyzed with a TA Instruments Q600 SDT analyzer (New Castle, Delaware, USA). Approximately 20 mg of sample was initially equilibrated at a temperature of 50°C prior to heating to 1000°C at a rate of 10.0°C/min. The chamber was continuously flushed with nitrogen throughout the heating process with a flow rate of 100 mL/min.

4.2.3 pH dependent leaching test

The aged granular samples were tested for pH dependent liquid-solid partitioning following EPA Method 1313 [131]. The test obtains the leaching behavior of Cast Stone by measuring the release of constituents from the material under conditions that approach equilibrium at different target pH values. For each pH test position, a 10-gram granular test sample was mixed with a predetermined amount of nitric acid or potassium hydroxide and de-oxygenated Milli-Q water to bring the liquid-solid ratio (L/S) to 10 mL/g at a given target pH value. The samples were then mixed in an end-over-end tumbler at room temperature for 48 hours. After mixing, eluate pH, electrical conductivity (EC), and oxidation-reduction potential (ORP) were measured. The samples were centrifuged and filtered through 0.45 µm filter. The filtrate was analyzed with ICP-OES for concentrations of Al, Sb, As, Ba, B, Ca, Cr, Fe, Li, Mg, Ni, P, K, Se, Si, Na, Sr, S, Ti, V, and Zn, and with ICP-MS for concentrations of Be, Cd, Cs, Co, Cu, Mn, Ni, Tl, Sn, Ti, and U.

4.2.4 Diffusion-controlled leaching test

A 1-D diffusion-controlled mass transport leaching test was performed on the aged monolithic Cast Stone samples following EPA Method 1315 [133]. The surface of the sample exposed to aging conditions was in direct contact with de-oxygenated Milli-Q water to bring the liquid-surface area ratio to 10 mL/cm^2 and to allow 1-D diffusion. The eluate was exchanged at 0.1, 1, 2, 7, 14, 28, 42, 49, 63, 91, and 105 days. Each eluate was analyzed for pH, EC, and ORP. Concentrations of constituents in the eluate were measured using the method described in section 4.2.3. Anions were additionally measured by ion chromatography (IC) using EPA Method 9056A [81] for concentrations of F, Cl, Br, NO_2, NO_3, SO_4, and PO_4.

4.3 Modeling approach

Geochemical speciation modeling and reactive transport modeling were performed using the LeachXS™/ORCHESTRA framework [99,139] to simulate the pH dependent liquid-solid partitioning of constituents as obtained by the pH dependent leaching test (EPA Method 1313) and mass transfer release of constituents as obtained by diffusion-controlled leaching test (EPA Method 1315). The reaction constants (log K's) of reactions used in the equilibrium calculations are obtained from several thermodynamic databases including MINTEQ.V4, CEMDATA18, Thermoddem2011, and LLNL.dat [87,88,156,157]. Activity coefficients were calculated using the modified Davies activity model [158]. Since the modified Davies activity model is applicable to a relatively low ionic strength range (I<1.2 mol/L), future research will include implementing the SIT activity model to account for the impact of ionic interactions at high ionic strength.

4.3.1 pH dependent leaching simulation and input parameters

Geochemical speciation modeling assumes chemical equilibrium of dissolution, precipitation, redox, and adsorption reactions in the modeled system. For all the Cast Stone materials aged under different environmental conditions, a single mineral assemblage (Table 4.1) as derived by Chen et al. [90] was used to describe the eluate concentrations of major and trace constituents (i.e., Ca, Si, Al, Na, Mg, Fe, S, and Cr). The description for leaching behaviors of carbonation sensitive species (i.e., Li, Ba, Sr) is evaluated in this work. The selection of the mineral assemblage and solid solutions for Cast Stone considered both the phases from characterization [32,90,123,124,159] and phases reported in literature [87,150,151]; the resulting assemblage was verified through comparing geochemical speciation modeling results with experimental measurements on non-carbonated Cast Stone (CS-N) and oxidized Cast Stone samples. For both the results from [90] and carried out here, the log-squared residuals for each constituent concentration at each tested pH were calculated and summed (*logRSS*) to evaluate the goodness of fit for the model prediction.

Table 4.1 Mineral assemblage controlling the solubility of constituents in Cast Stone materials.

Notation	*Formula*	*Log(K)*[a]	*Reaction*
CEM18_INFCNA_CNASHss [b]	$16CaO{\cdot}5.5Na_2O{\cdot}2.5Al_2O_3{\cdot}19SiO_2{\cdot}21H_2O$	-9.836	CEM18_INFCNA + 0.5 H_2O -> 0.3125 $Al[OH]_4^-$ + 1 CEM18_CNASH_ss + 1 Ca^{+2} + 1.1875 $H_2SiO_4^{-2}$ + 0.6875 Na^+
CEM18_T2C_CNASHss [b]	$3CaO{\cdot}2SiO_2{\cdot}5H_2O$	2.982	CEM18_T2C_CNASHss + 1 H^+ -> 1 CEM18_CNASH_ss + 1.5 Ca^{+2} + 2 H_2O + 1 $H_2SiO_4^{-2}$
CEM18_TobH_CNASHss [b]	$2CaO{\cdot}3SiO_2{\cdot}5H_2O$	-21.51	CEM18_TobH_CNASHss -> 1.5 CEM18_CNASH_ss + 1 Ca^{+2} + 1 H^+ + 0.5 H_2O + 1.5 $H_2SiO_4^{-2}$
Ca3[PO4]2[beta] [c]	$Ca_3(PO_4)_2$	-29.08	Ca3[PO4]2[beta] -> 3 Ca^{+2} + 2 PO_4^{-3}
CaCO3_BaCO3 [e]	$CaBa(CO_3)_2$	-21.10	CaCO3_BaCO3 -> 1 Ba^{+2} + 2 CO_3^{-2} + 1 Ca^{+2}
CaCO3_Li2CO3 [e]	$CaLi_2(CO_3)_2$	-21.30	CaCO3_Li2CO3 -> 2 CO_3^{-2} + 1 Ca^{+2} + 2 Li^+
CaCO3_SrCO3 [e]	$CaSr(CO_3)_2$	-19.75	CaCO3_SrCO3 -> 2 CO_3^{-2} + 1 Ca^{+2} + 1 Sr^{+2}
CEM18_Amor_Sl [b]	SiO_2	-25.72	CEM18_Amor_Sl + 2 H_2O -> 2 H^+ + 1 $H_2SiO_4^{-2}$
CEM18_Brc [b]	$Mg(OH)_2$	17.18	CEM18_Brc + 2 H^+ -> 2 H_2O + 1 Mg^{+2}
CEM18_C3S [b]	Ca_3SiO_5	51.63	CEM18_C3S + 4 H^+ -> 3 Ca^{+2} + 1 H_2O + 1 $H_2SiO_4^{-2}$
CEM18_Cal [b]	$CaCO_3$	-8.45	CEM18_Cal -> 1 CO_3^{-2} + 1 Ca^{+2}
CEM18_hemicarbonate [b]	$Ca_4Al_2(CO_3)_{0.5}(OH)_{13}{\cdot}5.5H_2O$	40.93	CEM18_hemicarbonate + 5 H^+ -> 2 $Al[OH]_4^-$ + 0.5 CO_3^{-2} + 4 Ca^{+2} + 10.5 H_2O
CEM18_hemihydrate [b]	$CaSO_4{\cdot}0.5H_2O$	-3.518	CEM18_hemihydrate -> 1 Ca^{+2} + 0.5 H_2O + 1 SO_4^{-2}
CEM18_Mgs [b]	$MgCO_3$	-8.206	CEM18_Mgs -> 1 CO_3^{-2} + 1 Mg^{+2}
CEM18_monocarbonate [b]	$Ca_4Al_2(CO_3)(OH)_{12}{\cdot}5H_2O$	24.38	CEM18_monocarbonate + 4 H^+ -> 2 $Al[OH]_4^-$ + 1 CO_3^{-2} + 4 Ca^{+2} + 9 H_2O
CEM18_monosulphate12 [b]	$Ca_4Al_2O_6(SO_4){\cdot}12H_2O$	26.66	CEM18_monosulphate12 + 4 H^+ -> 2 $Al[OH]_4^-$ + 4 Ca^{+2} + 10 H_2O + 1 SO_4^{-2}
CEM18_Ord_Dol [b]	$CaMg(CO_3)_2$	-16.99	CEM18_Ord_Dol -> 2 CO_3^{-2} + 1 Ca^{+2} + 1 Mg^{+2}
CEM18_Portlandite [b]	$Ca(OH)_2$	23.19	CEM18_Portlandite + 2 H^+ -> 1 Ca^{+2} + 2 H_2O
Diaspore [c]	α-AlO(OH)	-16.02	Diaspore + 2 H_2O -> 1 $Al[OH]_4^-$ + 1 H^+
Eskolaite [d]	Cr_2O_3	-147.5	Eskolaite + 5 H_2O -> 2 CrO_4^{-2} + 10 H^+ + 6 e^-
Ferrihydrite [c]	$Fe_2O_3{\cdot}0.5H_2O$	-18.18	Ferrihydrite + 1 H_2O -> 1 $Fe[OH]_4^-$ + 1 H^+
Gaylussite [d]	$Na_2Ca(CO_3)_2{\cdot}5H_2O$	-9.516	Gaylussite -> 2 CO_3^{-2} + 1 Ca^{+2} + 5 H_2O + 2 Na^+
Larnite [d]	Ca_2SiO_4	16.18	Larnite + 2 H^+ -> 2 Ca^{+2} + 1 $H_2SiO_4^{-2}$
Nahcolite [d]	$NaHCO_3$	-10.79	Nahcolite -> 1 CO_3^{-2} + 1 H^+ + 1 Na^+
Natron [c]	$Na_2CO_3{\cdot}10H_2O$	-1.508	Natron -> 1 CO_3^{-2} + 10 H_2O + 2 Na^+
Pyrite [c]	FeS_2	-121.1	Pyrite + 12 H_2O -> 1 $Fe[OH]_4^-$ + 20 H^+ + 2 SO_4^{-2} + 15 e^-
Pyrrhotite [d]	FeS	-72.27	Pyrrhotite + 8 H_2O -> 1 $Fe[OH]_4^-$ + 12 H^+ + 1 SO_4^{-2} + 9 e^-
Wairakite [d]	$Ca_8Al_{16}Si_{32}O_{96}{\cdot}16H_2O$	-119.4	Wairakite + 10 H_2O -> 2 $Al[OH]_4^-$ + 1 Ca^{+2} + 8 H^+ + 4 $H_2SiO_4^{-2}$
llnl_NaTcO4 [d]	$NaTcO_4$	-9.279	llnl_ $NaTcO_4$ + 1 e^- -> 1 Na^+ + 1 TcO_4^{-2}
llnl_TcO2:2H2O[am] [d]	$TcO_2{\cdot}2H_2O$	-48.46	llnl_TcO2:2H2O[am] -> 4 H^+ + 1 TcO_4^{-2} + 2 e^-
llnl_Tc3O4 [d]	Tc_3O_4	-192.9	llnl_Tc3O4 + 8 H_2O -> 16 H^+ + 3 TcO_4^{-2} + 10 e^-
llnl_TcOH [d]	TcOH	-110.4	llnl_TcOH + 3 H_2O -> 11 H^+ + 1 TcO_4^{-2} + 7 e^-

[a] *formation reaction constant;*
[b] *mineral from CEMDATA18 database;*
[c] *mineral from Minteq. V4 database;*
[d] *mineral from LLNL database;*
[e] *minerals proposed in the present study with calibrated logK.*

For each material, the available content (i.e., the content that can participate in geochemical speciation reactions) for each constituent except for silica and carbonate was determined by the maximum release of the constituents measured across the entire pH range in the Method 1313 test (Table 4.2). The reactions associated with silica were considered to be kinetically controlled and not near thermodynamic equilibrium after 48 hours of leaching, thus the silica available content was calibrated to fit the calcium leaching curve

at pH > 9 because the dissolution of calcium is sensitive to the Ca/Si ratio. The available content of carbonate was determined within the measured carbonate content from TGA and calibrated to fit the calcium leaching curve between pH 6 to 9 (Figure D2). The redox state (pe) at each pH condition was calibrated based on the predicted concentration of redox sensitive species because laboratory redox measurements during leaching tests were considered unreliable because of sample handling and test conditions. Among the redox sensitive species in the system (e.g., S, Fe and Cr), Cr was selected for calibration of pe. As will be discussed in section 4.4.4, the redox states of S and Fe are less sensitive to the range of pe in the test conditions compared to Cr. Calibrating pe by fitting the measured concentrations of S led to a poor description of Cr leaching (Appendix A, Figure S6).

The adsorption of ions on the surface of organic matter was modeled with the NICA-Donnan model [160] using parameters published by Milne, et al. [161,162]. Ion adsorption onto HFO was modeled using the generalized two layer model of Dzombak and Morel [163]. The amount of organic matter and HFO in the system were determined by fitting the aqueous partitioning curves of Cu and As, respectively.

Table 4.2 Total content and available content of elements in Cast Stone.

	Available content (mg/kg)			Total content (mg/kg)
	CS-N	**CS-A**	**CS-C**	
Al	6480	6480	6480	64500 [a]
As	7.1	6.2	8.6	8.6 [a]
B	23	36	39	-- [a]
Ba	17	17	7.7	579 [a]
Br	0.0059	0.0059	0.0059	-- [b]
Ca	71400	64100	54000	109000 [a]
Cd	0.12	0.12	0.13	0.60 [a]
Cl	552	708	771	483 [b]
Co	1.2	1.4	1.4	21 [a]
CO_3	36000	51000	81900	57600 [c]
Cr	353	418	424	1900 [a]
Cu	8.5	8.7	8.1	62 [a]
F	7.8	44	109	269 [b]
Fe	656	665	720	17800 [a]
K	3400	4200 d	3690	8580 [a]
Li	19	16	11	-- [a]
Mg	5300	4000	2800	8480 [a]
Mn	137	135	170	557 [a]
Mo	4.2	4.7	5.2	7.2 [a]
Na	42100	30400	28900	56700 [a]
Ni	1.7	1.8	1.7	50 [a]
NO_3	43400	43400	43400	45600 [b]
P	197	191	257	850 [a]
Pb	1.7	1.8	1.8	4.1 [a]
S	8020	8020	8020	8400 [a]
Sb	0.27	0.25	0.14	1.8 [a]
Se	3.8	4.1	4.9	25 [a]
Si	35700	3090	13200	143000 [a]
Sr	249	121	112	422 [a]
Zn	16	16	14	52 [a]

a. from $LiBO_2$ fusion (Li and B not measured due to addition of $LiBO_2$ in testing);
b. from simulant formulation (Br not added);
c. from TGA measurement;
d. maximum concentration of K in pH positions without KOH addition for pH adjustment

4.3.2 Diffusion-controlled leaching simulation and input parameters

The 1-D diffusion-controlled mass transport leaching from CS-N-48w, CS-A-48w, and CS-C-48w monoliths was simulated with geochemical speciation coupled with reactive transport modeling. In

monolithic diffusion modeling, the experimental condition was conceptualized (Figure D1) as a series of well-mixed cells representing the Cast Stone monolith (10-cm depth) and a well-mixed tank cell at the boundary representing the refresh solution (with solution volume accounting for experimental liquid-surface ratio). Chemical equilibrium is calculated at each time step within each cell. Transport of constituents through diffusion between adjacent cells was calculated at the end of each time step.

The same mineral assemblage as defined in pH dependent leaching simulation was used (Table 4.1). The available contents of the constituents except for the carbonate and silicate were assumed to be uniform across the solid matrix, and the values obtained from CS-N (Table 4.2) were used. The available content of silica that was previously determined through calibration to the Ca leaching curve was found to be very different in carbonated and uncarbonated materials (Table 4.2). Therefore, for the carbonated cells in CS-A-48w and CS-C-48w, the available content of Si was calculated from the available content ratio of Ca/Si in CS-A and CS-C, respectively. Also, the available content ratio of Ca/CO_3^{2-} from CS-A and CS-C was used as the basis for determining available content of carbonate in the carbonated cells. The available content of carbonate in the carbonated cells was further calibrated to fit the pH values of tank solutions. Illustration of the approach for determining the available content of carbonate is provided in Figure D3.

The initial redox state (pe) of the solid matrix prior to leaching was assumed to be variable as a function of depth from surface due to the interaction between pH and pe, depending on the redox reactions in the system. Hence, the initial pe of the pore solution in each cell was calibrated based on the measured Cr concentration in Method 1315 eluates as illustrated in Figure D3. The effective diffusivity ($D_{e,L}$) of an ion is controlled by the physical properties including porosity (ε), liquid phase tortuosity factor (τ_L), and saturation (S) of Cast Stone as governed by Eq. 4-1, where $D_{0,L}$ is the free diffusivity of ions in water [46].

$$D_{e,L} = \frac{S^{7/3} \times \varepsilon \times D_{0,L}}{{\tau_L}^2} \tag{4-1}$$

The tortuosity profile in the solid matrix was determined from the leaching curves of Na. Na is a relatively non-reactive element as discussed in section 4.4.1. The tortuosity factor in each cell was determined by minimizing the log-squared residuals (*logRSS*, Eq. 4-2) of the simulated sodium release concentrations ($\hat{y}$) compared to measurements (y).

$$logRSS = \sum (\log\left(\frac{\hat{y}}{y}\right))^2 \tag{4-2}$$

4.4 Results and discussion

4.4.1 pH dependent leaching of major constituents

The experimental results from Method 1313 and geochemical speciation prediction of acid neutralizing capacity (ANC) titration and solution ionic strength as a function of pH are shown in Figure 4.1. The titration curve for a carbonated material (CS-A, CS-C; Figure 4.1) was generally shifted to the left from the uncarbonated material (CS-N), indicating carbonation decreased the natural pH of the material (i.e., pH value measured with no acid or base addition during leaching; ANC=0 mol/kg) and also decreased the buffering capacity in the alkaline pH range between 7-13. The decrease in buffering capacity indicates the decrease of C-S-H, which contributes to the acid neutralization capacity in the system, and the greater extent of carbonation reaction results in lower buffering capacity. The natural pH of CS-A was slightly decreased compared to that in CS-N from 12.6 to 12.1 and further decreased to 9.9 in CS-C. The calculation of alkalinity from the ANC titration curves and the correlation between alkalinity, buffering capacity, and natural pH of the material were discussed in section 3.3.1. The geochemical speciation modeling closely predicted the measured ANC curve at pH greater than 6, and the natural pH of each material was well captured. The deviation of the modeled ANC from the experimental results at pH less than 6 may be attributed to the loss of carbonate in the system in the form of CO_2 gas, which was not considered in the model. The entrapment of Al in silica gel formed at lower pH conditions in the experiment [90] was not considered in the model. A previous study suggested that acid buffering in the system at pH below 4 is likely to be controlled by Al-bearing phases [164]; however, in Cast Stone, the maximum concentration measured in the eluate was less than 10% of the total content of Al (Table 4.2).

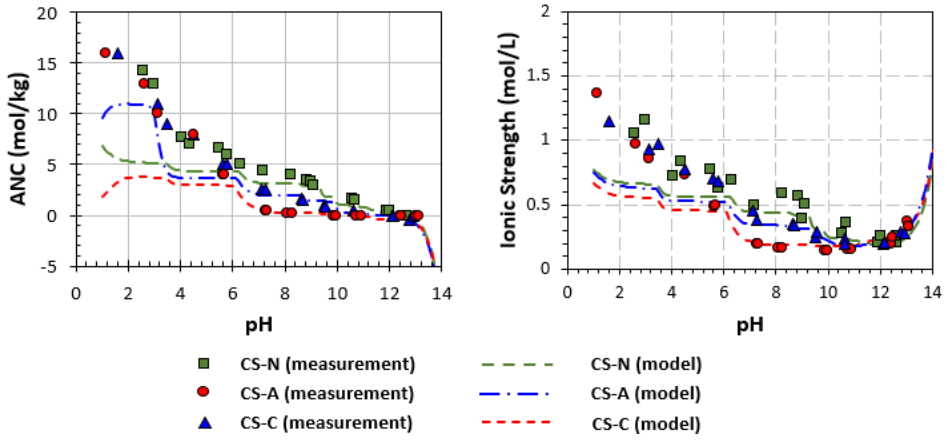

Figure 4.1 Experimental measurements and geochemical speciation modeling results of acid neutralizing capacity (ANC) and solution ionic strength for CS-N, CS-A, and CS-C.

The experimental results from Method 1313 and geochemical speciation modeling for major constituents leaching as a function of pH are presented in the first column in Figure 4.2. The circles indicate concentrations of constituents at the natural pH of the material (i.e., with no acid or base addition during leaching). Constituents with a total content of greater than 0.5 wt% including Ca, Si, Al, Mg, Na, and Fe are considered major constituents, and the results for Fe are presented later in section 4.4.4. Geochemical speciation modeling well described the leaching behavior of major constituents in the pH range between 7 and the natural pH of the materials, indicating good representativeness of the mineral set for uncarbonated and carbonated materials. Modeling results for speciation of major constituents are presented in Figure 4.2 to show the predicted partitioning of the constituents among the phases in the system (i.e., dissolved phase, minerals, solid solutions, and adsorption phases). The results for chemical speciation in CS-N and CS-C are presented as two bounding cases with minimum and maximum extent of carbonation.

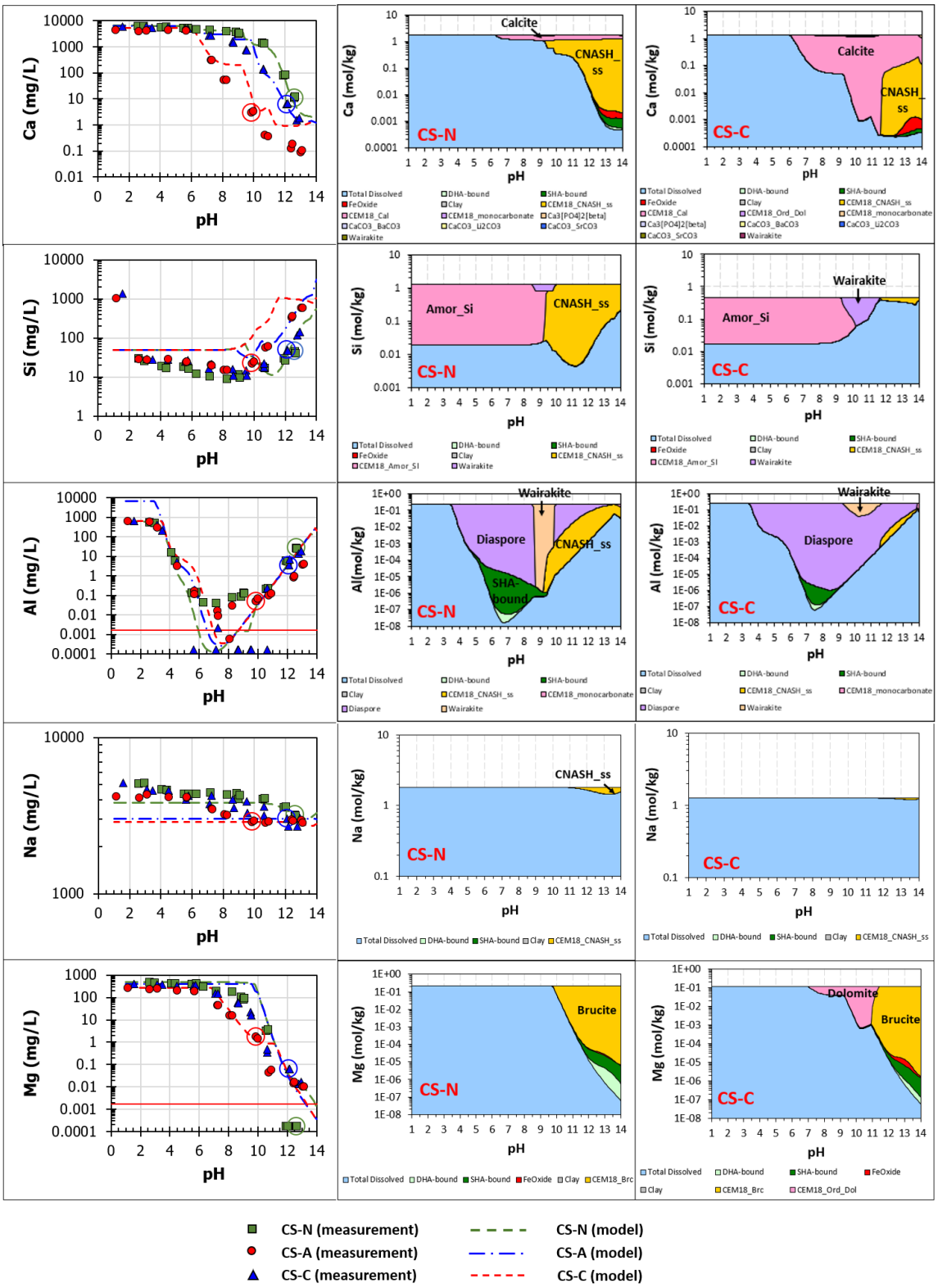

Figure 4.2 Experimental measurements and geochemical speciation modeling results of major constituents (Ca, Si, Al, Na, Mg) for CS-N, CS-A, and CS-C. Circles indicating the test position at the natural pH of the material. (Amor_Si: CEM18_Amor_Si; CNASH_ss: CNASH solid solution, Table 4.1).

The pH dependent leaching behavior of the major constituents in the carbonated material was also found shifted when compared to the uncarbonated material (Figure 4.2). The leaching of Ca decreased in the pH range of 6-13 as the extent of carbonation increased, which agrees with the observation from other studies on cementitious materials [13,40]. The differences in Ca concentration between the carbonated and uncarbonated material are most significant at pH 10.7 and decrease as pH further increases. A smaller difference is observed for the leaching of Ca under natural pH conditions of the three aged samples because the solubility of Ca is highly dependent on pH. The model prediction of Ca concentration from CS-N and CS-A agreed well with measurement. Although the prediction from CS-C is higher than the measured value by one order of magnitude at pH<10.5, the model closely predicted the Ca concentration at the natural pH of the material. From the geochemical speciation results for CS-N, the CNASH solid solution (CNASH_ss) was the controlling phase for the solubility of Ca, Si, Al, and Na in the simulated system at pH 9-14. The absence of portlandite in the Ca speciation, which is a major hydration phase in Portland cement, is the result of low Ca/Si ratio in the Cast Stone system. The absence of portlandite agrees with other characterization results on Cast Stone and materials with similar compositions [31,124]. Compared to CS-N, the amount of CNASH solid solution in CS-C was significantly decreased and only present at pH 11.5-14, indicating the decomposition of CNASH phases under carbonation. The CNASH decomposition leads to the release of Ca, Si, Al, and Na from the CNASH solid solution in the carbonated material. Instead, a large amount of calcite was formed in CS-C and was stable at pH 6.2-14, controlling the leaching of Ca in this pH range.

The concentration of Si increased in CS-C compared to CS-A and CS-N in the pH range of 9-13, which is in accordance with observations for concrete materials [16]. The decomposition of CNASH under carbonation resulted in the dissolution of Si (Figure 4.2). Although the available content of Si was lower in CS-C than CS-N as determined by calibration to the Ca leaching curve, the model captured the increased Si concentration in CS-C at pH 9-13. However, the accurate prediction of Si may be challenged because Si leaching may be kinetically controlled and near equilibrium conditions for Si may not be reached in the experimental system. The reaction rates can be dependent on the pH, and the dissolution of Si phases might be slower at higher pH range, causing the greater deviation.

The leaching of Al slightly decreased in the carbonated material compared to uncarbonated material at pH 5.5-13. Greater amounts of wairakite ($Ca_8Al_{16}Si_{32}O_{96}{\cdot}16H_2O$) and diaspore (α-AlO(OH)) were predicted to be stable below pH 11 in CS-C compared to CS-N, controlling the solubility of Al.

The leaching of Na is less dependent on pH in all three materials compared to other major constituents. A slight decrease of Na leaching was observed in the carbonated material in the high pH range; however, at

the natural pH values, the solubility of Na is similar in CS-N, CS-A, and CS-C all around 3000 mg/L, suggesting minimal impact of carbonation on the solubility of Na. From the result of geochemical speciation modeling, almost all the sodium in the system is dissolved in the solution at the natural pH (98.9% for CS-N, 99.8% for CS-C, Figure 4.2) instead of precipitated with the mineral phases. Therefore, it is reasonable to assume Na as a relatively non-reactive element that can be used for the calibration of tortuosity factor in Cast Stone monolith for reactive transport modeling.

A similar leaching pattern to Ca was observed for Mg, except for that the leaching of Mg at the natural pH condition is higher in the carbonated material than in the uncarbonated material. The solubility of Mg in both CS-N and CS-C was predominantly controlled by brucite at pH>10 and by dolomite ($CaMg(CO_3)_2$) in CS-C at pH 7-11.

The speciation of Ca, Si, Al, and Mg at the natural pH values of the three materials is summarized in Table 4.3. On the whole, the carbonation process in Cast Stone mainly consumes the CNASH phases and produces calcite, wairakite, dolomite, and amorphous silica phases. The difference in the solubility of these phases as a function of pH controls the pH dependent leaching of major constituents in the system.

Table 4.3 Speciation of the solubility controlling mineral phases for Ca, Si, Al, Mg in CS-N, CS-A, CS-C at the natural pH of the material.

Mineral	Ca (mg/kg)			Si (mg/kg)			Al (mg/kg)			Mg (mg/kg)		
	CS-N	CS-A	CS-C	CS-N	CS-A	CS-C	CS-N	CS-A	CS-C	CS-N	CS-A	CS-C
CNASH_ss	43200	30100	-	31600	28900	-	3300	-	-	-	-	
Calcite	21300	33500	45300	-	-	-	-	-	-	-	-	-
Dolomite	-	-	4520	-	-	-	-	-	-	-	-	274
Wairakite	-	-	3520	-	-	9880	-	-	4740	-	-	-
Amor silica	-	-	-	-	-	2190	-	-	-	-	-	-
Diaspore	-	-	-	-	-	-	2470	6430	1730	-	-	-
Brucite	-	3960	-	-	-	-	-	-	-	484	396	-
Dissolved	63	54	110	962	1970	1140	136	43	-	-	-	-

4.4.2 Diffusion-controlled leaching of major constituents

Diffusion-controlled leaching experiments using EPA Method 1315 were conducted on monolith samples to further evaluate the transport of constituents in the solid matrix. The profiles of physical and chemical properties of Cast Stone monoliths after aging can be derived from the diffusion-controlled leaching test results. The profiles of initial pe, tortuosity factor, and available content of carbonate in tested monolithic samples were determined from diffusion-controlled leaching tests results and presented in Figure 4.3. Carbonate content profiles, which were calibrated from eluate pH (Figure 4.5), indicated the increased extent of carbonation with increasing CO_2 concentration in the aging environment. A much deeper

carbonation front, as well as higher carbonate content, was observed in CS-C-48w compared to CS-A-48w. In CS-A-48w, carbonate is accumulated near the exposure surface, while in CS-C68-48w a peak in carbonate profile was predicted near the drying and carbonation front (around 4 cm from exposure surface). A plausible explanation is that, given the high sodium content in Cast Stone pore solution (around 4 mol/L), carbonation in Cast Stone under 2% CO_2 likely results in dissolved sodium bicarbonate species in pore solution in addition to the precipitation of calcite [31,151]. Sodium bicarbonate can be concentrated in the pore solution near drying front and migrates with the ingress of carbonation front. This explanation is supported by the SEM-EDS mapping of Na as previously shown in Figure 3.11. An accumulation of Na was observed in the scanned profile near the drying front, suggesting the precipitation of sodium salts, possibly in the form of sodium bicarbonate. The presence of sodium bicarbonate is further supported by the geochemical speciation modeling results of the pore solution speciation profile in CS-C-48w (Figure 4.4). Geochemical speciation for carbonate and sodium suggest that nahcolite ($NaHCO_3$) and natron ($Na_2CO_3 \cdot 10H_2O$) were present near the carbonation boundary that accounted for 31% and 25% of the total Na, respectively, and a large portion of carbonate was present in the form of dissolved species.

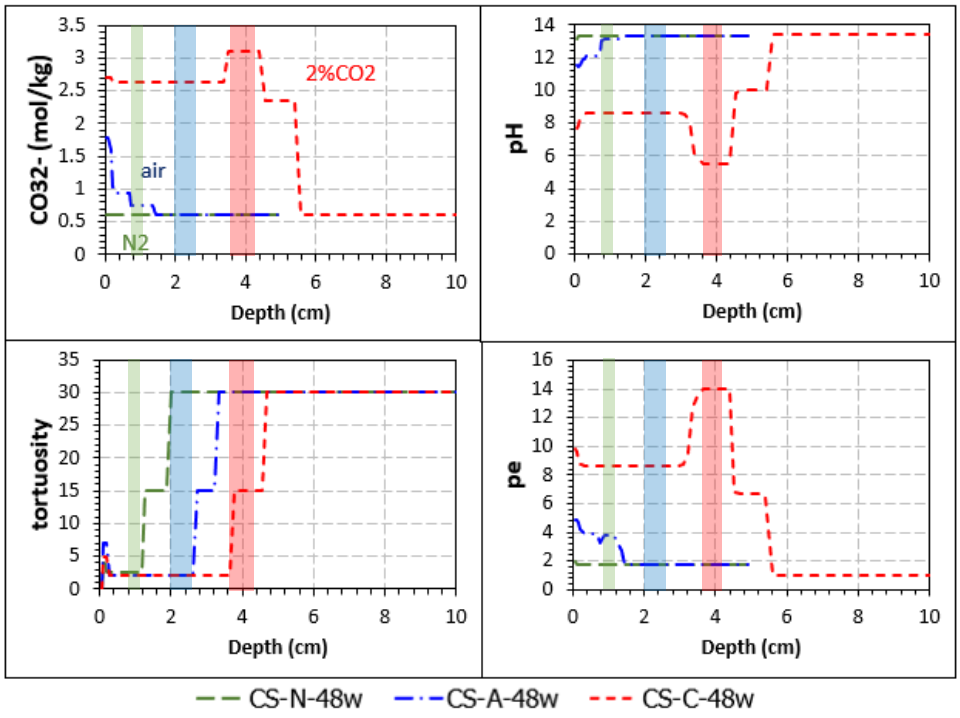

Figure 4.3 Initial profile of physical and chemical properties of Cast Stone monolith in diffusion-controlled leaching simulation (where the shaded regions indicate the range of drying front in the sample from measurements and model results).

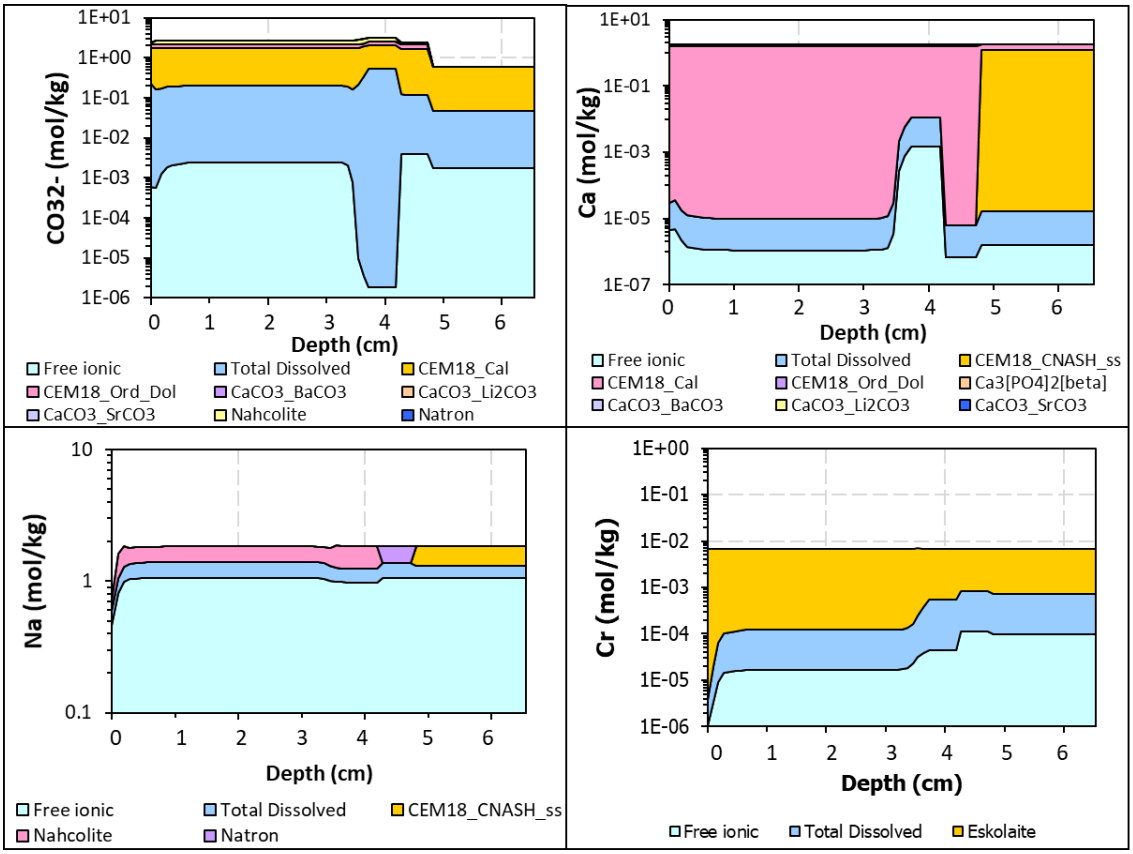

Figure 4.4 Geochemical speciation modeling results of key constituents in CS-C-48w at initial leaching (leaching time = 0.03 days).

Figure 4.5 shows the experimental results from Method 1315 and reactive transport modeling prediction of eluate pH and fluxes of major constituents in the eluate as a function of leaching time. The same set of proposed minerals was used in the reactive transport model. Results are also presented on the basis of measured concentrations for the constituents in Figure D4 to indicate the detection limits. Carbonation in air and 2% CO_2 significantly affected the eluate pH from Cast Stone, and the reactive transport model closely described the pH curves for all three samples, with overestimation of pH in CS-A at 1-2 days. The first exchange at 0.1 days was not included in the comparisons because sample preparation effects (e.g., surface wash-off) typically skew results. The eluate pH in the early stage (i.e., eluate pH at 0-7 days) of CS-A-48w and CS-C-48w were around 9, significantly lower than the pH of 11 in CS-N-48w. As leaching time increases, the eluate pH values in CS-N-48w and CS-A-48w increase steadily, both rising to pH>11 near the end of the leaching test. In CS-C-48w, pH was significantly lower through the entire time range of the leaching test compared to CS-N-48w. As discussed in section 3.3.1, the eluate pH is closely related to the alkalinity profile in the sample tested, which reflects the carbonation depth and reaction extent in the monolith after aging.

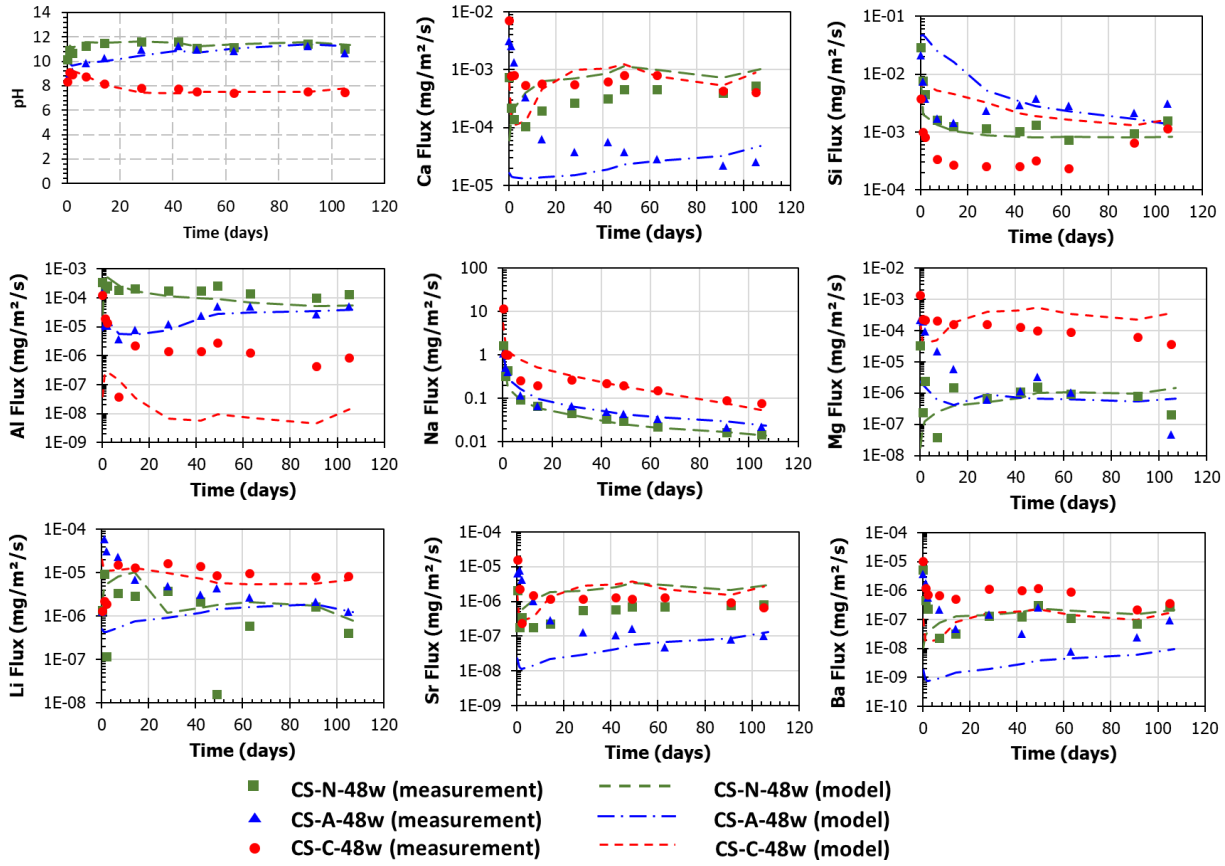

Figure 4.5 Experimental measurements and reactive transport modeling results of diffusion-controlled leaching fluxes of major constituents and carbonation sensitive constituents in CS-N-48w, CS-A-48w, and CS-C-48w.

As discussed in 4.4.1, Na was assumed to be relatively non-reactive in the system, and concentrations of Na during leaching were used to calibrate the liquid phase tortuosity factor in the monolith. Generally, tortuosity factor near the surface of the carbonated material was decreased (Figure 4.3), which was supported by the finding in 3.3.2 that moisture transport in CS-C-48w is much more rapid compared to CS-N-48w. In comparison, no significant change was observed in Na leaching between CS-N-48w and CS-A-48w, which was also supported by the similar moisture transport pattern observed in CS-N-48w and CS-A-48w. As a result of increased effective diffusivity in the carbonated material, Na flux is approximately five times greater across the entire time range in CS-C-48w compared to CS-N-48w and CS-A-48w (Figure 4.5).

For Ca leaching, a higher flux by an order of magnitude was observed in CS-A-48w and CS-C-48w than CS-N-48w during the first 7 days of leaching; the difference between CS-N-48w and CS-C-48w decreases as leaching time increases. Fluxes in CS-A-48w are consistently lower than those in CS-N-48w and CS-C-48w by an order of magnitude from 28 days to the end of the leaching period. These trends are different

from the trend of Ca solubility at the natural pH of the material as observed in Figure 4.2, in which CS-C has the lowest solubility at the natural pH due to the presence of calcite. A study on a Portland cement based material also found that compared to uncarbonated material, Ca leaching is lower from a partially carbonated material and higher in a completely carbonated material [39]. Pore solution pH in the carbonated region of CS-A is above 11; therefore, carbonate can be present as carbonate ions and precipitate as calcite. However, the pore solution pH in the carbonated region of CS-C is near 8. At this pH range, carbonate exists in the form of bicarbonate, which is much more soluble compared to carbonate. Hence, the higher extent of carbonation increases the leaching of Ca. However, the pore solution pH in the Cast Stone monolith may differ from the natural pH of the material measured from equilibrium leaching test (Method 1313) partly due to the different liquid-to-solid ratio in the two tests (0.31 mL/g in monolith and 10 mL/g in equilibrium leaching). For instance, the natural pH values of CS-N, CS-A, and CS-C are 12.6, 12.1, and 9.9, respectively, while the pore solution pH values in CS-N-48w, CS-A-48w, and CS-C-48w are 13.4, 11.5, and 9.8, respectively. Therefore, the solubility of Ca derived from Method 1313 cannot be directly used for comparing Ca solubility in Method 1315. Another major factor accounting for the differences in constituent release between equilibrium leaching and diffusion-controlled leaching is the diffusion of constituents in the monolith. Similar to Na, the effective diffusivity of Ca in CS-C-48w is approximately five times greater than CS-N-48w due to the decrease in calibrated tortuosity factor. The increase in effective diffusivity increases the Ca flux even though Ca solubility decreases. Comparatively, the tortuosity factor was not significantly changed in CS-A-48w (lesser extent of carbonation), leading to lower Ca flux.

Overall, the modeling results captured the experimental results of Ca leaching except for the flux in 1-7 days for CS-A-48w. The underestimation of Ca leaching in the early stage for CS-A-48w is most likely because the model overestimated the eluate pH in CS-A-48w and, thereby, underestimated Ca solubility. Compared to leaching in the later stage (28-105 days) with the leaching interval over the scale of weeks, leaching in the early stage (1-7 days) involves much shorter leaching intervals, which are on the scale of hours to days. Chemical equilibrium (i.e., a fundamental assumption in the reactive transport modeling described here) is less likely to be achieved during shorter leaching intervals, which leads to deviations of predictions from the measurements.

The leaching of Si from Cast Stone appears to be impeded after carbonation. Lower Si fluxes are also observed in CS-C-48w compared to CS-N-48w (Figure 4.5) despite the higher effective diffusivity of Si in CS-C-48w. This decrease is partly attributed to the change of Si-bounding phases under carbonation (CNASH_ss in CS-N; amorphous Si in CS-C). Also, the available content of Si in CS-C was found to be 67% lower than CS-N (Table 4.2) based on the calibration against pH dependent leaching of Ca. The model closely predicted the Si curve for CS-N-48w but overpredicted the Si flux in CS-A-48w and CS-C-48w at

the early stage of leaching. The prediction of Si might be inaccurate because Si leaching may be kinetically controlled.

The flux of Al also appears to be reduced after carbonation and has good correlation with the eluate pH (Figure 4.5), in that the Al solubility is proportional to pH in the alkaline range (Figure 4.2). Models well predicted the Al curves of CS-N-48w and CS-A-48w but were challenged for CS-C-48w. The pore solution pH in CS-C-48w falls into the range (pH 6-10) where the geochemical speciation model underpredicts the Al solubility. The model underestimation of Al and overestimation of Si suggest that the solubility of these two constituents might be sensitive to the Al/Si ratio. The leaching of Mg also correlates with the eluate pH. The flux of Mg is inversely proportional to the pH, and measured results were reasonably predicted by the model.

On the whole, in diffusion-controlled leaching tests, the solubilities of the constituents and transport properties of the material jointly controlled the leaching of constituents, and the goodness of fit of the model for diffusion-controlled leaching is closely related to the performance of the geochemical speciation model in the pH range of the simulated pore solution. The shorter leaching interval at the early stages of the test may have restricted the liquid-solid equilibrium in the system in a way that is not captured by the model but can be evaluated in future research.

4.4.3 Identification of phases for carbonation sensitive constituents

Alkaline earth metals (e.g., Ca, Mg, Sr, and Ba) and the alkaline metal Li were observed to have consistent transition in their pH dependent leaching behaviours at pH 6-13, as indicated in Figure 4.6. The solubilities of these constituents decrease with increasing pH and are consistently lower in the carbonated material than in the uncarbonated material. As shown previously, the solubility of Ca is dominated by calcite in CS-C. Therefore, the solubilities of Mg, Li, Sr, and Ba may also be controlled by carbonate minerals. However, it was found that the carbonates of these metals (i.e., magnesite ($MgCO_3$), lithium carbonate (Li_2CO_3), strontianite ($SrCO_3$), and witherite ($BaCO_3$)) in geochemical speciation modeling overpredict their concentrations in the eluate, suggesting the solubilities of these metals might be controlled by mineral phases other than the specified carbonates.

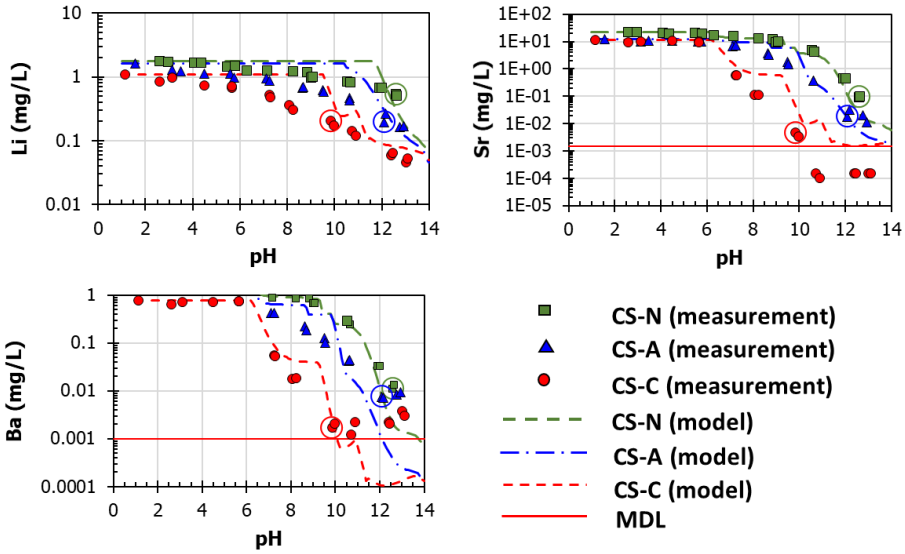

Figure 4.6 Experimental measurements and geochemical speciation modeling results of carbonation sensitive constituents (Li, Sr, and Ba) for CS-N, CS-A, and CS-C (results of Ca and Mg were shown in Figure 4.2).

Given the abundance of Ca in the leaching system, it is possible that Mg, Li, Sr, and Ba could precipitate together with calcite to form carbonated co-precipitates like dolomite ($CaMg(CO_3)_2$), which dominate their solubilities [165,166]. Compared to magnesite, dolomite, which is a (Ca, Mg)-carbonate, was found more capable in describing the leaching of Mg in CS-C, supporting the inference. In addition, dolomite and alstonite ($BaCa(CO_3)_2$) are found to be in a more stable region than magnesite and witherite based on free energies and solubility data [167]. Therefore, a set of minerals composed of (Ca, Li)-carbonate, (Ca, Sr)-carbonate, and (Ca, Ba)-carbonate was proposed to account for the solubilities of Li, Sr, and Ba. Their reaction constants were calibrated against the measured pH dependent concentrations (Table 4.1), and the modeling results are shown in Figure 4.6 with corresponding phase diagrams (in Figure D5). Leaching of Li, Sr, and Ba in CS-N, CS-A, and CS-C was reasonably predicted by the model incorporating their co-precipitates with calcium carbonate using a single set of log K values (Figure 4.6). Carbonation is assumed to promote the formation of carbonated co-precipitates to further inhibit the release of Li, Sr, and Ba.

The same set of proposed minerals was used in the diffusion-controlled leaching model, and the experimental and modeling results are presented in Figure 4.5. In the measurements that were above detection limits (detection limits of all constituents are presented in Figure D4), similarity was observed between the leaching of Ca and Sr. The leaching of Mg and Li from the three Cast Stone materials also showed a similar trend, for which the fluxes were higher in CS-C-48w (approximately 100× for Mg and 4× for Li) compared to CS-A-48w and CS-N-48w. The different response of leaching to carbonation among these constituents reflects the different binding ability of the metal to the proposed co-precipitate minerals

that were incorporated in the model. The performance of the model for the leaching behavior of Li, Sr, and Ba is closely related to the prediction of Ca. For Li, Sr, and Ca, their leaching fluxes from CS-N-48w and CS-C-48w for the measurements above detection limits (Figure D4) were relatively well captured by the model, and the leaching behaviour for CS-A-48w in the later stage was also well captured. The model was challenged in predicting the early stage leaching (1-7 days) for CS-C-48w and leaching at 1-14 days for CS-A-48w. The deviations are likely attributed to dis-equilibrium between liquid and solid phases.

4.4.4 Impact of carbonation on the leaching of redox-sensitive constituents

The solubilities of redox-sensitive constituents, including S, Fe, and Cr, are affected by the redox state in the system. From the results for the pH dependent leaching tests, carbonation was observed to impact the concentrations of Cr and Fe (Figure 4.7). Geochemical speciation of Cr for each sample is shown in Figure 4.8 with a dashed line indicating the natural pH of the material. The speciation of Cr at the natural pH of CS-A is dominated by Cr(VI), and the Cr solubility was two times greater than that in CS-N. The high solubility is mostly attributed to the oxidation of the material by reacting with O_2 in air. Conversely, the solubility of Cr in CS-C is one order of magnitude lower than that in the CS-N, where a higher portion of Cr is stabilized in the form of Cr(III). Studies found that the reduction of Cr(VI) can be kinetically controlled and the reaction rate is pH dependent [168,169]. A higher reaction rate is likely to be observed with decreasing pH in the system since the reduction reaction (Eq.4-3) consumes H^+, resulting in a rapid reduction of Cr(VI) and corresponding slow oxidation of Cr(III) during aging in CS-C, compared to CS-N and CS-A.

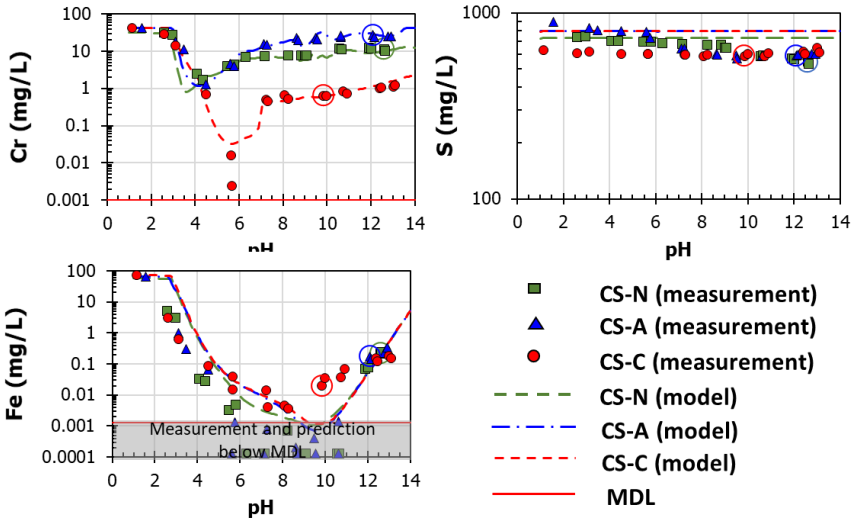

Figure 4.7 Experimental measurements and geochemical speciation modeling results of pH dependent leaching of selected redox sensitive constituents in CS-N, CS-A, and CS-C.

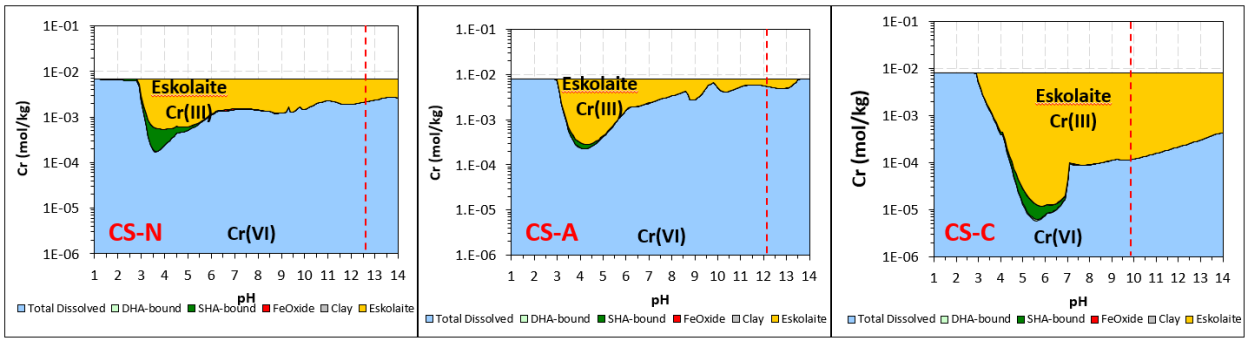

Figure 4.8 Geochemical speciation modeling results of Cr for CS-N, CS-A, and CS-C. The dashed line indicates the natural pH of the material.

In a previous study [90], multiple lines of evidence indicated that eskolaite (Cr_2O_3) was the dominant mineral retaining Cr in CS-N. The eluate pe (Table D1) at each test position was calibrated based on the measured Cr concentration. From these results, the pe at the natural pH trended as: CS-C > CS-A > CS-N (Table 4.4). With eskolaite controlling the solubility of Cr, the transformation of Cr from an oxidized and dissolved form to a reduced and stabilized form can be described as:

$$CrO_4^{2-}(aq) + 8H^+(aq) + 3e^- \rightarrow Cr^{3+}(aq) + 4H_2O \quad (4\text{-}3)$$

$$2Cr^{3+}(aq) + 3H_2O \rightarrow Cr_2O_3(s) + 6H^+(aq) \quad (4\text{-}4)$$

The decrease in pH contributes H^+ and consumes electrons (Eq.4-3). Therefore, the decrease in solution pH is accompanied by increase in solution pe. It also needs to be noted that, in pH dependent leaching, nitric acid was used for pH adjustment. The use of nitric acid may lead to the partial oxidation of the material. As for the pH dependent leaching of Fe, the concentration of Fe was unimpacted at the higher and lower end of the pH range but was found highest in CS-C in the pH range of 4-12 (where values for CS-N and CS-A were under the detection limit). Carbonation has a negligible impact on the pH dependent leaching of S.

Table 4.4 Natural pH and calibrated natural pe for Cast Stone materials.

	natural pH (experiments)	natural pe (calibrated)	2pH+3pe
CS-N	12.6	2.1	42
CS-A	12.1	3.2	42.7
CS-C	9.9	6.3	42.3

To better understand the dependence on the solubilities of redox sensitive constituents on pH and pe, the measured pH and calibrated pe values of all test positions were projected on the predominance diagrams of

Cr, Fe, and S (Figure 4.9) [90]. As indicated in the diagrams, regardless of the carbonation condition of the material, pe is inversely proportional to pH. With the defined mineral sets and chemical equilibrium assumed, under the test conditions, Fe was present predominantly as ferrihydrite (Fe_2O_3•$0.5H_2O$) and S was present in the system predominantly as S^{2-} in solid and as SO_4^{2-} in solution when insoluble S^{2-} were oxidized. The pH and pe for the test conditions lie on the boundary between eskolaite and CrO_4^{2-}, so the solubility of Cr is relatively sensitive to the testing conditions.

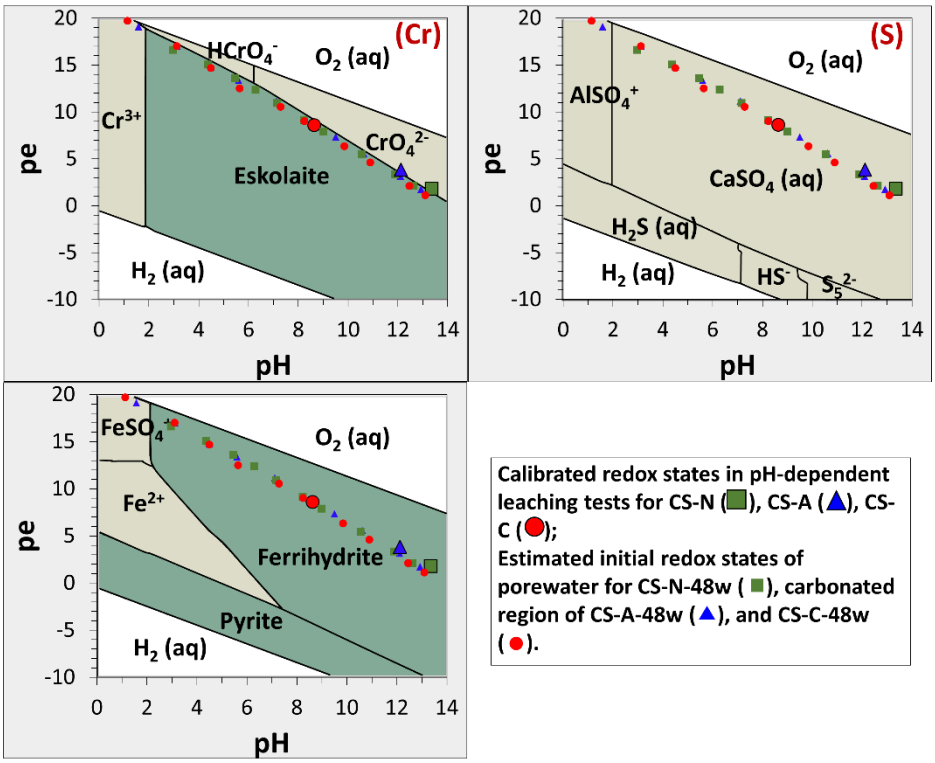

Figure 4.9 Predominance diagrams of Cr, Fe, and S [90] with pH and pe in testing conditions projected.

The geochemical speciation model reasonably predicted the leaching of S and Fe concentrations as a function of pH for all three materials using the pe calibrated from Cr concentrations (Figure 4.7). The predictions of Fe in CS-C were significantly below measured values at pH 8-12. Two reasons may explain the deviation. First, Fe might form complexes and present in the solution, which was not calculated by the model. Second, Cr-bearing phases other than eskolaite might be formed under carbonation that control the solubility of Cr, leading to biased pe values based on the calibration against Cr assuming an eskolaite phase.

In diffusion-controlled leaching, carbonation manifested a strong impact on Cr leaching (Figure 4.10). The Cr flux in the early stage of leaching in CS-C-48w is two orders of magnitude lower than that in CS-N-48w,

and the difference decreases gradually as leaching time increases. The lower flux of Cr is mostly likely the result of the lower Cr solubility in CS-C as earlier found from pH dependent leaching (Figure 4.7). Leaching from CS-A-48w was additionally impacted by oxidation and, therefore, the flux in the early stage was higher than that for CS-N-48w. From the predominance diagram of Cr (Figure 4.9), under the assumed mineral set, eskolaite is the predominant phase for Cr in equilibrium with the pore solution of CS-C-48w, while CrO_4^{2-} dominates in CS-N-48w and CS-A-48w. Leaching of S was increased in the carbonated material. This increase might be a result of increased diffusivity in the carbonated material, because the solubility of S is barely affected by carbonation or pH as indicated from pH dependent leaching. As for Fe, carbonation reduced the Fe leaching as a result of solubility reduction with reduced pH.

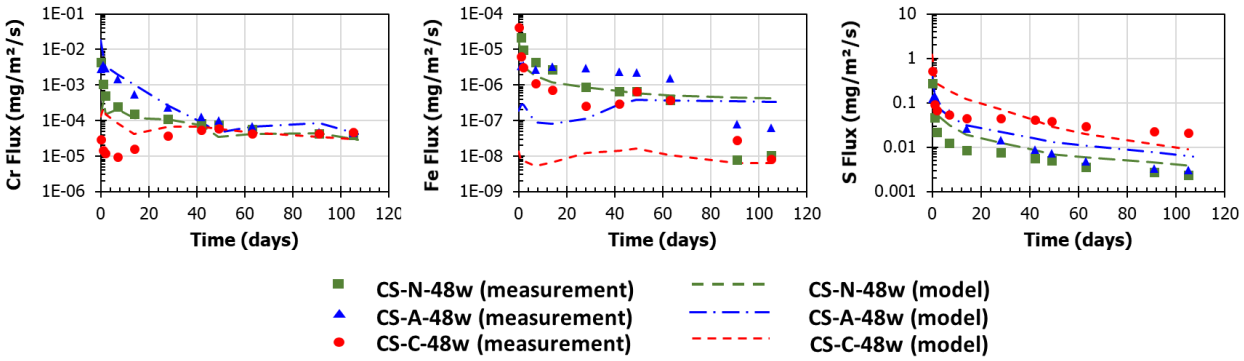

Figure 4.10 Experimental measurements and reactive transport modeling results of diffusion-controlled leaching of selected redox sensitive constituents in CS-N-48w, CS-A-48w, and CS-C-48w.

In reactive transport modelling, the initial pe of the pore solution in each cell was calibrated based on the model prediction of Cr leaching. The model reasonably predicted the leaching of Cr and S for CS-N-48w and CS-A-48w. However, the prediction of Cr flux from CS-C-48w was lower than experimental results in the early stage, despite the close prediction of Cr solubility from CS-C, which might be the result of disequilibrium in the system, given the high effective diffusivity at the early leaching stage in CS-C-48w. As for Fe, model results underpredicted the flux in CS-C-48w and CS-A-48w, which is mostly attributed to the underestimation of Fe solubility at the natural pH of the material.

4.5 Conclusions

This chapter focused on investigating the effect of carbonation on the leaching of major and trace constituents from Cast Stone materials. Geochemical speciation coupled with reactive transport modeling was used to better understand the potential impacts of carbonation on leaching behavior.

Results from geochemical modeling indicate that Cast Stone lacks portlandite as a hydration phase due to the low Ca/Si ratio in binder. Instead, CNASH phases are predicted to be stable in the material at alkaline pH conditions, which governs the dissolution of Ca, Si, and Al. Carbonation impacts the pH dependent leaching of Ca, Si, Al, and Mg due to the formation of calcite, wairakite, dolomite, and amorphous silica and the depletion of CNASH solid solution and brucite under carbonation. The pH dependent leaching behavior of carbonation-sensitive constituents including Li, Sr, and Mg was accurately described in the geochemical speciation model by using carbonated co-precipitates with calcite. Carbonation was also found to reduce the pH dependent leaching of Cr due to the decrease in pH. Less impact from carbonation was observed for pH dependent leaching of Na and S, indicating the lack of binding phases in the system.

Diffusion-controlled leaching tests demonstrated the coupled effect of solubility and diffusivity of the constituents. A carbonate peak is found near the drying front in CS-C-48w, which is likely due to the accumulation of dissolved sodium bicarbonate. Effective diffusivity was found higher in samples carbonated under 2% CO_2 compared to uncarbonated samples, but effective diffusivity was not significantly increased in samples carbonated in air. As a result, carbonation under 2% CO_2 increased the leaching of Na, Mg, Li, and S and decreased the leaching of Si, Al, and Cr. The sample carbonated in air has decreased leaching of Ca, Al, and Sr and increased leaching of Cr compared to the uncarbonated material. Therefore, the retention ability of Cast Stone for Cr is highly sensitive to the pH and pe in the system, which are dependent on the carbonation environment. Reactive transport model prediction of the early stage (1-7 days) leaching showed poor agreement with measurements for some constituents, possibly due to the dis-equilibrium between liquid and solid in the short leaching intervals. However, the diffusion-controlled leaching of major constituents over the range of entire leaching time was generally well captured by the model for all three materials.

5. COUPLED EFFECTS OF DRYING AND CARBONATION ON LEACHING OF A CEMENTITIOUS LOW ACTIVITY WASTE FORM

Abstract

Arid or semi-arid environmental conditions are commonly expected in the disposal sites for nuclear waste. Under dry conditions, carbonation reactions in monolithic waste forms can progress at different ingress rates and reaction extents compared to saturated conditions, impacting the leaching behavior of constituents. This study investigated using a combination of experiments and simulation the coupled effects of drying and carbonation on leaching behavior of Cast Stone, a proposed cementitious waste form for low activity radioactive waste. Diffusion-controlled mass transport leaching tests were carried out to determine the leaching rate of constituents from samples carbonated under 15%, 40%, 68%, and 100% relative humidity (RH) conditions for various aging times. Reactive transport modeling calibrated to simulate leaching test results was used to estimate the extent and depth of carbonation in the monoliths. The carbonation depth estimated from the leaching simulation generally agreed with the predictions from a carbonation ingress model and the experimentally measured carbonation depth, whereby, differences between estimates indicated the range of uncertainty associated with model and measurement. Results from diffusion-controlled leaching tests showed that a dry environment increases the leaching rate of highly soluble constituents as a result of increased effective diffusivity further into the material caused by carbonation. The relative positions of the carbonation and leaching fronts determined the subsequent leaching rates of Ca and Cr with pore water solubilities of both constituents highly dependent on pore water pH.

5.1 Introduction

As part of the disposal permitting process, the potential releases of constituents of potential concern (COPCs) from the waste form to the environment during disposal need to be carefully estimated for a long-term period (i.e., 1000 years) due to the extended decay process of several radionuclides, some of which may be highly mobile in the environment [8,95]. During the service life of the disposal facility, potential interactions between the waste form and the environment include the exchange of water through drying, wetting through infiltration and water vapor condensation, and reactions with reactive gases, including carbon dioxide and oxygen leading to material carbonation and oxidation. The rate and extent of these interactions are dependent on the waste form material properties such as reaction capacity and porosity, as well as on the environmental conditions such as reactive gas content and relative humidity in the disposal

site. Waste disposal facilities often are located in arid or semi-arid environments to help minimize interactions with the environment through infiltrating water. For example, at the Hanford Site, which is a potential disposal site for Cast Stone waste form, the annual infiltration rate is estimated to be 0.9 mm/y and the lowest monthly average relative humidity (RH) recorded has been 21.9% [24,170]. Surface disposal of the initially water-saturated waste form under such conditions before an engineered cover is installed can result in extensive surface evaporation and interior drying. Bulk drying can increase the effective diffusion of reactive gases, which can alter the extent of reactions and penetration depth of aging effects [48,60,129]. As a related example, saltstone is a waste form currently being used for radioactive salt waste disposal at the Savannah River Site Saltstone Disposal Facility (SDF); saltstone has a similar formulation to Cast Stone [171]. The saltstone waste form is disposed using a concrete vault as a barrier, creating a high moisture content or water-saturated condition in the waste form. The variation in the environmental RH at the SDF has been considered as a factor when predicting the release of COPCs from the waste form, but bounding assumptions have been used in the absence of more refined methods to estimate the impacts under drying and carbonation processes [37,171].

Previous studies on Portland cement-based materials have identified impacts of intermittent wetting under leaching and drying in a carbonating atmosphere with various RH; these impacts introduce changes in constituent leaching, mainly due to the different extent of carbonation in the material [10,11]. Compared to uncarbonated materials, carbonation under intermediate RH (e.g., around 65% RH) showed the largest decrease in the leaching flux of hydroxide and an increase in the degree of drying, resulting in decreased leaching fluxes of sodium and potassium. However, no similar leaching study has been carried out on materials similar to Cast Stone, which contain a high soluble salt content in pore solution and a low calcium content in the cement matrix. As previously reported in Chapter 3, carbonation in Cast Stone behaves very differently under drying conditions compared to Portland cement materials. The carbonation ingress rate increases in Cast Stone as RH decreases, whereas the maximum ingress rate in a Portland cement material is at intermediate RH [21,25]. Carbonation in Portland cement refines the pore structure resulting in decreased mass transport rates [26,129], while in Cast Stone, increased porosity and cracking was observed in the carbonated material, leading to faster diffusion of CO_2 and accelerated diffusion of constituents (section 3.3.2). However, the carbonation reaction in Cast Stone is constrained under very dry conditions due to the limited interfacial area between liquid and vapor for the mass transfer of CO_2. Thus, competing processes can have mixed effects on the leaching of constituents from Cast Stone, adding to the uncertainty in predicting the long-term performance of the material in the field.

The objective of this study was to assess the coupled impact of drying and carbonation on diffusion-controlled leaching rates of major and trace constituents. The impacts of aging time and environmental RH

on the leaching of major constituents (Ca, Al, Si, Mg), highly soluble constituents (Na, K, S), and a redox sensitive COPC (Cr) from the carbonated Cast Stone were studied using a combination of diffusion-controlled leaching experiments and geochemical speciation coupled with reactive transport modeling. Monolithic Cast Stone materials were aged under different RH and 2% CO_2 for several time intervals. Samples then were subjected to diffusion-controlled mass transport leaching tests to evaluate the release of constituents after carbonation. Reactive transport modeling was used to simulate the leaching of constituents from Cast Stone, using parameters derived for Cast Stone in an earlier study [90] or derived from calibrating to the leaching test results. The carbonation front depth estimated from the reactive transport model was compared with predictions from the carbonation model and the previously measured depth, allowing the estimation of uncertainty for future modelling and long-term projections. The diffusion-controlled leaching results in this study in conjunction with the pH dependent leaching results of carbonated Cast Stone presented in Chapter 4 provide insights for understanding controlling mechanisms (e.g., solubility, effective diffusivity) for the leaching of constituents in Cast Stone with progressive carbonation under the impact of environmental RH. This study provides additional lines of evidence towards predicting the leaching behavior of Cast Stone under anticipated field disposal conditions.

5.2 Material and methods

5.2.1 Aging experiment

Cast Stone samples were prepared following the formulation and method introduced in section 3.2.1. Waste simulant was prepared using a recipe based on anticipated Hanford Site low activity waste (LAW) composition [74]. Chromium was added in the form of Na_2CrO_4 to achieve a 0.2 wt% loading. Chromium serves as a redox indicator in the system and also is a major RCRA metal component of LAW. Monolithic Cast Stone samples were transferred into an aging environment after hydration under N_2 for 90 days and pre-conditioning at a specified aging RH for 60 days. As discussed in section 4.2.1, initially doped Cr(VI) is assumed to be fully reduced during the hydration period through reacting with the waste form ingredients (especially blast furnace slag). Samples were aged under 2% CO_2 for 16, 28 and 48 weeks at 15% RH (CS-C15-16w, CS-C15-28w, CS-C15-48w), 40% RH (CS-C40-16w, CS-C40-28w, CS-C40-48w), 68% RH (CS-C68-16w, CS-C68-28w, CS-C68-48w), and 100% RH (CS-C100-16w, CS-C100-28w, CS-C100-48w). The detailed aging method is described in section 3.2.2.

5.2.2 Diffusion-controlled leaching test

A 1-D diffusion-controlled mass transport leaching test was carried out on the aged monolithic Cast Stone samples following EPA Method 1315 [133]. The surface of the sample exposed to aging conditions was in direct contact with de-oxygenated Milli-Q water with minimal headspace to bring the liquid-surface area ratio to 10 mL/cm^2 and to allow 1-D diffusion. The eluate was exchanged at 0.1, 1, 2, 7, 14, 28, 42, 49, 63, 91, and 105 days. Each eluate was measured for pH, electrical conductivity (EC), and oxidation-reduction potential (ORP). Concentrations of constituents in the eluate were analyzed with ICP-OES and ICP-MS, using the methods described in section 4.2.4.

5.3. Reactive transport modeling approach

Reactive transport modeling was performed using the LeachXS™/ORCHESTRA (LXO) framework [99,139] to simulate mass transfer release of constituents as obtained from the diffusion-controlled leaching test (EPA Method 1315). The conceptual model of the diffusion-controlled leaching was described in section 4.3.2. Local equilibrium conditions were calculated for each time step within each cell of the finite volume model constructed in LXO for the test conditions. The time step and discretization were defined to meet both local equilibrium and stable finite volume solution. Transport of constituents through diffusion between adjacent cells was calculated at the end of each time step.

The mineral assemblage as defined in Table 4.1 was used across the samples [90]. The reaction constants used in the equilibrium calculations were obtained from thermodynamic databases including MINTEQ.V4, CEMDATA18, Thermoddem2011, and LLNL.dat [87,88,156,157]. Activity coefficients were calculated using the modified Davies activity model [158]. The determination of the available content profile is described in section 4.3.2. The available contents of constituents for reaction and leaching, except for carbonate and silica, were assumed to be uniform across the solid matrix, whereby, the values obtained from uncarbonated Cast Stone (Table 4.2) were used. Although migration of sodium toward the exposed surface was observed by SEM-EDS for CS-C68-48w (section 3.3.4), it was assumed that the initial wetting process during the leaching test introduced capillary water ingress that relaxed the accumulation of sodium at the surface. Carbonate content as a function of depth was calibrated to best fit the measured eluate pH as a function of time. The available content of Si in the cells with elevated carbonate contents was calculated based on the available content ratio of Ca/Si in the carbonated Cast Stone (Table 4.2). The initial redox state (pe) in each cell was calibrated based on the measured Cr concentrations in eluates [90].

Effective diffusivities ($D_{e,L}$) of ions are controlled by the physical properties including porosity (ε), liquid phase tortuosity factor (τ_L), and saturation (S) of Cast Stone as governed by Eq. 5-1, where $D_{0,L}$ is the free diffusivity of ions in water.

$$D_{e,L} = \frac{S^{7/3} \times \varepsilon \times D_{0,L}}{{\tau_L}^2} \quad (5\text{-}1)$$

An average free liquid diffusivity of 2×10^{-9} m^2/s was used for all species [172]. A porosity of 0.41 as previously measured (section 2.2.1) and saturation of 1 were uniformly assigned to all cells. A saturation of 1 is a reasonable assumption for the leaching test condition used in this study because it has been previously identified that the wetting process in the unsaturated Cast Stone during the initial leaching cycle has negligible impact on the leaching of constituents [173]. Tortuosity factor in each cell was determined by minimizing the log squared residuals (*logRSS*, Eq. 5-2) of the simulated sodium release concentrations ($\hat{y}$) compared to measurements (y):

$$logRSS = \sum (\log\left(\frac{\hat{y}}{y}\right))^2 \quad (5\text{-}2)$$

The free diffusivity $D_{0,L}$ of sodium [174] was used when calibrating tortuosity factor from the measured sodium concentration in the eluates. The adsorption of ions on the surface of organic matter was modeled with the NICA-Donnan model [160] using parameters published by Milne, et al. [161,162]. Ion adsorption onto hydrous ferric oxide (HFO) was modeled using the generalized two layer model of Dzombak and Morel [163].

5.4. Results and discussion

5.4.1 Carbonation depth

5.4.1.1 Determination of carbonation depth from leaching simulation

Carbonation depth in aged monolithic samples can be estimated from the pore solution pH profile in the monolith at initial leaching (leaching time=0) calculated using a geochemical speciation reactive transport model. As one of the key chemical inputs, carbonate content in carbonated cell was calibrated against the eluate pH from the measurements. Figure 5.1.a(i) and Figure 5.1.b(i) compared the eluate pH from samples aged for different times and samples aged in different RH conditions, respectively. For samples carbonated for different aging times at 68% RH, the eluate pH was similar during 1-14 days of leaching time. As

leaching time increased, the eluate pH from CS-C68-28w and CS-C68-48w decreased, while the eluate pH from CS-C68-16w steadily increased. The resultant available content profile of carbonate (Figure 5.1.a(ii)) showed a higher content in the carbonated region, and the depth of the carbonated region increased with longer aging time, both as expected. The carbonate content at 0-18 mm was the same at 2.6 mol/kg for samples carbonated for different times, suggesting the same extent of carbonation reaction in the carbonated region of the sample regardless of aging time. The carbonate content of 2.6 mol/kg was close to the TIC measurement for carbonated Cast Stone (2.4 mol/kg; Figure 3.1). It was found that carbonate content increased to a greater value in the cells near the carbonation front within the material than in the cells closer to the exposed surface for CS-C68-28w and CS-C68-48w, indicating an accumulation of carbonate near the carbonation front. As previously discussed in section 4.2, the carbonate peak is possibly due to the condensation of sodium bicarbonate near the drying front, which migrates as the carbonation front ingresses. This explanation is supported by the peak of Na content measured at the drying front of CS-C68-48w sample from SEM-EDS (Figure 3.11), and is further supported by the geochemical speciation modeling results of pore solution speciation profile in CS-C68-48w (Figure 4.4).

Pore solution pH is inversely correlated to the carbonate profile (Figure 5.1.a(iii)). The pore solution pH near the surface is around 8.3, and a dip in pH is observed near the carbonation boundary for CS-C68-28w and CS-C68-48w as result of elevated carbonate content. The carbonation front was selected as the depth at which pore solution pH increases to above 9 [175]; results are summarized in Figure 5.2.

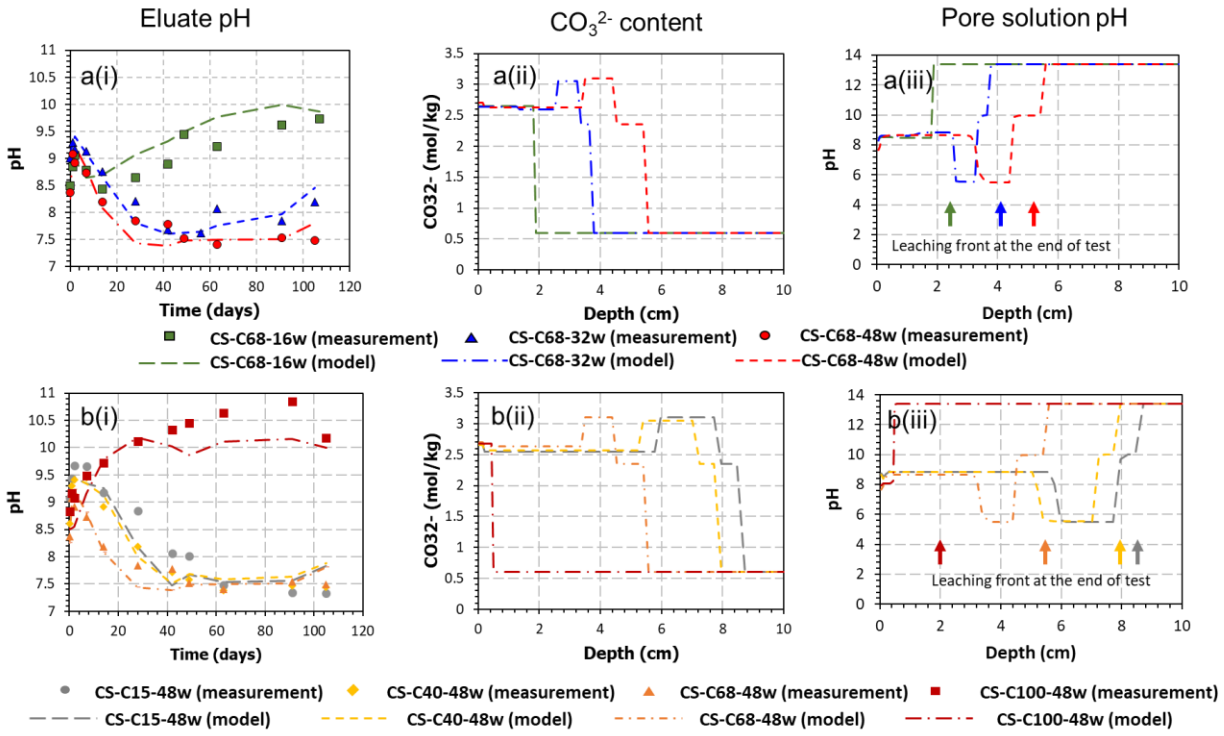

Figure 5.1 Determination of carbonation front from leaching simulation. (i) Experimental measurement and reactive transport modeling results of eluate pH; (ii) carbonate available content profile from calibration; and (iii) initial pore solution pH profile from diffusion-controlled leaching simulation; a. comparison among samples carbonated for different times in 68% RH; b. comparison among samples aged in different RH conditions for 48 weeks.

Among samples carbonated under four RH conditions (Figure 5.1b), CS-C100-48w (saturated aging) shows a completely different pattern when compared to other samples that were aged in unsaturated conditions. Eluate pH from CS-C100-48w increases as a function of leaching time and was much higher when compared to the eluate pH measured in other samples, suggesting limited impact from carbonation. For the unsaturated samples, the eluate pH generally decreased as leaching time increased, and the fastest initial pH drop was found in CS-C68-48w. The pH profile can be explained by the calibration results of the carbonate content profile (Figure 5.1b(ii)). CS-C68-48w contained a slightly greater amount of carbonate at the depth of 0-3.4 cm compared to CS-C15-48w and CS-C40-48w, resulting in the lower eluate pH in the initial leaching (2-28 days). From the pore solution pH profile (Figure 5.1b(iii)), the carbonation front penetrated deeper as RH decreases, which is consistent with the trend observed from the phenolphthalein test (3.3.2). During sample aging, drier conditions facilitated the diffusion of gaseous CO_2, resulting in the faster penetration of carbonation front. A dip in pH was observed near the carbonation boundary in all samples except for CS-C100-48w. Under saturated conditions, the lack of a drying front restricted the condensation of sodium bicarbonate and prevented the accumulation of sodium bicarbonate. Overall, the

eluate pH as a function of leaching time provides an indication of the pore solution pH profile and carbonation history in the tested sample.

5.4.1.2 Carbonation depth as a function of time

The carbonation depth derived from leaching simulation is compared to the predictions from the carbonation model and the experimental measurements by phenolphthalein test in Figure 5.2. The carbonation model is a reactive transport model incorporating the transport of moisture and CO_2 (Appendix E-I). The carbonation depth from both the leaching simulation and carbonation model generally followed the measured trend as functions of time and RH. However, the difference among the three sources of results appears to increase as aging time increases and RH decreases. The depths from both simulations are greater than the depth measurements from phenolphthalein test. Although phenolphthalein indicator is a commonly used for monitoring carbonation depth, many studies also have reported the underestimation of carbonation front by the test method [136,137]. Calcite has been found formed beyond the phenolphthalein color change border [136]. Moreover, the depletion of moisture may decrease the reaction gradient in the sample thus increasing the uncertainty in the measurement. The differences in carbonation depth from the three methods indicated the range of uncertainty in model prediction and experimental measurements as a function of aging time, which can be used for estimating the uncertainty in long-term projections.

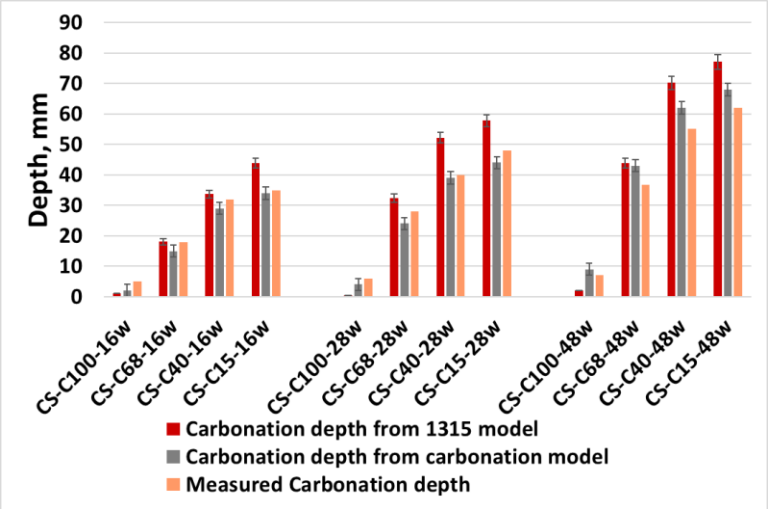

Figure 5.2 Comparison between carbonation front from diffusion-controlled leaching simulation and measurement.

The carbonation depth from measurement and simulation were plotted against square root of time ($\sqrt{t}$) in Figure 5.3. If gas phase Fickian diffusion is assumed as the rate limiting reaction step, the carbonation depth should be proportional to square root of time [17]. It was found that both linear and 2nd order polynomial

functions are capable of fitting for the measurement with R^2 close to 1 (for linear fitting see Figure 3.4b), but the 2nd order polynomial is better in fitting the carbonation ingress depth at 68% RH for both measurements and leaching simulation (Figure 5.3). The 2nd order polynomial function implies a slightly increased effective diffusivity during carbonation. It was found previously that among the four RH cases, the greatest increase in effective diffusivity after carbonation was at 68% RH, due to the high reaction extent at intermediate RH (section 3.3.2).

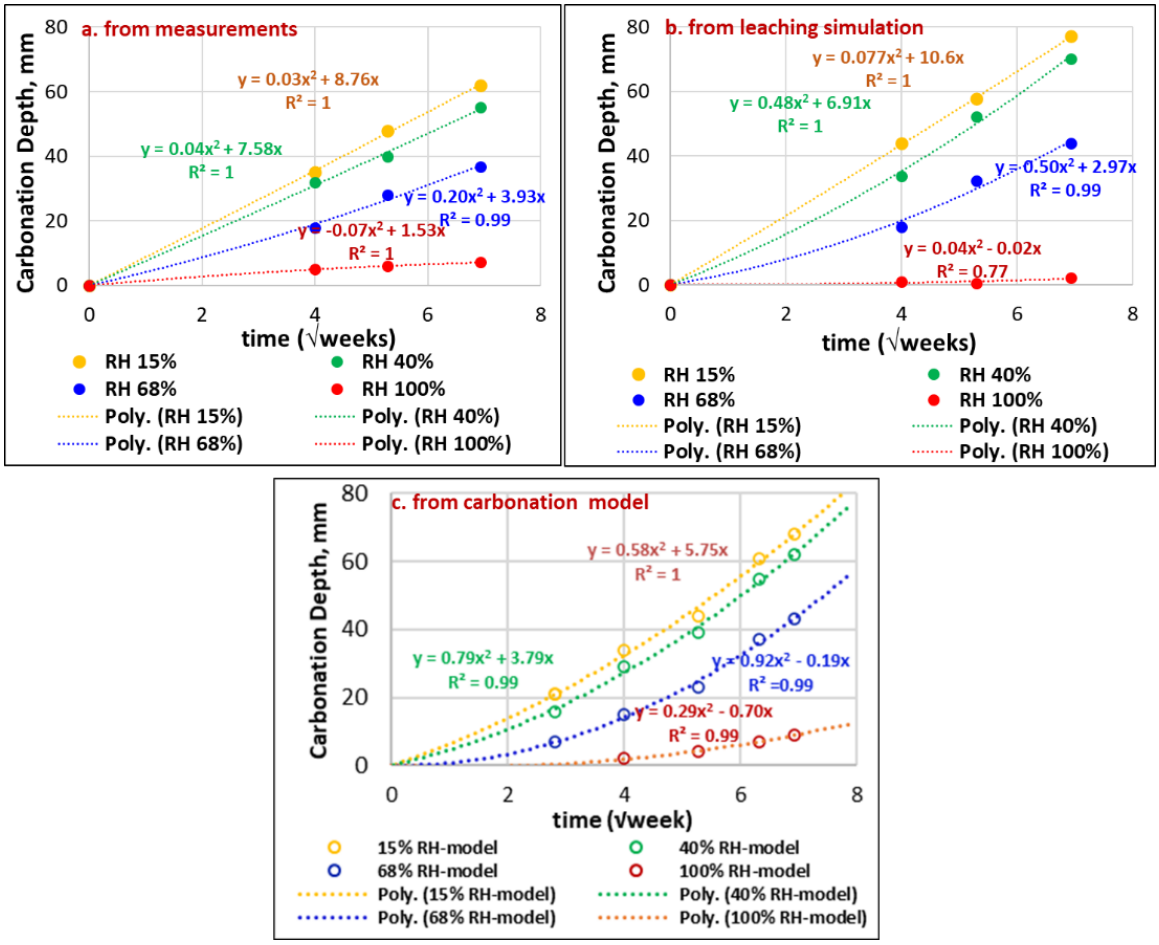

Figure 5.3 Carbonation depth as a function of square root of time.

5.4.2 Impact of coupled drying and carbonation on effective diffusivity

As discussed in Section 4.4.1, Na and S in Cast Stone are highly soluble and their solubilities are not highly dependent on the variation in pore water pH or on the carbonation of the material. Similarly, K also is a highly soluble constituent with similar chemical behavior to Na. The diffusion-controlled leaching of highly soluble constituents is assumed controlled by diffusion (and not constrained by pore water solubility), which

is governed by the pore structure of Cast Stone. Therefore, the tortuosity factor profile in each material was adjusted (Figure 5.4) to account for the change in the pore structure of the material and to reflect the measured Na flux (Figure 5.5). Tortuosity factors derived from Na flux also were used to predict K flux (Figure 5.5), and showed good agreement with measurements. The results showed a decrease in tortuosity factor from a value of 30 deep in the material to a value of 2 near the exposure surface. Decreasing tortuosity factor by a factor of 15 increases the effective diffusivity by a factor of 225 (Eq. 5-1). For all the materials carbonated in RH≥68%, a stepwise decrease of tortuosity factor was derived. The decrease of tortuosity factor in carbonated material reflects the change in pore structure, which can be induced by both carbonation and drying. As discussed in section 3.3.2, carbonation leads to more rapid moisture transport in the material as a result of porosity increase and formation of cracks partly due to the reduced molar volumes of phases in carbonated material. Meanwhile, drying causes a shift of micropores to mesopores due to the C-S-H agglomeration (or drying shrinkage) [106]. The depth of the low-tortuosity region increases with increasing aging time (Figure 5.4a) and decreasing environmental RH (Figure 5.4b). Notably, the difference in the region with low tortuosity factor between CS-C15-48w and CS-C40-48w was limited, which resulted from a receding progression of the carbonation front under dry environmental conditions. For CS-C100-48w, a smaller decrease in tortuosity factor (by a factor of 3) was observed in the shallower region of the material compared with samples carbonated under other RH conditions, suggesting carbonation under saturated conditions has a minor impact on the effective diffusivities of constituents.

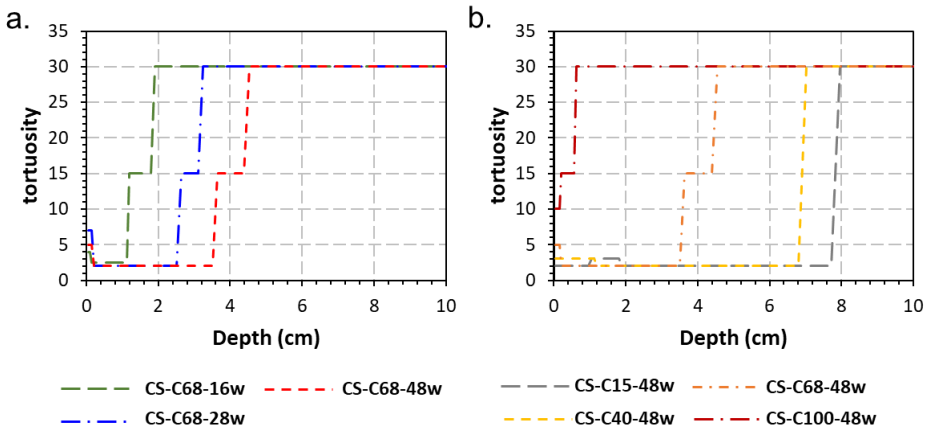

Figure 5.4 Tortuosity factor profile calibrated based on Na leaching in samples carbonated (a) for different aging times under 68% RH; (b) under different RH for 48 weeks.

Figure 5.5 shows the experimental results from Method 1315 and reactive transport modeling prediction of ionic strength in the eluate and fluxes of highly soluble constituents as a function of leaching time. The

calibrated tortuosity profile based on measured Na concentration reasonably predicted the fluxes of other highly soluble species including K and S, indicating a good representation of the transport property of the material by the calibration. The ionic strength results of CS-C68-48w and CS-C100-48w were well predicted by the model; however, the ionic strength results of CS-C15-48w and CS-C40-48w were overpredicted by 0.1 mol/L, despite the close prediction of Na, K, and S. The prediction of ionic strength is affected by the predictions of all constituents in the system. Besides, the ionic strength in pore solution was simulated in the range of 4-5 mol/L by the model (Figure E1), which is much higher than the applicable range for modified Davies model (<1.2 mol/L [158]). As a result, the model calculation on the activity of constituents may not be accurate, which may have led to biased calibration results of tortuosity factor. In the future, the SIT activity model will be incorporated to improve the accuracy of activity coefficients to account for effects from ionic interactions.

The fluxes of Na, K, and S decreased monotonically with increasing leaching time, except for Na flux from CS-C68-48w during 7-14 days. Comparing the three samples with different aging times (Figure 5.5a), the longer aging time under 68% RH decreased the fluxes of Na, K, and S during the early stage (1-14 days) of leaching and increased fluxes between 28-105 days. The difference between CS-C68-48w and CS-C68-28w was smaller than the difference between CS-C68-28w and CS-C68-16w, suggesting the impact of carbonation on the effective diffusivity was limited over longer aging times.

Results from samples aged under different RH for 48 weeks are compared in Figure 5.5b. The fluxes of the Na, K, and S from CS-C15-48w and CS-C40-48w were nearly identical and were greater than the fluxes from samples aged in higher RH conditions during 28-105 days of leaching. This result differs from that observed for Portland cement [11], in which leaching of Na and K decreased when the material was carbonated under a drier environment. This departure from Portland cement behavior is likely due to the high salt content in the pore solution, as well as the increased effective diffusivity under carbonation in Cast Stone. The fluxes of Na, S, and K from CS-C100-48w was one order of magnitude less on average than those from CS-C15-48w and CS-C40-48w. For CS-C68-48w, the fluxes of Na and K were slightly less than those for CS-C15-48w and CS-C40-48w, and the differences became greater with increasing leaching time; the fluxes of S were similar from the three samples.

The ionic strength in the eluate generally increases with decreasing RH. This observation on the relationship between carbonation extent and the ionic strength is very different from results reported on a previous study on cement paste material [39]. In that study, carbonation was found to yield decreased ionic strength in the leaching eluate, likely due to refinement of the pore structure from carbonation. As for Cast Stone, carbonation increases the porosity and introduces cracking in the material, leading to a more rapid diffusion in the system.

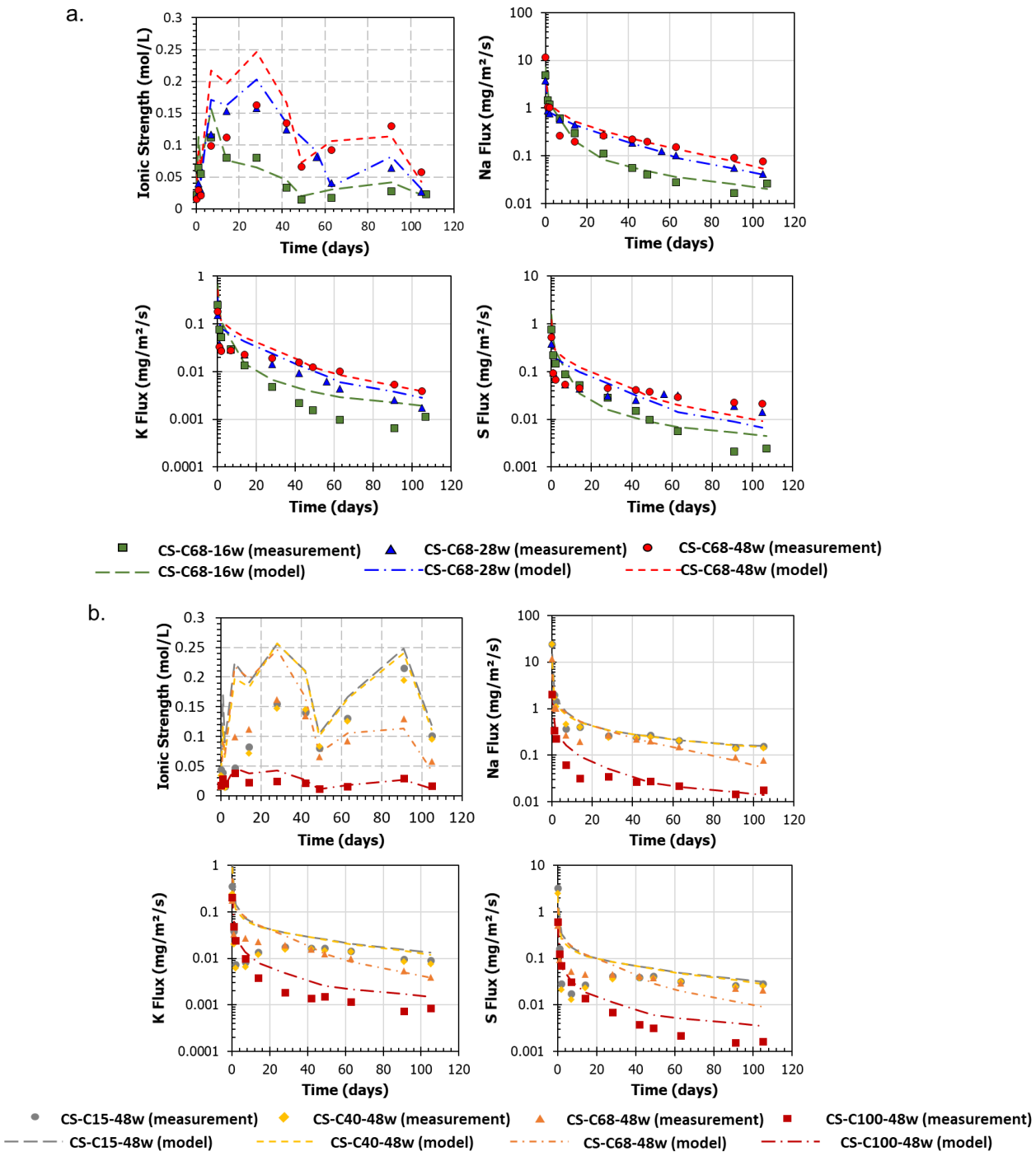

Figure 5.5 Experimental measurements and reactive transport modeling results of diffusion-controlled leaching of Na, K, and S from samples carbonated (a) for 16, 28, and 48 weeks under 68% RH; (b) under 15%, 40%, 68%, and 100% RH for 48 weeks.

5.4.3 Effect of drying and carbonation on leaching depth

The change in effective diffusivity as a result of carbonation impacted the penetration of the leaching front differently among samples with different extent of carbonation. During leaching, the leaching front for a constituent ingresses into the material at a rate governed by the effective diffusivity. The leaching front can be identified from the concentration profile of constituents in pore solution. In this study, the Na concentration profile was selected for determining the leaching front due to its relatively high solubility. The leaching front at a given leaching time is defined in this study as the deepest cell with Na concentration lower than 99% of initial concentration in the pore water (illustration in Figure E2 [173]).

The leaching front depth as a function of time was compared among samples aged under different RH conditions in Figure 5.6. The leaching front penetrated quickly into the sample during the initial stage of leaching (0-14 days), followed by a declining rate of ingress as leaching time increased. Slow migration of the leaching front is observed for all samples after 47 days of leaching. The fast ingress during the initial leaching resulted from increased effective diffusivity (Figure 5.4, Figure 5.5) in the near surface region of the sample where materials are carbonated. As soon as the leaching front passed through the carbonation front (depth indicated by the dashed lines) and reached the uncarbonated region, the effective diffusivity decreased sharply (Figure 5.4, Figure 5.5), causing the relatively slow migration of the leaching front thereafter (Figure 5.6). The depth involved in the leaching process is greater than the carbonation depth by 1-2 cm for all samples. The carbonation front was found greater in lower RH conditions. This observation explains the identical leaching fluxes of Na, K, and S observed for CS-C15-48w and CS-C40-48w. Relatively similar carbonation fronts ingress depths were measured in the two samples (62 mm in CS-C15-48w and 55 mm in CS-C40-48w; Figure 3.4), leading to similar effective diffusivity profiles (Figure 5.4 and Figure 5.5). The diffusion-controlled leaching of highly soluble constituents can be assumed as diffusion-controlled, which is governed by effective diffusivity. Therefore, similar effective diffusivity profiles in the samples yields the relatively close leaching rates for highly soluble constituents.

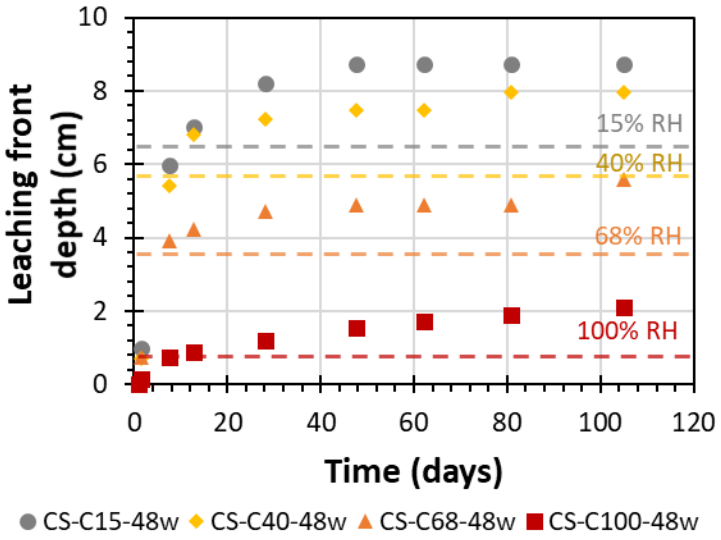

Figure 5.6 Leaching depth in sample carbonated under different RH based on pore solution Na concentration. Dashed lines indicating the measured depth of the carbonation front in samples carbonated for 48 weeks.

5.4.4 Diffusion-controlled leaching of major constituents

Figure 5.7 shows the experimental results from Method 1315 and reactive transport modeling prediction of fluxes of major constituents as a function of leaching time. For the three samples carbonated under 68% RH, increased aging time from 16 to 28 weeks significantly increased the fluxes of Ca, Mg, and Al by approximately one order of magnitude from 28-105 days of leaching but further increased aging time to 48 weeks did not further increase the fluxes as significantly. Although Ca solubility decreases under carbonation due to the formation of calcite (Figure 4.2), the low pH in the pore solution (5.5-8.3) in the carbonated region favors the dissolution of Ca and increased Ca fluxes [39]. The Ca fluxes in samples aged for longer periods of time were additionally facilitated by the decreased tortuosity factor. No apparent pattern was observed for the fluxes of Si. The reactive transport model captured the Ca fluxes relatively well for the later stage of leaching (28-105 days). Because the model also well predicted pH, this suggested an accurate estimation of carbonate content in the eluate. The model prediction for Si and Al are challenged for all three samples. The eluate pH in CS-C68-16w falls between 8.5-9.5, while the eluate pH in CS-C68-32w and CS-C68-48w is from 7.5-8. As shown previously in the results of pH dependent leaching modeling (Figure 4.2), the model prediction of pH dependent leaching of Al is less than the measurements by two orders of magnitude at pH 7.5-8 and by one order of magnitude at pH 8.5-9.5, leading to the underestimation of Al leaching. Possible factors leading to the deviation include the inaccurate calculation of Al activity by using modified Davies activity model, a missing reaction in the geochemical speciation model (e.g.,

solution complexation) and/or the formation of Al colloids in the mid-pH range. The model prediction of Si flux generally captures the leaching behavior of the three samples, but the prediction is one order of magnitude greater than the measurement. The concentrations of Si are systematically predicted higher by the model because silica reactions are unlikely near equilibrium in the experimental system, due to the slow dissolution kinetics.

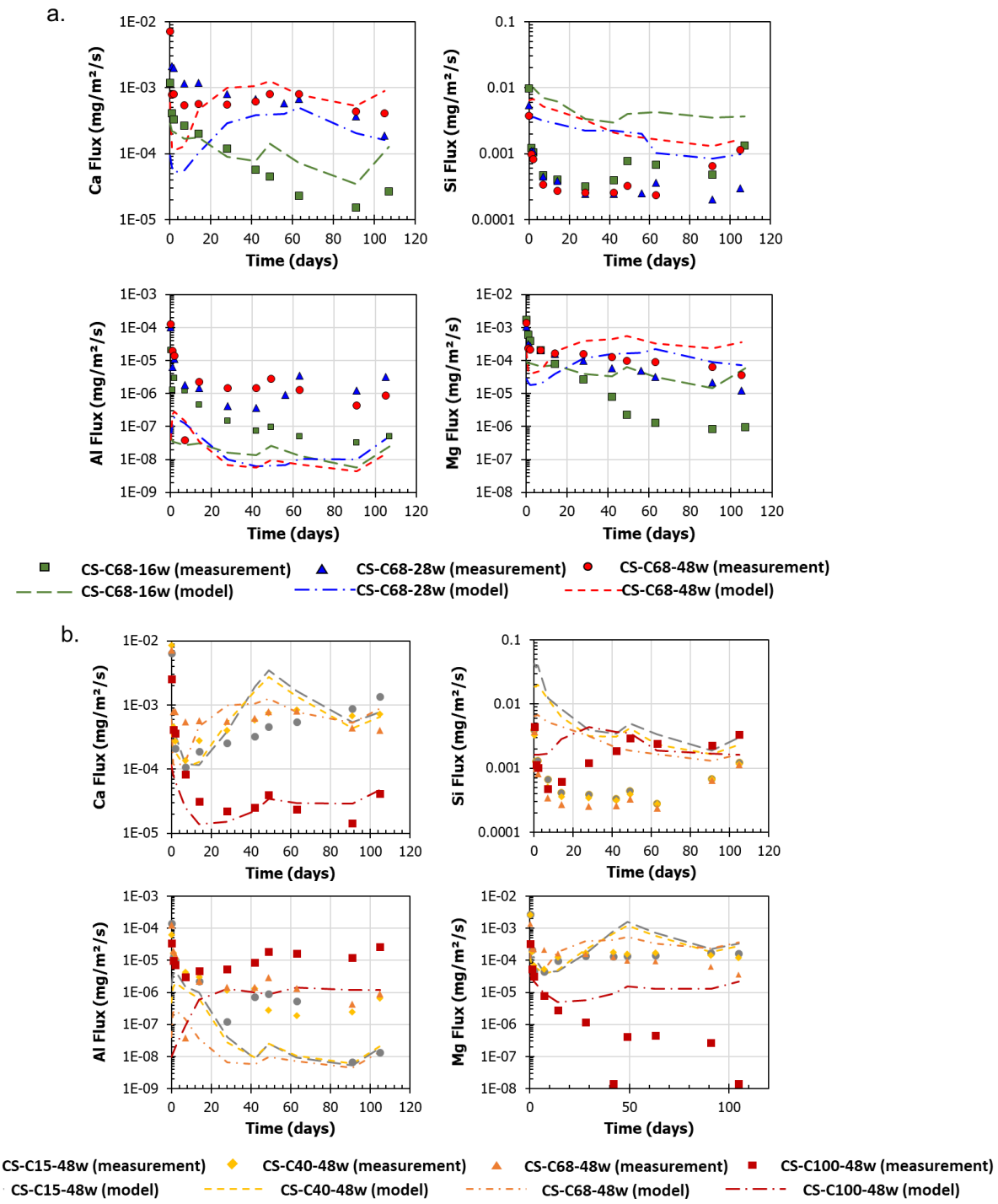

Figure 5.7 Eluate pH and diffusion-controlled leaching of major constituents (Ca, Si, Al) from samples carbonated (a) for 16, 28, and 48 weeks under 68% RH; (b) under 15%, 40%, 68%, and 100% RH for 48 weeks.

The RH in the aging conditions also has a significant impact on the leaching of major constituents (Figure 5.7b). Notably, the leaching behaviors of major constituents from the saturated sample was substantially different from the unsaturated samples, due to the difference in their carbonation histories. CS-C100-48w showed the lowest fluxes of Ca and Mg and the highest fluxes of Al and Si. The solubility of Ca is strongly dependent on pH. Figure 5.8 presented the pH dependent leaching concentration of Ca at a liquid-to-solid ratio of 0.75. At the pH range of 5.5-12, Ca solubility decreases with increasing pH. The evolution of pore solution pH profiles with leaching time is presented in Figure 5.9. The relative position of the leaching front (arrows) and carbonation front (shaded regions) at a given leaching time yield different pore solution pH values (dashed lines) at the leaching front, affecting the Ca solubility and leaching. For example, the highest Ca flux was observed in CS-C68-48w in early stage of leaching (1-28 days) compared to CS-C15-48w and CS-C40-48w. As shown in Figure 5.9, at 12 days of leaching, the leaching front in CS-C68-48w was within the range of the carbonation front. Pore solution pH at the leaching front of CS-C68-48w was lower than other samples, resulting in the greater leaching flux. As leaching extended past 43 days, the differences in Ca fluxes between CS-C40-48w and CS-C68-48w started to decrease, which was accompanied by smaller differences in eluate pH. At this stage, the leaching front passed the carbonation front in all the samples (Figure 5.9) and the difference in pore solution pH at the leaching front decreased. At the end of the leaching test, the Ca flux decreased with time in CS-C68-48w and increased in CS-C15-48w. A lower pore solution pH was observed at the leaching front of CS-C15-48w compared to other samples, resulting in a higher solubility of Ca. The difference in the Ca leaching was additionally impacted by the effective diffusivity in each sample. Among three unsaturated samples, CS-C15-48w has the highest effective diffusivity over the widest range of depth, increasing the diffusion of constituents. Therefore, Ca fluxes indicated the coupled effect of physical and chemical changes in the sample as a result of carbonation, and the reactive transport model incorporated both effects. The model captured the trend in Ca fluxes for the four samples as described above. The model also captured the Al and Si fluxes in CS-C100-48w, but was challenged for the predictions in unsaturated samples for the same reasons stated above. On the contrary, the model reasonably predicted the fluxes of Mg from unsaturated samples but overestimated the leaching in the saturated sample. The pore solution pH of CS-C100-48w is close to 14, which is in the pH range where magnesium solubility is predicted higher than the corresponding measurements, resulting in the overestimation of Mg concentration (Figure 4.2).

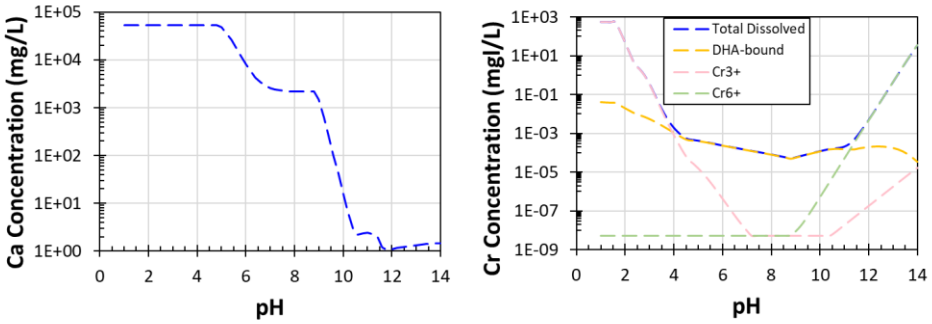

Figure 5.8 pH dependent leaching of Ca and Cr in carbonated material (liquid-to-solid ratio of 0.75 mL/g; pH+pe=14)

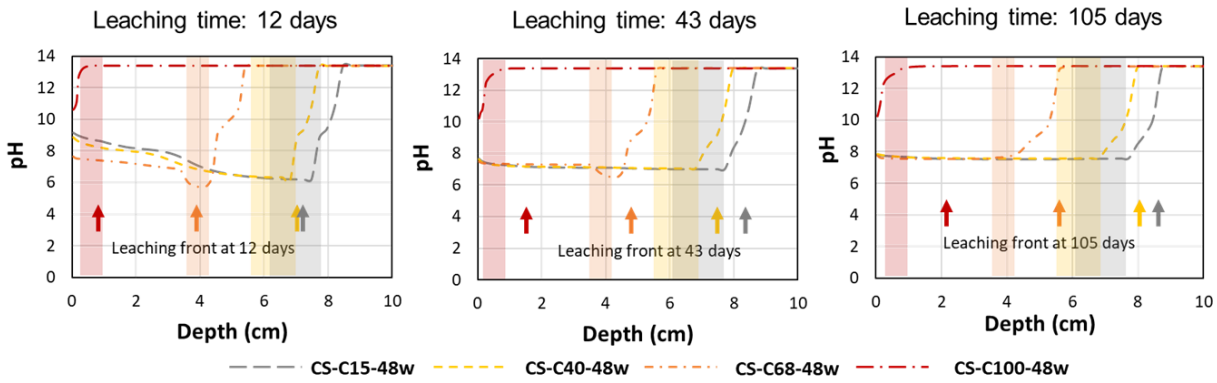

Figure 5.9 Pore solution pH profile from simulation at selected leaching time (the shaded regions indicate the range of carbonation front in the sample from measurements and model results; the arrows indicate the position of the leaching front)

5.4.5 Diffusion-controlled leaching of redox-sensitive constituents

Compared to the leaching of major constituents, less impact on the leaching of redox-sensitive constituents from both aging time (Figure 5.10a) and RH (Figure 5.10b) was observed from the 1315 test. The solubility of Cr in Cast Stone under low liquid-to-solid ratio is highly dependent on the pH (Figure 5.8). The sample with highest pore solution pH (CS-C100-48w) had the highest initial Cr leaching flux. The differences in Cr fluxes among samples with different aging times gradually diminished as the leaching front progressed with leaching time and the pore solution pH at the leaching front merged. At the end of the leaching test, Cr fluxes among samples with different RH ranged over two magnitudes between greatest value from CS-C68-48w (4.7×10^{-5} mg/m^2/s) and the least value of CS-C15-48w (2.8×10^{-7} mg/m^2/s). The low flux in CS-C15-48w resulted from lower pH (Figure 5.9) at the leaching front, which decreased the solubility of Cr (Figure 5.8). In addition, Cr leaching is dependent on both pH and redox state of the material (Figure 4.9).

The migration of the redox profile during leaching can additionally impact the leaching of Cr. As for the leaching of Fe, the initial leaching flux was not affected by either aging time or RH; however, the fluxes in the later stage of the leaching decreased in samples with longer aging times and among samples aged under different RH, CS-C40-48w has the highest Fe flux at the end of the leaching test. On the whole, the longer aging time under carbonation favors the stabilization of Cr, and the relative humidity in the carbonation environment impacts the Cr leaching flux by affecting the pH profile in the system.

In the reactive transport model, the Cr leaching concentrations were used to estimate the initial pore solution pe profile. It was found that the modeled eluate pe was significantly higher than the measurement (Figure 5.10). Since eskolaite is the single mineral phase that was used in the model to describe the dissolution of Cr, the deviation in pe prediction strongly suggests that there may exist Cr-bearing phases other than eskolaite in carbonated Cast Stone that control the solubility of Cr. It is possible that Cr might be incorporated into and coprecipitate with $CaCO_3$ in carbonated Cast Stone [176]. Meanwhile, the redox reactions of Cr can be kinetically controlled and the reaction rates are dependent on pH [168]. This might lead to more complete reduction of Cr in carbonated Cast Stone during the aging period. Although pe measurement from the lab might be systematically biased due to the sample handling and testing conditions, the difference in the eluate pe measurement among samples revealed the impact of the carbonation reaction extent on the redox condition in the samples. Overall, the measured eluate pe was greater in the samples with greater extent of carbonation reaction (i.e., CS-C68-48w), which was also captured by the model. The predictions of initial fluxes of Fe are much lower than the corresponding measurements, mostly because the solubility of Fe is underpredicted by the geochemical speciation model for CS-C between pH 8-9 (Figure 4.7), which is the range of initial eluate pH in the diffusion-controlled leaching experiments (Figure 5.1). The solubility prediction of Fe in carbonated material might be improved after considering the effects of complexation.

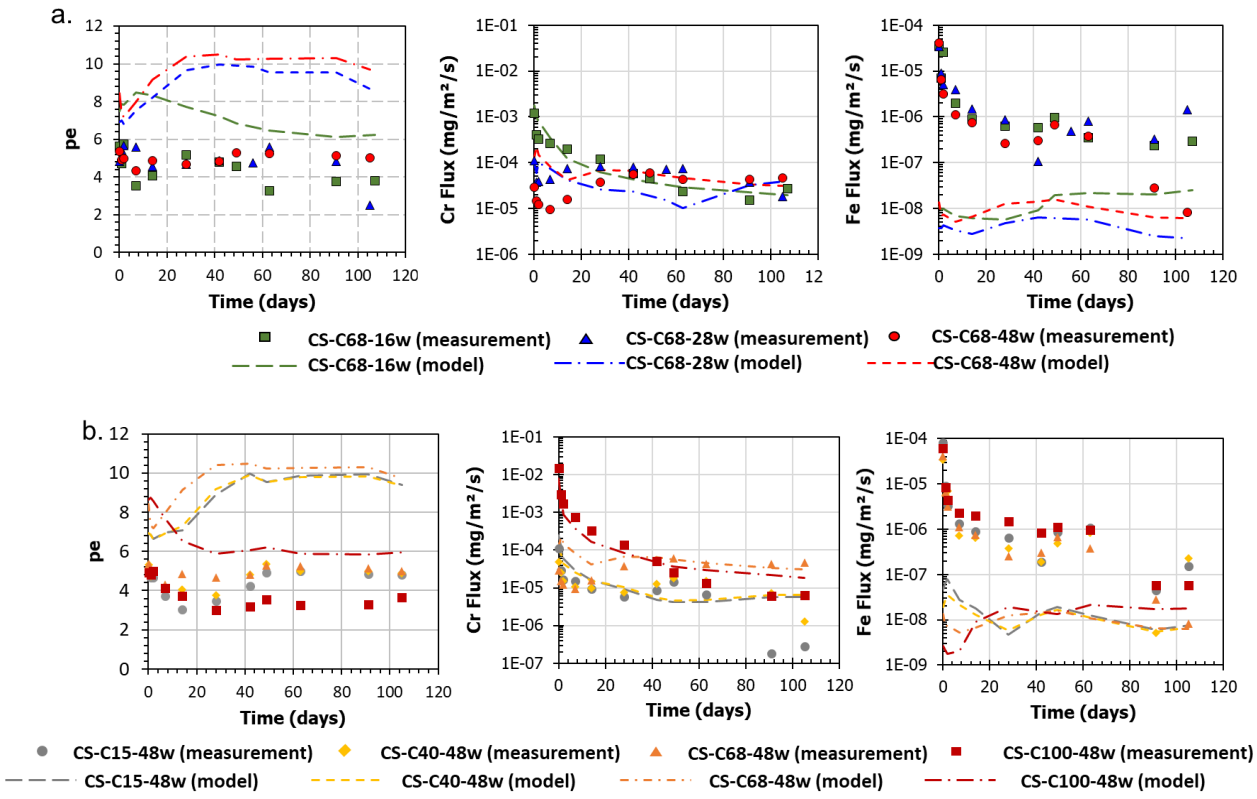

Figure 5.10 Eluate pe and diffusion-controlled leaching of selected redox sensitive constituents (Cr, Fe), from samples carbonated (a) for 16, 28, and 48 weeks under 68% RH; (b) under 15%, 40%, 68%, and 100% RH for 48 weeks.

5.5 Conclusions

This study focused on investigating the coupled effects of drying and carbonation on the leaching of major and trace constituents from Cast Stone. Geochemical speciation coupled with reactive transport modeling was used to describe the leaching test results and to derive key physical and chemical profiles in the solid matrix after aging. The carbonation front was derived independently from the leaching test using two separate modeling approaches and compared to the corresponding phenolphthalein measurements.

Diffusion-controlled leaching demonstrated the mixed effect of extent of carbonation and carbonation depth under different RH conditions. The ingress depth of the carbonation front increased with increasing aging time following a 2nd order polynomial function, but the extent of carbonation in the carbonated region of the sample at the same environmental RH did not increase with aging time. The chemical profile in the pore solution also supported the previous finding that as RH decreases, the carbonation depth increases, with 68% RH yielded the greatest extent of reaction. The carbonation depth estimated from this study compared with

predictions from carbonation model and the previously measured depth provides the range of uncertainty as a function of aging time, which can be beneficial for estimating uncertainty for long-term prediction.

The leaching of highly soluble constituents was found to be enhanced by aging in dry conditions, which is different from observations for Portland cement material. The decreased tortuosity factor and increased carbonation depth are the main factors enhancing the leaching of highly soluble constituents under dry conditions. Leaching behavior of Ca is highly pH dependent, and the relative position of leaching front and carbonation front in the samples dynamically impacts pore solution pH at the leaching front, as well as the flux of Ca as a function of leaching time. The solubility of Cr is also highly dependent on pH. At the end of the leaching test, Cr flux was observed two orders of magnitude greater in samples carbonated at 68% RH than in 15% RH, which can be attributed to the higher pH in pore solution at the leaching front. The leaching rate of Ca, Na, K, S, and Mg was one order of magnitude lower from sample carbonated under 100% RH compared to unsaturated samples, due to the large difference in carbonation history in the samples. Therefore, when estimating the performance of the waste form, it is necessary to consider unsaturated conditions in the field.

With the parameter calibration based on eluate pH and sodium concentration, the diffusion-controlled leaching simulation reasonably predicted the leaching of Na, K, S, Ca, and Mg. The calibration of pe based on Cr concentrations and eskolaite yield higher eluate pe compared to measurements. To improve the model prediction on redox sensitive constituents, other Cr-bearing phases will be needed to describe the speciation of Cr in carbonated Cast Stone. In addition, to further improve the model calculation, the SIT activity model will be implemented.

6. SUMMARY, CONCLUSIONS AND FUTURE WORK

This dissertation investigated the impact of drying, carbonation and leaching in the Cast Stone waste form proposed for the disposal of nuclear waste at DOE Hanford Site. The conclusions from each chapter are presented below.

Chapter 2 presented a water transport model coupling capillary liquid flow with vapor diffusion for predicting drying in Cast Stone. The vapor-liquid equilibrium formulation based on Kelvin's equation was used as the driving force for vapor diffusion, and the model accounts for pore capillary and high salinity effects on water activity. Average pore size, pore water surface tension, and activity as a function of saturation state, as well as drying rates as function of external relative humidity (RH), were measured through experiments. Independent model calibration and validation were used to demonstrate prediction of drying rates. The theoretical relationship between relative humidity and water saturation generally agrees with experimental measurements, and the developed model is capable of predicting drying rates under external relative humidity conditions, ranging from 15% to 100% RH. The construct of the model allows for the prediction of salt redistribution under drying, and dynamically calculates the pore water activity as drying progresses, both of which are crucial for simulation moisture transport in high salt content cementitious material.

Chapter 3 investigated the impact of environmental CO_2 concentration and RH on the carbonation of Cast Stone. The rate of carbonation front ingress and the extent of carbonation reaction were characterized for samples aged up to 48 weeks at four RH levels and three CO_2 concentrations. Results showed carbonation in Cast Stone responds differently to environmental RH compared to ordinary Portland cement. The 68% RH environment allowed the greatest carbonation reaction extent in carbonated locations within the matrix due to the relatively high moisture content that serves as the reaction medium, and 15% RH environment yielded the deepest carbonation front ingress as a result of low saturation and high effective diffusivity of gaseous CO_2. Carbonation resulted in the formation of free water as a result of changes in mineral phase distributions and carbonation reactions. Carbonation reactions increased the drying rate of Cast Stone as a result of increased porosity and microcracking. At 68% RH, extent of carbonation reaction increases with CO_2 concentration, ingress rate was proportional to CO_2 concentration, which confirms the gas phase CO_2 concentration gradient as the driving force for diffusion followed by dissolution and reaction of CO_2 in Cast Stone. Redistribution of sodium toward the exposure surface as well as accumulation of sodium near the carbonation front were observed under coupled drying and carbonation conditions, as a result of enhanced capillary water movement under carbonation.

Chapter 4 investigated the effect of carbonation on the leaching of major and trace constituents from Cast Stone through leaching experiments and simulations. Comparison between the Cast Stone aged in nitrogen, air, and 2% CO_2 showed that carbonation impacts both solubility and diffusivity of major and trace constituents. The solubilities of major constituents were affected by carbonation due to the formation of calcite, wairakite, dolomite, and amorphous silica and the depletion of CNASH solid solution and brucite under carbonation. The pH dependent leaching behavior of carbonation-sensitive constituents was well described in the geochemical speciation model by using carbonated co-precipitates with calcite. For Cr, which was used as a redox indicator and one constituent of potential concern, carbonation under 2% CO_2 reduced the diffusion-controlled leaching by two orders of magnitude, apparently as a result of decreased pore water solubility at decreased pH under reducing conditions that maintained the Cr(III) speciation. The liquid-solid partitioning of Cr was found strongly dependent on the pH and pe state in the system. Aging in air increased the solubility and diffusion-controlled leaching of Cr as a result of oxidation. Effective diffusivity was found increased in the sample carbonated in 2% CO_2 but was not significantly increased in the samples carbonated in air. The change of solubility and effective diffusivity of constituents during carbonation both affected the diffusion-controlled leaching. The reactive transport model with tortuosity and carbonate content calibrated to leaching test results well described the diffusion-controlled leaching behavior of Cast Stone.

In Chapter 5, the coupled effect of drying and carbonation on the leaching of major and trace constituents from Cast Stone was investigated. The diffusion-controlled leaching of highly soluble constituents was found to be enhanced by carbonation in dry conditions, which is different from the observation from studies with Portland cement material published by other researchers. The decreased tortuosity and increased carbonation depth are the main factors enhancing the diffusion-controlled leaching in dry conditions. Since carbonation under 2% CO_2 generally increases the Ca leaching rate, the relative position of the leaching and carbonation fronts in the samples dynamically impacted the flux of Ca as a function of time. Carbonation under 15% RH had the lowest leaching rate of Cr, which can be a result of coupled effects of carbonation depth and reaction extent. The leaching rate of Ca, Na, K, S, and Mg decreased by one order of magnitude for samples carbonated under 100% RH compared to the unsaturated samples, due to the large difference in carbonation histories in the samples. Therefore, when estimating the performance of the waste form, it is necessary to consider unsaturated conditions in the field.

Key physical and chemical profiles in the solid matrix after aging were derived from reactive transport modeling. The derived carbonation depth generally described the progression of carbonation front in different RH conditions when compared with measurements from Chapter 3, with slight overestimation of carbonation front for low RH conditions. Additional effort is needed to improve the reactive transport

simulation and includes: 1) refining the description for Cr in the mineral set to improve the prediction of redox sensitive species, 2) implementing the SIT activity model to account for the ionic interactions in pore solution with high ionic strength, and 3) implementing the multi-ionic diffusion model to account for specific ionic diffusivities.

This study provided data and models than can be used for predicting the leaching behavior of Cast Stone under anticipated field disposal conditions and informs the understanding of drying and carbonation in alkali-activated cementitious materials. A summary of the models used in the dissertation and key input parameters are provided in Table F1. Future study will focus on implementing the developed reactive transport models for the prediction of drying, carbonation, and leaching of Cast Stone in the field conditions. More complexity is anticipated in field conditions and factors other than drying and carbonation such as oxidation and intermittent wetting will be encountered. In addition, the performance of the material needs to be evaluated for a much longer periods of time. The conclusions from this dissertation provide insights into the relationships between drying and oxidation, and the moisture transport model can be further extended for the prediction of constituent re-distribution under intermittent wetting.

REFERENCES

[1] R.A. Peterson, E.C. Buck, J. Chun, R.C. Daniel, D.L. Herting, E.S. Ilton, G.J. Lumetta, S.B. Clark, Review of the Scientific Understanding of Radioactive Waste At the U.S. Doe Hanford Site, Environ. Sci. Technol. (2017) acs.est.7b04077. https://doi.org/10.1021/acs.est.7b04077.

[2] DOE/RL-2018-45, 2019 Hanford Lifecycle Scope, Schedule and Cost Report, 2019.

[3] National Academies of Sciences, Engineering, and Medicine, Review of the Analysis of Supplemental Treatment Approaches of Low-Activity Waste at the Hanford Nuclear Reservation: Review #1 (2018), The National Academies Press, 2018. https://doi.org/10.17226/25093.

[4] L.L. Lockrem, Cast stone technology for treatment and disposal of iodine-rich caustic waste demonstration - final report, No. RPP-RPT-26725, Rev. 0. CH2M, (2005).

[5] R.M. Asmussen, C.I. Pearce, B.W. Miller, A.R. Lawter, J.J. Neeway, W.W. Lukens, M.E. Bowden, M.A. Miller, E.C. Buck, R.J. Serne, N.P. Qafoku, Getters for improved technetium containment in cementitious waste forms, J. Hazard. Mater. 341 (2018) 238–247. https://doi.org/10.1016/j.jhazmat.2017.07.055.

[6] W. Um, B. Williams, M. Snyder, G. Wang, Liquid Secondary Waste Grout Formulation and Waste Form Qualification. No. PNNL-25129; RPT-SWCS-005, REV0. Pacific Northwest National Lab, Richland, WA (United States), 2016. https://doi.org/SRNL-STI-2015-00685, Revision 0.

[7] K. Dixon, J. Harbour, M. Phifer, Hydraulic and Physical Properties of Saltstone Grouts and Vault Concretes, (2008).

[8] DOE M. "435.1-1 Chg1 2001," Radioactive Waste Management Manual.

[9] R. Malviya, R. Chaudhary, Factors affecting hazardous waste solidification/stabilization: A review, J. Hazard. Mater. 137 (2006) 267–276. https://doi.org/10.1016/j.jhazmat.2006.01.065.

[10] F. Sanchez, C. Gervais, A.C. Garrabrants, R. Barna, D.S. Kosson, Leaching of inorganic contaminants from cement-based waste materials as a result of carbonation during intermittent wetting, Waste Manag. 22 (2002) 249–260. https://doi.org/10.1016/S0956-053X(01)00076-9.

[11] C. Gervais, A.C. Garrabrants, F. Sanchez, R. Barna, P. Moszkowicz, D.S. Kosson, The effects of carbonation and drying during intermittent leaching on the release of inorganic constituents from a cement-based matrix, Cem. Concr. Res. 34 (2004) 119–131. https://doi.org/10.1016/S0008-8846(03)00248-5.

[12] C.F. Pereira, Y.L. Galiano, M.A. Rodríguez-Piñero, J.V. Parapar, Long and short-term performance of a stabilized/solidified electric arc furnace dust, J. Hazard. Mater. 148 (2007) 701–707. https://doi.org/10.1016/j.jhazmat.2007.03.034.

[13] A.C. Garrabrants, F. Sanchez, D.S. Kosson, Changes in constituent equilibrium leaching and pore water characteristics of a Portland cement mortar as a result of carbonation, Waste Manag. 24 (2004) 19–36. https://doi.org/10.1016/S0956-053X(03)00135-1.

[14] S. Sarkar, S. Mahadevan, J.C.L. Meeussen, H. van der Sloot, D.S. Kosson, Numerical simulation of cementitious materials degradation under external sulfate attack, Cem. Concr. Compos. 32 (2010) 241–252. https://doi.org/10.1016/j.cemconcomp.2009.12.005.

[15] V.G. Papadakis, Effect of supplementary cementing materials on concrete resistance against carbonation and chloride ingress, Cem. Concr. Res. 30 (2000) 291–299. https://doi.org/10.1016/S0008-8846(99)00249-5.

[16] W. Müllauer, R.E. Beddoe, D. Heinz, Effect of carbonation, chloride and external sulphates on the leaching behaviour of major and trace elements from concrete, Cem. Concr. Compos. 34 (2012) 618–626. https://doi.org/10.1016/j.cemconcomp.2012.02.002.

[17] V.G. Papadakis, M.N. Fardis, A reaction engineering approach to the problem of concrete carbonation, Am. Inst. Chem. Eng. 35 (1989) 1639–1651. https://doi.org/https://doi.org/10.1002/aic.690351008.

[18] V. Shah, S. Bishnoi, Carbonation resistance of cements containing supplementary cementitious materials and its relation to various parameters of concrete, Constr. Build. Mater. 178 (2018) 219–232. https://doi.org/10.1016/j.conbuildmat.2018.05.162.

[19] G. Verbeck, Carbonation of Hydrated Portland Cement, Cem. Concr. (1958) 17-17–20. https://doi.org/10.1520/stp39460s.

[20] D. Russell, P.A.M. Basheer, G.I.B. Rankin, A.E. Long, Effect of relative humidity and air permeability on prediction of the rate of carbonation of concrete, Proc. Inst. Civ. Eng. - Struct. Build. 146 (2009) 319–326. https://doi.org/10.1680/stbu.2001.146.3.319.

[21] E. Drouet, S. Poyet, P. Le Bescop, J.M. Torrenti, X. Bourbon, Carbonation of hardened cement pastes: Influence of temperature, Cem. Concr. Res. 115 (2019) 445–459. https://doi.org/10.1016/j.cemconres.2018.09.019.

[22] A. Leemann, F. Moro, Carbonation of concrete: the role of CO2 concentration, relative humidity and CO2 buffer capacity, Mater. Struct. 50 (2017) 30. https://doi.org/10.1617/s11527-016-0917-2.

[23] D. Zhang, Z. Ghouleh, Y. Shao, Review on carbonation curing of cement-based materials, J. CO2 Util. 21 (2017) 119–131. https://doi.org/10.1016/j.jcou.2017.07.003.

[24] DOE. US., Final Tank Closure and Waste Management Environmental Impact Statement for the Hanford Site, Richland, Washington, (2012).

[25] V.G. Papadakis, C.G. Vayenas, M.N. Fardis, Experimental investigation and mathematical modeling of the concrete carbonation problem, Chem. Eng. Sci. 46 (1991) 1333–1338. https://doi.org/10.1016/0009-2509(91)85060-B.

[26] Z. Shi, B. Lothenbach, M.R. Geiker, J. Kaufmann, A. Leemann, S. Ferreiro, J. Skibsted, Experimental studies and thermodynamic modeling of the carbonation of Portland cement, metakaolin and limestone mortars, Cem. Concr. Res. 88 (2016) 60–72. https://doi.org/10.1016/j.cemconres.2016.06.006.

[27] J.W. Carey, P.C. Lichtner, Calcium silicate hydrate (CSH) solid solution model applied to cement degradation using the continuum reactive transport model FLOTRAN, Transp. Prop. Concr. Qual. Mater. Sci. Concr. 73 (2007) 106.

[28] K. Kobayashi, K. Suzuki, Y. Uno, Carbonation of concrete structures and decomposition of C-S-H, Cem. Concr. Res. 24 (1994) 55–61.

[29] A. Morandeau, M. Thiéry, P. Dangla, Impact of accelerated carbonation on OPC cement paste blended with fly ash, Cem. Concr. Res. 67 (2015) 226–236. https://doi.org/10.1016/j.cemconres.2014.10.003.

[30] K. Sisomphon, L. Franke, Carbonation rates of concretes containing high volume of pozzolanic materials, Cem. Concr. Res. 37 (2007) 1647–1653. https://doi.org/10.1016/j.cemconres.2007.08.014.

[31] S.A. Bernal, J.L. Provis, B. Walkley, R. San Nicolas, J.D. Gehman, D.G. Brice, A.R. Kilcullen, P. Duxson, J.S.J. Van Deventer, Gel nanostructure in alkali-activated binders based on slag and fly ash, and effects of accelerated carbonation, Cem. Concr. Res. 53 (2013) 127–144. https://doi.org/10.1016/j.cemconres.2013.06.007.

[32] J.L. Branch, Impact of aging in the presence of reactive gases on cementitious waste forms and barriers, 2018.

[33] J.E. Renew, C.H. Huang, S.E. Burns, M. Carrasquillo, W. Sun, K.M. Ellison, Immobilization of Heavy Metals by Solidification/Stabilization of Co-Disposed Flue Gas Desulfurization Brine and Coal Fly Ash, Energy and Fuels. 30 (2016) 5042–5051. https://doi.org/10.1021/acs.energyfuels.6b00321.

[34] J.S. Mahlaba, E.P. Kearsley, R.A. Kruger, P.C. Pretorius, Evaluation of workability and strength development of fly ash pastes prepared with industrial brines rich in SO4= and Cl- to expand brine utilisation, Miner. Eng. 24 (2011) 1077–1081.

[35] J.L. Provis, Alkali-activated materials, Cem. Concr. Res. 114 (2018) 40–48. https://doi.org/10.1016/j.cemconres.2017.02.009.

[36] K. Sharma, A. Kumar, Utilization of industrial waste—based geopolymers as a soil stabilizer—a review, Innov. Infrastruct. Solut. 5 (2020). https://doi.org/10.1007/s41062-020-00350-7.

[37] Performance Metric for Cementitious Waste Form Inventory Release in the Integrated Disposal Facility No. PNNL-28992. Pacific Northwest National Lab.(PNNL), Richland, WA (United States), 2019.

[38] J.C. Walton, S. Bin-Shafique, R.W. Smith, N. Gutierrez, A. Tarquin, Role of carbonation in transient leaching of cementitious wasteforms, Environ. Sci. Technol. 31 (1997) 2345–2349.

[39] T. Van Gerven, G. Cornelis, E. Vandoren, C. Vandecasteele, A.C. Garrabrants, F. Sanchez, D.S. Kosson, Effects of progressive carbonation on heavy metal leaching from cement-bound waste, AIChE J. 52 (2006) 826–837. https://doi.org/10.1002/aic.10662.

[40] J.L. Branch, D.S. Kosson, A.C. Garrabrants, P.J. He, The impact of carbonation on the microstructure and solubility of major constituents in microconcrete materials with varying alkalinities due to fly ash replacement of ordinary Portland cement, Cem. Concr. Res. 89 (2016) 297–309. https://doi.org/10.1016/j.cemconres.2016.08.019.

[41] E. Najafi Kani, A. Allahverdi, J.L. Provis, Efflorescence control in geopolymer binders based on natural pozzolan, Cem. Concr. Compos. 34 (2012) 25–33. https://doi.org/10.1016/j.cemconcomp.2011.07.007.

[42] J.L. Branch, Impact of aging in the presence of reactive gases on cementitious waste forms and barriers, Vanderbilt University, 2018.

[43] V. Baroghel-Bouny, M. Mainguy, T. Lassabatere, O. Coussy, Characterization and identification of equilibrium and transfer moisture properties for ordinary and high-performance cementitious materials, Cem. Concr. Res. 29 (1999) 1225–1238. https://doi.org/10.1016/S0008-8846(99)00102-7.

[44] A. Morandeau, M. Thiéry, P. Dangla, Investigation of the carbonation mechanism of CH and C-S-

H in terms of kinetics, microstructure changes and moisture properties, Cem. Concr. Res. 56 (2014) 153–170. https://doi.org/10.1016/j.cemconres.2013.11.015.

[45] M. Criado, A. Palomo, A. Fernandezjimenez, Alkali activation of fly ashes. Part 1: Effect of curing conditions on the carbonation of the reaction products, Fuel. 84 (2005) 2048–2054. https://doi.org/10.1016/j.fuel.2005.03.030.

[46] E. Samson, J. Marchand, Modeling the transport of ions in unsaturated cement-based materials, Comput. Struct. 85 (2007) 1740–1756. https://doi.org/10.1016/j.compstruc.2007.04.008.

[47] O. Coussy, Deformation and stress from in-pore drying-induced crystallization of salt, J. Mech. Phys. Solids. 54 (2006) 1517–1547. https://doi.org/10.1016/j.jmps.2006.03.002.

[48] J.R. Fitch, C.R. Cheeseman, Characterisation of environmentally exposed cement-based stabilised/solidified industrial waste, J. Hazard. Mater. 101 (2003) 239–255. https://doi.org/10.1016/S0304-3894(03)00174-2.

[49] A. Naillon, P. Duru, M. Marcoux, M. Prat, Evaporation with sodium chloride crystallization in a capillary tube, J. Cryst. Growth. 422 (2015) 52–61. https://doi.org/10.1016/j.jcrysgro.2015.04.010.

[50] H.W. Wellman, A.T. Wilson., Salt weathering, a neglected geological erosive agent in coastal and arid environments, Nature. 205 (1965) 1097–1098. https://doi.org/https://doi.org/10.1038/2051097a0.

[51] M. Maguregui, A. Sarmiento, I. Martínez-Arkarazo, M. Angulo, K. Castro, G. Arana, N. Etxebarria, J.M. Madariaga, Analytical diagnosis methodology to evaluate nitrate impact on historical building materials, Anal. Bioanal. Chem. 391 (2008) 1361–1370. https://doi.org/10.1007/s00216-008-1844-z.

[52] D. Benavente, M.A. García del Cura, J. García-Guinea, S. Sánchez-Moral, S. Ordóñez, Role of pore structure in salt crystallisation in unsaturated porous stone, J. Cryst. Growth. 260 (2004) 532–544. https://doi.org/10.1016/j.jcrysgro.2003.09.004.

[53] V. Brito, T. Diaz Gonçalves, Drying Kinetics of Porous Stones in the Presence of NaCl and NaNO3: Experimental Assessment of the Factors Affecting Liquid and Vapour Transport, Transp. Porous Media. 100 (2013) 193–210. https://doi.org/10.1007/s11242-013-0211-5.

[54] C. Dow, F.P. Glasser, Calcium carbonate efflorescence on Portland cement and building materials, Cem. Concr. Res. 33 (2003) 147–154. https://doi.org/10.1016/S0008-8846(02)00937-7.

[55] H.A. Van der Sloot, D.S. Kosson, Use of characterisation leaching tests and associated modelling tools in assessing the hazardous nature of wastes, J. Hazard. Mater. 207–208 (2012) 36–43. https://doi.org/10.1016/j.jhazmat.2011.03.119.

[56] J. Hendrych, R. Hejralová, J. Kroužek, P. Špaček, J. Sobek, Stabilisation/solidification of landfill leachate concentrate and its residue obtained by partial evaporation, Waste Manag. 95 (2019) 560–568. https://doi.org/10.1016/j.wasman.2019.06.046.

[57] A. Bradford, D. Esh, A. Ridge, M. Thaggard, R. Whited, S. Treby, S. Flanders, L.W. Camper., US Nuclear Regulatory Commission Technical Evaluation Report for the US Department of Energy Savannah River Site Draft Section 3116 Waste Determination for Salt Waste Disposal, 2005.

[58] W. Um, B. Williams, M. Snyder, G. Wang, Liquid Secondary Waste Grout Formulation and Preliminary Waste Form Qualification, 2016.

[59] M. Collin, A. Rasmuson, A Comparison of Gas Diffusivity Models for Unsaturated Porous Media,

Soil Sci. Soc. Am. J. 52 (1988) 1559. https://doi.org/10.2136/sssaj1988.03615995005200060007x.

[60] C.E. Schaefer, R.R. Arands, H.A. Van Der Sloot, D.S. Kosson, Modeling of the gaseous diffusion coefficient through unsaturated soil systems, J. Contam. Hydrol. 29 (1997) 1–21. https://doi.org/10.1016/S0169-7722(96)00097-6.

[61] M. Bakhshi, B. Mobasher, C. Soranakom, Moisture loss characteristics of cement-based materials under early-age drying and shrinkage conditions, Constr. Build. Mater. 30 (2012) 413–425. https://doi.org/10.1016/j.conbuildmat.2011.11.015.

[62] Z.P. Bažant, L.J. Najjar., Nonlinear water diffusion in nonsaturated concrete, Matériaux Constr. 5 (1972) 3–20. https://doi.org/https://doi.org/10.1007/BF02479073.

[63] A.C. Garrabrants, D.S. Kosson, Modeling moisture transport from a portland cement-based material during storage in reactive and inert atmospheres, Dry. Technol. 21 (2003) 775–805. https://doi.org/10.1081/DRT-120021686.

[64] P. Coussot, Scaling approach of the convective drying of a porous medium, Eur. Phys. J. B. 15 (2000) 557–566. https://doi.org/10.1007/s100510051160.

[65] B.F. Johannesson, Prestudy on diffusion and transient condensation of water vapor in cement mortar, Cem. Concr. Res. 32 (2002) 955–962. https://doi.org/10.1016/S0008-8846(02)00736-6.

[66] B. Johannesson, U. Nyman, A Numerical Approach for Non-Linear Moisture Flow in Porous Materials with Account to Sorption Hysteresis, Transp. Porous Media. 84 (2010) 735–754. https://doi.org/10.1007/s11242-010-9538-3.

[67] E. Samson, J. Marchand, K.A. Snyder, J.J. Beaudoin, Modeling ion and fluid transport in unsaturated cement systems in isothermal conditions, Cem. Concr. Res. 35 (2005) 141–153. https://doi.org/10.1016/j.cemconres.2004.07.016.

[68] L.A. Richards, Capillary conduction of liquids through porous mediums, J. Appl. Phys. 1 (1931) 318–333. https://doi.org/10.1063/1.1745010.

[69] R. von Helmholtz, Untersuchungen über Dämpfe und Nebel, besonders über solche von Lösungen, Ann. Phys. 263 (1886) 508–543. https://doi.org/https://doi.org/10.1002/andp.18862630403.

[70] F. Collins, J.G. Sanjayan, Effect of pore size distribution on drying shrinkage of alkali-activated slag concrete, Cem. Concr. Res. 30 (2000) 1401–1406. https://doi.org/https://doi.org/10.1016/S0008-8846(00)00327-6.

[71] C.E. Schaefer, R.R. Arands, H.A. van der Sloot, D.S. Kosson, Prediction and experimental validation of liquid-phase diffusion resistance in unsaturated soils, J. Contam. Hydrol. 20 (1995) 145–166. https://doi.org/10.1016/0169-7722(95)00020-V.

[72] J. Letey, W.D. Kemper, L. Noonan., The Effect of Osmotic Pressure Gradients on Water Movement in Unsaturated Soil, Soil Sci. Soc. Am. J. 33 (1969) 15–18. https://doi.org/https://doi.org/10.2136/sssaj1969.03615995003300010010x.

[73] E.J. Henry, J.E. Smith, The effect of surface-active solutes on water flow and contaminant transport in variably saturated porous media with capillary fringe effects, J. Contam. Hydrol. 56 (2002) 247–270. https://doi.org/10.1016/S0169-7722(01)00206-6.

[74] R.L. Russell, Letter Report : LAW Simulant Development for Cast Stone Screening Tests, (2013).

[75] J.S.J. Van Deventer, J.L. Provis, P. Duxson, Technical and commercial progress in the adoption of geopolymer cement, Miner. Eng. 29 (2012) 89–104. https://doi.org/10.1016/j.mineng.2011.09.009.

[76] E.P. Barrett, L.G. Joyner, P.P. Halenda, The Determination of Pore Volume and Area Distributions in Porous Substances. I. Computations from Nitrogen Isotherms, J. Am. Chem. Soc. 73 (1951) 373–380. https://doi.org/10.1021/ja01145a126.

[77] V. Baroghel-bouny, Water vapour sorption experiments on hardened cementitious materials Part I: Essential tool for analysis of hygral behaviour and its relation to pore structure, Cem. Concr. Res. 37 (2007) 414–437. https://doi.org/10.1016/j.cemconres.2006.11.019.

[78] Q. Zeng, D. Zhang, H. Sun, K. Li, Characterizing pore structure of cement blend pastes using water vapor sorption analysis, Mater. Charact. 95 (2014) 72–84. https://doi.org/10.1016/j.matchar.2014.06.007.

[79] J. Kaufmann, R. Loser, A. Leemann, Analysis of cement-bonded materials by multi-cycle mercury intrusion and nitrogen sorption, J. Colloid Interface Sci. 336 (2009) 730–737. https://doi.org/10.1016/j.jcis.2009.05.029.

[80] U.S. EPA. 2014., Method 6010D: Inductively Coupled Plasma-Atomic Emission Spectrometry, (2014).

[81] U.S. EPA. 2007., Method 9056A: Determination of Inorganic Anions by Ion Chromatography, (2007).

[82] A.C. Garrabrants, R.C. DeLapp, J.L. Branch, K.G. Brown, D.S. Kosson, Cast stone materials: porosity determination and relative humidity–saturation relationship. Consortium for Risk Evaluation with Stakeholder Participation report, 2016.

[83] L. Greenspan, Humidity Fixed Points of Binary Saturated Aqueous Solutions., J Res Natl Bur Stand Sect A Phys Chem. 81 A (1977) 89–96. https://doi.org/10.6028/jres.081A.011.

[84] I. Maruyama, T. Ohkubo, T. Haji, R. Kurihara, Dynamic microstructural evolution of hardened cement paste during first drying monitored by 1H NMR relaxometry, Cem. Concr. Res. 122 (2019) 107–117. https://doi.org/10.1016/j.cemconres.2019.04.017.

[85] B. Wu, G. Ye, Development of porosity of cement paste blended with supplementary cementitious materials after carbonation, Constr. Build. Mater. 145 (2017) 52–61. https://doi.org/10.1016/j.conbuildmat.2017.03.176.

[86] D.L. Parkhurst, C.A.J. Appelo, Description of input and examples for PHREEQC version 3: a computer program for speciation, batch-reaction, one-dimensional transport, and inverse geochemical calculations. No. 6-A43. US Geological Survey, 2013.

[87] B. Lothenbach, D.A. Kulik, T. Matschei, M. Balonis, L. Baquerizo, B. Dilnesa, G.D. Miron, R.J. Myers, Cemdata18: A chemical thermodynamic database for hydrated Portland cements and alkali-activated materials, Cem. Concr. Res. 115 (2019) 472–506. https://doi.org/10.1016/j.cemconres.2018.04.018.

[88] J.M. Delany, S.R. Lundeen., The LLNL thermodynamic database." Lawrence Livermore National Laboratory Report UCRL-21658. Lawrence Livermore National Laboratory, Livermore, California, USA, 1990.

[89] G. Faure, Principles and applications of inorganic geochemistry: a comprehensive textbook for geology students, Macmillan Collier Macmillan. Maxwell Macmillan International., 1991.

[90] Z. Chen, P. Zhang, K.G. Brown, J.L. Branch, H.A. van der Sloot, J.C.L. Meeussen, R.C. Delapp, W. Um, D.S. Kosson, Development of a geochemical speciation model for use in evaluating leaching from a cementitious low activity waste form, Environ. Sci. Technol. 2021, in review, (n.d.).

[91] K.S. Pitzer, G. Mayorga, Thermodynamics of electrolytes. II. Activity and osmotic coefficients for strong electrolytes with one or both ions univalent, J. Phys. Chem. 77 (1973) 2300–2308. https://doi.org/10.1021/j100638a009.

[92] L.N. Plummer, D.L. Parkhurst, G.W. Fleming, S.A. Dunkle, A computer program incorporating Pitzer's equations for calculation of geochemical reactions in brines. US Geological Survey, 1988.

[93] E. Washburn, C. West, International critical tables of numerical data, physics, chemistry and technology (1st electronic edition), The National Academies Press, 1930. https://doi.org/https://doi.org/10.17226/20230.

[94] C.A.J. Appelo, D. Postma, Geochemistry, groundwater and pollution, CRC press, 2004.

[95] R.J. Millington, J.P. Quirk, Permeability of porous solids, Trans. Faraday Soc. 57 (1961) 1200–1207. https://doi.org/10.1039/TF9615701200.

[96] J. Zhang, J. Wang, X. Ding, Test and simulation on moisture flow in earlyage concrete under drying, Dry. Technol. 36 (2018) 221–233. https://doi.org/10.1080/07373937.2017.1315588.

[97] M.T. van Genuchten, A closed-form equation for predicting.pdf, Soil Sci. Soc. Am. J. (1980) 892–898. https://doi.org/https://doi.org/10.2136/sssaj1980.03615995004400050002x.

[98] K. Dixon, Moisture retention properties of high temperature cure ARP/MCU saltstone grout, Savannah River National Laboratory, SRNL-STI-2011-00661, 2011.

[99] J.C.L. Meeussen, Orchestra: An object-oriented framework for implementing chemical equilibrium models, Environ. Sci. Technol. 37 (2003) 1175–1182. https://doi.org/10.1021/es025597s.

[100] J. Crank, The mathematics of diffusion, Oxford university press, 1979.

[101] H. Akita, T. Fujiwara, Y. Ozaka, A practical procedure for the analysis ofmoisture transfer within concrete due to drying, Mag. Concr. Res. 49 (1997) 129–137. https://doi.org/10.1680/macr.1997.49.179.129.

[102] Q. Zeng, D. Zhang, K. Li, Kinetics and Equilibrium Isotherms of Water Vapor Adsorption/Desorption in Cement-Based Porous Materials, Transp. Porous Media. 109 (2015) 469–493. https://doi.org/10.1007/s11242-015-0531-8.

[103] R.J. Myers, S.A. Bernal, J.L. Provis, A thermodynamic model for C-(N-)A-S-H gel: CNASH-ss. Derivation and validation, Cem. Concr. Res. 66 (2014) 27–47. https://doi.org/10.1016/j.cemconres.2014.07.005.

[104] L. Onsager, N.N.T. Samaras, The Surface Tension of Debye-Hückel Electrolytes The Surface Tension of Debye-Huckel Electrolytes, J. Chem. Phys. 528 (1934). https://doi.org/http://doi.org/10.1063/1.1749522.

[105] M. Boström, D.R.M. Williams, B.W. Ninham, Surface tension of electrolytes: Specific ion effects explained by dispersion forces, Langmuir. 17 (2001) 4475–4478. https://doi.org/10.1021/la0102298.

[106] I. Maruyama, T. Ohkubo, T. Haji, R. Kurihara, Dynamic microstructural evolution of hardened cement paste during first drying monitored by 1H NMR relaxometry, Cem. Concr. Res. 122 (2019) 107–117. https://doi.org/10.1016/j.cemconres.2019.04.017.

[107] E. Gartner, I. Maruyama, J. Chen, A new model for the C-S-H phase formed during the hydration of Portland cements, Cem. Concr. Res. 97 (2017) 95–106. https://doi.org/10.1016/j.cemconres.2017.03.001.

[108] M. Mastali, P. Kinnunen, A. Dalvand, R. Mohammadi Firouz, M. Illikainen, Drying shrinkage in alkali-activated binders – A critical review, Constr. Build. Mater. 190 (2018) 533–550. https://doi.org/10.1016/j.conbuildmat.2018.09.125.

[109] S. Hanjitsuwan, S. Hunpratub, P. Thongbai, S. Maensiri, V. Sata, P. Chindaprasirt, Effects of NaOH concentrations on physical and electrical properties of high calcium fly ash geopolymer paste, Cem. Concr. Compos. 45 (2014) 9–14. https://doi.org/10.1016/j.cemconcomp.2013.09.012.

[110] Z. Zhang, Y. Zhu, H. Zhu, Y. Zhang, J.L. Provis, H. Wang, Effect of drying procedures on pore structure and phase evolution of alkali-activated cements, Cem. Concr. Compos. 96 (2019) 194–203. https://doi.org/10.1016/j.cemconcomp.2018.12.003.

[111] A.M. Fernandez-Jimenez, A. Palomo, C. Lopez-Hombrados, Engineering Properties of Compacted Fly Ash, ACI Mater. J. (2006).

[112] D.R. Ceratti, M. Faustini, C. Sinturel, M. Vayer, V. Dahirel, M. Jardat, D. Grosso, Critical effect of pore characteristics on capillary infiltration in mesoporous films, Nanoscale. 7 (2015) 5371–5382. https://doi.org/10.1039/c4nr03021d.

[113] N.C. Collier, N.B. Milestone, L.E. Gordon, S.-C. Ko, The suitability of a supersulfated cement for nuclear waste immobilisation, J. Nucl. Mater. 452 (2014) 457–464. https://doi.org/10.1016/j.jnucmat.2014.05.078.

[114] A.M. El-Kamash, M.R. El-Naggar, M.I. El-Dessouky, Immobilization of cesium and strontium radionuclides in zeolite-cement blends, J. Hazard. Mater. 136 (2006) 310–316. https://doi.org/10.1016/j.jhazmat.2005.12.020.

[115] E.M. Pierce, K.J. Cantrell, J.H. Westsik, K.E. Parker, W. Um, M.M. Valenta, R.J. Serne, Secondary Waste Form Screening Test Results — Cast Stone and Alkali Alumino-Silicate Geopolymer, Pnnl-19505. (2010).

[116] D. Bonen, S.L. Sarkar, The superplasticizer adsorption capacity of cement pastes, pore solution composition, and parameters affecting flow loss, Cem. Concr. Res. 25 (1995) 1423–1434.

[117] B. Johannesson, P. Utgenannt, Microstructural changes caused by carbonation of cement mortar, Cem. Concr. Res. 31 (2001) 925–931. https://doi.org/10.1016/S0008-8846(01)00498-7.

[118] J.C. Walton, Models for Estimation of _Service Life of Concrete Barriers in Low-Level Radioactive Waste Didposal, (1990).

[119] S.A. Bernal, J.L. Provis, D.G. Brice, A. Kilcullen, P. Duxson, J.S.J. Van Deventer, Accelerated carbonation testing of alkali-activated binders significantly underestimates service life: The role of pore solution chemistry, Cem. Concr. Res. 42 (2012) 1317–1326. https://doi.org/10.1016/j.cemconres.2012.07.002.

[120] I. Galan, C. Andrade, M. Castellote, Natural and accelerated CO2 binding kinetics in cement paste at different relative humidities, Cem. Concr. Res. 49 (2013) 21–28. https://doi.org/10.1016/j.cemconres.2013.03.009.

[121] B.D. Wood, C.K. Keller, D.L. Johnstone, In situ measurement of microbial activity and controls on microbial CO2 production in the unsaturated zone, Water Resour. Res. 29 (1993) 647–659. https://doi.org/10.1029/92WR02315.

[122] S.A. Saslow, G. Wang, W. Um, R.M. Asmussen, R.L. Russell, R. Sahajpal, Updated Liquid Secondary Waste Grout Formulation and Preliminary Waste Form Qualification, (2017). https://www.pnnl.gov/main/publications/external/technical_reports/PNNL-26443.pdf.

[123] R.M. Asmussen, J. Stephenson, C.I. Pearce, R.E. Clayton, A.R. Lawter, M. Bowden, J.J. Neeway, E. Buck, B. Miller, E. Cordova, B. Lee Bd, W.N. Washton, N.P. Qafoku, Getter Incorporation into Cast Stone and Solid State Characterizations, (2016).

[124] C.W. Chung, W. Um, M.M. Valenta, S.K. Sundaram, J. Chun, K.E. Parker, M.L. Kimura, J.H. Westsik, Characteristics of Cast Stone cementitious waste form for immobilization of secondary wastes from vitrification process, J. Nucl. Mater. 420 (2012) 164–174. https://doi.org/10.1016/j.jnucmat.2011.09.021.

[125] R. Taylor, I.G. Richardson, R.M.D. Brydson, Composition and microstructure of 20-year-old ordinary Portland cement-ground granulated blast-furnace slag blends containing 0 to 100% slag, Cem. Concr. Res. 40 (2010) 971–983. https://doi.org/10.1016/j.cemconres.2010.02.012.

[126] M. Nedeljković, B. Ghiassi, S. van der Laan, Z. Li, G. Ye, Effect of curing conditions on the pore solution and carbonation resistance of alkali-activated fly ash and slag pastes, Cem. Concr. Res. 116 (2019) 146–158. https://doi.org/10.1016/j.cemconres.2018.11.011.

[127] H. Ye, R. Cai, Z. Tian, Natural carbonation-induced phase and molecular evolution of alkali-activated slag: Effect of activator composition and curing temperature, Constr. Build. Mater. 248 (2020) 118726. https://doi.org/10.1016/j.conbuildmat.2020.118726.

[128] M. Nedeljković, Y. Zuo, K. Arbi, G. Ye, Carbonation resistance of alkali-activated slag under natural and accelerated conditions, J. Sustain. Metall. 4 (2018) 33–49.

[129] V. Dutzer, W. Dridi, S. Poyet, P. Le Bescop, X. Bourbon, The link between gas diffusion and carbonation in hardened cement pastes, Cem. Concr. Res. 123 (2019) 105795. https://doi.org/10.1016/j.cemconres.2019.105795.

[130] F. Puertas, M. Palacios, T. Vázquez, Carbonation process of alkali-activated slag mortars, J. Mater. Sci. 41 (2006) 3071–3082. https://doi.org/10.1007/s10853-005-1821-2.

[131] US. EPA, Method 1313: Liquid Solid Partitioning as a Function of Extract pH using a Parallel Batch Extraction Procedure, 2012. https://www.epa.gov/sites/production/files/2015-12/documents/1313.pdf.

[132] A.C. Garrabrants, R.C. DeLapp, J.L. Branch, K.G. Brown, D.S. Kosson, Cast Stone Materials - porosity determination and relative humidity-saturation relationships, 2016.

[133] U.S. EPA., Method 1315, Mass transfer rates of constituents in monolith or compacted granular materials using a semi-dynamic tank leaching procedure, 2017. https://www.epa.gov/sites/production/files/2017-10/documents/method_1315_-_final_8-3-17.pdf,.

[134] J.L. Branch, R. Epps, D.S. Kosson, The impact of carbonation on bulk and ITZ porosity in microconcrete materials with fly ash replacement, Cem. Concr. Res. 103 (2018) 170–178. https://doi.org/10.1016/j.cemconres.2017.10.012.

[135] H. Cui, W. Tang, W. Liu, Z. Dong, F. Xing, Experimental study on effects of CO2 concentrations on concrete carbonation and diffusion mechanisms, Constr. Build. Mater. 93 (2015) 522–527. https://doi.org/10.1016/j.conbuildmat.2015.06.007.

[136] M. Thiery, G. Villain, P. Dangla, G. Platret, Investigation of the carbonation front shape on cementitious materials: Effects of the chemical kinetics, Cem. Concr. Res. 37 (2007) 1047–1058. https://doi.org/10.1016/j.cemconres.2007.04.002.

[137] Y.S. Ji, M. Wu, B. Ding, F. Liu, F. Gao, The experimental investigation of width of semi-carbonation zone in carbonated concrete, Constr. Build. Mater. 65 (2014) 67–75.

https://doi.org/10.1016/j.conbuildmat.2014.04.095.

[138] P. Zhang, Z. Chen, K. Brown, J. Meeussen, C. Gruber, A. Garrabrants, D. Kosson, Drying model of a high salt content cementitious waste form: effect of capillary forces and salt solution. (Submitted for publication), Cem. Concr. Res.

[139] H.A. Van der Sloot, P.F.A.B. Seignette, J.C.L. Meeussen, O. Hjelmar, D.S. Kosson, A database, speciation modelling and decision support tool for soil, sludge, sediments, wastes and construction products: LeachXS^{TM}-Orchestra, in: Second Int. Symp. Energy from Biomass Waste, Venice, 2008.

[140] A. Patmonoaji, T. Suekane, Investigation of CO2 dissolution via mass transfer inside a porous medium, Adv. Water Resour. 110 (2017) 97–106. https://doi.org/10.1016/j.advwatres.2017.10.008.

[141] C. Miller, M. Poirier-McNeil, A. Mayer, Dissolution of trapped nonaqueous phase liquids: Mass transfer characteristics, Water Resour. Res. 26 (1990). https://doi.org/https://doi.org/10.1029/WR026i011p02783.

[142] J. Jeong, H. Ramézani, E. Chuta, Reactive transport numerical modeling of mortar carbonation: Atmospheric and accelerated carbonation, J. Build. Eng. 23 (2019) 351–368. https://doi.org/10.1016/j.jobe.2019.01.038.

[143] J. Han, D.A. Eimer, M.C. Melaaen, Liquid phase mass transfer coefficient of carbon dioxide absorption by water droplet, Energy Procedia. 37 (2013) 1728–1735. https://doi.org/10.1016/j.egypro.2013.06.048.

[144] H.J. Cho, J. Choi, Calculation of the mass transfer coefficient for the dissolution of multiple carbon dioxide bubbles in sea water under varying conditions, J. Mar. Sci. Eng. 7 (2019). https://doi.org/10.3390/JMSE7120457.

[145] K. Kobayashi, Y. Uno, Influence of alkali on carbonation of concrete, part I. Preliminary tests with mortar specimens, Cem. Concr. Res. 19 (1989) 821–826. https://doi.org/10.1016/0008-8846(89)90053-7.

[146] R.D. Spence, C. Shi, Stabilization and solidification of hazardous, radioactive, and mixed wastes, CRC press, 2004.

[147] National Academies of Sciences, Engineering, and Medicine 2020. Final Review of the Study on Supplemental Treatment Approaches of Low-Activity Waste at the Hanford Nuclear Reservation, The National Academies Press, 2020. https://doi.org/10.17226/25710.

[148] K.J. Cantrell, J.H. Westsik, R.J. Serne, W. Um, A.D. Cozzi, Secondary Waste Cementitious Waste Form Data Package for the Integrated Disposal Facility Performance Assessment, 2016.

[149] C.J. Engelsen, H.A. Van Der Sloot, G. Wibetoe, H. Justnes, W. Lund, E. Stoltenberg-Hansson, Leaching characterisation and geochemical modelling of minor and trace elements released from recycled concrete aggregates, Cem. Concr. Res. 40 (2010) 1639–1649. https://doi.org/10.1016/j.cemconres.2010.08.001.

[150] R.J. Myers, B. Lothenbach, S.A. Bernal, J.L. Provis, Thermodynamic modelling of alkali-activated slag cements, Appl. Geochemistry. 61 (2015) 233–247. https://doi.org/10.1016/j.apgeochem.2015.06.006.

[151] S.A. Bernal, J.L. Provis, D.G. Brice, A. Kilcullen, P. Duxson, J.S.J. Van Deventer, Accelerated carbonation testing of alkali-activated binders significantly underestimates service life: The role of pore solution chemistry, Cem. Concr. Res. 42 (2012) 1317–1326. https://doi.org/10.1016/j.cemconres.2012.07.002.

[152] P.M. Almond, D.B. Stefanko, C.A. Langton, Effect of Oxidation on Chromium Leaching and Redox Capacity of Slag-Containing Waste Forms, 2013. https://www.osti.gov/servlets/purl/1088991%0Ahttps://www.osti.gov/biblio/1088991/.

[153] P.M. Almond, D.I. Kaplan, C.A. Langton, D.B. Stefanko, W.A. Spencer, Method Evaluation and Field Sample Measurements for the Rate of Movement of the Oxidation Front in Saltstone, (2012).

[154] A.A. Verbeek, M.C. Mitchell, A.M. Ure, The analysis of small samples of rock and soil by atomic absorption and emission spectrometry after a lithium metaborate fusion/nitric acid dissolution procedure, Anal. Chim. Acta. 135 (1982) 215–228. https://doi.org/10.1016/S0003-2670(01)93902-9.

[155] U.S. EPA. 2014., Method 6020B: Inductively Coupled Plasma—Mass Spectrometry, (2014).

[156] V. Herndon, MINTEQA2/PRODEFA2, A Geochemical Assessment Model for Environmental Systems: User Manual Supplement for Version 4.0., 1998.

[157] P. Blanc, A. Lassin, P. Piantone, M. Azaroual, N. Jacquemet, A. Fabbri, E.C. Gaucher, Thermoddem: A geochemical database focused on low temperature water/rock interactions and waste materials., Appl. Geochemistry. 27 (2012) 2107–2116.

[158] E. Samson, G. Lemaire, J. Marchand, J.J. Beaudoin, Modeling chemical activity effects in strong ionic solutions, Comput. Mater. Sci. 15 (1999) 285–294. https://doi.org/10.1016/s0927-0256(99)00017-8.

[159] C.W. Chung, J. Chun, W. Um, S.K. Sundaram, J.H. Westsik, Setting and stiffening of cementitious components in Cast Stone waste form for disposal of secondary wastes from the Hanford waste treatment and immobilization plant, Cem. Concr. Res. 46 (2013) 14–22. https://doi.org/10.1016/j.cemconres.2013.01.003.

[160] D.G.. Kinniburgh, W.H.. van Riemsdijk, L.K.. Koopal, M.. Borkovec, M.F.. Benedetti, M.J. Avena, Ion binding to natural organic matter: competition, heterogeneity, stoichiometry and thermodynamic consistency, Colloids Surfaces A Physicochem. Eng. Asp. 151 (1999) 147–166. https://doi.org/https://doi.org/10.1016/S0927-7757(98)00637-2.

[161] C.J.. Milne, D.G.. Kinniburgh, E. Tipping, Generic NICA-Donnan model parameters for proton binding by humic substances, Environ. Sci. Technol. 35 (2001) 2049–2025. https://doi.org/https://doi.org/10.1021/es000123j.

[162] C.J. Milne, D.G. Kinniburgh, W.H. Van Riemsdijk, E. Tipping, Generic NICA- Donnan model parameters for metal-ion binding by humic substances, Environ. Sci. Technol. 37 (2003) 958–971.

[163] D.A. Dzombak, others, Surface complexation modeling: hydrous ferric oxide, John Wiley & Sons, 1990.

[164] B. Kostura, H. Kulveitova, J. Leško, Blast furnace slags as sorbents of phosphate from water solutions, Water Res. 39 (2005) 1795–1802.

[165] W.J.J. Huijgen, R.N.J. Comans, Carbonation of steel slag for CO2 sequestration: Leaching of products and reaction mechanisms, Environ. Sci. Technol. 40 (2006) 2790–2796. https://doi.org/10.1021/es052534b.

[166] A. V. Radha, A. Navrotsky, Thermodynamics of carbonates, Rev. Mineral. Geochemistry. 77 (2013) 73–121. https://doi.org/10.2138/rmg.2013.77.3.

[167] L.B. Railsback, Patterns in the compositions, properties, and geochemistry of carbonate minerals,

Carbonates and Evaporites. 14 (1999) 1–20.

[168] J.S. Geelhoed, J.C.L. Meeussen, M.J. Roe, S. Hillier, R.P. Thomas, J.G. Farmer, E. Paterson, Chromium remediation or release? Effect of iron(II) sulfate addition on chromium(VI) leaching from columns of chromite ore processing residue, Environ. Sci. Technol. 37 (2003) 3206–3213. https://doi.org/10.1021/es0264798.

[169] S.J. Fuller, D.I. Stewart, I.T. Burke, Chromate reduction in highly alkaline groundwater by zerovalent iron: Implications for its use in a permeable reactive barrier, Ind. Eng. Chem. Res. 52 (2013) 4704–4714. https://doi.org/10.1021/ie302914b.

[170] D.J. Hoitink, K.W. Burk, J. V Ramsdell, W.J. Shaw, Hanford Site Climatological Summary 2004 with Historical Data, 2005.

[171] Performance Assessment for the Saltstone Disposal Facility at the Savannah River Site, SRR Closure & Waste Disposal Authority Aiken, 2009.

[172] J. Arnold, R. Duddu, K. Brown, D.S. Kosson, Influence of multi-species solute transport on modeling of hydrated Portland cement leaching in strong nitrate solutions, Cem. Concr. Res. 100 (2017) 227–244. https://doi.org/10.1016/j.cemconres.2017.06.002.

[173] Z. Chen, P. Zhang, K.G. Brown, H.A. van der Sloot, J.C.L. Meeussen, R.C. DeLapp, W. Um, D.S. Kosson, Monolithic Diffusion Model Development for Evaluating the Leaching from Cementitious Low Activity Waste Forms Aged under Drying Conditions, (2021).

[174] W.M. Haynes, CRC handbook of chemistry and physics, CRC press, 2014.

[175] K.G. Brown, J. Arnold, S. Sarkar, G. Flach, H. van der Sloot, J.C.L. Meeussen, D.S. Kosson, Modeling Carbonation of High-Level Waste Tank Integrity and Closure, EPJ Web Conf. 56 (2013) 05003. https://doi.org/10.1051/epjconf/20135605003.

[176] A.P. Brady, Chromate incorporation into calcium carbonate minerals and associated chromium isotope fractionation, Georgia Institute of Technology, 2017.

[177] K.S. Pitzer, Thermodynamics of electrolytes. I. Theoretical basis and general equations, J. Phys. Chem. 77 (1973) 268–277. https://doi.org/10.1021/j100621a026.

[178] J.G. Reynolds, R. Carter, A.R. Felmy, A pitzer interaction model for the NaNO3-NaNO2-NaOH-H2O system from 0 to 100°C, Ind. Eng. Chem. Res. 54 (2015) 3062–3070. https://doi.org/10.1021/acs.iecr.5b00016.

[179] J.G. Reynolds, R. Carter, A sulfate and darapskite solubility model with Pitzer interaction coefficients for aqueous solutions containing NaNO2, NaNO3, and NaOH, J. Chem. Thermodyn. 101 (2016) 380–386. https://doi.org/10.1016/j.jct.2016.06.027.

[180] J.P. Hershey, F.J. Millero, The dependence of the acidity constants of silicic acid, Mar. Chem. 18 (1986) 101–105.

[181] D.J. Wesolowski, Aluminum speciation and equilibria in aqueous solution: I. The solubility of gibbsite in the system Na-K-Cl-OH-Al(OH)4 from 0 to 100°C, Geochim. Cosmochim. Acta. 56 (1992) 1065–1091. https://doi.org/10.1016/0016-7037(92)90047-M.

[182] A. Lach, L. André, S. Guignot, C. Christov, P. Henocq, A. Lassin, A Pitzer Parametrization to Predict Solution Properties and Salt Solubility in the H-Na-K-Ca-Mg-NO3-H2O System at 298.15 K, J. Chem. Eng. Data. 63 (2018) 787–800. https://doi.org/10.1021/acs.jced.7b00953.

[183] V.K. Filippov, D.S. Barkov, Y.A. Fedorov, Applcation of the Pitzer equations to the solubility of

ternary aqueous nitrate solutions at 25°C, J. Solution Chem. 15 (1986) 611–619. https://doi.org/10.1007/BF00645814.

[184] B. Lothenbach, K. Scrivener, R.D. Hooton, Supplementary cementitious materials, Cem. Concr. Res. 41 (2011) 1244–1256. https://doi.org/10.1016/j.cemconres.2010.12.001.

APPENDIX A:

DEVELOPMENT OF A GEOCHEMICAL SPECIATION MODEL FOR USE IN EVALUATING LEACHING FROM A CEMENTITIOUS LOW ACTIVITY WASTE FORM ǂ

Zhiliang Chen, Peng Zhang, Kevin G. Brown, Janelle L. Branch, Hans A. van der Sloot, Johannes C.L. Meeussen, Rossane C. Delapp, Wooyong Um, David S. Kosson

ǂ Submitted for publication to Environmental Science & Technology

ABSTRACT

Cast Stone has been developed to immobilize low activity radioactive waste at the Hanford Site; however, constituents of potential concern (COPCs) can be released when in contact with water during disposal. Herein, a representative mineral and parameter set for geochemical speciation modeling was developed for Cast Stone aged in inert and oxic environments, to simulate leaching concentrations of major and trace constituents. The geochemical speciation model was verified using a monolithic diffusion model in conjunction with independent monolith diffusion test results. Eskolaite (Cr_2O_3) was confirmed as the dominant mineral retaining Cr in Cast Stone doped with 0.1 or 0.2 wt.% Cr. The immobilization of Tc as a primary COPC in Cast Stone was evaluated, and the redox states of pore water within monolithic Cast Stone indicated by Cr are insufficient for the reduction of Tc. However, redox states provided by blast furnace slag (BFS) within the interior of Cast Stone are capable of reducing Tc for immobilization, with the immobilization reaction rate postulated to be controlled by the diffusive migration of soluble Tc in pore water to the surface of reducing BFS particles. Aging in oxic conditions increased the flux of Cr and Tc from monolithic Cast Stone.

INTRODUCTION

Cementitious materials are often selected for nuclear waste disposal because of their ability to stabilize radionuclides and inorganic contaminants [1], their low costs, and easy production [2]. Cast Stone [3] is a waste form produced from coal fly ash (FA), granular ground blast furnace slag (BFS), and ordinary Portland cement (OPC) that has been proposed to solidify and immobilize liquid low activity radioactive waste (LAW) at the Department of Energy Hanford Site in Richland, Washington [4-6]. During its service life, Cast Stone is likely to come in contact with infiltrating water, and constituents of potential concern (COPCs)

could be remobilized. Moreover, Cast Stone is subject to evolving physical and chemical properties because of oxidation and carbonation from oxygen and carbon dioxide in the air or soil gas and dissolved in infiltrating water [7-8]; reactions with oxygen and carbon dioxide could impact the retention of COPCs [9-13]. Therefore, it is important to improve the understanding of the complex mechanisms that are responsible for the leaching behavior of constituents, where insights can be gained through use of leaching tests coupled with geochemical speciation modeling [14].

Defining a representative mineral and parameter set accounting for the aqueous-solid partitioning of constituents in Cast Stone is a necessary step for geochemical speciation model development [15]. The mineralogy of Cast Stone has been investigated in several studies through techniques of X-ray diffraction (XRD) [5,6,16] and X-ray adsorption spectroscopy (XAS) [4,17]. However, the identified minerals should be verified for inclusion in a geochemical speciation model based on test data because some observed minerals may not be controlling with respect to leaching behavior due to dissolution kinetics, pore structure (e.g., pore size and connectivity), and occlusion within the material structure, and often a range of thermodynamic solubility values are available for individual minerals. So far, a geochemical speciation-based model for simulating Cast Stone leaching has not been established, and the mineral assemblage and related parameterization accounting for the leaching behavior of constituents from Cast Stone have not been defined or verified.

Understanding the evolution of minerals during aging is needed for assessing performance of Cast Stone with respect to the long-term retention and leaching of COPCs. Technetium (^{99}Tc), a fission product with a half-life of 213,000 years, is of concern because the primary form under aerobic conditions (TcO_4^-) is highly mobile [17,19]. Under reducing conditions, technetium can be in a low valence state (i.e., $Tc(IV)O_2 \cdot 2H_2O$ and $Tc(IV)_2S_7$), which is much less soluble and also can be easily adsorbed by particulate organic matter [20]. Cast Stone achieves an internal reducing environment using BFS bearing sulfur with low redox potential (e.g., oldhamite, pyrrhotite, and niningerite) [21-24]. However, reoxidation of Tc(IV) in Cast Stone by reaction with dissolved or gaseous O_2 is of concern [20]. Chromium, in addition to being a COPC, can be used as a redox state indicator because the reduction potentials of Cr (i.e., CrO_4^{2-} and Cr^{3+}, -0.13 V) and Tc (i.e., TcO_4^- and Tc^{4+}, -0.36 V) redox couples are relatively close [25-26] and Cr, like Tc, has a very limited solubility in its low valence state (Cr(III)) and is highly soluble in its high valence state (Cr(VI)) [27,28] . For comparison, the reduction potentials of S (SO_4^{2-} and S^{2-}) and Fe (Fe^{3+} and Fe^{2+}) redox couples are -2.10 and 0.77 V, respectively.

The objective of this study is to develop and demonstrate a geochemical speciation model that predicts the leaching of COPCs from Cast Stone waste forms under reducing and oxidizing conditions. The model was calibrated based on mineral phases experimentally measured and those inferred from constituent pH-

dependent liquid-solid partitioning results in Cast Stone spiked with Cr as an indicator for redox-sensitive constituents. The resulting mineral and parameter set then was verified through simulation of monolith diffusion test results. Inclusion of an assumed reaction set for Tc is used to demonstrate the potential impact of oxidation on leaching of Tc as a primary COPC. Subsequent studies will explore the impacts of carbonation and combined oxidation and carbonation on geochemical speciation reaction sets and parameterization, as well as long-term leaching scenarios.

MATERIALS AND METHODS

Materials and pre-treatment

Cast Stone samples were prepared with class F fly ash (FAF), grade 100 ground blast furnace slag (BFS), type I/II ordinary Portland cement (OPC), and liquid low activity radioactive waste (LAW) simulant (where 0.2 wt.% Cr on the basis of Cast Stone weight was added as Na_2CrO_4 as a redox indicator), following the procedure of Lockrem [3]. Each ingredient was used to form a water-to-binder ratio of 0.48 (Table S1a), and the composition of liquid LAW simulant followed the recipe for Hanford Tank Waste Operational System (HTWOS) Average 5M (i.e., 5 mol/L) Na simulant [29] (Table S1b). The OPC was purchased from concrete vendors, and FAF and BFS were provided by the Savannah River National Laboratory (SRNL) and the Pacific Northwest National Laboratory (PNNL), respectively. The Cast Stone slurry was set in cylindrical molds with 25-mm diameter and 110-mm length for 72 hours, then the molds were removed and the monolithic samples were cured in N_2 at 25 °C under 100 % relative humidity for 90 days.

Experimental procedures

Aging of materials under oxic and anoxic conditions: A subset of the cured monolithic samples (doped with 0.2 wt.% Cr) was ground in a N_2 atmosphere to particles with 85 wt.% less than 2-mm diameter. Subsequently, the granular and monolithic samples were separately aged in N_2 and 21 vol.% of O_2 (in N_2) for 16 weeks under a relative humidity of 68 % at room temperature (20±2 °C); these aged samples are identified as CS-N-16w and CS-O-16w, correspondingly.

A separate set of Cast Stone samples [16] was prepared following a similar procedure using 0.1 wt.% mass fraction of Cr and is included in this study. Granular and monolithic samples from this preparation of Cast Stone were aged at room temperature in either N_2 or 21 vol.% of O_2 (in N_2) for 9 weeks under a relative humidity of 65 %; these aged samples are denoted as CS-N-9w and CS-O-9w, respectively. Both the amount of spiked Cr and aging time were set to be different for two sets of samples, resulting in Cast Stone materials with different apparent redox states.

pH-dependent leaching tests: the aged granular samples and BFS were subject to pH-dependent leaching tests according to Environmental Protection Agency (EPA) Method 1313 [30-32], using Milli-Q water (deoxygenated by nitrogen bubbling) along with predetermined amount of nitric acid (2N HNO_3) or potassium hydroxide (1N KOH) as the eluent at a liquid-solid ratio (L/S) of 10 mL/g-dry weight. The amount of nitric acid or potassium hydroxide added to reach each target end-state pH was determined by pH titration on separate aliquots of the material prior to the test. The equilibrium pH and pe of the eluate for the test condition without acid or base addition (deoxygenated deionized water only) are referred to as the natural pH and natural pe of the material. For the test conditions with eluate pH less than the natural pH, samples were subject to oxidation by the addition of nitric acid for pH adjustment. The mixture of sample and extracting solution was tumbled in an end-over-end tumbler at 20 °C for 48 hours. Two parallel sets of tests were conducted for each sample.

Monolith diffusion leaching tests: the mass transfer rates of constituents from aged monolithic samples were tested following the 1-D configuration of EPA Method 1315 [33, 34]. The exposed surface of each monolith was contacted with deoxygenated Milli-Q water using a liquid-surface-area ratio of 9 ± 1 mL/cm^2 at 20 °C in sealed containers with minimal headspace. The surface area was calculated based on the geometric area of the face of monolith exposed to leaching. The eluate was entirely exchanged with deoxygenated Milli-Q water at 0.1, 1, 2, 7, 14, 28, 42, 49, 63, 91, and 107 days. Method 1315 tests used only deoxygenated water as the eluent to prevent the oxidation of material by nitric acid (as occurs in Method 1313 testing) and to provide independent results for verifying the minerals controlling the solubility of redox-sensitive constituents calibrated using Method 1313 test results.

Analytical methods

All leaching test eluates were collected and measured for pH, conductivity, pe (converted from oxidation-reduction potential measurements as described in Supporting Information-I), and concentrations of constituents. The concentrations of major and trace elements in the eluates were quantified by inductively-coupled plasma optical emission spectroscopy (ICP-OES, Agilent Technologies, Santa Clara, CA) following U.S. EPA Method 6010C [35]. Anions in eluates were measured by ion chromatography (IC, Metrohm USA, Riverview, FL) following EPA Method 9056A [36]. Quality assurance (QA) and quality control (QC) procedures are provided in Supporting Information (SI-II) along with method detection limits (MDL), and lower limits of quantitation (Table S2).

Mass fractions of carbonate minerals in Cast Stone were analyzed by thermogravimetric analysis (TGA; TA Instruments Q600 SDT analyzer, New Castle, Delaware, USA); the procedures are described in Supporting Information (SI-III). Porosity of each monolithic sample was measured by a modified water

exchange method [37]. The elemental compositions of FAF, BFS, OPC, and CS-N-16w were analyzed by X-ray fluorescence (XRF, S4 Explorer X-ray Spectrometer, Bruker-AXS, Germany). The crystalline structures of unleached and leached CS-N-16w were determined by X-ray diffraction (XRD, SmartLab, Rigaku, Japan) after being powdered in a N_2 chamber (leached cases carried out on solid residues from pH-dependent leaching tests at pH of 4.00 and natural pH of 12.64).

Modeling Approach

The modeling of aqueous-solid partitioning and monolithic diffusion of constituents in aged Cast Stone and the development of predominance diagrams for Cr, Fe, S, and Tc were accomplished using the LeachXS-ORCHESTRA (Vanderbilt University, Nashville, TN) modeling framework [38] based on results of the pH-dependent leaching tests and monolith diffusion leaching tests. The aqueous phase speciation reaction set used in the modeling was from the Minteq.V4 thermodynamic database at 20 °C [39]. Minerals controlling the solubility of constituents were selected from the Minteq.V4, Cemdata18 (CEM18) [40], and Lawrence Livermore National Laboratory (LLNL) [41] thermodynamic databases at 20 °C. Specifically for Tc, aqueous phase speciation reactions and minerals were taken from the LLNL database. A basic assumption for the geochemical speciation modeling is that the dissolution, precipitation, and adsorption reactions of all constituents reach equilibrium. For the monolithic diffusion modeling, local equilibrium conditions are assumed for each time step within each cell, which assumes that the chemical reaction takes place much faster than the transport process.

The model parameters (natural pH, L/S, and amount of hydrous ferric oxides (HFO) and humic acid (HA) for adsorption) and available contents of constituents, which are typically the highest release values (mg/kg) in pH-dependent leaching tests for the constituents, are listed in Table S3 for the four Cast Stone materials. A brief description of the modeling framework and parameters is given here and more details are available [15]. The adsorption of ions on the surface of organic matter was modeled with the NICA-Donnan model [42] using parameters published by Milne, et al. [43, 44]. Ion adsorption onto HFO was modeled using the generalized two layer model of Dzombak and Morel [45]. Mineral set was selected by calibration in the geochemical speciation model based on minerals identified in Cast Stone by XRD, XAS, and XANES analyses [4-6,14] and solid solutions developed from alkali-activated slag [46,47]. Specifically, calibration of mineral set and available contents of Si and carbonate is provided in SI-IV in detail.

The monolithic diffusion model is illustrated in Figure S1. This model consists of local chemical equilibrium of solid with pore water and diffusion of species from within the Cast Stone material where release occurs into a well-mixed tank of leaching eluent. The simulated eluent refresh solution and refresh scheme in the tank are the same as in the corresponding monolith diffusion leaching tests. Local equilibrium

as calculated based on the selected mineral set, available contents of individual elements, and HFO and organic matter adsorption determines the pore water composition. Effective diffusivity of ions is controlled by the physical properties of Cast Stone including porosity and tortuosity. Tortuosity was calibrated based on Method 1315 Na leaching (see Supplemental Information, SI-V and Figure S2). Chemical parameters used in the monolith diffusion model were the same as in the geochemical speciation model for simulating pH dependence batch testing, and the physical parameters are displayed in Table S4.

RESULTS AND DISCUSSIONS

Elemental composition and crystalline structure of Cast Stone

Primary elements (>5.00 wt.%) in Cast Stone were identified as Si, Ca, Al, Na, and Fe (Table S5). The mineral composition of the unleached CS-N-16w (Figure 1) was identified as mullite ($Al_6Si_2O_{13}$), quartz (SiO_2), hematite (Fe_2O_3), calcite ($CaCO_3$), tobermorite ($Ca_5Si_6O_{16}(OH)_2 \cdot 4H_2O$), tricalcium silicate ($Ca_3SiO_5$), and magnesite ($MgCO_3$). Some of the phases (i.e., mullite, quartz, and hematite) frequently reported in coal fly ash [48, 49] were directly from FAF because only a small part of fly ash in Cast Stone was likely to participate in hydration reactions [6]. Other identified minerals could be formed during the hydration of BFS and OPC.

Referring to the XRD results of Cast Stone from Chung, et al. [6] and Asmussen, et al. [4], the broad peak at 11° of 2θ is likely to be a mixture of calcium aluminate hydrates (AFm phases) including hemicarbonate ($Ca_4(Al(OH)_6)_2(OH)(CO_3)_{0.5} \cdot 5.5H_2O$) and monocarbonate ($Ca_4(Al(OH)_6)_2(CO_3) \cdot 6H_2O$) with a low degree of crystallization. Chung, et al. [5, 6] identified ettringite, stable at pH range of 10.50-12.00, in Cast Stone materials prepared with simulant containing Na at less than 2 mol/L. However, the additional alkalinity in the Cast Stone by adding LAW simulants with a Na concentration greater than 2 mol/L (e.g., 5 mol/L in this study) likely inhibited formation of ettringite and thus no ettringite peaks were observed by XRD for the materials studied here. Minerals bearing sodium and nitrate also were not detected here, but nitratine ($NaNO_3$) was identified by Branch [16]. Sodium could also have been incorporated into amorphous gels.

Aside from crystalline minerals, a majority of phases (*ca.* 83 wt.% according to studies of either Asmussen, et al. [4] or Branch [16]) in Cast Stone were not readily detected by XRD and considered amorphous. This fraction could be composed of glassly-like phases from FAF and amorphous calcium (alkali) aluminosilicate hydrate (CNASH) gel. During the pozzolanic reaction of alkali-activated Ca-rich cementitious materials (e.g., BFS), aluminum and sodium might have been incorporated within the structure of calcium silicate hydrate (CSH) gel to form CNASH gel [50].

Leaching at the natural pH (12.64) minimally altered the XRD detected minerals in Cast Stone based on the similarity of the XRD pattern after leaching compared to that before leaching (Figure 1). However, leaching at pH 4.00 changed the XRD-detected mineralogy of Cast Stone by: i) dissolving carbonate minerals such as calcite and magnesite and ii) forming gypsum ($CaSO_4 \cdot 2H_2O$). Gypsum was not detected in either unleached Cast Stone or leached Cast Stone at the natural pH because Ca in a strong alkaline environment (pH > 12.00) tends to form more thermodynamically stable phases such as CNASH gel rather than gypsum. The gradual disappearance of gypsum in Cast Stone was observed by Chung, et al. [5] as the alkalinity of the simulant increased. However, leaching of Cast Stone at pH 4.00 released Ca to form gypsum (Figure 1). Overall, leaching at alkaline (natural pH = 12.64) or acidic (pH = 4.00) conditions only slightly altered the crystalline structure of Cast Stone because of the relatively small fraction of minerals that were involved in leaching.

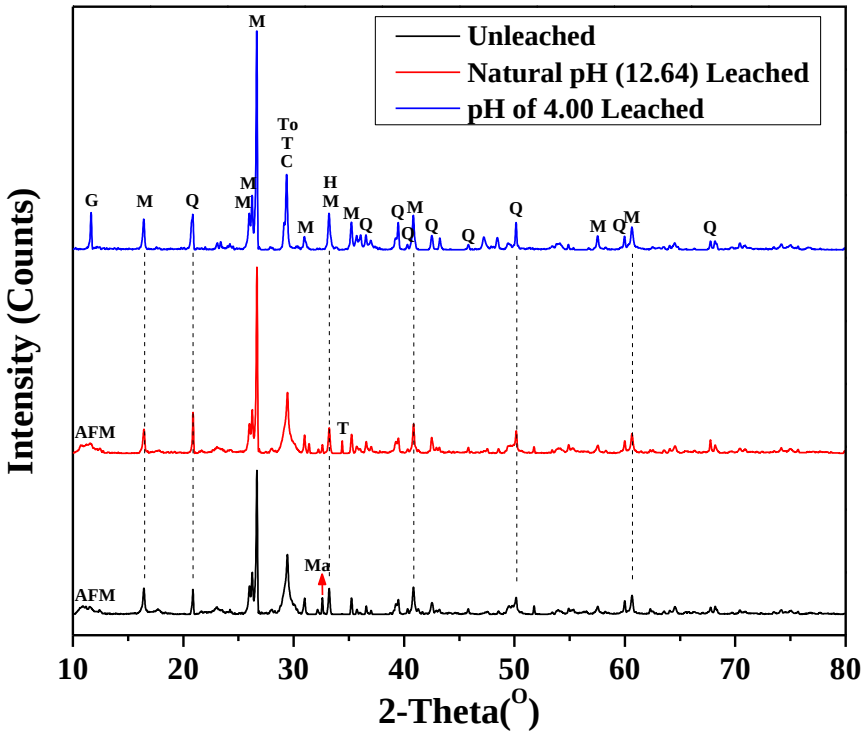

Figure A1 XRD patterns of original Cast Stone aged in N_2 and its residues after leaching carried out at natural pH of 12.64 and pH of 4.00.

(Legend: AFm-hemicarbonate ($Ca_4(Al(OH)_6)_2(OH)(CO_3)_{0.5} \cdot 5.5H_2O$) + monocarbonate ($Ca_4(Al(OH)_6)_2(CO_3) \cdot 6H_2O$);C- Calcite ($CaCO_3$); G- Gypsum ($CaSO_4 \cdot 2H_2O$); H- Hematite ($Fe_2O_3$); M- Mullite ($Al_6Si_2O_{13}$); Ma- Magnesite ($MgCO_3$); Q- Quartz ($SiO_2$); T- Tricalcium silicate (Ca_3SiO_5); To- Tobermorite ($Ca_5Si_6O_{16}(OH)_2 \cdot 4H_2O$))

Representative mineral set describing leaching of constituents from Cast Stone

The mineral assemblage proposed to represent the Cast Stone materials in this study is presented in Table S6, including consideration of the XRD results in Figure 1 and mineralogy characterization results of Cast Stone from Asmussen, *et al* [4]. The main reaction product of alkali-activated Ca-rich cementitious materials (e.g., BFS) is CNASH gel, represented as the ideal solid solution (CNASH_ss) developed and verified to describe the chemical compositions of alkali-activated slag cements by Myers, *et al* [47, 51]. Three CNASH_ss end-members from thermodynamic database of CEM18 (i.e., CEM18_INFCNA_CNASHss, CEM18_T2C_CNASHss, and CEM18_TobH_CNASHss) were included in the mineral set of this study. Not all eight proposed CNASH_ss end-members were included in the mineral set because Cast Stone is a more complicated mixture than the geopolymer for which CNASH_ss was developed and inclusion of the full set of CNASH_ss end-members resulted in a poorer prediction of leaching. Dolomite ($CaMg(CO_3)_2$), gaylussite ($Na_2Ca(CO_3)_2 \bullet 5H_2O$), nahcolite (NaHCO3), and natron (Na_2CO_3) were included based on a previous study on minerals in alkali-activated slag pastes [46].

Quartz and hematite (Figure A1) are unlikely to be in thermodynamic equilibrium with the eluates because of their kinetically-limited dissolution/precipitation [48], and thus they were replaced with amorphous silica (SiO_2) and ferrihydrite ($Fe_2O_3 \bullet 3H_2O$), respectively. Instead of gypsum ($CaSO_4 \bullet 2H_2O$), its formation precursor, hemihydrate ($CaSO_4 \bullet 0.5H_2O$) [52], was included in the mineral set because gypsum was found to under predict the solubility of sulfur. The formation of gypsum in leached CS-N-16w at pH 4.00 (Figure A1) could be attributed to the precipitation and crystallization of gypsum during the drying of leached Cast Stone. The chemical speciation of chromium and technetium was selected to be eskolaite, $NaTcO_4$, and $Tc(IV)O_2 \bullet 2H_2O$ to account for the solubility of Cr and Tc, respectively, as observed by Asmussen, et al. [4] through XAS and XANES.

The CO_2 losses from TGA on non-oxidized (CS-N-16w) and oxidized (CS-O-16w) Cast Stone material, 4.24 and 7.49 wt.% (0.96 and 1.70 mol/kg), respectively, were used to determine the upper limit of carbonate content in simulations (SI-III and Figure S3). The available contents of carbonate in CS-N-16w and CS-O-16w were calibrated as 0.60 and 1.09 mol/kg, respectively. The higher content of carbonate in CS-O-16w may be attributed to the heterogeneity of formulation materials (e.g., of BFS [53]), oxidation of organic matter during leaching (e.g., from addition of HNO_3), or inadvertent atmospheric carbonation during handling.

Geochemical speciation identification and verification for major constituents in Cast Stone

As shown in Figure A2a, the predicted acid neutralization capacity (ANC) curve by the geochemical speciation model agrees well with the experimental results at pH greater than 5.00, and the natural pH from the model (blue circles) is almost the same as the measured value (red circles). The modeled ANC values deviate from the experimental results at pH < 5.00, and the deviation increases as pH becomes more acidic. Theoretically, the acid buffering equilibrium is likely to be established by Al-bearing phases at pH less than approximately 4.00 [54], with corresponding increases in eluate concentrations. However, the observed concentration of Al is much less than expected, which can be the result of Al(III) entrapment in silica gel formed at low pH; more studies are required to address this discrepancy.

The leaching behaviors of the seven major constituents are well-described by the model (Figure A2a), indicating good representativeness of the proposed mineral set. Simulation results with the full set of CNASH_ss end-members did not provide as good predictions of test data compared to when only a partial set of end-members was used (Figure A2a). At alkaline pH from 9.00 to 14.00, the CNASH solid solution was formed by incorporating Ca, Si, Al, and Na, so CNASH_ss is a presumed major phase controlling the solubility of these elements at this pH range as indicated in Figure A2a. Leaching of Ca also was impacted by calcite above pH 6.00 given the abundance of carbonate present. At pH less than 9.00, CNASH_ss was dissolved and the liberated Si and Al recrystallized as amorphous silica (SiO_2) and diaspore (α-AlO(OH)), respectively. Other constituents such as Mg and Fe are predominantly controlled by brucite ($Mg(OH)_2$) and ferrihydrite, respectively. Although mullite was detected in Cast Stone (Figure A1), it is usually considered as a non-reactive mineral in aqueous solutions [55] and is not the major source of dissolved Al. The concentration of S in Method 1313 eluates is lower than the solubility described by hemihydrate and monosulfate, so the modeled concentrations of S are limited by the available content of S; more discussion regarding the chemical speciation of S will be presented later.

Although the selection of a mineral set for describing the pH-dependent leaching behavior of a constituent is under multiple constraints by simultaneously simulating a large set of elements at multiple pH conditions, multiple mineral and parameter sets may provide simulations that reasonably reflect experimental results; therefore, screening or verifying minerals under additional experimental conditions should be evaluated. Unlike pH-dependent leaching tests in which the liquid-solid partitioning of constituents reaches equilibrium at L/S of 10 mL/g, the pore water within the monolith during the monolith diffusion leaching test has a much lower equilibrium L/S that is dependent on porosity (e.g., 0.31 mL/g for CS-N-16w with a porosity of 0.41 and 0.23 mL/g for CS-N-9w with a porosity of 0.34). In addition, pH and pe within the monolith pore water are expected to be spatially and temporally variable, with the external eluent bath serving as the exposed surface boundary condition. Therefore, the performance of the selected mineral and

parameter set was verified by simulating the monolithic diffusion test results from Method 1315 (Figure A2b).

The monolithic diffusion model assumes local chemical equilibrium of solid with pore water and diffusion of species between adjacent finite element cells. The flux and the leaching concentration of Na were well simulated, indicating a good description of the physical retention properties of monolithic CS-N-16w. In addition, selected variables (i.e., pH, conductivity, and pe) and other constituents including K, S, Ca, Al, Si, and Fe are fairly well described by the model, which reflects that the chemical composition of pore water predicted by the selected minerals reasonably represents reality. Particularly for Mg, the model fails to predict leaching at early stage but matches concentrations at longer times. Thus, overall the proposed mineral set is deemed reasonable for describing the leaching of major constituents from Cast Stone.

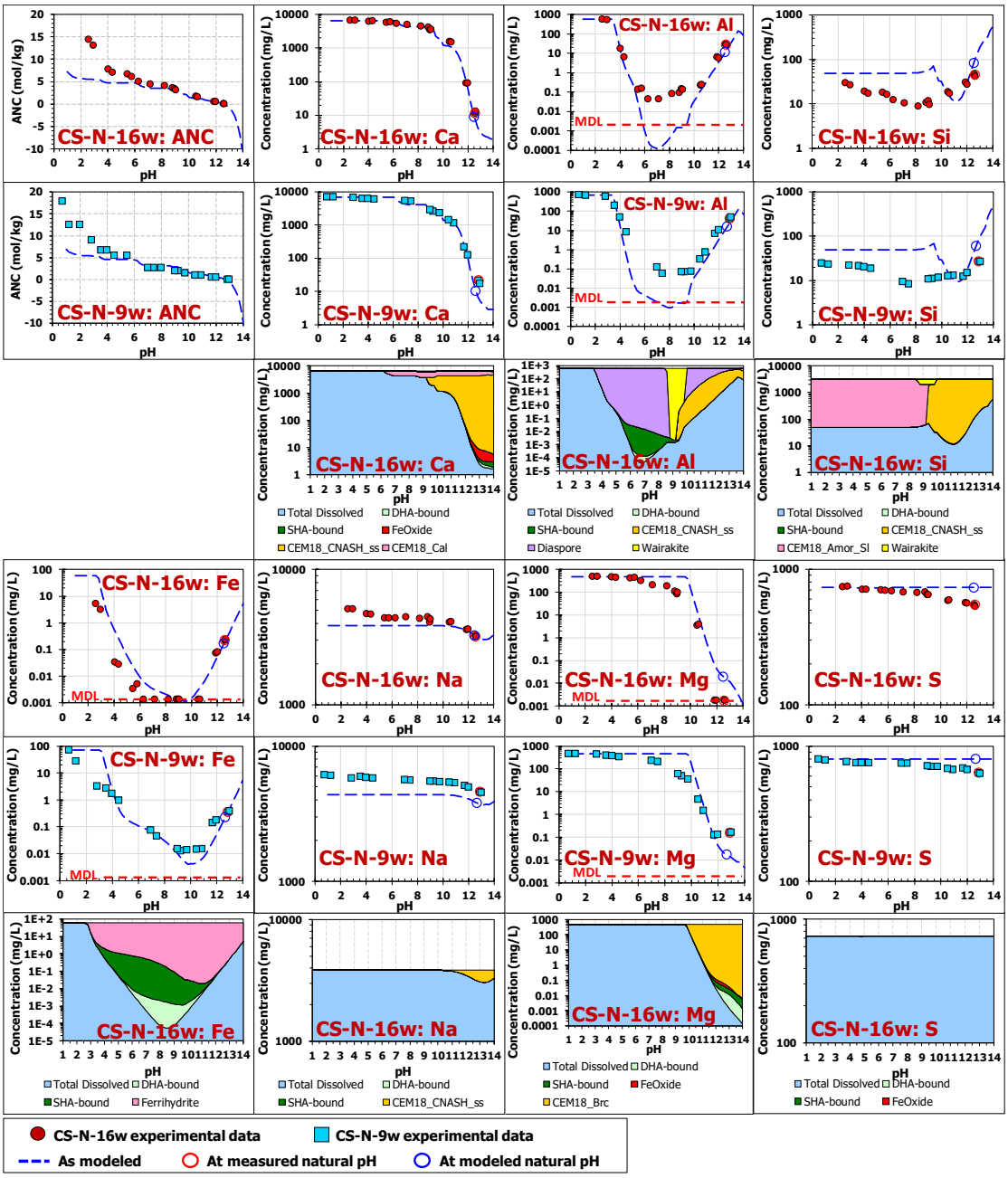

CEM18_CNASH_ss: prefix of "CEM18" indicates that the dissolution reaction constant (logK) of "CNASH_ss" is from thermodynamic database of CEM18; three CNASH_ss end-members are presented together as "CEM18_CNASH_ss" because they work together as an entity.

Figure A2a. Geochemical speciation modeling results of major constituents from granular CS-N-16w and CS-N-9w. (*Experimental data from duplicate tests were merged for each sample; and the phase diagrams for CS-N-9w are similar to that for CS-N-16w*)

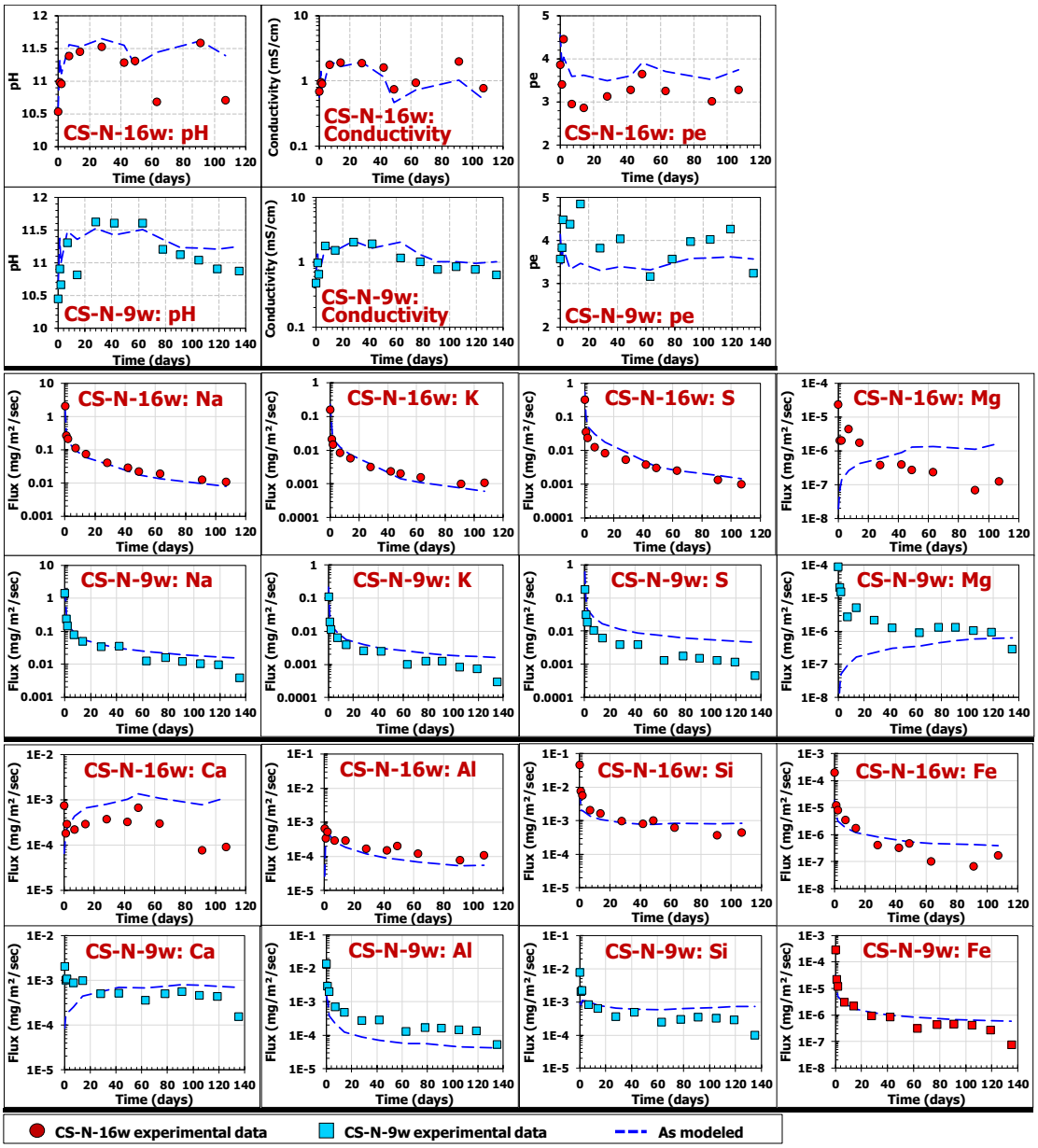

Figure A2b. Monolithic diffusion modeling results of variables and major constituents from monolithic CS-N-16w and CS-N-9w.

Impact of redox state changes on leaching of redox-sensitive constituents

In this study, Cr and S in Cast Stone serve as indicators to understand the redox state and mechanisms controlling leaching after aging in oxic and anoxic conditions. Also, Cr and S were used to provide insights into the progression of the oxidation front within the aged material and potential retention of Tc. Both Tc and Cr have substantially increased solubility and hence leachability when oxidized to form oxyanions (pertechnetate and chromate, respectively), albeit the standard half-cell potential of each reaction is

different (TcO_4^- and Tc^{4+}, -0.36 V; CrO_4^{2-} and Cr^{3+}, -0.13 V) making Tc possibly more recalcitrant to reduction and potentially more susceptible to oxidation than Cr at standard conditions (as reference, because actual experimental conditions are different).

Minerals responsible for the solubility of Cr in cementitious materials have been reported as $CaCrO_4 \cdot 2H_2O$, $Ca_2Cr_2O_5 \cdot 6H_2O$, Cr-ettringite ($3CaO \cdot Al_2O_3 \cdot 3CaCrO_4 \cdot 32H_2O$) and $Cr(OH)_3$ [56-58], which either significantly overpredict the pH-dependent eluate concentrations or are incapable of describing the leaching behavior in this study. The chemical speciation of Cr in Cast Stone doped with *ca.* 0.02 wt.% Cr was analyzed by XAS in a previous study [4], indicating presence of eskolaite (Cr_2O_3). So, eskolaite is likely a Cr-bearing mineral that controls leaching when Cr is present as Cr(III).

Laboratory redox measurements during leaching tests are considered unreliable because of sample handling and test conditions. Therefore, the pe values in the model (Table S7) has been calibrated based on the measured Cr concentration in eluates as illustrated in Figure S4. A segmentation fitting approach was used to specify the pe values subsequently used in geochemical speciation modeling (Figure S5). The agreement between pH-dependent leaching behaviors and modeling results of Cr (Figure 3a) for the four Cast Stone materials aged under inert and oxic conditions (doped with 0.1 or 0.2 wt.% Cr) supports eskolaite as the mineral controlling Cr leaching. Leaching results indicate some Cr immobilization at pH 5.50-13.00 in CS-N-16w and CS-N-9w, which is attributed to the reducing environment provided by BFS [22] and lower solubility of Cr(III) compared to Cr(VI) [28, 59]. However, aging in an oxidizing environment converted Cr(III) to Cr(VI) and decreased the Cr retention capacity of Cast Stone at pH above 5.50 for CS-O-16w and CS-O-9w (Figure A3a).

Cast Stone materials for the pH-dependent leaching test positions with eluate pH values lower than the natural pH were partially oxidized because of the nitric acid addition, which influenced the pH-dependent leaching concentration of Cr and may influence the calibrated mineral selected to account for the solubility of Cr. To verify the appropriate mineral selection, eskolaite also was used for simulation of results from monolith diffusion testing (Figures A3b) where only deoxygenated water was used as the eluant. The initial redox states of the monoliths referred to the natural pe values calibrated based on Method 1313 test results (Table S7). The flux of Cr from monoliths is well described by the model, and the simulated pe values of tank solutions are consistent with measured pe values. Thus, eskolaite was confirmed as the dominant mineral for Cr leaching in Cast Stone materials in the present study where Cr content has been increased.

Chemical speciation of S in Cast Stone is rarely studied but S speciation in BFS has been well investigated [23, 60], indicating most S is present as sulfides in BFS. Since oldhamite (CaS) decomposes upon contact with water, pyrrhotite (FeS) [24] was used to account for the solubility of S in its low valence state. With the pe

values calibrated based on measured S concentrations (Figure S6), the leaching behavior of S is well described but the modeling results for other redox-sensitive elements (i.e., Fe and Cr) deviate significantly from the experimental data. These results indicate that the slight decrease of S concentration at high pH is not because of the precipitation of sulfides, and redox states calibrated based on S concentrations are not representative for the leaching system.

The pH-dependent leaching behaviors of S, Fe, and Cr in BFS are well described by the model (Figure S7), and it is noted that S mostly exists as $S(VI)O_4^{2-}$. Therefore, even though S in BFS is mostly present as sulfides [23,60], the S is very susceptible to oxidation considering its low reduction potential (SO_4^{2-} and S^{2-}, -2.10 V) and the observed S leaching as sulfate. In leaching of Cast Stone, which is a more oxidizing system compared to BFS, chemical speciation of S partitioning into solution is likely to be SO_4^{2-}.

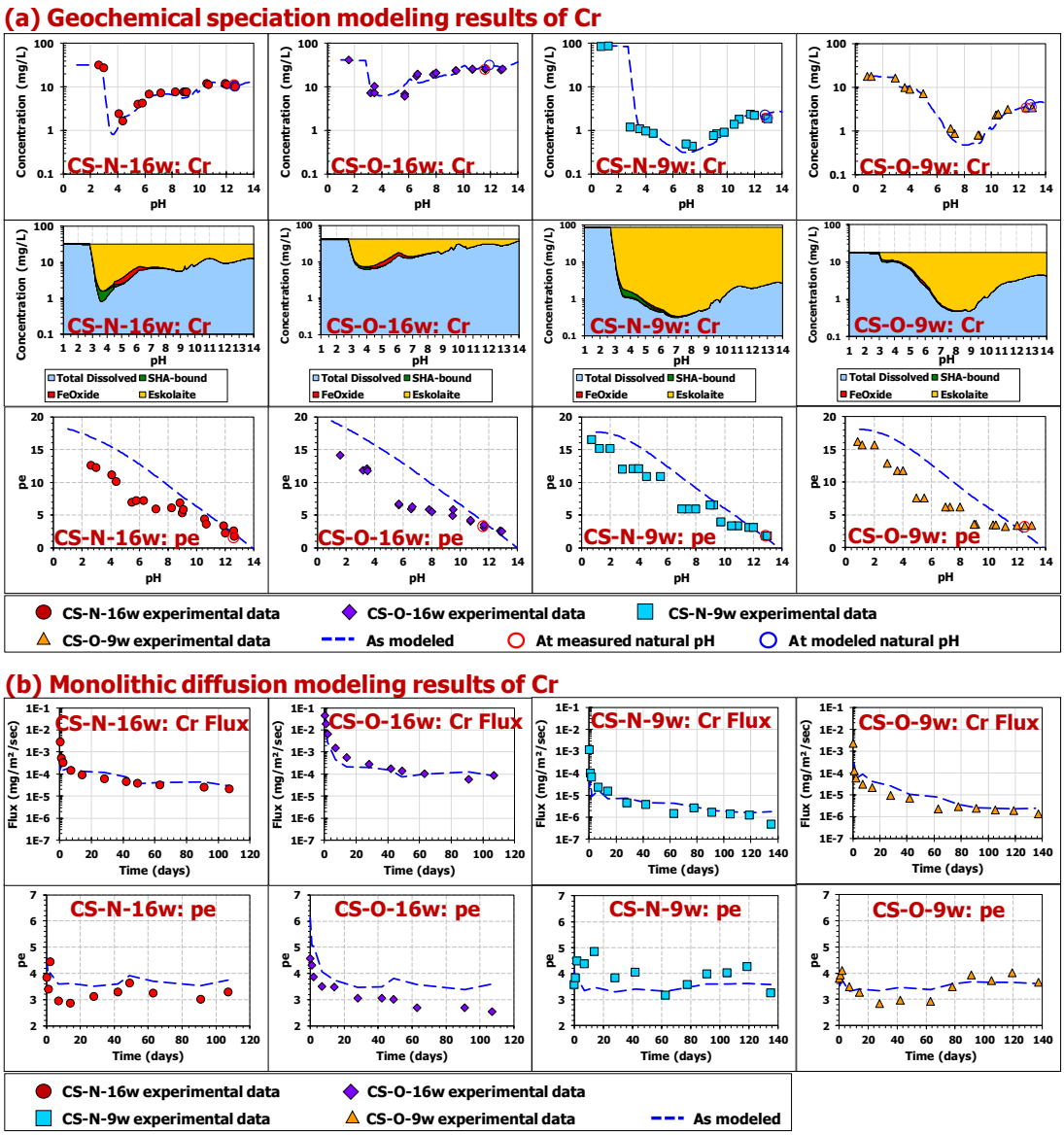

Figure A3. (a) Geochemical speciation modeling results of Cr; and (b) monolithic diffusion modeling results of Cr for four Cast Stone materials.

Implications for technetium leaching

To gain insights concerning Tc reduction and the impact of oxidation, redox states calibrated from the geochemical speciation modeling of both Cast Stone materials and BFS and estimated initial pH and pe within the monoliths under inert and oxic aging conditions, are projected on the predominance diagrams of Cr, Tc, Fe, and S (Figure A4). In addition, the redox state in Cast Stone of similar composition containing Tc-99 from the study of Um's (i.e., CS-T13) [61] was calibrated based on the monolithic diffusion leaching

behavior of Tc (Figure S8), and the calibrated redox state also is indicated in Figure A4. For the four Cast Stone materials, a slight increase in redox state was observed after oxidation but this barely impacted the pH-dependent leaching behaviors of Fe and S (Figure S9) because the calibrated pe values are within the region dominated by ferrihydrite and SO_4^{2-}, respectively.

The modeling results agree well with the pH-dependent leaching behaviors of redox-sensitive constituents of Cr, Fe, and S from both non-oxidized and oxidized Cast Stone materials (Figure A3a and S9). Also, the monolithic diffusion fluxes of Cr and Tc from Cast Stone materials with varied redox states and CS-T13 with lower redox state than Cast Stone, respectively, are well predicted by the model (Figure A3b and S8). Therefore, the developed geochemical speciation model is well capable in describing and predicting the leaching behavior of redox-sensitive constituents (e.g., Tc, Cr, Fe, and S) from Cast Stone materials with different redox states.

The redox states estimated in the monolith pore water and calibrated from 1313 tests for four Cast Stone materials are consistent (Figure A4) but not sufficient to reduce Tc (Figure A5). Under the redox states calibrated in CS-T13, TcO_4^- is able to be effectively reduced to Tc^{4+} and the leaching concentration of Tc is dramatically suppressed by the adsorption to the small amount solid organic matter (represented as humic acid, likely present from the fly ash component) over a wide range of pH as shown in Figure S9. The redox states in Cast Stone materials prepared for this study are less reduced than that in CS-T13, which might be attributed to the addition of Na_2CrO_4 or the unintentional exposure of samples to air.

The BFS is the main component responsible for the reductive capacity of Cast Stone, so the redox states indicated by BFS are much more reducing than those in Cast Stone materials (Figure A5) and are well capable of reducing TcO_4^- for immobilization. However, the reduction of TcO_4^- is a slow process at the scale of months or even years as observed by Lukens, *et al* [20]. This slow process may be the result of reduction of Tc occurring primarily at the surface of BFS particles, and therefore, the reduction rate of Tc is postulated to be controlled by the diffusive migration of soluble Tc in pore water to the surface of BFS particles.

The estimated initial pH and pe profiles of monolithic Cast Stone materials (Figure S10) indicate that the oxidation depth and degree for CS-O-16w are greater than those for CS-O-9w, because more reductive capacity was consumed for CS-O-16w with a higher load of Cr (0.2 wt.% CrO_4^{2-}) and a longer oxidation time (16 weeks) than for CS-O-9w (0.1 wt.% CrO_4^{2-} loading and 9 weeks of oxidation). The modeled flux and fractional cumulative release of Tc for CS-N-16w and CS-N-9w under the redox states calibrated either from BFS (pe ≈ -6.00) or from CS-T13 (pe ≈ -1.80) (Figure S11b) are much lower than that under the redox states calibrated based on the leaching behavior of Cr (pe ≈ 1.75 or 0.90, respectively) (Figure S11a),

indicating a good Tc immobilization capacity of both BFS and CS-T13 consistent with the results shown in Figures 4 and 5. However, shifting redox states of BFS or CS-T13 to those indicated by the oxidized front from CS-O-16w or CS-O-9w (pe ≈ 3.85 or 1.20, respectively) notably elevated the flux of Tc (Figure S11b). In addition, oxidation appeared to decrease the physical retention ability of the material indicated by lower tortuosity comparing CS-O-16w with CS-N-16w (Tables S4), resulting in an increased flux of Tc from CS-O-16w compared to CS-N-16w.

The application of the developed geochemical speciation model for evaluating the leaching from Cast Stone materials under anticipated field conditions needs to consider additional factors. Under field conditions, disposed Cast Stone will come into contact with water where the composition, pH, and redox state will be influenced by overburden and infill materials (e.g., soils) and co-disposed wastes, in contrast to the deionized water used in this study. The effective diffusivity of ions will be influenced by the physical properties of Cast Stone including porosity and tortuosity as disposed, which may differ from laboratory prepared samples. Also under field disposal conditions, the degree of water saturation, intermittent wetting, and the amount of oxygen and carbon dioxide or carbonate present in pore water and gas-filled pores will vary.

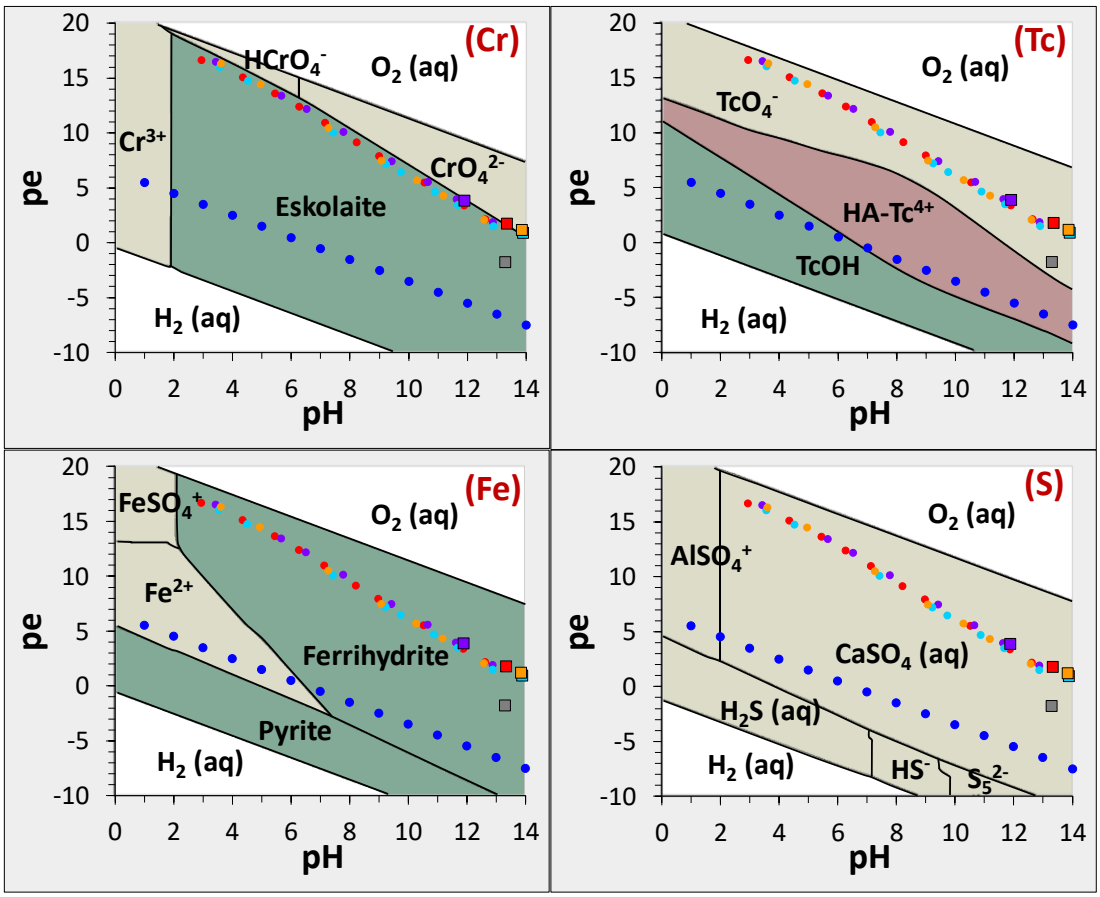

Calibrated redox states in pH-dependent leaching tests for CS-N-16w (●), CS-O-16w (●), CS-N-9w (●), CS-O-9w (●), and BFS (●);
Estimated initial redox states of porewater for monolithic CS-N-16w (■), oxidized region of CS-O-16w (■), monolithic CS-N-9w (■), oxidized region of CS-O-9w (■), and monolithic CS-T13 (■).

aq: aqueous phase;

HA-Tc^{4+}: Tc adsorbed onto humic acid as Tc^{4+}.

Figure A4. Predominance diagrams of Cr, Tc, Fe, and S with calibrated redox states projected.

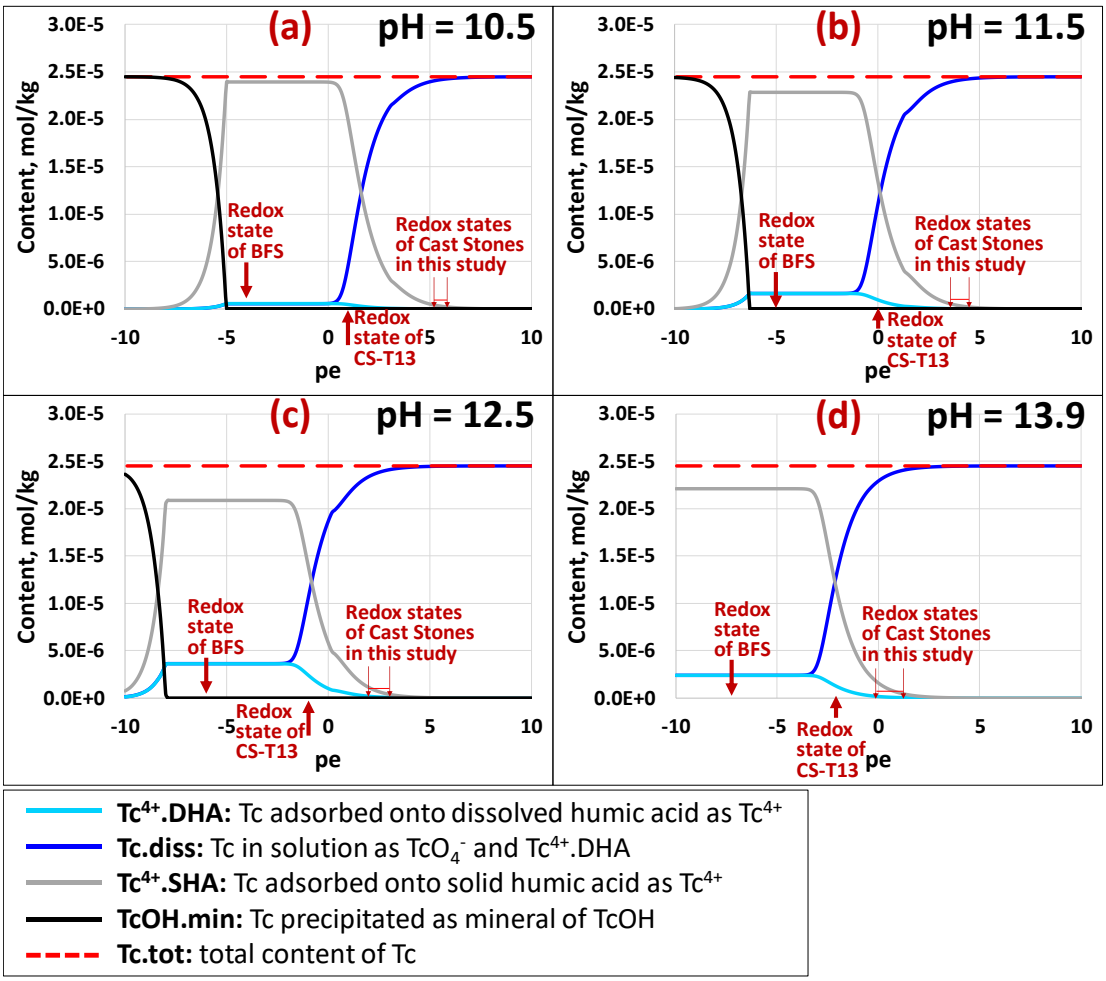

Note: pe of CS-T13 at different pH values is derived by fixing the value of pH+pe as 11.5 as shown in Figure S8.

Figure A5. Variation of chemical speciation of Tc as a function of pe at different pH values.

REFERENCES

1. El-Kamash, A.; El-Naggar, M.; El-Dessouky, M., Immobilization of cesium and strontium radionuclides in zeolite-cement blends. Journal of Hazardous Materials 2006, 136, (2), 310-316.
2. Dezerald, L.; Kohanoff, J. J.; Correa, A. A.; Caro, A.; Pellenq, R. J.-M.; Ulm, F. J.; Saúl, A. s., Cement as a waste form for nuclear fission products: the case of 90Sr and its daughters. Environmental Science & Technology 2015, 49, (22), 13676-13683.
3. Lockrem, L. L., Cast stone technology for treatment and disposal of iodine rich caustic waste demostration- final report, No. RPP-RPT-26725, Rev. 0. CH2M: 2005.
4. Asmussen, R. M.; Lawter, A. R.; Stephenson, J. R.; Bowden, M. E.; Washton, N. M.; Neeway, J. J.; Du, Y.; Pearce, C. I.; Clayton, R. E.; Saslow, S. A., Getter Incorporation into Cast Stone and Solid State Characterizations, No. PNNL-25577 Rev. 0; RPT-SLAW-003 Rev A. Pacific Northwest National Lab.(PNNL), Richland, WA (United States), 2016.
5. Chung, C.-W.; Chun, J.; Um, W.; Sundaram, S.; Westsik Jr, J. H., Setting and stiffening of cementitious components in Cast Stone waste form for disposal of secondary wastes from the Hanford waste treatment and immobilization plant. Cement and Concrete Research 2013, 46, 14-22.
6. Chung, C.-W.; Um, W.; Valenta, M. M.; Sundaram, S.; Chun, J.; Parker, K. E.; Kimura, M. L.; Westsik Jr, J. H., Characteristics of Cast Stone cementitious waste form for immobilization of secondary wastes from vitrification process. Journal of Nuclear Materials 2012, 420, (1-3), 164-174.
7. Ashraf, W., Carbonation of cement-based materials: challenges and opportunities. Construction and Building Materials 2016, 120, 558-570.
8. Šavija, B.; Luković, M., Carbonation of cement paste: Understanding, challenges, and opportunities. Construction and Building Materials 2016, 117, 285-301.
9. Branch, J.; Kosson, D.; Garrabrants, A.; He, P., The impact of carbonation on the microstructure and solubility of major constituents in microconcrete materials with varying alkalinities due to fly ash replacement of ordinary Portland cement. Cement and Concrete Research 2016, 89, 297-309.
10. Garrabrants, A.; Sanchez, F.; Kosson, D., Changes in constituent equilibrium leaching and pore water characteristics of a Portland cement mortar as a result of carbonation. Waste Management 2004, 24, (1), 19-36.
11. Huijgen, W. J.; Comans, R. N., Carbonation of steel slag for CO2 sequestration: leaching of products and reaction mechanisms. Environmental Science & Technology 2006, 40, (8), 2790-2796.
12. Meena, A. H.; Kaplan, D. I.; Powell, B. A.; Arai, Y., Chemical stabilization of chromate in blast furnace slag mixed cementitious materials. Chemosphere 2015, 138, 247-252.
13. Bertos, M. F.; Simons, S.; Hills, C.; Carey, P., A review of accelerated carbonation technology in the treatment of cement-based materials and sequestration of CO2. Journal of Hazardous Materials 2004, 112, (3), 193-205.
14. Kosson, D. S.; van der Sloot, H. A.; Sanchez, F.; Garrabrants, A. C., An integrated framework for evaluating leaching in waste management and utilization of secondary materials. Environmental Engineering Science 2002, 19, (3), 159-204.
15. Van der Sloot, H.; Kosson, D.; Van Zomeren, A., Leaching, geochemical modelling and field verification of a municipal solid waste and a predominantly non-degradable waste landfill. Waste Management 2017, 63, 74-95.
16. Branch, J. L., Impact of Aging in the Presence of Reactive Gases on Cementitious Waste Forms and Barriers. ProQuest Dissertations Publishing, 2018.
17. Asmussen, R. M.; Pearce, C. I.; Miller, B. W.; Lawter, A. R.; Neeway, J. J.; Lukens, W. W.; Bowden, M. E.; Miller, M. A.; Buck, E. C.; Serne, R. J., Getters for improved technetium containment in cementitious waste forms. Journal of Hazardous Materials 2018, 341, 238-247.
18. Um, W.; Chang, H.-S.; Icenhower, J. P.; Lukens, W. W.; Serne, R. J.; Qafoku, N. P.; Westsik Jr, J. H.; Buck, E. C.; Smith, S. C., Immobilization of 99-technetium (VII) by Fe (II)-goethite and limited reoxidation. Environmental Science & Technology 2011, 45, (11), 4904-4913.

19. Masters-Waage, N. K.; Morris, K.; Lloyd, J. R.; Shaw, S.; Mosselmans, J. F. W.; Boothman, C.; Bots, P.; Rizoulis, A.; Livens, F. R.; Law, G. T., Impacts of repeated redox cycling on technetium mobility in the environment. Environmental Science & Technology 2017, 51, (24), 14301-14310.
20. Lukens, W. W.; Bucher, J. J.; Shuh, D. K.; Edelstein, N. M., Evolution of technetium speciation in reducing grout. Environmental Science & Technology 2005, 39, (20), 8064-8070.
21. Allan, M.; Kukacka, L., Blast furnace slag-modified grouts for in situ stabilization of chromium-contaminated soil. Waste Management 1995, 15, (3), 193-202.
22. Özbay, E.; Erdemir, M.; Durmuş, H. İ., Utilization and efficiency of ground granulated blast furnace slag on concrete properties–A review. Construction and Building Materials 2016, 105, 423-434.
23. Roy, A., Sulfur speciation in granulated blast furnace slag: An X-ray absorption spectroscopic investigation. Cement and Concrete Research 2009, 39, (8), 659-663.
24. Schwab, A.; Hickey, J.; Hunter, J.; Banks, M., Characteristics of blast furnace slag leachate produced under reduced and oxidized conditions. Journal of Environmental Science and Health Part A 2006, 41, (3), 381-395.
25. Sandino, M. A.; Östbols, E., Chemical thermodynamics of technetium. Elsevier: 1999.
26. Bard, A. J.; Ketelaar, J., Encyclopedia of Electrochemistry of the Elements. Journal of The Electrochemical Society 1974, 121, (6), 212C-212C.
27. Saslow, S. A.; Um, W.; Pearce, C. I.; Bowden, M. E.; Engelhard, M. H.; Lukens, W. L.; Kim, D.-S.; Schweiger, M. J.; Kruger, A. A., Cr (VI) Effect on Tc-99 Removal from Hanford Low-Activity Waste Simulant by Ferrous Hydroxide. Environmental Science & Technology 2018, 52, (20), 11752-11759.
28. Liao, W.; Ye, Z.; Yuan, S.; Cai, Q.; Tong, M.; Qian, A.; Cheng, D., Effect of Coexisting Fe (III)(oxyhydr) oxides on Cr (VI) Reduction by Fe (II)-Bearing Clay Minerals. Environmental Science & Technology 2019, 53, (23), 13767-13775.
29. Russell, R. L.; Westsik, J. H.; Swanberg, D. J.; Eibling, R. E.; Cozzi, A.; Lindberg, M. J.; Josephson, G. B.; Rinehart, D. E., Letter Report: LAW Simulant Development for Cast Stone Screening Test, No. PNNL-22352. Pacific Northwest National Lab.(PNNL), Richland, WA (United States), 2013.
30. US EPA, Method 1313: Liquid Solid Partitioning as a Function of Extract pH using a Parallel Batch Extraction Procedure, 2012.
31. Kosson, D. S.; Garrabrants, A. C.; DeLapp, R.; van der Sloot, H. A., pH-dependent leaching of constituents of potential concern from concrete materials containing coal combustion fly ash. Chemosphere 2014, 103, 140-147.
32. Thorneloe, S. A.; Kosson, D. S.; Sanchez, F.; Garrabrants, A. C.; Helms, G., Evaluating the fate of metals in air pollution control residues from coal-fired power plants. Environmental Science & Technology 2010, 44, (19), 7351-7356.
33. US EPA, Method 1315—Mass transfer rates of constituents in monolithic or compacted granular materials using a semi-dynamic tank leaching procedure. Test methods for evaluating solid waste, physical/chemical methods 2013.
34. Garrabrants, A. C.; Kosson, D. S.; DeLapp, R.; van der Sloot, H. A., Effect of coal combustion fly ash use in concrete on the mass transport release of constituents of potential concern. Chemosphere 2014, 103, 131-139.
35. US EPA, Method 6010C: Inductively coupled plasma-atomic emission spectrometry 3, 2007.
36. US EPA, SW-846 Test Method 9056A: Determination of Inorganic Anions by Ion Chromatography, 2007.
37. Garrabrants, A.; DeLapp, R.; Branch, J.; Brown, K.; Kosson, D., Cast stone materials: porosity determination and relativehumidity–saturation relationship. Consortium for Risk Evaluation with Stakeholder Participation report 2016.
38. Meeussen, J. C., ORCHESTRA: An object-oriented framework for implementing chemical equilibrium models. Environmental Science & Technology 2003, 37, (6), 1175-1182.
39. EPA, M.; PRODEFA, A., Geochemical Assessment Model for Environmental Systems: User Manual Supplement for Version 4.0. US EPA, National Exposure Research Laboratory, Ecosystems Research Division, Athens, Georgia 1998.

40. Lothenbach, B.; Kulik, D. A.; Matschei, T.; Balonis, M.; Baquerizo, L.; Dilnesa, B.; Miron, G. D.; Myers, R. J., Cemdata18: A chemical thermodynamic database for hydrated Portland cements and alkali-activated materials. Cement and Concrete Research 2019, 115, 472-506.
41. Delany, J.; Lundeen, S., The LLNL thermochemical database. Lawrence Livermore National Laboratory Report UCRL-21658 1990, 150.
42. Kinniburgh, D. G.; van Riemsdijk, W. H.; Koopal, L. K.; Borkovec, M.; Benedetti, M. F.; Avena, M. J., Ion binding to natural organic matter: competition, heterogeneity, stoichiometry and thermodynamic consistency. Colloids and Surfaces A: Physicochemical and Engineering Aspects 1999, 151, (1-2), 147-166.
43. Milne, C. J.; Kinniburgh, D. G.; Tipping, E., Generic NICA-Donnan model parameters for proton binding by humic substances. Environmental Science & Technology 2001, 35, (10), 2049-2059.
44. Milne, C. J.; Kinniburgh, D. G.; Van Riemsdijk, W. H.; Tipping, E., Generic NICA− Donnan model parameters for metal-ion binding by humic substances. Environmental Science & Technology 2003, 37, (5), 958-971.
45. Dzombak, D. A.; Morel, F. M., Surface complexation modeling: hydrous ferric oxide. John Wiley & Sons: 1990.
46. Bernal, S. A.; Provis, J. L.; Brice, D. G.; Kilcullen, A.; Duxson, P.; van Deventer, J. S., Accelerated carbonation testing of alkali-activated binders significantly underestimates service life: The role of pore solution chemistry. Cement and Concrete Research 2012, 42, (10), 1317-1326.
47. Myers, R. J.; Lothenbach, B.; Bernal, S. A.; Provis, J. L., Thermodynamic modelling of alkali-activated slag cements. Applied Geochemistry 2015, 61, 233-247.
48. Hareeparsad, S.; Tiruta-Barna, L.; Brouckaert, C. J.; Buckley, C. A., Quantitative geochemical modelling using leaching tests: application for coal ashes produced by two South African thermal processes. Journal of Hazardous Materials 2011, 186, (2-3), 1163-1173.
49. Ilic, M.; Cheeseman, C.; Sollars, C.; Knight, J., Mineralogy and microstructure of sintered lignite coal fly ash☆. Fuel 2003, 82, (3), 331-336.
50. Myers, R. J.; Bernal, S. A.; San Nicolas, R.; Provis, J. L., Generalized structural description of calcium–sodium aluminosilicate hydrate gels: the cross-linked substituted tobermorite model. Langmuir 2013, 29, (17), 5294-5306.
51. Myers, R. J.; Bernal, S. A.; Provis, J. L., A thermodynamic model for C-(N-) ASH gel: CNASH_ss. Derivation and validation. Cement and Concrete Research 2014, 66, 27-47.
52. Van Driessche, A.; Benning, L.; Rodriguez-Blanco, J.; Ossorio, M.; Bots, P.; García-Ruiz, J., The role and implications of bassanite as a stable precursor phase to gypsum precipitation. Science 2012, 336, (6077), 69-72.
53. Rondón-Quintana, H. A.; Ruge-Cárdenas, J. C.; Patiño-Sánchez, D. F.; Vacca-Gamez, H. A.; Reyes-Lizcano, F. A.; Muniz de Farias, M., Blast furnace slag as a substitute for the fine fraction of aggregates in an asphalt mixture. Journal of Materials in Civil Engineering 2018, 30, (10), 04018244.
54. Kostura, B.; Kulveitova, H.; Leško, J., Blast furnace slags as sorbents of phosphate from water solutions. Water Research 2005, 39, (9), 1795-1802.
55. Izquierdo, M.; Querol, X., Leaching behaviour of elements from coal combustion fly ash: an overview. International Journal of Coal Geology 2012, 94, 54-66.
56. Halim, C. E.; Scott, J. A.; Natawardaya, H.; Amal, R.; Beydoun, D.; Low, G., Comparison between acetic acid and landfill leachates for the leaching of Pb (II), Cd (II), As (V), and Cr (VI) from cementitious wastes. Environmental Science & Technology 2004, 38, (14), 3977-3983.
57. Macias, A.; Kindness, A.; Glasser, F., Impact of carbon dioxide on the immobilization potential of cemented wastes: chromium. Cement and Concrete Research 1997, 27, (2), 215-225.
58. Guo, B.; Liu, B.; Yang, J.; Zhang, S., The mechanisms of heavy metal immobilization by cementitious material treatments and thermal treatments: A review. Journal of Environmental Management 2017, 193, 410-422.

59. Shevchenko, N.; Zaitsev, V.; Walcarius, A., Bifunctionalized mesoporous silicas for Cr (VI) reduction and concomitant Cr (III) immobilization. Environmental Science & Technology 2008, 42, (18), 6922-6928.
60. Arai, Y.; Powell, B. A.; Kaplan, D. I., Sulfur speciation in untreated and alkali treated ground-granulated blast furnace slag. Science of The Total Environment 2017, 589, 117-121.
61. Um, W.; Williams, B. D.; Snyder, M. M. V.; Wang, G., Liquid Secondary Waste Grout Formulation and Waste Form Qualification, No. PNNL-25129; RPT-SWCS-005, REV0. Pacific Northwest National Lab.(PNNL), Richland, WA (United States), 2016.

Supporting Information for

Development of a Geochemical Speciation Model for Use in Evaluating Leaching from a Cementitious Low Activity Waste Form

NOMENCLATURE

Amor/am	Amorphous
ANC	Acid neutralization capacity
BFS	Blast furnace slag
Brc	Brucite
C3S	Tricalcium silicate
Cal	Calcite
CEM18	Cemdata18
CNASH	Calcium (alkali) aluminosilicate hydrate
CNASH_ss	Calcium (alkali) aluminosilicate hydrate ideal solid solution
COPCs	Constituents of potential concern
CS-N-9w	Cast Stone (0.1 wt.% Cr doped) aged in nitrogen under 65 % RH for 9 weeks
CS-O-9w	Cast Stone (0.1 wt.% Cr doped) aged in air with CO_2 removed under 65 % RH for 9 weeks
CS-N-16w	Cast Stone (0.2 wt.% Cr doped) aged in nitrogen under 68 % RH for 16 weeks
CS-O-16w	Cast Stone (0.2 wt.% Cr doped) aged in air with CO_2 removed under 68 % RH for 16 weeks
CSH	Calcium silicate hydrate
Dol	Dolomite
dw	Dry weight
EPA	Environmental Protection Agency
FA	Fly ash
FAF	Class F fly ash
HA	Humic acid
HFO	Hydrous ferric oxides
HTWOS	Hanford Tank Waste Operational System
IC	Ion chromatography
ICP-OES	Inductively-coupled plasma-optical emission spectroscopy
K_{sp}	The solubility product constant
L/S	Liquid-solid ratio, mL/g
LAW	Low activity radioactive waste
LLOQ	Lower limit of quantification, mg/L
logK	Log_{10} of dissolution reaction constants
Mgs	Magnesite
MDL	Method detection limit, mg/L
OPC	Ordinary Portland cement
Ord	Ordered
ORP	Oxidation-reduction potential
PNNL	Pacific Northwest National Laboratory
QA	Quality assurance
QC	Quality control
RH	Relative humidity
Si	Silica

SRNL	Savannah River National Laboratory
TGA	Thermogravimetric analysis
TIC	Total inorganic carbon
XAS	X-ray adsorption spectroscopy
XANES	X-ray absorption near edge spectroscopy
XRD	X-ray diffraction
XRF	X-ray fluorescence

I. pe calculation from oxidation-reduction potential (ORP)

ORP values were measured with an Ag/AgCl probe at room temperature (20 °C), and the redox potential (Eh) was calculated by adding ORP voltage and a probe-specific correction factor of 228 mV at 20 °C. Then, the pe values of eluates were calculated as:

$$pe = \frac{F}{2.303RT}(Eh/1000) \qquad (1)$$

Where F is the Faraday constant (23,061 cal/(V mol)); Eh is the redox potential of the solution (mV); 2.303 is a conversion ($\ln[e^-]/2.303 \log[e^-]$); R is the gas constant (1.987 cal/(K mol)); T is the temperature (K), and 1000 is a units conversion (1,000 mV = 1 V).

II. Quality assurance (QA) and quality control (QC) procedures for ICP-OES and IC measurements

ICP-OES: Analytical QA/QC included initial and continuing calibration checks and blanks, matrix spikes, and method blanks. Calibration check standards and matrix blanks were evaluated every 10 to 20 samples with check standards required to be within 15% of the specified value and blanks required to be less than lower limits of quantification (LLOQs). Matrix spikes were required to have recoveries within 20% of the calculated concentration considering the spiked mass. Initial and continuing calibration check standards for ICP-OES were at 0.5 mg/L. Analyte concentrations measured at less than the method detection limit (MDL) were reported and graphed at the MDL values to indicate that the measurement was carried out. Analytical results measured at less than the LLOQ but greater than the MDL are estimated values.

IC: Analytical QA/QC included initial and continuing calibration checks and blanks, matrix spikes, and method blanks. Calibration check standards were required to be within 15% of the specified value, while acceptable analytical blanks were measured below the quantification limits.

III. Procedures of thermogravimetric analysis (TGA)

TGA: A TA Instruments Q600 SDT analyzer (New Castle, Delaware, USA) was used to analyze the content of carbonate minerals in Cast Stone. Prior to analysis, the TGA chamber was initially equilibrated at a temperature of 30 °C. For each sample analysis, approximately 25 mg was heated from 30 °C to 1000 °C at a rate of 10.0 °C/min, with a continuous flow of nitrogen at 100 mL/min^{-1} during the heating process. The mass fraction of carbonate minerals was quantified as the mass loss in the temperature range between 500 °C to 1000 °C according to the literature [1].

IV. Calibration of mineral set and available contents of Si and carbonate

The dissolution of Si was assumed kinetically controlled and not near thermodynamic equilibrium after 48 hours of leaching, so the Si available content was calibrated to get the best fit of the Ca leaching curve at pH > 9.00. The calibrated available content of Si is 2-3 times greater than the maximum measured value from Method 1313 but only accounts for less than 40 wt.% of the total Si content. The available content of carbonate was calibrated against the leaching behavior of Ca at a pH range of 6.00-9.00; the upper limit on carbonate content is based on the measured total carbonates by TGA.

To select the mineral assemblage, minerals identified by XRD, XAS, and XANES analysis of Cast Stone, from this work and from other studies [2-5], were collected as a preliminary mineral set for screening. Minerals characterized and solid solutions developed from alkali-activated slag [6, 7], which was used for Cast Stone preparation, were also included in the preliminary mineral set. Then, minerals from the preliminary mineral set were verified in the geochemical speciation model to remove minerals providing poor descriptions of the measurements. Additionally, some minerals not from the preliminary mineral set were iteratively selected and evaluated to determine if they provided an improved description of pH-dependent leaching behavior. The goodness of fit was based on minimizing the residuals between model predictions and experimentally measured eluate concentrations. After the above steps, the phases remaining constituted the selected mineral set.

For each constituent, the log-squared residual between the pH-dependent leaching concentration (C_e) and modeled result (C_m) at each pH point over the pH range of interest was calculated and then summed according to the following equation to get the summed log-squared residuals (logRSS):

$$logRSS = \sum (\log\left(\frac{C_m}{C_e}\right))^2$$

The pH range of interest was decided by the highest and lowest extract pH from pH-dependent leaching tests. Experimental data below MDL were excluded from residuals calculation.

V. Tortuosity calibration using sodium

The effective diffusivity of each constituent is controlled by physical parameters including porosity (the fraction of the volume of voids over the total volume), skeletal density of monolithic samples, relative saturation (ratio of the volume of pore solution to the volume of voids), and tortuosity (the property of a path being tortuous and used to describe diffusion and fluid flow in porous media). During the monolithic diffusion modeling, porosity and skeletal density were assumed to be constant. Besides, each cell was assumed to reach a fully-saturated state quickly during the EPA Method 1315 test and so the saturation was assumed to be constant at 1.0 for every cell from the beginning of the simulation.

The tortuosity for each cell was calibrated based on the effective diffusivity of sodium measured from Method 1315 test, because Na-bearing minerals are highly soluble and the concentration of Na in the tank is dominated by the diffusion process. Since Na is a dominant ion in system, calibrating tortuosity with Na would diminish uncertainties caused by measurement and heterogeneity of materials. During calibration, the tortuosity values were adjusted to yield the minimum sum log-squared residual of the experimental versus modeled Na flux. The final tortuosity values for four samples are displayed in Table S4; the comparison between measured and simulated Na flux is shown in Figure S2.

VI. pe calibration based on the pH-dependent leaching behavior of Cr and S

pe calibration based on Cr leaching:

The assumed reactions relevant to Cr leaching are shown as reactions (2) and (3), from which the pe value of the leaching system was estimated based on the measured Cr concentration and the method details are as follows: at a given pH, the concentration of Cr^{3+}(aq) was calculated from reaction (3) with activity coefficient of Cr^{3+}(aq) calculated by the modified Davies model [8]; then, the concentration of CrO_4^{2-}(aq) was derived by subtracting the calculated Cr^{3+}(aq) concentration from the measured total soluble concentration of Cr; with the concentration of Cr^{3+}(aq) and CrO_4^{2-}(aq), their chemical activities were calculated and so the reduction potential of half-cell reaction (2) was derived from the Nernst equation (4); finally, the estimated pe value of the leaching system was obtained by converting the reduction potential of half-cell reaction (2) to pe through Eq. (1).

$$CrO_4^{2-}(aq) + 8H^+(aq) + 3e^- \rightarrow Cr^{3+}(aq) + 4H_2O \qquad (2)$$

$$2Cr^{3+}(aq) + 3H_2O \rightarrow Cr_2O_3(s) + 6H^+(aq) \qquad (3)$$

$$E_{red} = E_{red}^{\theta} - \frac{RT}{zF}\ln\frac{a_{Red}}{a_{Ox}} \qquad (4)^*$$

*Nernst equation for half-cell reaction; logK (reaction 2) = 77.64; logK (reaction 3) = 7.76; *aq*: aqueous phase; *s*: solid phase; E_{red}: the half-cell reduction potential at 20 °C (V); E_{red}^{Θ}: the standard half-cell reduction potential (-0.13 V for reaction (2)); *R*: the universal gas constant (8.314 J/(K mol)); *T*: the temperature (K); *z*: the number of electrons transferred in the half-cell reaction; *F*: the Faraday constant (96485 C/mol); a_{Red}: the chemical activity of species in reduced form; a_{Ox}: the chemical activity of species in oxidized form.

The pe value of the leaching system can be directly estimated based on the measured total soluble Cr concentration as described above, but the geochemical speciation model works in a reverse direction, i.e., the model calculates the leaching concentration of Cr based on the inputted pe value. Besides the precipitation/ dissolution reactions, the model also includes the calculation of Cr adsorption onto the surface of hydrous ferric oxides and organic matter. Therefore, the pe value of the leaching system was estimated by calibrating the pe to fit the measured Cr concentration with the modeling result. For example, to get the calibrated pe value for CS-N-16w at pH 11.9, the pH in the LeachXS/ORCHESTRA model was fixed at 11.9 (Figure S4c) and pe was varied from 0 to 4 (Figure S4b). It was found that the Cr concentration at pe 3.35 (Figure S4b) was equal to the measured concentration in Figure S4a, so the value of calibrated pe at pH 11.9 for CS-N-16w was 3.35. The calibrated pe values are shown in Table S7 for four samples and the geochemical speciation modeling results of Cr are presented in Figure 3a of the paper.

pe calibration based on S leaching:

The solubility of S at reducing conditions is assumed to be controlled by Pyrrhotite (FeS) [9]. So, the assumed reactions relevant to S leaching are shown as reactions (5) through (8). Similar to the method described above for Cr, the pe value of the leaching system can be estimated by simultaneously solving these equations together with the corresponding Nernst equation (equation (4)) in the basis of the measured total soluble S concentration.

$$Fe^{3+}(aq) + e^- \rightarrow Fe^{2+}(aq) \qquad (5)$$

$$SO_4^{2-}(aq) + 8H^+ + 8e^- \rightarrow S^{2-}(aq) + 4H_2O \quad (6)$$

$$Fe^{3+}(aq) + 3H_2O \rightarrow Fe(HO)_3(s) + 3H^+ \quad (7)$$

$$Fe^{2+}(aq) + S^{2-}(aq) \rightarrow FeS(s) \quad (8)$$

logK (reaction 5) = 13.03; logK (reaction 6) = 21.88; logK (reaction 7) = -3.19; logK (reaction 8) = 16.65; *aq*: aqueous phase; *s*: solid phase; E_{red}^{Θ} (reaction 5) = 0.77 V; E_{red}^{Θ} (reaction 6) = -2.1 V.

Since the geochemical speciation model works in the way of calculating the leaching concentration of S based on the inputted pe value, the pe value of the leaching system was estimated by calibrating the pe to fit the measured S concentration with the modeling result. The calibration method is similar to that described in Figure S4. To get the calibrated pe at a given pH, the pH is fixed, then the pe value is varied within a reasonable range to capture the measured S concentration at the given pH. The pe value at the point at which the S concentration matches the measured concentration is the calibrated pe value. For example as illustrated in Figure S6a, to get the calibrated pe at pH 12.64 for CS-N-16w, the pe was varied from -9.9 to -9.6 while pH was fixed at 12.64. At pe of -9.70, the S concentration equaled the measured leaching concentration of 0.018 mol/L, and so the calibrated pe at pH 12.64 was -9.70. The calibrated pe values and the geochemical speciation modeling results of S are presented in Figure S6.

Additional Tables and Figures.

Table S1a. Mixture composition used in preparation of Cast Stone.

Component	Proportion (wt.%)
ordinary Portland cement (OPC)	4.8
class F fly ash (FAF)	27.0
blast furnace slag (BFS)	28.2
low activity radioactive waste (LAW) simulant	40.0

Table S1b. Composition of low activity radioactive waste (LAW) simulant used in preparation of Cast Stone.

Chemicals	Content (g/L)
H_2O	650.00
$Al(NO_3)_3•9H_2O$	114.00
Na_2SO4	12.10
NaCl	2.47
NaF	1.33
NaOH (50% solution)	223.00
$Na_3PO_4•12H_2O$	18.70
Na_2CO_3	29.00
$NaNO_2$	39.00
$NaCH_3COO•3H_2O$	5.11
KNO_3	3.31
$NaNO_3$	56.90
Na_2CrO_4	19.40
H_2O	70.70

Table S2. Methods, MDLs, and LLOQs for Analysis of Eluates by ICP-OES and IC.

Analyte	Symbol	Method	MDL (mg/L)	LLOQ (mg/L)
Aluminum	Al	ICP-OES	0.002	0.025
Barium	Ba	ICP-OES	0.001	0.025
Calcium	Ca	ICP-OES	0.002	0.025
Chromium	Cr	ICP-OES	0.001	0.025
Iron	Fe	ICP-OES	0.001	0.025
Lithium	Li	ICP-OES	0.001	0.025
Magnesium	Mg	ICP-OES	0.002	0.025
Potassium	K	ICP-OES	0.002	0.025
Silicon	Si	ICP-OES	0.003	0.025
Sodium	Na	ICP-OES	0.004	0.025
Strontium	Sr	ICP-OES	0.001	0.025
Sulfur	S	ICP-OES	0.005	0.025
Bromide	Br^-	IC	0.006	0.025
Chloride	Cl^-	IC	0.010	0.050
Fluoride	F^-	IC	0.006	0.020
Nitrate	NO_3^-	IC	0.010	0.100
Nitrite	NO_2^-	IC	0.010	0.050
Phosphate	PO_4^{3-}	IC	0.020	0.150
Sulfate	SO_4^{2-}	IC	0.020	0.150

Note: MDL- method detection limit; LLOQ- lower limit of quantification.

Table S3. Model parameters and available content of constituents for four Cast Stone materials.

Model Parameters					
Entity	**Unit**	***CS-N-16w***	***CS-O-16w***	***CS-N-9w***	***CS-O-9w***
Clay	mg/kg	3000	3000	3000	3000
Hydrous Ferric Oxide	mg/kg	1100	1100	200	300
L/S	L/kg	10.95	10.00	10.00	10.00
pH		12.64	11.62	12.90	12.60
Solid Humic Acid	mg/kg	1200	1200	1200	1200
Available Content					
Entity	**Unit**	***CS-N-16w***	***CS-O-16w***	***CS-N-9w***	***CS-O-9w***
Al	mg/kg	6500	6600	6700	5800
As	mg/kg	7.1	5.9	2.0	2.7
Ba	mg/kg	17	11	18	6.0
Br	mg/kg	0.0059	0.0059	8.0E-09	8.00E-09
Ca	mg/kg	71000	63000	68000	46000
Cd	mg/kg	0.12	0.12	1.1E-08	1.1E-08
Cl	mg/kg	550	730	3.5E-09	3.5E-09
Co	mg/kg	1.2	1.4	2.0	1.0
CO_3^{2-}	mg/kg	36000	65000	42000	33000
Cr	mg/kg	350	420	870	180
Cu	mg/kg	8.5	8.6	4.5	5.3
F	mg/kg	7.8	48	1.9E-09	1.9E-09
Fe	mg/kg	650	640	730	340
B	mg/kg	23	47	65	31
Si	mg/kg	36000	22000	28000	17000
K	mg/kg	3400	1800	2900	2700
Li	mg/kg	19	8.8	23	20
Mg	mg/kg	5300	3300	4700	2800
Mn	mg/kg	140	140	190	160
Mo	mg/kg	4.2	4.9	4.3	5.1
Na	mg/kg	42000	37000	44000	41000
Ni	mg/kg	1.7	2.0	2.3	2.2
NO_3	mg/kg	43000	43000	46000	46000
Pb	mg/kg	1.7	1.7	0.94	0.98
P	mg/kg	200	180	98	75
Sb	mg/kg	0.27	0.22	1.2E-08	1.2E-08
Se	mg/kg	3.8	3.7	3.6	4.6
S	mg/kg	8000	8000	8000	8000
Sr	mg/kg	250	100	170	88
Tc	mg/kg	2.4	2.4	2.4	2.4
V	mg/kg	19	18	5.8	7.8
Zn	mg/kg	16	16	12	16

Table S4. Physical parameters of monoliths for CS-N-16w, CS-O-16w, CS-N-9w, and CS-O-9w in monolithic diffusion model.

Cell No.	A, m^2	density, g/cm^3	depth, m	dx, m	porosity	S	tortuosity				totvolume, L
							CS-N-16w	CS-O-16w	CS-N-9w	CS-O-9w	
1*	0.000507	2.22	0.000478	0.000239	0.41	1	10	6	10	10	0.000242
2	0.000507	2.22	0.001030	0.000275	0.41	1	15	6	20	20	0.000279
3	0.000507	2.22	0.001660	0.000316	0.41	1	15	6	20	20	0.000321
4	0.000507	2.22	0.002390	0.000364	0.41	1	15	6	20	20	0.000369
5	0.000507	2.22	0.003220	0.000418	0.41	1	15	6	20	20	0.000424
6	0.000507	2.22	0.004190	0.000481	0.41	1	15	10	20	20	0.000488
7	0.000507	2.22	0.005290	0.000553	0.41	1	15	10	20	20	0.000561
8	0.000507	2.22	0.006570	0.000636	0.41	1	85	10	80	80	0.000645
9	0.000507	2.22	0.008030	0.000732	0.41	1	85	10	120	120	0.000741
10	0.000507	2.22	0.009710	0.000841	0.41	1	85	10	120	120	0.000853
11	0.000507	2.22	0.011600	0.000968	0.41	1	85	10	120	120	0.000981
12	0.000507	2.22	0.013900	0.001110	0.41	1	85	10	120	120	0.001130
13	0.000507	2.22	0.016400	0.001280	0.41	1	85	10	120	120	0.001300
14	0.000507	2.22	0.019400	0.001470	0.41	1	85	10	120	120	0.001490
15	0.000507	2.22	0.022800	0.001690	0.41	1	85	80	120	120	0.001710
16	0.000507	2.22	0.026600	0.001950	0.41	1	85	80	120	120	0.001970
17	0.000507	2.22	0.031100	0.002240	0.41	1	85	80	120	120	0.002270
18	0.000507	2.22	0.036300	0.002570	0.41	1	85	80	120	120	0.002610
19	0.000507	2.22	0.042200	0.002960	0.41	1	85	80	120	120	0.003000
20	0.000507	2.22	0.049000	0.003400	0.41	1	85	80	120	120	0.003450

: the first cell is in contact with the tank solutions.* ***Variables definition**: A- surface area exposed to refresh solution, m^2; density- skeletal density of monolithic sample, g/cm^3; depth- depth between the interior surface of current cell and the surface exposed to refresh solution, m; dx- half of the thickness of the current cell, m; porosity- the fraction of the volume of voids (i.e., internal pores) over the total volume; S (saturation)- ratio of the volume of pore solution to the volume of voids; tortuosity- the property of a curve being tortuous and used to describe diffusion and fluid flow in porous media; totvolume- the total volume of current cell.*

Table S5. Elemental composition of class F fly ash (FAF), blast furnace slag (BFS), ordinary Portland cement (OPC), and Cast Stone (wt.%).

Elements	FAF	BFS	OPC	Cast Stone
Na_2O	0.44	ND	0.50	7.50
MgO	1.35	4.57	3.20	2.10
Al_2O_3	35.00	14.00	5.70	18.00
SiO_2	52.00	32.00	20.00	34.00
P_2O_5	0.30	ND	0.16	0.34
SO_3	ND	6.30	4.80	2.20
K_2O	2.50	0.53	0.44	1.50
CaO	1.20	40.00	61.00	27.00
TiO_2	1.20	0.39	0.28	0.97
Cr_2O_3	ND	ND	ND	0.32*
MnO	ND	0.21	0.11	0.13
Fe_2O_3	6.50	0.63	3.60	5.00
ZnO	ND	ND	0.02	ND
CuO	0.03	ND	ND	ND

ND: Not detected, where the detection limit was 0.1%.

**: a greater amount than normally present in Cast Stone was included in the formulation so that Cr could serve as an indicator species.*

Table S6. Mineral set controlling the solubility of constituents in Cast Stone materials.

Notation	*Formula*	*Log(K)*[a]	*Reaction*
CEM18_INFCNA_CNASHss [b]	$16CaO{\cdot}5.5Na_2O{\cdot}2.5Al_2O_3{\cdot}19SiO_2{\cdot}21H_2O$	-9.836	CEM18_INFCNA + 0.5 H_2O -> 0.3125 $Al[OH]_4^-$ + 1 CEM18_CNASH_ss + 1 Ca^{+2} + 1.1875 $H_2SiO_4^{-2}$ + 0.6875 Na^+
CEM18_T2C_CNASHss [b]	$3CaO{\cdot}2SiO_2{\cdot}5H_2O$	2.982	CEM18_T2C_CNASHss + 1 H^+ -> 1 CEM18_CNASH_ss + 1.5 Ca^{+2} + 2 H_2O + 1 $H_2SiO_4^{-2}$
CEM18_TobH_CNASHss [b]	$2CaO{\cdot}3SiO_2{\cdot}5H_2O$	-21.51	CEM18_TobH_CNASHss -> 1.5 CEM18_CNASH_ss + 1 Ca^{+2} + 1 H^+ + 0.5 H_2O + 1.5 $H_2SiO_4^{-2}$
Ca3[PO4]2[beta] [c]	$Ca_3(PO_4)_2$	-29.08	Ca3[PO4]2[beta] -> 3 Ca^{+2} + 2 PO_4^{-3}
CaCO3_BaCO3 [e]	$CaBa(CO_3)_2$	-21.10	CaCO3_BaCO3 -> 1 Ba^{+2} + 2 CO_3^{-2} + 1 Ca^{+2}
CaCO3_Li2CO3 [e]	$CaLi_2(CO_3)_2$	-21.30	CaCO3_Li2CO3 -> 2 CO_3^{-2} + 1 Ca^{+2} + 2 Li^+
CaCO3_SrCO3 [e]	$CaSr(CO_3)_2$	-19.75	CaCO3_SrCO3 -> 2 CO_3^{-2} + 1 Ca^{+2} + 1 Sr^{+2}
CEM18_Amor_Sl [b]	SiO_2	-25.72	CEM18_Amor_Sl + 2 H_2O -> 2 H^+ + 1 $H_2SiO_4^{-2}$
CEM18_Brc [b]	$Mg(OH)_2$	17.18	CEM18_Brc + 2 H^+ -> 2 H_2O + 1 Mg^{+2}
CEM18_C3S [b]	Ca_3SiO_5	51.63	CEM18_C3S + 4 H^+ -> 3 Ca^{+2} + 1 H_2O + 1 $H_2SiO_4^{-2}$
CEM18_Cal [b]	$CaCO_3$	-8.45	CEM18_Cal -> 1 CO_3^{-2} + 1 Ca^{+2}
CEM18_hemicarbonate [b]	$Ca_4Al_2(CO_3)_{0.5}(OH)_{13}{\cdot}5.5H_2O$	40.93	CEM18_hemicarbonate + 5 H^+ -> 2 $Al[OH]_4^-$ + 0.5 CO_3^{-2} + 4 Ca^{+2} + 10.5 H_2O
CEM18_hemihydrate [b]	$CaSO_4{\cdot}0.5H_2O$	-3.518	CEM18_hemihydrate -> 1 Ca^{+2} + 0.5 H_2O + 1 SO_4^{-2}
CEM18_Mgs [b]	$MgCO_3$	-8.206	CEM18_Mgs -> 1 CO_3^{-2} + 1 Mg^{+2}
CEM18_monocarbonate [b]	$Ca_4Al_2(CO_3)(OH)_{12}{\cdot}5H_2O$	24.38	CEM18_monocarbonate + 4 H^+ -> 2 $Al[OH]_4^-$ + 1 CO_3^{-2} + 4 Ca^{+2} + 9 H_2O
CEM18_monosulphate12 [b]	$Ca_4Al_2O_6(SO_4){\cdot}12H_2O$	26.66	CEM18_monosulphate12 + 4 H^+ -> 2 $Al[OH]_4^-$ + 4 Ca^{+2} + 10 H_2O + 1 SO_4^{-2}
CEM18_Ord_Dol [b]	$CaMg(CO_3)_2$	-16.99	CEM18_Ord_Dol -> 2 CO_3^{-2} + 1 Ca^{+2} + 1 Mg^{+2}
CEM18_Portlandite [b]	$Ca(OH)_2$	23.19	CEM18_Portlandite + 2 H^+ -> 1 Ca^{+2} + 2 H_2O
Diaspore [c]	α-AlO(OH)	-16.02	Diaspore + 2 H_2O -> 1 $Al[OH]_4^-$ + 1 H^+
Eskolaite [d]	Cr_2O_3	-147.5	Eskolaite + 5 H_2O -> 2 CrO_4^{-2} + 10 H^+ + 6 e^-
Ferrihydrite [c]	$Fe_2O_3{\cdot}3H_2O$	-18.18	Ferrihydrite + 1 H_2O -> 1 $Fe[OH]_4^-$ + 1 H^+
Gaylussite [d]	$Na_2Ca(CO_3)_2{\cdot}5H_2O$	-9.516	Gaylussite -> 2 CO_3^{-2} + 1 Ca^{+2} + 5 H_2O + 2 Na^+
Larnite [d]	Ca_2SiO_4	16.18	Larnite + 2 H^+ -> 2 Ca^{+2} + 1 $H_2SiO_4^{-2}$
Nahcolite [d]	$NaHCO_3$	-10.79	Nahcolite -> 1 CO_3^{-2} + 1 H^+ + 1 Na^+
Natron [c]	$Na_2CO_3{\cdot}10H_2O$	-1.508	Natron -> 1 CO_3^{-2} + 10 H_2O + 2 Na^+
Pyrite [c]	FeS_2	-121.1	Pyrite + 12 H_2O -> 1 $Fe[OH]_4^-$ + 20 H^+ + 2 SO_4^{-2} + 15 e^-
Pyrrhotite [d]	FeS	-72.27	Pyrrhotite + 8 H_2O -> 1 $Fe[OH]_4^-$ + 12 H^+ + 1 SO_4^{-2} + 9 e^-
Wairakite [d]	$Ca_8Al_{16}Si_{32}O_{96}{\cdot}16H_2O$	-119.4	Wairakite + 10 H_2O -> 2 $Al[OH]_4^-$ + 1 Ca^{+2} + 8 H^+ + 4 $H_2SiO_4^{-2}$
llnl_$NaTcO_4$ [d]	$NaTcO_4$	-9.279	llnl_ $NaTcO_4$ + 1 e^- -> 1 Na^+ + 1 TcO_4^{-2}
llnl_TcO2:2H2O[am] [d]	$TcO_2{\cdot}2H_2O$	-48.46	llnl_TcO2:2H2O[am] -> 4 H^+ + 1 TcO_4^{-2} + 2 e^-
llnl_Tc_3O_4 [d]	Tc_3O_4	-192.9	llnl_Tc_3O_4 + 8 H_2O -> 16 H^+ + 3 TcO_4^{-2} + 10 e^-
llnl_TcOH [d]	TcOH	-110.4	llnl_TcOH + 3 H_2O -> 11 H^+ + 1 TcO_4^{-2} + 7 e^-

[a] *formation reaction constant;*
[b] *mineral from Cemdata 18 database;*
[c] *mineral from Minteq. V4 database;*
[d] *mineral from LLNL database;*
[e] *minerals proposed in the present study with calibrated logK.*

Table S7. Calibrated pe for Cast Stone materials based on Cr eluate concentrations from Method 1313 pH-dependent testing.

CS-N-16w		CS-O-16w		CS-N-9w		CS-O-9w	
pH	**pe**	**pH**	**pe**	**pH**	**pe**	**pH**	**pe**
12.64	2.10	12.89	1.83	12.90	1.45	12.60	2.03
11.90	3.34	11.65	3.91	11.70	3.43	11.20	4.25
10.55	5.46	10.68	5.50	10.90	4.62	10.30	5.65
9.00	7.88	9.44	7.395	9.76	6.395	9.09	7.42
8.24	9.10	7.80	10.07	9.25	7.15	7.29	10.45
7.16	10.92	6.54	12.13	7.45	10.01	4.97	14.40
6.29	12.35	5.68	13.37	4.54	14.70	3.63	16.275
5.47	13.57	3.45	16.47	3.58	16.00		
4.37	15.03						
2.96	16.60						

*****Natural pH
******Natural pe

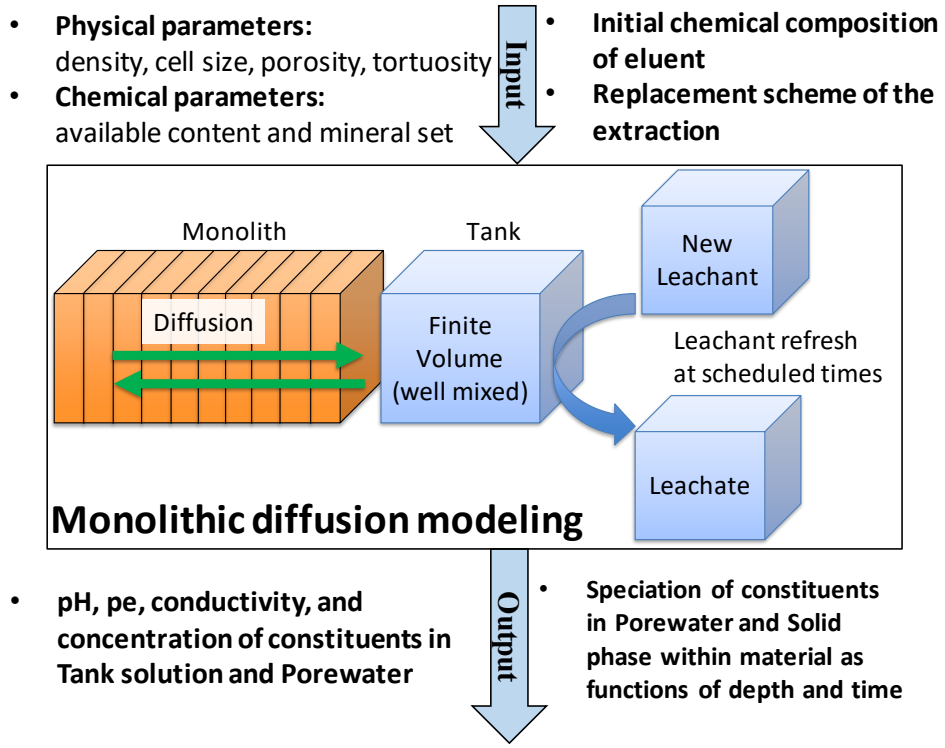

Figure S1. Conceptual illustration of the monolithic diffusion model.

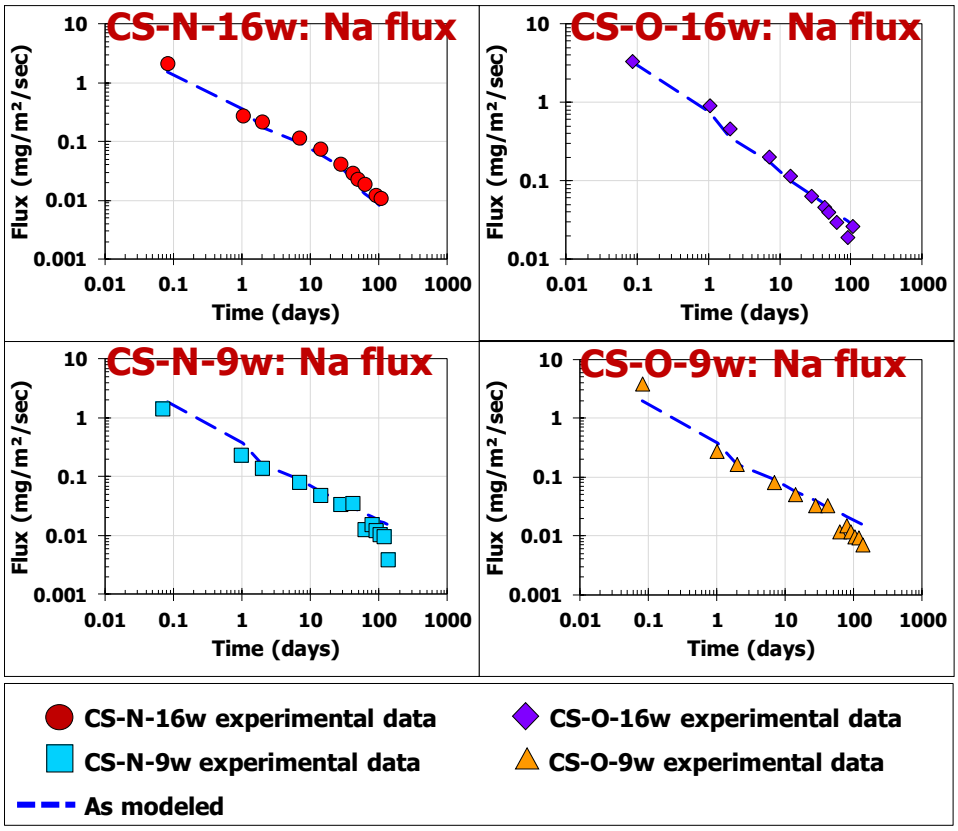

Figure S2. Illustration of simulated versus measured Na flux after calibrating tortuosity based on Na leaching for four samples.

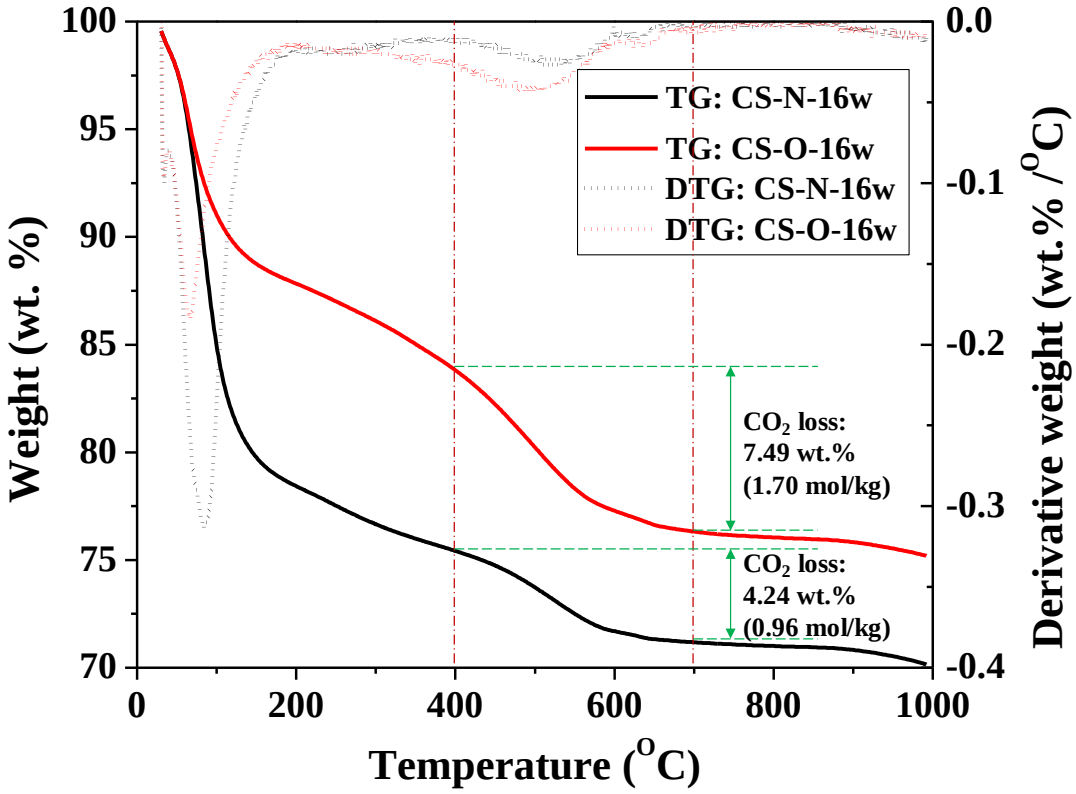

Figure S3. Thermogravimetric analysis results of CS-N-16w and CS-O-16w.

(note: With a theoretical decomposition temperature range of 420-895 °C for carbonate [11], the weight loss peak at temperature from ca. 400 to 700 °C is attributed to CO_2 loss, which is 4.24 and 7.49 wt.%, respectively for CS-N-16w and CS-O-16w. Correspondingly, the upper limit of carbonate in CS-N-16w and CS-O-16w is calculated as 0.96 and 1.70 mol/kg.)

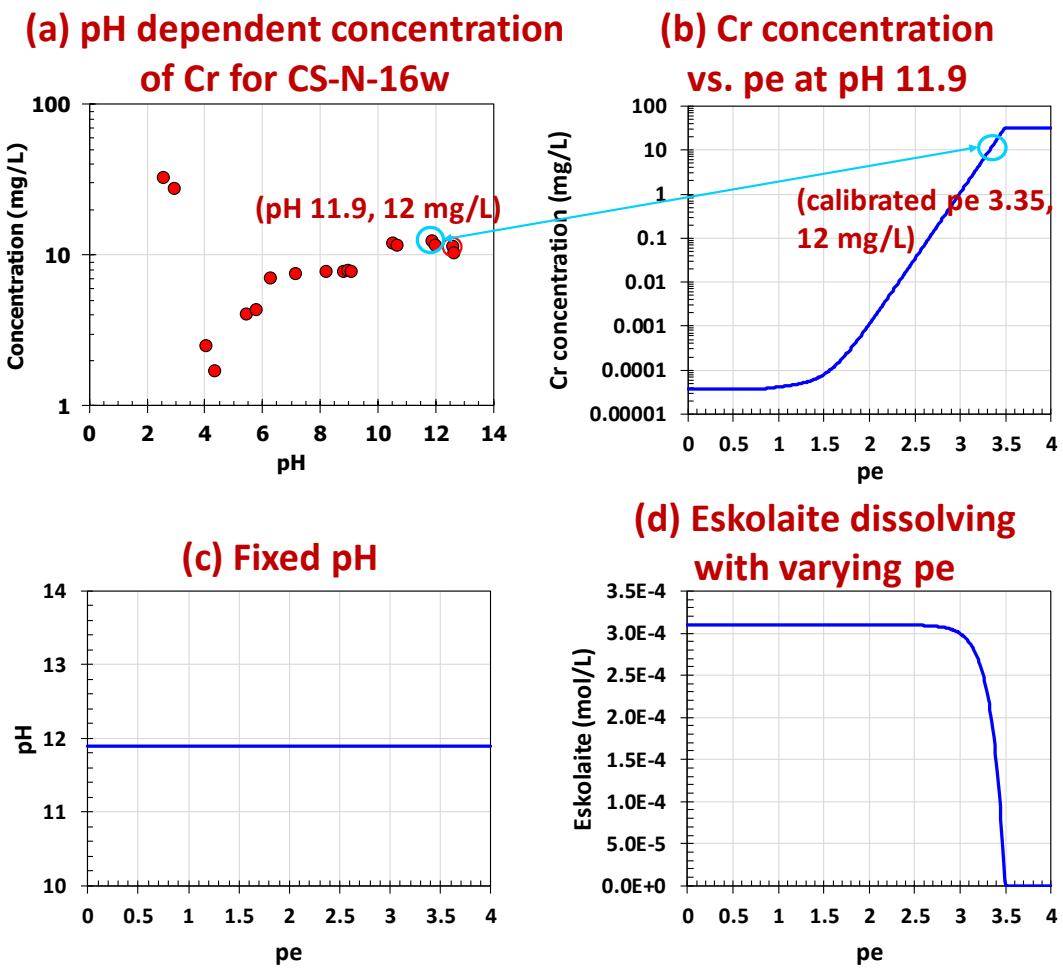

Figure S4. Illustration of pe calibration based on measured total soluble concentration of Cr in Method 1313 tests.

(note: At a given pH, the corresponding pe value was calibrated based on the measured concentration of Cr. For example, to get the calibrated pe value for CS-N-16w at pH 11.9, the pH in the LeachXS/ORCHESTRA model was fixed at 11.9 (Figure S4c) and pe was varied from 0 to 4 (Figure S4b). It was found that the Cr concentration at pe 3.35 (Figure S4b) was equal to the measured concentration in Figure S4a, so the value of calibrated pe at pH 11.9 for CS-N-16w was 3.35. The calibrated pe values are shown in Table S7 for four samples and the geochemical speciation modeling results of Cr are presented in Figure A3a.)

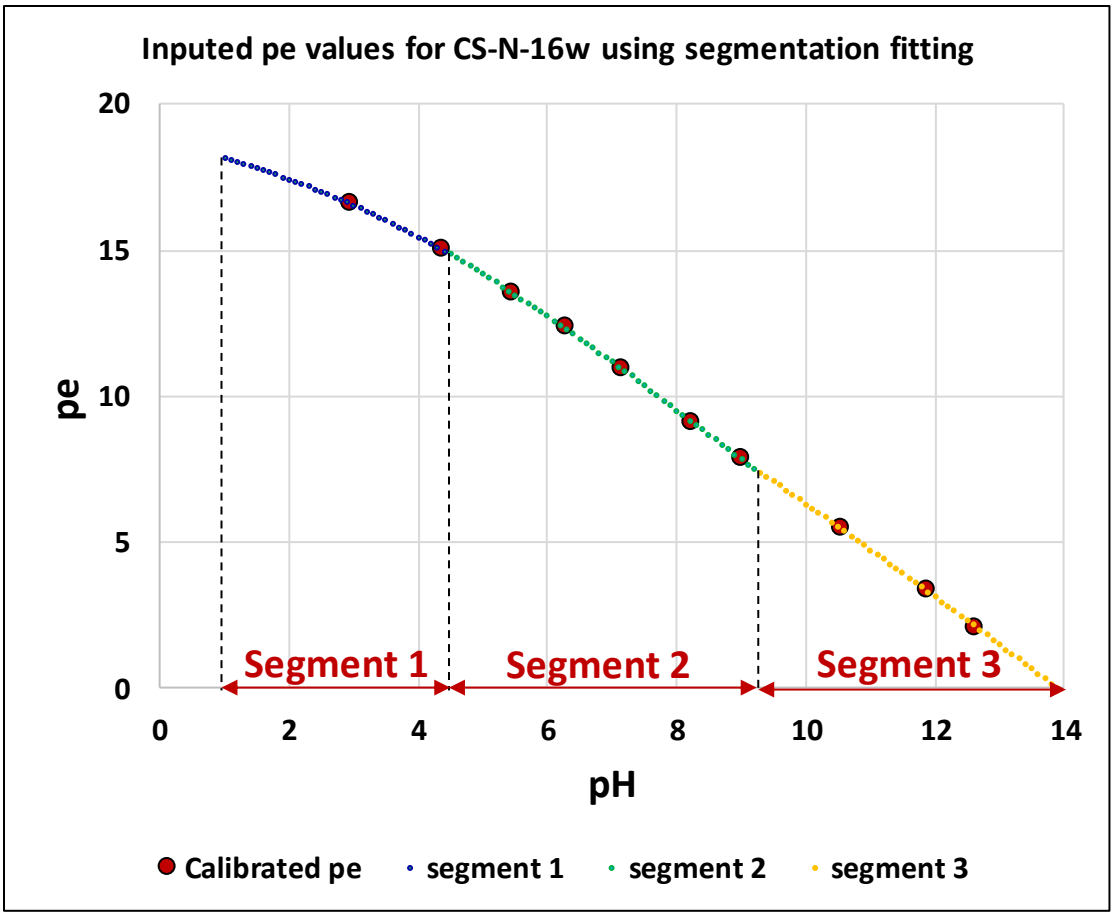

Figure S5. Illustration of using segmentation fitting to select the inputted pe values in geochemical speciation model for CS-N-16w.

(approach description: In light of the calibrated pe values shown in Table S7, the pe values inputted into the geochemical speciation model as a function of pH are obtained using a segmentation fitting approach. Take CS-N-16w as an example; the calibrated pe values for CS-N-16w in Table S7 are fitted in three segments to minimize residuals as shown in Figure S5, and then the pe values obtained from fitting are inputted for the geochemical speciation modeling of CS-N-16w.)

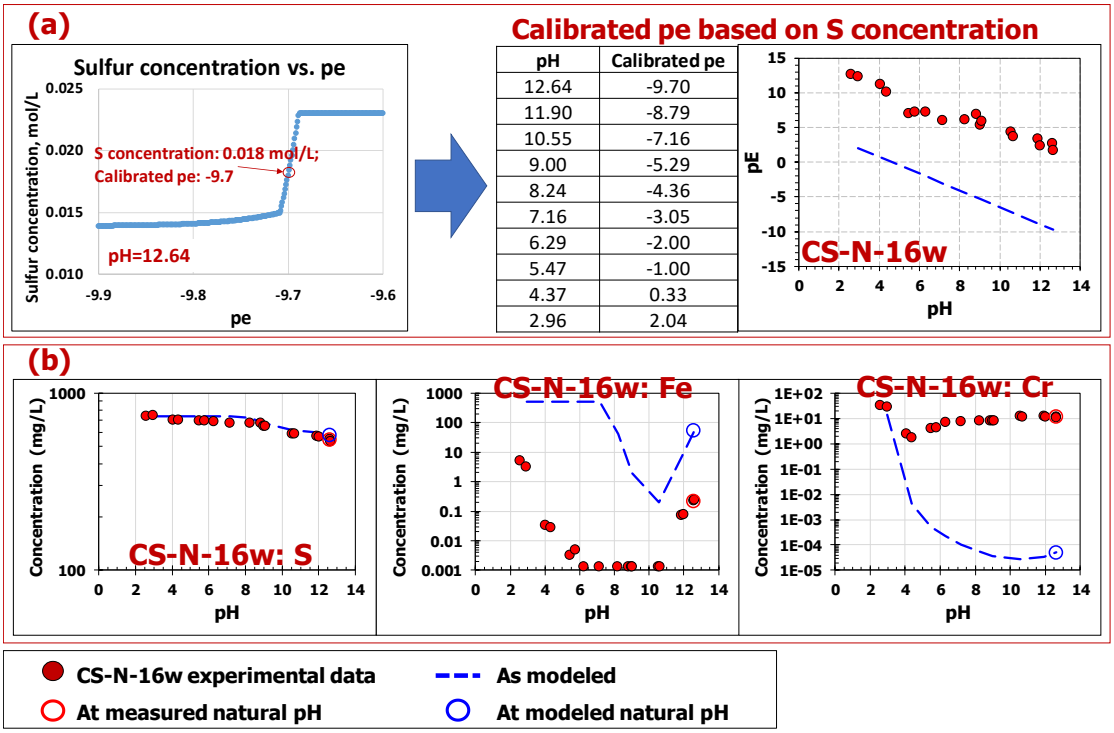

Figure S6. (a) Illustration of pe calibration based on S concentrations; (b) Geochemical modeling results of S, Fe, and Cr in CS-N-16w with calibrated pe values. *Calibration of pe based on S does not provide reasonable results for Fe and Cr.*

(approach description of pe calibration: the calibration method is similar to that described in Figure S4. The solubility of S at reducing conditions is assumed to be controlled by Pyrrhotite (FeS) [9]. To get the calibrated pe at a given pH, the pH is fixed, then the pe value is varied within a reasonable range to capture the measured S concentration at this pH. The pe value at the point at which the S concentration matches the measured concentration is the calibrated pe value. For example, to get the calibrated pe at pH 12.64 for CS-N-16w, the pe was varied from -9.9 to -9.6 while pH was fixed at 12.64. At pe of -9.70, the S concentration equaled the measured leaching concentration of 0.018 mol/L, and so the calibrated pe at pH 12.64 was -9.70.)

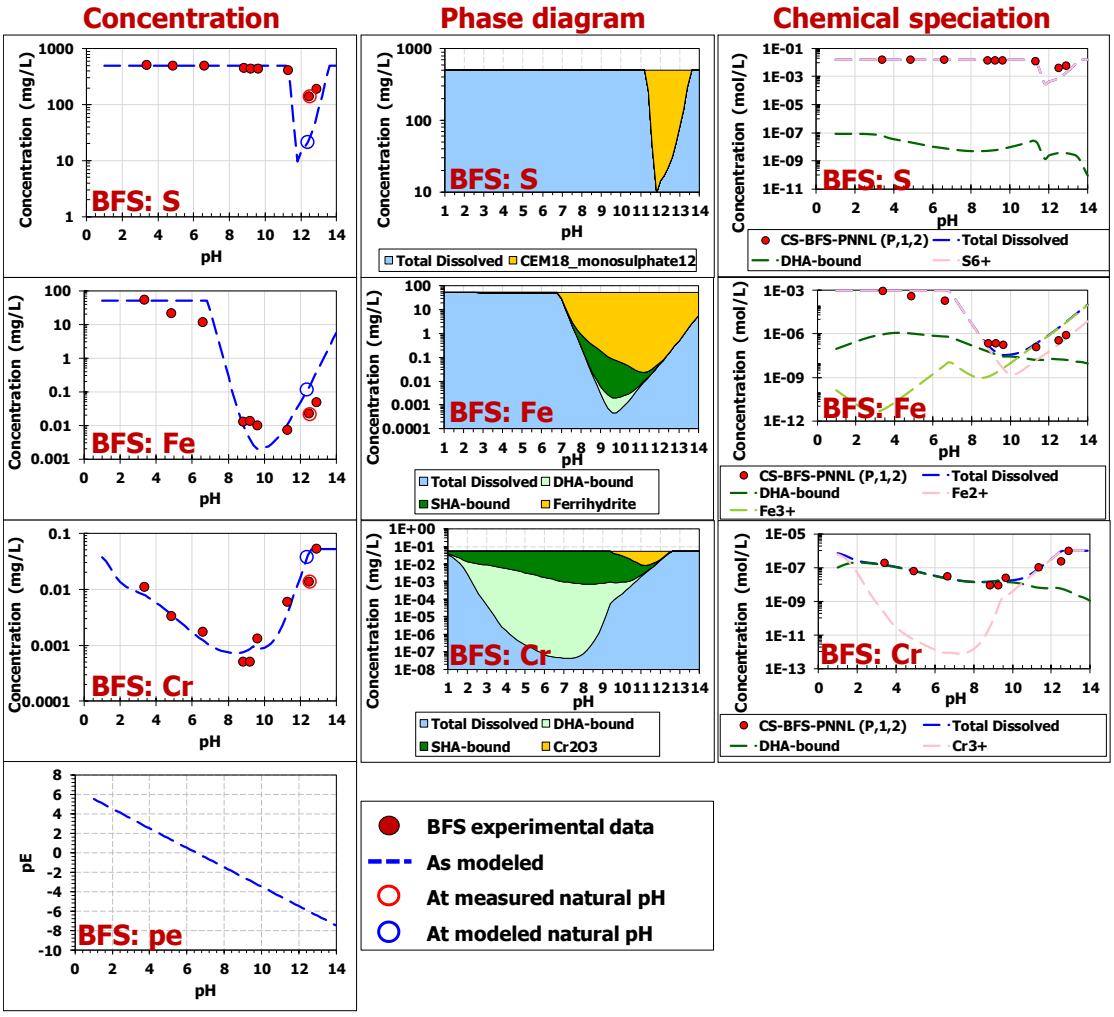

Figure S7. Geochemical speciation modeling results for redox sensitive constituents (i.e., S, Fe, and Cr) in BFS.

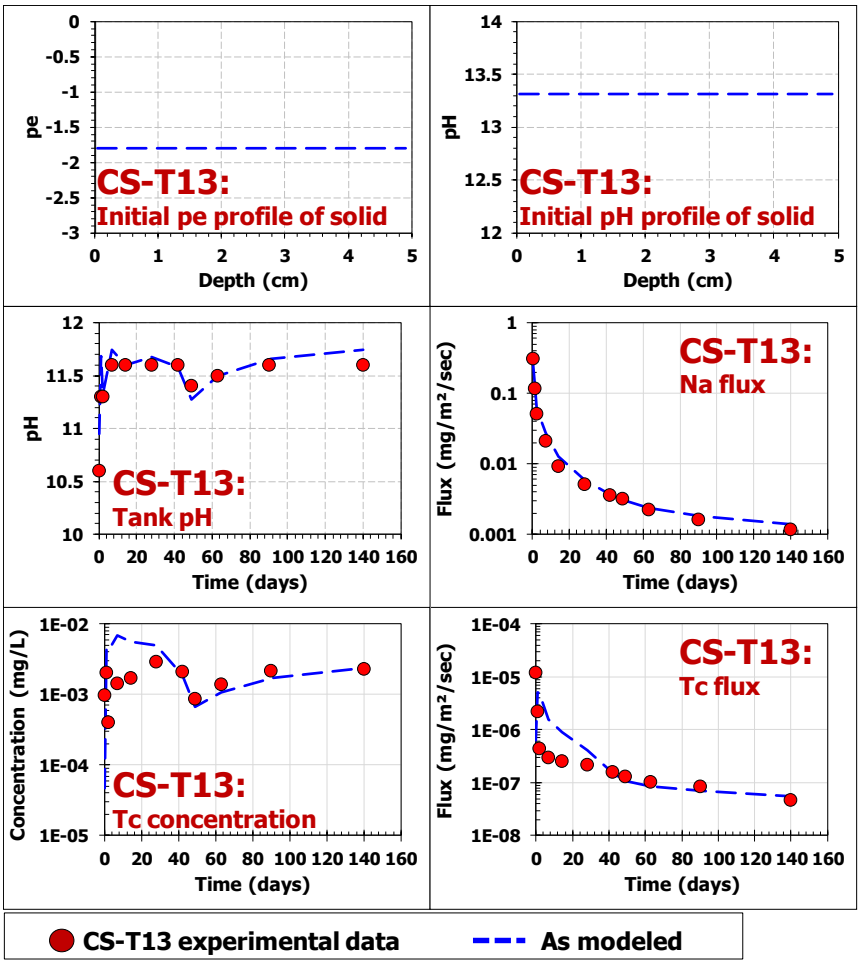

Figure S8. Calibration of redox state in a material similar to Cast Stone from the study of Um's (CS-T13) [10] based on the monolithic diffusion leaching results.

(note: the flux of Na is well described, indicating a good description of the effective diffusivities of constituents from solid to tank. Tank pH and the concentration and flux of Tc are well predicted by the model with the initial pe of -1.8 within the monolith, so the calibrated pe in CS-T13 is -1.8.)

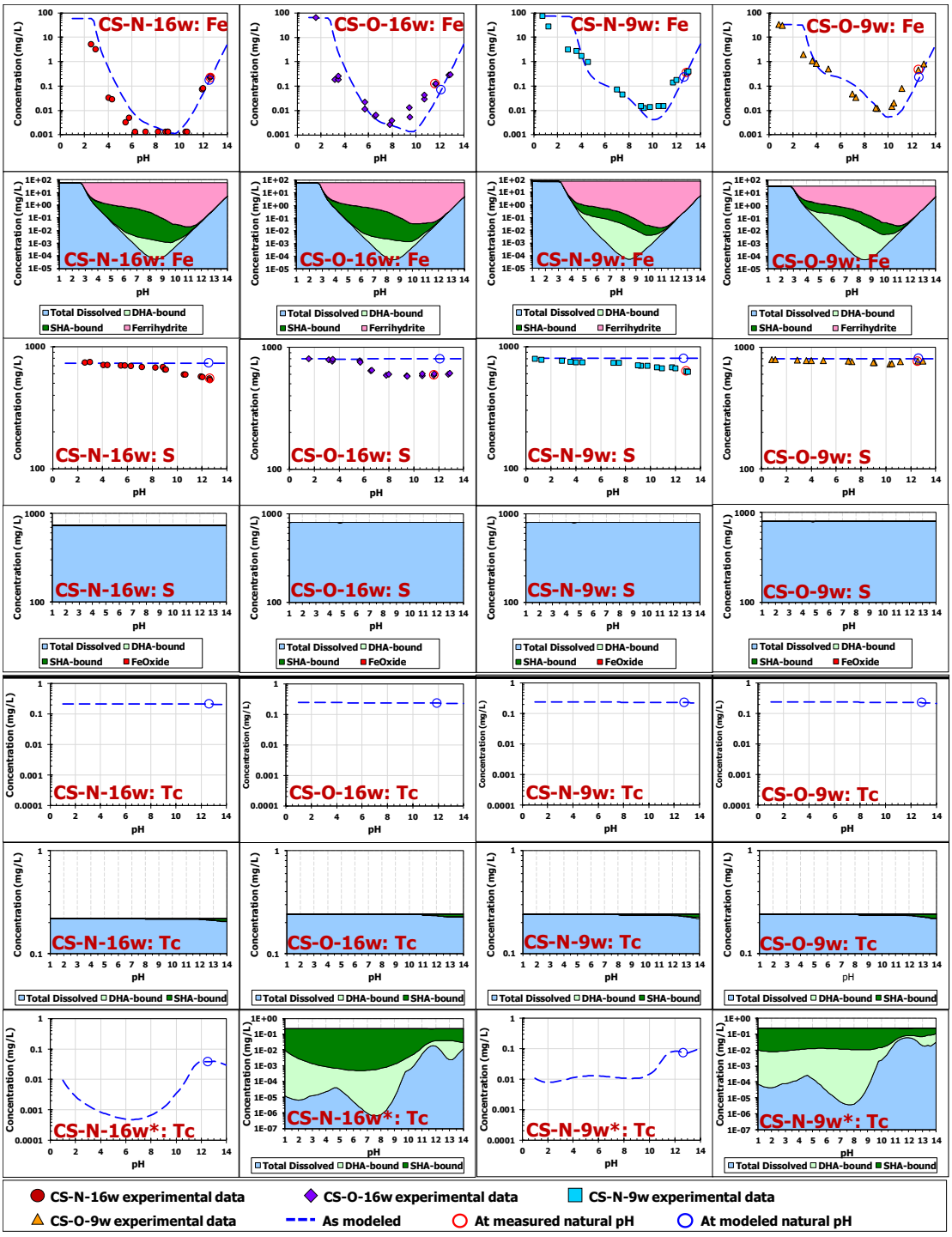

*: modeling results of Tc with the redox state calibrated from the Cast Stone of Um's as in Figure S8 (pH + pe = 11.5).

Figure S9. pH-dependent concentration of redox-sensitive constituents (i.e., Fe, S, and Tc) and corresponding phase diagram for four Cast Stone materials.

(note: Specifically for Tc, only modeling results predicted by the geochemical speciation model developed in this study are shown. Chemical speciation of Tc in Cast Stone was identified to be primarily as TcO_4^- and secondarily as the mineral $Tc(IV)O_2{\cdot}2H_2O$ [12], which is a common product from the reduction of TcO_4^- [13]. Thus, $NaTcO_4$ and

$Tc(IV)O_2 \cdot 2H_2O$ are selected as minerals accounting for Tc solubility in this work. In addition, minerals TcOH and Tc_3O_4 are also included in the mineral set to describe the solubility of Tc at strongly reducing conditions. The available content of Tc was set based on the content from Saslow [10].)

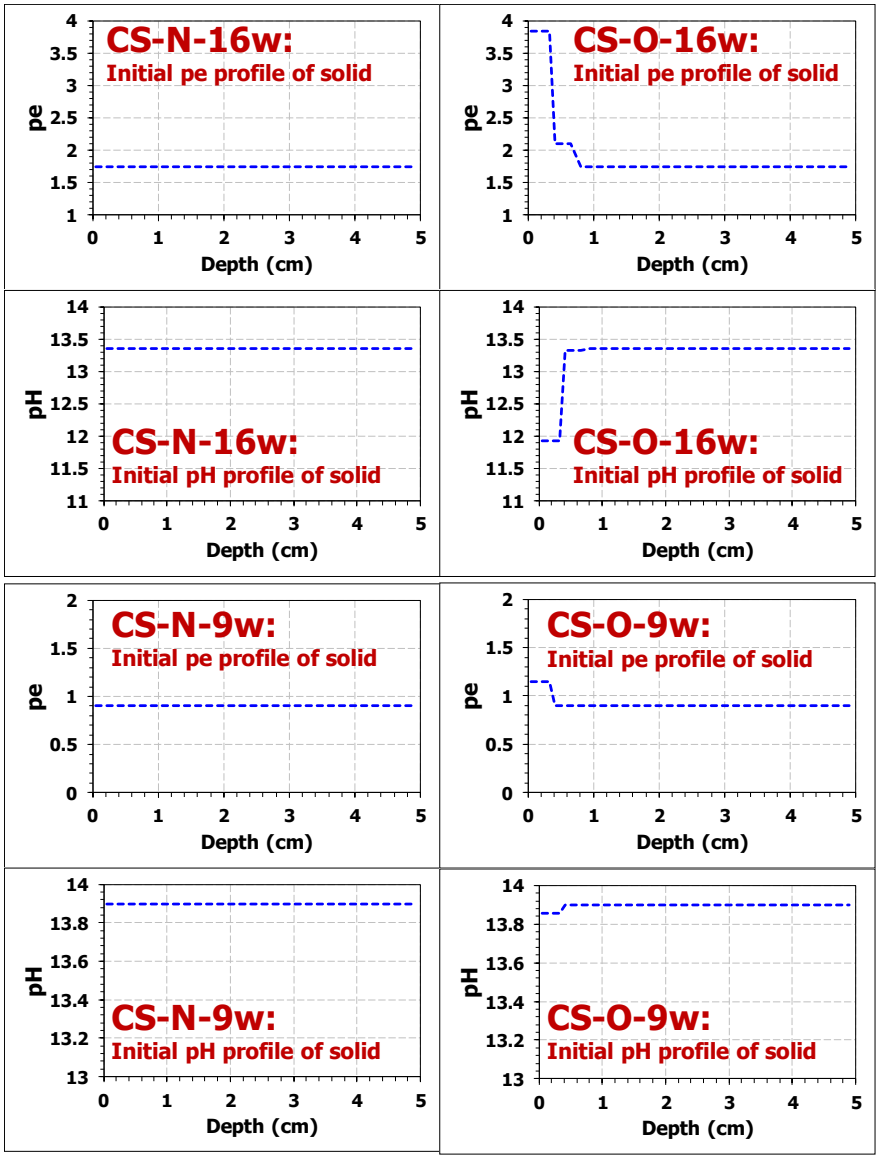

Figure S10. Estimated initial pH and pe profiles of monolithic Cast Stone materials.

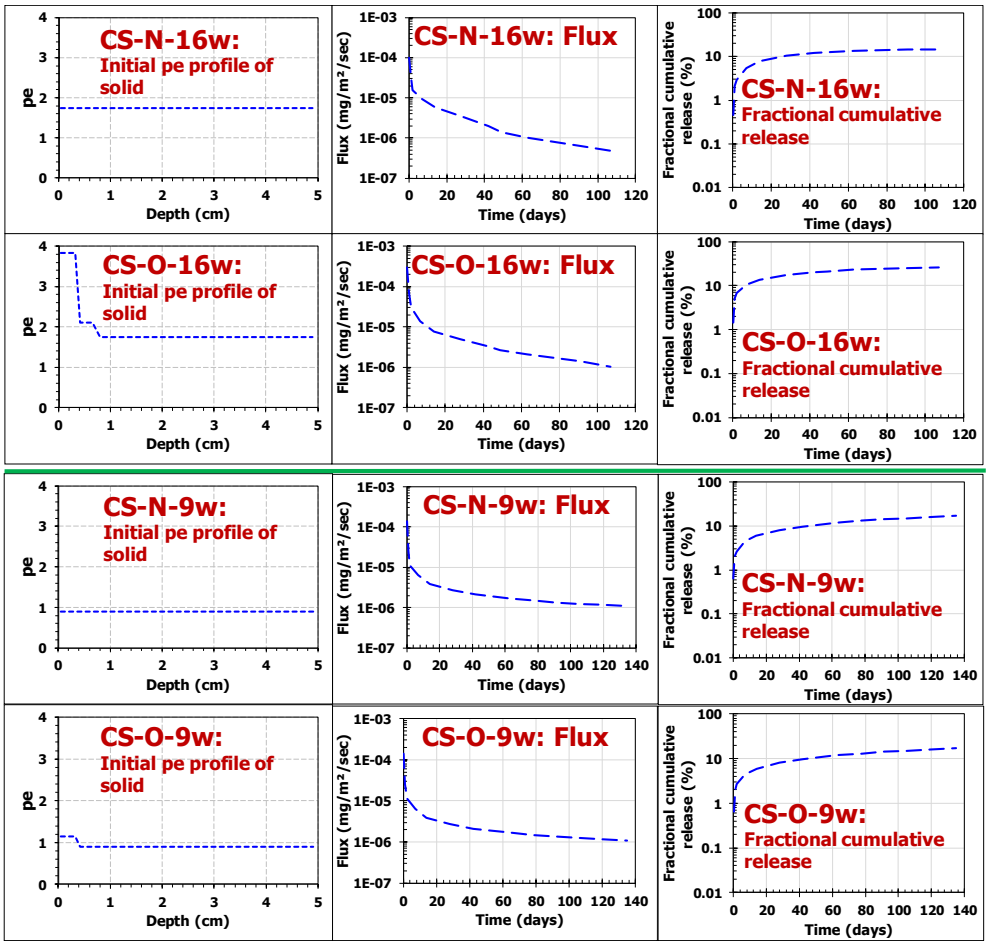

Figure S11a. Monolithic diffusion simulated flux and fractional cumulative release of Tc under estimated redox states of Cast Stone materials as shown in Figure S10.

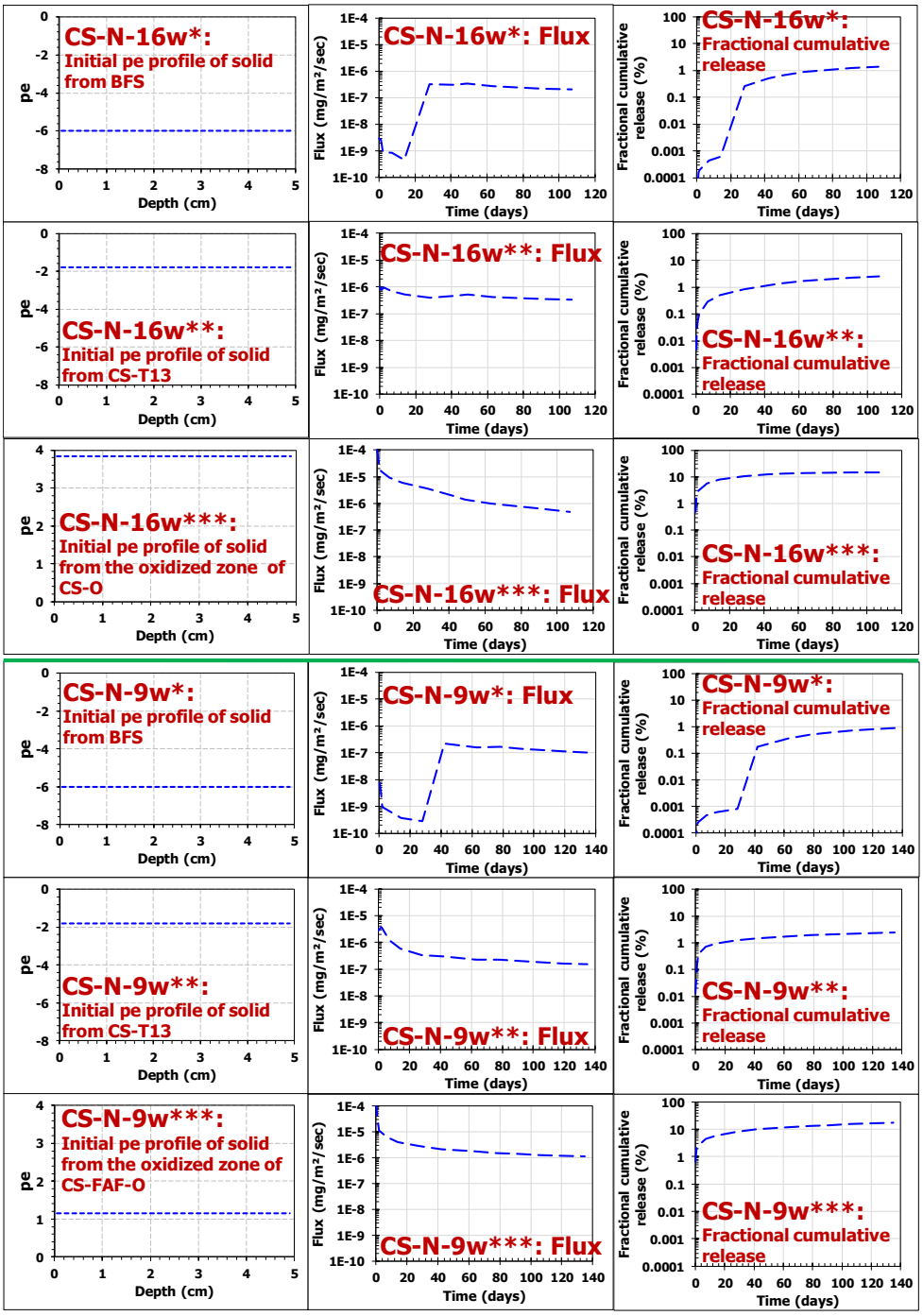

*: modeling results of Tc with the initial solid redox state of BFS as calibrated in Figure S7;
**: modeling results of Tc with the initial solid redox state of CS-T13 as calibrated in Figure S8;
***: modeling results of Tc with the initial solid redox state at the oxidized front of CS-O-16w or CS-O-9w as in Figure S10.

Figure S11b. Monolithic diffusion simulated flux and fractional cumulative release of Tc for CS-N-16w and CS-N-9w under various initial solid redox states (i.e., redox states calibrated from BFS, CS-T13, and the oxidized front of CS-O-16w and CS-O-9w).

REFERENCES

1. Haselbach, L., Potential for carbon dioxide absorption in concrete. Journal of Environmental Engineering 2009, 135, (6), 465-472.

2. Asmussen, R. M.; Lawter, A. R.; Stephenson, J. R.; Bowden, M. E.; Washton, N. M.; Neeway, J. J.; Du, Y.; Pearce, C. I.; Clayton, R. E.; Saslow, S. A. Getter Incorporation into Cast Stone and Solid State Characterizations; Pacific Northwest National Lab.(PNNL), Richland, WA (United States): 2016.

3. Branch, J. L. Impact of Aging in the Presence of Reactive Gases on Cementitious Waste Forms and Barriers. ProQuest Dissertations Publishing, 2018.

4. Chung, C.-W.; Chun, J.; Um, W.; Sundaram, S.; Westsik Jr, J. H., Setting and stiffening of cementitious components in Cast Stone waste form for disposal of secondary wastes from the Hanford waste treatment and immobilization plant. Cement and concrete research 2013, 46, 14-22.

5. Chung, C.-W.; Um, W.; Valenta, M. M.; Sundaram, S.; Chun, J.; Parker, K. E.; Kimura, M. L.; Westsik Jr, J. H., Characteristics of Cast Stone cementitious waste form for immobilization of secondary wastes from vitrification process. Journal of nuclear materials 2012, 420, (1-3), 164-174.

6. Bernal, S. A.; Provis, J. L.; Brice, D. G.; Kilcullen, A.; Duxson, P.; van Deventer, J. S., Accelerated carbonation testing of alkali-activated binders significantly underestimates service life: The role of pore solution chemistry. Cement and Concrete Research 2012, 42, (10), 1317-1326.

7. Myers, R. J.; Lothenbach, B.; Bernal, S. A.; Provis, J. L., Thermodynamic modelling of alkali-activated slag cements. Applied Geochemistry 2015, 61, 233-247.

8. Samson, E.; Lemaire, G.; Marchand, J.; Beaudoin, J., Modeling chemical activity effects in strong ionic solutions. Computational Materials Science 1999, 15, (3), 285-294.

9. Schwab, A.; Hickey, J.; Hunter, J.; Banks, M., Characteristics of blast furnace slag leachate produced under reduced and oxidized conditions. Journal of Environmental Science and Health Part A 2006, 41, (3), 381-395.

10. Um, W.; Williams, B. D.; Snyder, M. M. V.; Wang, G. Liquid Secondary Waste Grout Formulation and Waste Form Qualification; United States, 2016; p 195.

11. Du, B.; Li, J.; Fang, W.; Liu, Y.; Yu, S.; Li, Y.; Liu, J., Characterization of naturally aged cement-solidified MSWI fly ash. Waste management 2018, 80, 101-111.

12. Asmussen, R. M.; Pearce, C. I.; Miller, B. W.; Lawter, A. R.; Neeway, J. J.; Lukens, W. W.; Bowden, M. E.; Miller, M. A.; Buck, E. C.; Serne, R. J., Getters for improved technetium containment in cementitious waste forms. Journal of hazardous materials 2018, 341, 238-247.

13. Fan, D.; Anitori, R. P.; Tebo, B. M.; Tratnyek, P. G.; Lezama Pacheco, J. S.; Kukkadapu, R. K.; Engelhard, M. H.; Bowden, M. E.; Kovarik, L.; Arey, B. W., Reductive sequestration of pertechnetate (99TcO4–) by nano zerovalent iron (nZVI) transformed by abiotic sulfide. Environmental Science & Technology 2013, 47, (10), 5302-5310.

APPENDIX B: SUPPLEMENTARY INFORMATION FOR CHAPTER 2

Table B1 Surface tension of sodium nitrate solution [93].

M (mol/L)	σ (N/m)	a_0*
1.0	0.0776	1.016
2.0	0.0788	1.031
3.0	0.0799	1.046
4.0	0.0810	1.060
5.0	0.0820	1.074
6.0	0.0830	1.086
7.0	0.0839	1.098
10.0	0.0863	1.130
12.2	0.0877	1.148

* $a_0 = \sigma/\sigma_0$, σ_0=0.076 N/m.

PHREEQC simulation

B-I. Derivation of mineral assemblage of Cast Stone

In PHREEQC simulations, the Cast Stone system is represented using a set of mineral phases that describes the dissolution of the major constituents in the system (i.e., Na, Ca, Si, Al, S, K, N, and C) based on agreement between simulated aqueous concentrations and measurements obtained through experiments. Selection of the appropriate mineral and parameter set for Cast Stone has been based on calibration using data from EPA Method 1313 (liquid-solid partitioning as a function of extract pH using a parallel batch extraction [131]) in conjunction with instrument-based phase identification and then validated based on data from EPA Method 1315 (from the mass transfer rates of constituents in monolithic materials using a semi-dynamic tank leaching [133]). The C-N-A-S-H phase is represented using CNASH solid solution (CNASH_ss), which was derived specifically for describing dissolution of alkali-activated material [103]; the most recent version of the thermodynamic database relative to this group of material was used [87]. Phases that do not control the dissolution due to their high solubility (mostly sodium salts) also have been included in the reaction set when they were identified as present using XRD (nitratine, trona, nahcolite, natron, thenardite, and mirabilite) [31,42,122].

Table B2 Mineral assemblage of Cast Stone used in geochemical speciation modeling.

Name	**Formula**	**Log K $_{(25°C)}$** **	**Reaction**
TobH-CNASHss*	$CaO{\cdot}1.5SiO_2{\cdot}2.5H_2O$	12.79 [87]	$CaO{\cdot}1.5SiO_2{\cdot}\ 2.5H_2O + 2H_+ = Ca^{2+} + 3.5H_2O + 1.5SiO_2$
T2C-CNASHss*	$1.5CaO{\cdot}SiO_2{\cdot}2.5H_2O$	25.56 [87]	$1.5CaO{\cdot}SiO_2{\cdot}2.5H_2O + 2.5H^+ = 1.25Ca^{2+} + 3.75H_2O + 1.25SiO_2$
INFCNA-CNASHss*	$CaO{\cdot}1.2SiO_2{\cdot}0.15 Al_2O_3{\cdot}\ 0.35\ Na_2O{\cdot}1.3\ H_2O$	17.23 [87]	$CaO{\cdot}1.2SiO_2{\cdot}0.15Al_2O_3{\cdot}0.35\ Na_2O{\cdot}1.3H_2O + 2.4H^+ = 0.3AlO_2^- + Ca^{2+} + 0.7Na^+ + 2.5H_2O + 1.2SiO_2$
Calcite	$CaCO_3$	-8.48 [87]	$CaCO_3 = CO_3^{2-} + Ca^{2+}$
Gibbsite	$Al(OH)_3$	7.7 [88]	$Al(OH)_3 + 3H^+ = Al^{3+} + 3H_2O$
Gypsum	$CaSO_4{\cdot}2H_2O$	-4.48 [88]	$CaSO_4{\cdot}2H_2O = Ca^{2+} + SO_4^{2-} + 2H_2O$
Nahcolite	$NaHCO_3$	-0.11 [88]	$NaHCO_3 = HCO_3^- + Na^+$
Natron	$Na_2CO_3{\cdot}10H_2O$	-9.61 [88]	$Na_2CO_3{\cdot}10H_2O + H^+ = HCO_3^- + 2Na^+ + 10H_2O$
Trona	$Na_3H(CO_3)_2{\cdot}2H_2O$	-11.38 [88]	$Na_3H(CO_3)_2{\cdot}2H_2O = 3Na^+ + H^+ + 2CO_3^{2-} + 2H_2O$
Nitratine	$NaNO_3$	1.70 [89]	$NaNO_3 = Na^+ + NO_3^-$
Mirabilite	$Na_2SO_4{\cdot}10H_2O$	-1.14 [88]	$Na_2SO_4{\cdot}10H_2O = SO_4^{2-} + 2Na^+ + 10H_2O$
Thenardite	Na_2SO_4	-0.31 [88]	$Na_2SO_4 = 2Na^+ + SO_4^{2-}$

* End members of CNASH solid solution.
**Citations for indicated values are provided in [ ].

Table B3 Aqueous composition of initial Cast Stone pore solution used in geochemical speciation modeling.

	Na	**N**	**C**	**S**	**K**	**Si**	**Ca**	**Al**	**pH**
mol/L	2.61	1.52	0.25	0.22	0.16	0.005	0.001	0.003	12.98

Aqueous activity coefficients were calculated using the Pitzer model as described in Pitzer 1973 [177]. The model uses interaction parameters ($\beta^{(0)}$, $\beta^{(1)}$, $\beta^{(2)}$, and C) of ion pairs relevant to the current system are included and listed in Table B4.

Table B4 Pitzer binary ion-interaction parameters used in PHREEQC simulation.

Interaction pair	$\beta^{(0)}$	$\beta^{(1)}$	$\beta^{(2)}$	C	**References**
Na^+-NO_3^-	0.0283	0.3307		0	[178]
Na^+-NO_2^-	-0.0723	0.1604		-0.0017	[178]
Na^+-CO_3^{2-}	0.0399	1.3890		0.0044	[92]
Na^+-SO_4^{2-}	0.0172	1.1479		0.0020	[179]
Na^+-OH^-	0.0918	0.2127		0.0017	[178]
Na^+-$H_3SiO_4^-$	0.043	0.240			[180]
Na^+-$H_2SiO_4^{2-}$	0.32	0.13			[180]
Na^+-$Al(OH)_4^-$	0.051	0.25		-0.0009	[181]
K^+-NO_3^-	-0.161	0.8675		0.0222	[182]
K^+-CO_3^{2-}	0.1488	1.43		-0.0015	[92]
K^+-SO_4^{2-}	0.0317	0.756		0.0082	[92]
K^+-OH^-	0.1298	0.32		0.0041	[92]
Ca^{2+}-NO_3^-	0.1292	0.7943	0.4288	-0.0026	[183]
Ca^{2+}-CO_3^{2-}	0.16	2.1	-69		[92]
Ca^{2+}-SO_4^{2-}	0	3.546	-59.3	0.114	[92]
Ca^{2+}-OH^-	-0.1747	-0.2303	-5.72		[92]

PHREEQC Script

```
SOLUTION_SPECIES
        Al+3 + 2H2O = AlO2- + 4H+
        log_k     0
    H4SiO4 = H4(SiO4)
        log_k     0

Phases
Nitratine# REF - 1
        NaNO3 = NO3- + Na+
        log_k 1.699

Amor-Si# REF - 2
        SiO2    = H4(SiO4) - 2H2O
        log_k -2.714066

Brucite  # REF - 2
        Mg(OH)2 + 2H+ = Mg+2 + 2H2O
        log_k  16.8401

C2S      # REF - 2
        (CaO)2SiO2 + 4H+ = 2Ca+2 + H4(SiO4)
        log_k  38.567691

C3S      # REF - 2
        (CaO)3SiO2 + 6H+ = 3Ca+2 + H2O +
H4(SiO4)
        log_k  73.405906

Calcite  # REF - 2
        CaCO3 = CO3-2 + Ca+2
        log_k  -8.479966

hemicarbonate    # REF - 2
        (CaO)3Al2O3(CaCO3)0.5(CaO2H2)0.5(H2
O)11.5 + 5H+ = 0.5CO3-2 + 4Ca+2 + 2AlO2- +
14.5H2O
        log_k  40.870354

monocarbonate    # REF - 2
        Ca4Al2CO9(H2O)11 + 4H+ = CO3-2 +
4Ca+2 + 2AlO2- + 13H2O
        log_k  24.530285

Dolomite         # REF - 2
        CaMg(CO3)2 = 2CO3-2 + Ca+2 + Mg+2
        log_k  -17.089923

Portlandite      # REF - 2
        Ca(OH)2 + 2H+ = Ca+2 + 2H2O
        log_k  22.799937

Ferrihydrite     # REF - 4
        Fe(OH)3 + 3H+ = Fe+3 + 3H2O
        log_k  3.191

Gaylussite       # REF - 3
        CaNa2(CO3)2:5H2O +2H+  = Ca+2 +
2HCO3- + 2Na+ + 5H2O
        log_k  11.1641

Gibbsite # REF - 3
        Al(OH)3 +3H+  =  Al+3 + 3H2O
        log_k  7.7560

Gypsum # REF - 3
        CaSO4:2H2O  =  Ca+2 +SO4-2 + 2H2O
        log_k  -4.4823

Nahcolite        # REF - 3
        NaHCO3  = HCO3- + Na+
        log_k  -0.1118

Natron   # REF - 3
        Na2CO3:10H2O +H+  =  HCO3- + 2Na+ +
10H2O
        log_k  9.6102

Thermonatrite    # REF - 3
        Na2CO3:H2O +H+  =  H2O + HCO3- +
2Na+
        log_k  10.9623

TobH-CNASHss # REF - 2
        (CaO)1(SiO2)1.5(H2O)2.5 + 2H+ = Ca+2 +
0.5H2O + 1.5H4(SiO4)
        log_k    12.797208

T5C-CNASHss   # REF - 2
        (CaO)1.25(SiO2)1.25(H2O)2.5 + 2.5H+ =
1.25Ca+2 + 1.25H2O + 1.25H4(SiO4)
        log_k    18.445467

T2C-CNASHss      # REF - 2
        (CaO)1.5(SiO2)1(H2O)2.5 + 3H+ =
1.5Ca+2 + 2H2O + H4(SiO4)
        log_k    25.565334

INFCNA-CNASHss   # REF - 2
        (CaO)1(SiO2)1.1875(Al2O3)0.15625(Na2O
)0.34375(H2O)1.3125 + 2.375H+ = 0.3125AlO2- +
Ca+2 + 0.6875Na+ + 0.125H2O + 1.1875H4(SiO4)
        log_k    17.23247

INFCN-CNASHss    # REF - 2
        (CaO)1(SiO2)1.5(Na2O)0.3125(H2O)1.187
5 + 2.625H+ + 0.5H2O = Ca+2 + 0.625Na+ +
1.5H4(SiO4)
        log_k    18.759957

INFCA-CNASHss    # REF - 2
```

```
        (CaO)1(SiO2)1.1875(Al2O3)0.15625(H2O)
1.65625 + 1.6875H+ = Ca+2 + 0.3125AlO2- +
0.125H2O + 1.1875H4(SiO4)
        log_k     8.953727

5CNA-CNASHss# REF - 2
        (CaO)1.25(SiO2)1(Al2O3)0.125(Na2O)0.25
(H2O)1.375 + 2.75H+ = 1.25Ca+2 + 0.5Na+ +
0.25AlO2- + 0.75H2O + H4(SiO4)
        log_k     23.240018

5CA-CNASHss   # REF - 2
        (CaO)1.25(SiO2)1(Al2O3)0.125(H2O)1.625
+ 2.25H+ = 1.25Ca+2 + 0.25AlO2- + 0.75H2O +
H4(SiO4)
        log_k     15.88995

# CG - References: 1. Principles and Applications of
Inorganic Geochemistry (Faure, 1991), 2.
CEMDATA 18, 3. LLNL, 4. Minteq V4


SOLUTION_SPREAD
   -units    mol/l
 pH          Na       C(4)        S        N(5)       N(3)
Ca              Si          Al          K
 13        2.61       0.25       0.24       1.12        0.4
0.001451              0.004888              0.002633
0.16109

EQUILIBRIUM_PHASES 1 phases
   Nitratine 0 0 precipitate_only
Save solution 1
END

Use solution 1
EQUILIBRIUM_PHASES 2 phases
        Nitratine 0 0 precipitate_only
        Mirabilite 0 0 precipitate_only
        Thenardite 0 0 precipitate_only
        Trona 0 0 precipitate_only
        Calcite 0 0 precipitate_only
Save solution 2
END

Use solution 2
EQUILIBRIUM_PHASES 3 phases
        Nitratine 0 0  precipitate_only
        Gibbsite 0 0.028 precipitate_only
        Gypsum 0 0.1 precipitate_only
        Nahcolite 0 0 precipitate_only
        Natron 0 0 precipitate_only
        Mirabilite 0 0 precipitate_only
        Thenardite 0 0 precipitate_only
        Trona 0 0 precipitate_only
        Calcite 0 0 precipitate_only
Save solution 3
END

Use solution 3
EQUILIBRIUM_PHASES 4 phases
        Nitratine 0 0 precipitate_only
        Gibbsite 0 0.028 precipitate_only
        Gypsum 0 0.1 precipitate_only#0.10
        Nahcolite 0 0 precipitate_only
        Natron 0 0 precipitate_only
        Mirabilite 0 0 precipitate_only
        Thenardite 0 0 precipitate_only
        Trona 0 0 precipitate_only
        Calcite 0 0 precipitate_only

SOLID_SOLUTIONS 1
   CEM18_CNASHss
      -comp TobH-CNASHss 0.15
      -comp T2C-CNASHss 0.15
      -comp INFCNA-CNASHss 0.15


REACTION 1
   H2O      -1
   55.1 moles in 1000 steps

INCREMENTAL_REACTIONS True

USER_PRINT
      -start
10 Eva_factor = 55.551/(55.551-
STEP_NO*(55.5/1000))
20 PUT(Eva_factor, i, 1)
   -end

USER_GRAPH 1
   -headings            Na+ Ca+2 Cl- Al(OH)4- CO3-2
K+ NO3- SO4-2
   -axis_titles         "Evaporation Factor" "Majors
Activty Coefficent"
   -chart_title         "Majors Activity Coefficents vs.
Evaporation Factor"
   -axis_scale x_axis     1 100 auto auto
   -axis_scale y_axis     auto auto auto auto log
   -initial_solutions     true
   -connect_simulations   true
   -plot_concentration_vs  x
  -start
 10 PLOT_XY GET(i,1), GAMMA("Na+")
 20 PLOT_XY GET(i,1), GAMMA("Ca+2")
 30 PLOT_XY GET(i,1), GAMMA("Cl-")
 40 PLOT_XY GET(i,1), GAMMA("Al+3")
 50 PLOT_XY GET(i,1), GAMMA("CO3-2")
 60 PLOT_XY GET(i,1), GAMMA("K+")
 70 PLOT_XY GET(i,1), GAMMA("NO3-")
 80 PLOT_XY GET(i,1), GAMMA("SO4-2")
```

```
  -end
    -active               true

USER_GRAPH 2
    -headings             Water_Activity_Hsol
Ionic_Strength
    -axis_titles          "Evaporation Factor" "Hsol"
"Ionic Strength (mol/L)"
#    -chart_title          "Ionic_Strength and
Water_Activtiy vs. Evaporation Factor"
    -axis_scale x_axis      1 20 auto auto
    -axis_scale y_axis      0 1 1 auto
    -initial_solutions      true
    -connect_simulations    true
    -plot_concentration_vs  x
  -start
10 PLOT_XY GET(i,1), ACT("H2O")
20 PLOT_XY GET(i,1), MU,y-axis = 2, symbol =
None, color = black, line_width = 5
  -end
    -active               true

USER_GRAPH 3
    -headings             Nitratine Gibbsite  Gypsum
Nahcolite Natron  TobH-CNASHss T2C-CNASHss
INFCNA-CNASHss Mirabilite Thernardite Trona
Calcite
    -axis_titles          "Evaporation Factor"
"Saturation Index"
    -axis_scale x_axis      1 20 auto auto
    -axis_scale y_axis      auto auto auto auto
    -initial_solutions      true
    -connect_simulations    true
    -plot_concentration_vs  x
  -start
 10 PLOT_XY GET(i,1), SI("Nitratine")
 20 PLOT_XY GET(i,1), SI("Gibbsite")
 30 PLOT_XY GET(i,1), SI("Gypsum")
 40 PLOT_XY GET(i,1), SI("Nahcolite")
 50 PLOT_XY GET(i,1), SI("Natron")
 60 PLOT_XY GET(i,1), SI("TobH-CNASHss")
 70 PLOT_XY GET(i,1), SI("T2C-CNASHss")
 80 PLOT_XY GET(i,1), SI("INFCNA-CNASHss")
 90 PLOT_XY GET(i,1), SI("Mirabilite")
100 PLOT_XY GET(i,1), SI("Thenardite")
110 PLOT_XY GET(i,1), SI("Trona")
120 PLOT_XY GET(i,1), SI("Calcite")
  -end
    -active               true

USER_GRAPH 4
    -headings             TobH-CNASHss INFCNA-
CNASHss T2C-CNASHss pH
    -axis_titles          "Evaporation Factor"
"Concentration (mol/L)"
    -axis_scale x_axis      1 20 auto auto
    -axis_scale y_axis      auto auto auto auto
    -initial_solutions      true
    -connect_simulations    true
    -plot_concentration_vs  x
  -start
 10 PLOT_XY GET(i,1), S_S("TobH-CNASHss")
 20 PLOT_XY GET(i,1), S_S("INFCNA-
CNASHss")
 40 PLOT_XY GET(i,1), S_S("T2C-CNASHss")
  -end
    -active               true

END
```

B-II. Model verification

For model verification, an ORCHESTRA simulation is run for the drying case described in Bakhshi, et al. [61] with a known analytical solution. The drying process is conceptualized into two stages in this model. In the first stage, when the material is nearly saturated, the drying is considered to be controlled by the mass transfer at the external boundary with a constant drying rate, and thus the boundary condition in Stage 1 is:

$$J = F_0 \tag{B-1}$$

where F_0 is the rate of evaporation which represents the constant flux in stage 1 drying. In the second stage, drying is considered to be controlled by the convective diffusive transfer of vapor at the surface, and thus the boundary condition is represented by a convection equation:

$$J = -D' \frac{\partial C}{\partial x} = k(C_S - C_*) \tag{B-2}$$

where C is the moisture concentration, D' is the effective moisture diffusion coefficient, k is a surface factor that represents the convective moisture mass transfer coefficient, C_s is the moisture concentration of the sample surface, and C_* is the moisture concentration of the environment.

In both stages, moisture transport within the material is governed by the Fickian diffusion equation:

$$\frac{\partial C}{\partial t} = D' \frac{\partial^2 C}{\partial x^2} \tag{B-3}$$

Different values of D' are taken in Stage 1 and Stage 2 and are noted as D_1 and D_2, respectively. The analytical solution for the diffusion equation with each boundary condition is given in Bakhshi, et al. (Eq. 21, Eq. 23-24) [61]:

Stage 1:
$$C(t,x) = C_i + \frac{F_0 L}{D_1}\left\{\frac{D_1 t}{L^2} + \frac{3x^2 - L^2}{6L^2} - \frac{2}{\pi^2}\sum_{n=1}^{\infty}\frac{(-1)^n}{n^2}\cos\left(\frac{n\pi x}{L}\right)e^{\left(-\frac{D_1 n^2 \pi^2 t}{L^2}\right)}\right\} \tag{B-4}$$

Stage 2:
$$C(t,x) = C_* + (C_i - C_*)\sum_{n=1}^{\infty}\frac{2\sin(\lambda_n)}{\lambda_n + \sin(\lambda_n)\cos(\lambda_n)}\cos\left(\lambda_n \frac{x}{L}\right)e^{\left(-{\lambda_n}^2 \frac{D_2 t}{L^2}\right)} \tag{B-5}$$

where

$$\lambda_n \tan(\lambda_n) = \frac{kL}{D_2} \tag{B-6}$$

The selected value for each parameter is provided in Table B5.

Table B5 Parameters selected for drying case in Bakhshi, et al. [61] used for model verification.

	Parameter	Value
L	Thickness (m)	0.01
A	Drying surface area (m^2)	0.01
F_0	Rate of evaporation ($kg/m^2 \cdot h$)	-0.4
C_i	Initial moisture concentration (kg/m^3)	630
D_1	Stage 1 effective diffusivity (m^2/h)	1.8×10^{-3}
D_2	Stage 2 effective diffusivity (m^2/h)	1.8×10^{-5}
k	Surface factor (m/h)	0.001
t_{trans}	Transition time from stage I to II (h)	10

The ORCHESTRA simulation result of drying under 11% RH closely agrees with the analytical solution in Eqs. B-4 to B-6 (Figure B1).

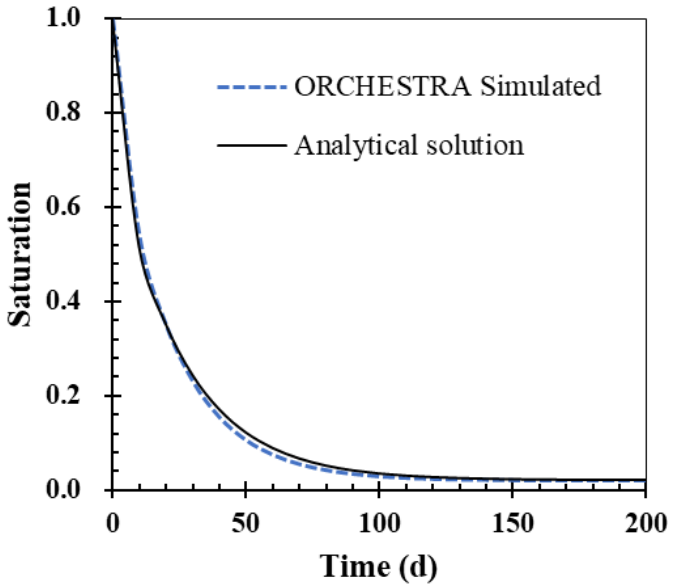

Figure B1 Simulation result of an independent case compared with the result from analytical solution.

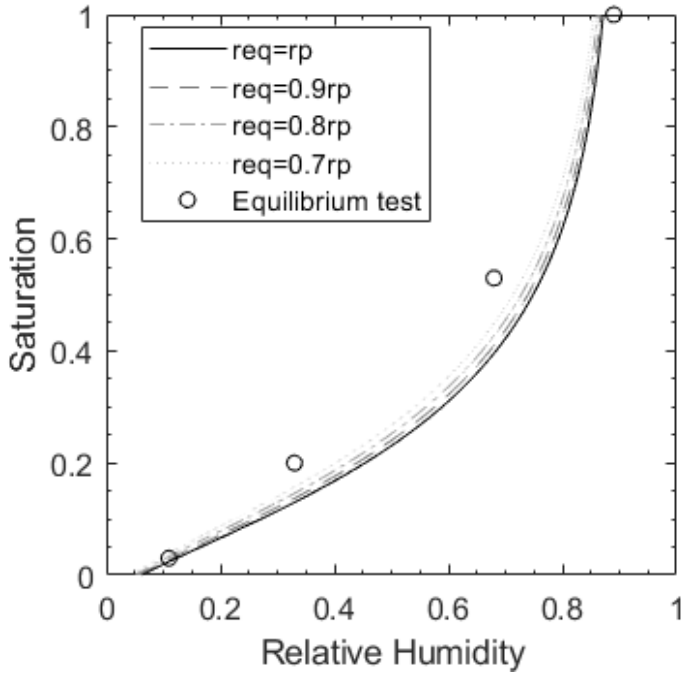

Figure B2 Sensitivity analysis of pore radius on water saturation as a function of relative humidity calculated by Kelvin's equation. (*req* is the effective pore radius used in Kelvin's equation and *rp* is the measured pore radius.)

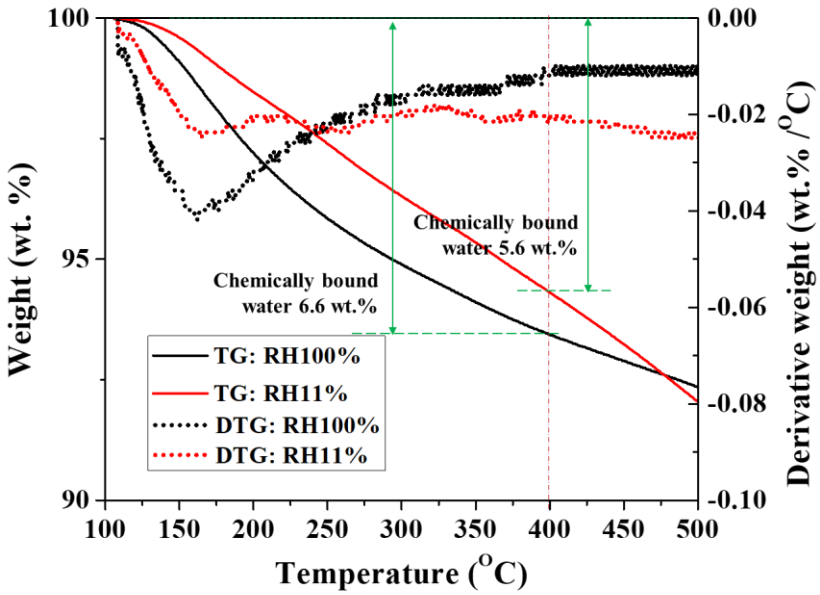

Figure B3 Determination of chemically bound water content from thermogravimetric analysis (samples equilibrated under RH 100% and RH 11% are shown as bounding cases)

B-III. $CaO–Al_2O_3–SiO_2$ ratio in Cast Stone

The weight ratio between $CaO–Al_2O_3–SiO_2$ in the Cast Stone dry blend was compared with common cementitious materials in Figure B4. The composition of the dry blend was calculated from the XRF results of the respective dry ingredients (FAF, BFS, OPC) used in the formulations.

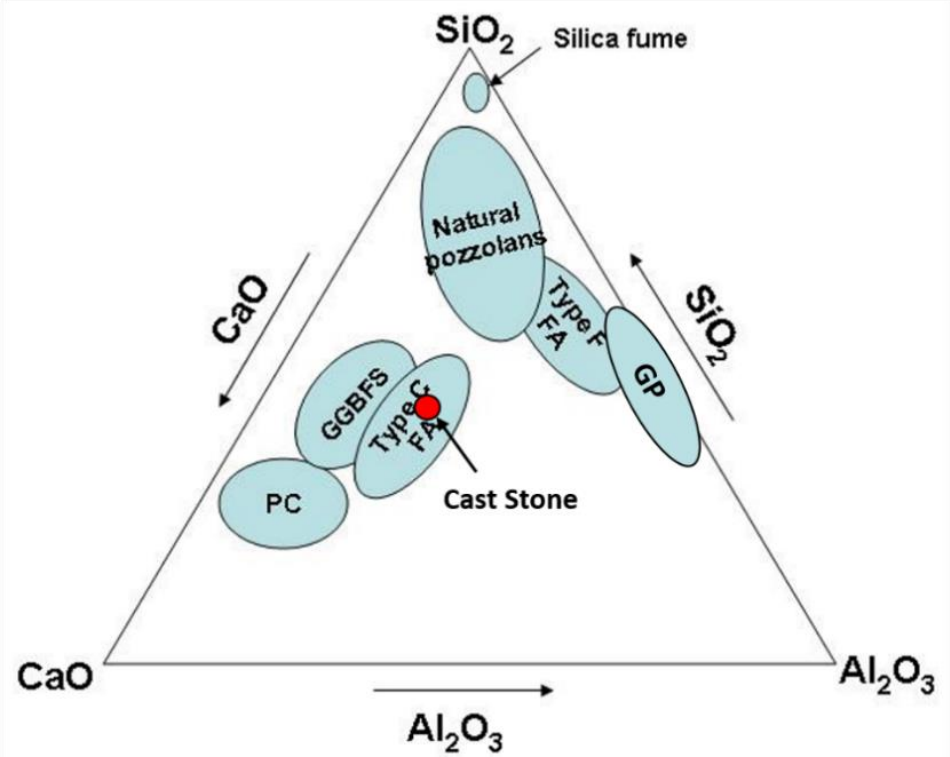

Figure B4 $CaO–Al_2O_3–SiO_2$ ternary diagram of Cast Stone dry blend compared with common cementitious materials (wt%; PC: Portland cement, BFS: blast-furnace slag, FA: fly ash, GP: geopolymer) [184]

APPENDIX C: SUPPLEMENTARY INFORMATION FOR CHAPTER 3

Table C1 Main chemical components in cementitious materials in Cast Stone.

	OPC (%)	FAF (%)	BFS (%)
Al_2O_3	5.67	34.6	14.4
SiO_2	20	51.6	32.4
Na_2O	0.501	0.441	-
MgO	3.18	1.35	0.457
SO_3	4.78	-	6.33
K_2O	0.445	2.53	0.534
CaO	61.2	1.19	40.2
Fe_2O_3	3.59	6.48	0.634

Table C2 Sample mass change before and after pre-conditioning for 60 days; drying front at the beginning of aging estimated by a drying model [138] compared with drying front at the end of aging from measurements.

RH	Mass change (g)	Drying Front after pre-conditioning (mm)	Drying front after 48 weeks of aging (mm)
15%	-0.87	6.6	25.7
40%	-0.74	4.5	15.0
68%	-0.33	2.6	4.5
100%	-0.16	0	0

Table C3 Hydroxide flux from 1-D leaching test for samples aged under various gaseous conditions for 16 weeks.

Leaching	Flux of hydroxides (mol/m^2/s)			
Time (days)	CS-N68-16w	CS-A68-16w	CS-2C68-16w	CS-5C68-16w
0	4.6E-09	2.5E-10	4.2E-11	8.4E-14
1	1.1E-09	1.9E-10	8.3E-12	4.2E-14
2	1.1E-09	7.4E-10	1.4E-11	1.7E-13
7	5.4E-10	5.1E-10	1.4E-12	3.7E-14
14	4.7E-10	1.0E-09	4.4E-13	2.4E-13
28	2.7E-10	7.7E-10	3.6E-13	2.7E-14
42	1.6E-10	6.1E-10	6.3E-13	4.6E-14
49	3.3E-10	5.7E-10	4.4E-12	2.6E-14
63	3.8E-11	2.5E-10	1.4E-12	8.2E-14
91	1.5E-10	2.2E-10	1.7E-12	2.6E-13
107	3.7E-11	3.2E-10	3.8E-12	4.4E-13

C-I Determination of mineral composition of carbonated and uncarbonated Cast Stone from geochemical speciation modeling

Given the complex minerology of the Cast Stone material, the mineral compositions of the material were determined with the aid of geochemical speciation modeling. In the geochemical speciation model, both carbonated and uncarbonated materials are represented using a single set of mineral phases and solid solution (Table C4) derived to describe the dissolution of the major and trace constituents in the system [90]. Selection of the appropriate mineral and parameter set for Cast Stone has been based on calibration using data from EPA Method 1313 (liquid-solid partitioning as a function of extract pH using a parallel batch extraction [131]) in conjunction with instrument-based phase identification and then validated based on data from EPA Method 1315 (mass transfer rates of constituents in monolithic materials using a semi-dynamic tank leaching [133]). The C-N-A-S-H phase is represented using CNASH solid solution (CNASH_ss), which was derived specifically for describing dissolution of alkali-activated material [87,103]. The CNASH solid solution included three selected endmembers: CEM18_INFCNA, CEM18_T2C, CEM18_TobH, with formulae given in Table C4.

The quantities of minerals and solid solutions in carbonated and uncarbonated materials were derived by simulating the liquid-solid partitioning of the material with water under a liquid-to-solid ratio of 1. The solid compositions calculated by the model are considered as the mineral composition in the respective material. The minerals and solid solutions with contents higher than 0.01 mol/kg in either carbonated or uncarbonated materials were included for the calculation of CO_2 and water change.

Table C4 Mineral assemblage of Cast Stone used in geochemical speciation modeling.

Notation	Formula	Log(K)[a]	Reaction
CEM18_INFCNA_CNASHss [b]	$16CaO{\cdot}5.5Na_2O{\cdot}2.5Al_2O_3{\cdot}19SiO_2{\cdot}21H_2O$	-9.836	CEM18_INFCNA + 0.5 H_2O -> 0.3125 $Al[OH]_4^-$ + 1 CEM18_CNASH_ss + 1 Ca^{+2} + 1.1875 $H_2SiO_4^{-2}$ + 0.6875 Na^+
CEM18_T2C_ CNASHss [b]	$3CaO{\cdot}2SiO_2{\cdot}5H_2O$	2.982	CEM18_T2C_CNASHss + 1 H^+ -> 1 CEM18_CNASH_ss + 1.5 Ca^{+2} + 2 H_2O + 1 $H_2SiO_4^{-2}$
CEM18_TobH_ CNASHss [b]	$2CaO{\cdot}3SiO_2{\cdot}5H_2O$	-21.51	CEM18_TobH_CNASHss -> 1.5 CEM18_CNASH_ss + 1 Ca^{+2} + 1 H^+ + 0.5 H_2O + 1.5 $H_2SiO_4^{-2}$
Ca3[PO4]2[beta] [c]	$Ca_3(PO_4)_2$	-29.08	Ca3[PO4]2[beta] -> 3 Ca^{+2} + 2 PO_4^{-3}
CaCO3_BaCO3 [e]	$CaBa(CO_3)_2$	-21.10	CaCO3_BaCO3 -> 1 Ba^{+2} + 2 CO_3^{-2} + 1 Ca^{+2}
CaCO3_Li2CO3 [e]	$CaLi_2(CO_3)_2$	-21.30	CaCO3_Li2CO3 -> 2 CO_3^{-2} + 1 Ca^{+2} + 2 Li^+
CaCO3_SrCO3 [e]	$CaSr(CO_3)_2$	-19.75	CaCO3_SrCO3 -> 2 CO_3^{-2} + 1 Ca^{+2} + 1 Sr^{+2}
CEM18_Amor_Sl [b]	SiO_2	-25.72	CEM18_Amor_Sl + 2 H_2O -> 2 H^+ + 1 $H_2SiO_4^{-2}$
CEM18_Brc [b]	$Mg(OH)_2$	17.18	CEM18_Brc + 2 H^+ -> 2 H_2O + 1 Mg^{+2}
CEM18_C3S [b]	Ca_3SiO_5	51.63	CEM18_C3S + 4 H^+ -> 3 Ca^{+2} + 1 H_2O + 1 $H_2SiO_4^{-2}$
CEM18_Cal [b]	$CaCO_3$	-8.45	CEM18_Cal -> 1 CO_3^{-2} + 1 Ca^{+2}
CEM18_hemicarbonate [b]	$Ca_4Al_2(CO_3)_{0.5}(OH)_{13}{\cdot}5.5H_2O$	40.93	CEM18_hemicarbonate + 5 H^+ -> 2 $Al[OH]_4^-$ + 0.5 CO_3^{-2} + 4 Ca^{+2} + 10.5 H_2O
CEM18_hemihydrate [b]	$CaSO_4{\cdot}0.5H_2O$	-3.518	CEM18_hemihydrate -> 1 Ca^{+2} + 0.5 H_2O + 1 SO_4^{-2}
CEM18_Mgs [b]	$MgCO_3$	-8.206	CEM18_Mgs -> 1 CO_3^{-2} + 1 Mg^{+2}
CEM18_monocarbonate [b]	$Ca_4Al_2(CO_3)(OH)_{12}{\cdot}5H_2O$	24.38	CEM18_monocarbonate + 4 H^+ -> 2 $Al[OH]_4^-$ + 1 CO_3^{-2} + 4 Ca^{+2} + 9 H_2O
CEM18_monosulphate12 [b]	$Ca_4Al_2O_6(SO_4){\cdot}12H_2O$	26.66	CEM18_monosulphate12 + 4 H^+ -> 2 $Al[OH]_4^-$ + 4 Ca^{+2} + 10 H_2O + 1 SO_4^{-2}
CEM18_Ord_Dol [b]	$CaMg(CO_3)_2$	-16.99	CEM18_Ord_Dol -> 2 CO_3^{-2} + 1 Ca^{+2} + 1 Mg^{+2}
CEM18_Portlandite [b]	$Ca(OH)_2$	23.19	CEM18_Portlandite + 2 H^+ -> 1 Ca^{+2} + 2 H_2O
Diaspore [c]	α-AlO(OH)	-16.02	Diaspore + 2 H_2O -> 1 $Al[OH]_4^-$ + 1 H^+
Eskolaite [d]	Cr_2O_3	-147.5	Eskolaite + 5 H_2O -> 2 CrO_4^{-2} + 10 H^+ + 6 e^-
Ferrihydrite [c]	$Fe_2O_3{\cdot}3H_2O$	-18.18	Ferrihydrite + 1 H_2O -> 1 $Fe[OH]_4^-$ + 1 H^+
Gaylussite [d]	$Na_2Ca(CO_3)_2{\cdot}5H_2O$	-9.516	Gaylussite -> 2 CO_3^{-2} + 1 Ca^{+2} + 5 H_2O + 2 Na^+
Larnite [d]	Ca_2SiO_4	16.18	Larnite + 2 H^+ -> 2 Ca^{+2} + 1 $H_2SiO_4^{-2}$
Nahcolite [d]	$NaHCO_3$	-10.79	Nahcolite -> 1 CO_3^{-2} + 1 H^+ + 1 Na^+
Natron [c]	$Na_2CO_3{\cdot}10H_2O$	-1.508	Natron -> 1 CO_3^{-2} + 10 H_2O + 2 Na^+
Pyrite [c]	FeS_2	-121.1	Pyrite + 12 H_2O -> 1 $Fe[OH]_4^-$ + 20 H^+ + 2 SO_4^{-2} + 15 e^-
Pyrrhotite [d]	FeS	-72.27	Pyrrhotite + 8 H_2O -> 1 $Fe[OH]_4^-$ + 12 H^+ + 1 SO_4^{-2} + 9 e^-
Wairakite [d]	$Ca_8Al_{16}Si_{32}O_{96}{\cdot}16H_2O$	-119.4	Wairakite + 10 H_2O -> 2 $Al[OH]_4^-$ + 1 Ca^{+2} + 8 H^+ + 4 $H_2SiO_4^{-2}$
llnl_$NaTcO_4$ [d]	$NaTcO_4$	-9.279	llnl_ $NaTcO_4$ + 1 e^- -> 1 Na^+ + 1 TcO_4^{-2}
llnl_TcO2:2H2O[am] [d]	$TcO_2{\cdot}2H_2O$	-48.46	llnl_TcO2:2H2O[am] -> 4 H^+ + 1 TcO_4^{-2} + 2 e^-
llnl_Tc3O4 [d]	Tc_3O_4	-192.9	llnl_Tc3O4 + 8 H_2O -> 16 H^+ + 3 TcO_4^{-2} + 10 e^-
llnl_TcOH [d]	TcOH	-110.4	llnl_TcOH + 3 H_2O -> 11 H^+ + 1 TcO_4^{-2} + 7 e^-

[a] formation reaction constant;
[b] mineral from CEMDATA 18 database [87];
[c] mineral from Minteq. V4 database [156];
[d] mineral from LLNL database [88];
[e] minerals with calibrated logK.

Table C5 Hydroxide flux from 1-D leaching test for samples aged under various RH for 16 weeks.

Leaching Time (days)	Flux of hydroxides (mol/m^2/s)			
	CS-N15-16w	CS-N40-16w	CS-N68-16w	CS-N100-16w
0	2.1E-10	1.1E-10	2.7E-10	5.1E-10
1	1.9E-10	1.0E-10	6.6E-11	1.1E-10
2	1.4E-10	8.2E-11	6.4E-11	6.4E-11
7	9.6E-11	4.4E-11	3.2E-11	2.7E-11
14	9.5E-11	5.4E-11	2.7E-11	2.0E-11
28	4.2E-11	2.7E-11	1.6E-11	1.3E-11
42	4.6E-11	1.0E-11	9.1E-12	5.9E-12
49	4.4E-11	3.0E-11	1.9E-11	1.1E-11
63	2.3E-11	1.3E-11	2.2E-12	5.4E-12
91	2.2E-11	1.5E-12	9.1E-12	6.3E-12
107	1.5E-11	9.7E-13	2.2E-12	2.4E-12

Leaching Time (days)	Flux of hydroxides (mol/m^2/s)			
	CS-A15-16w	CS-A40-16w	CS-A68-16w	CS-A100-16w
0	1.06E-10	1.73E-11	1.49E-11	4.55E-11
1	1.77E-10	1.25E-11	1.11E-11	2.96E-11
2	1.25E-10	3.37E-11	4.33E-11	3.29E-11
7	5.92E-11	3.05E-11	3.03E-11	1.33E-11
14	4.34E-11	8.23E-11	6.17E-11	2.17E-11
28	9.94E-11	7.06E-11	4.54E-11	2.23E-11
42	6.42E-11	5.75E-11	3.59E-11	1.47E-11
49	9.3E-11	5.62E-11	3.36E-11	1.14E-11
63	2.84E-11	1.58E-11	1.47E-11	1.58E-12
91	3.05E-11	2.13E-11	1.31E-11	3.64E-12
107	2.57E-11	3.45E-11	1.85E-11	2.27E-11

Leaching time (days)	Flux of hydroxides (mol/m^2/s)			
	CS-C15-16w	CS-C40-16w	CS-C68-16w	CS-C100-16w
0	8.09E-12	8.09E-12	2.47E-12	6.73E-12
1	1.97E-12	1.97E-12	4.89E-13	2.16E-12
2	2.11E-12	2.11E-12	7.95E-13	3.56E-12
7	1.73E-13	1.73E-13	8.19E-14	1.53E-12
14	7.14E-14	7.14E-14	2.58E-14	1.14E-12
28	1.25E-14	1.25E-14	2.11E-14	4.64E-12
42	3.53E-15	3.53E-15	3.73E-14	7.89E-12
49	1.52E-14	1.52E-14	2.58E-13	1.6E-11
63	1.83E-15	1.83E-15	8E-14	5.17E-12
91	2.62E-15	2.62E-15	9.89E-14	7.68E-13
107	9.73E-15	9.73E-15	2.22E-13	1.14E-11

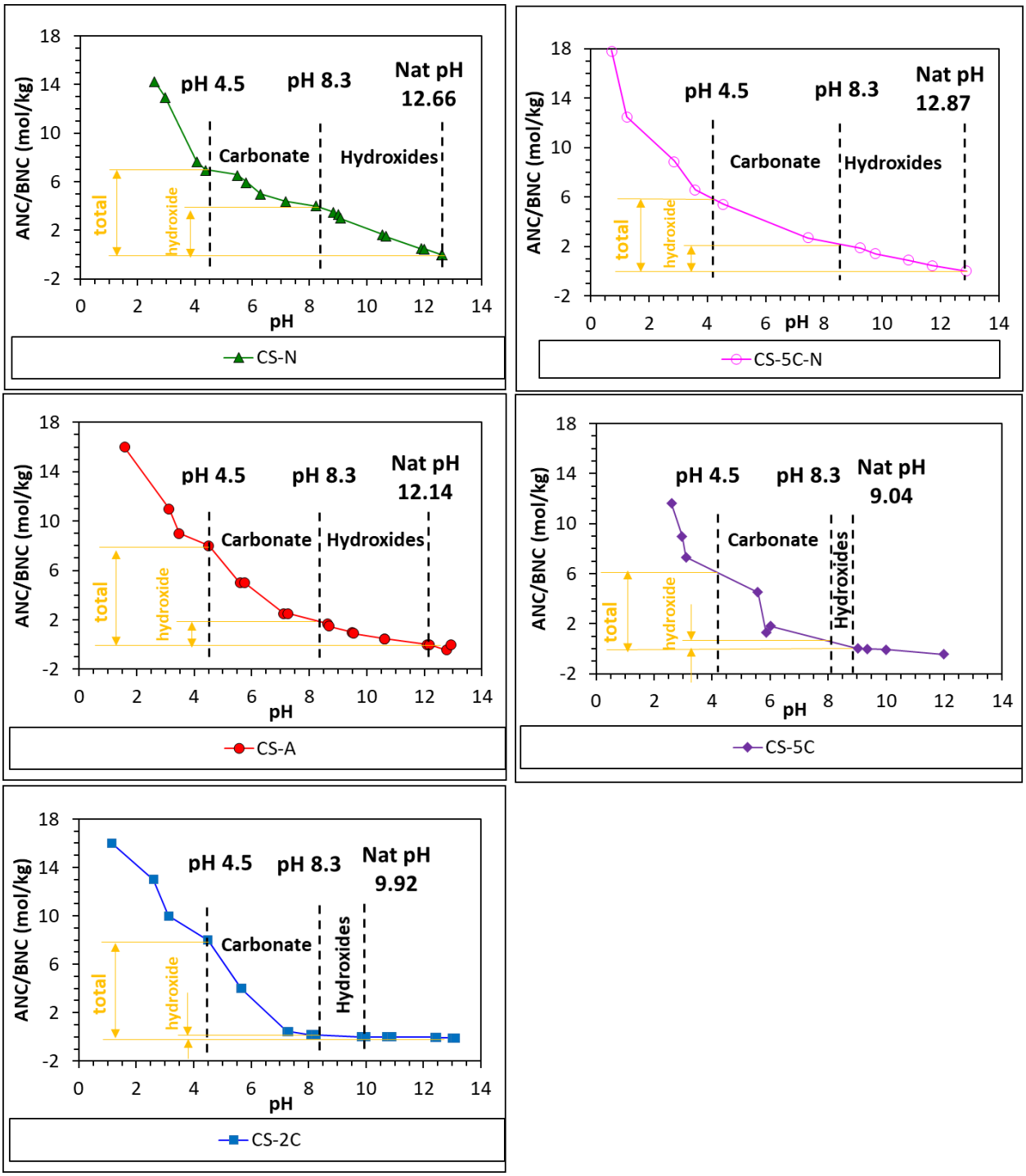

Figure C1 Estimation of carbonate and hydroxide alkalinity for Cast Stone.

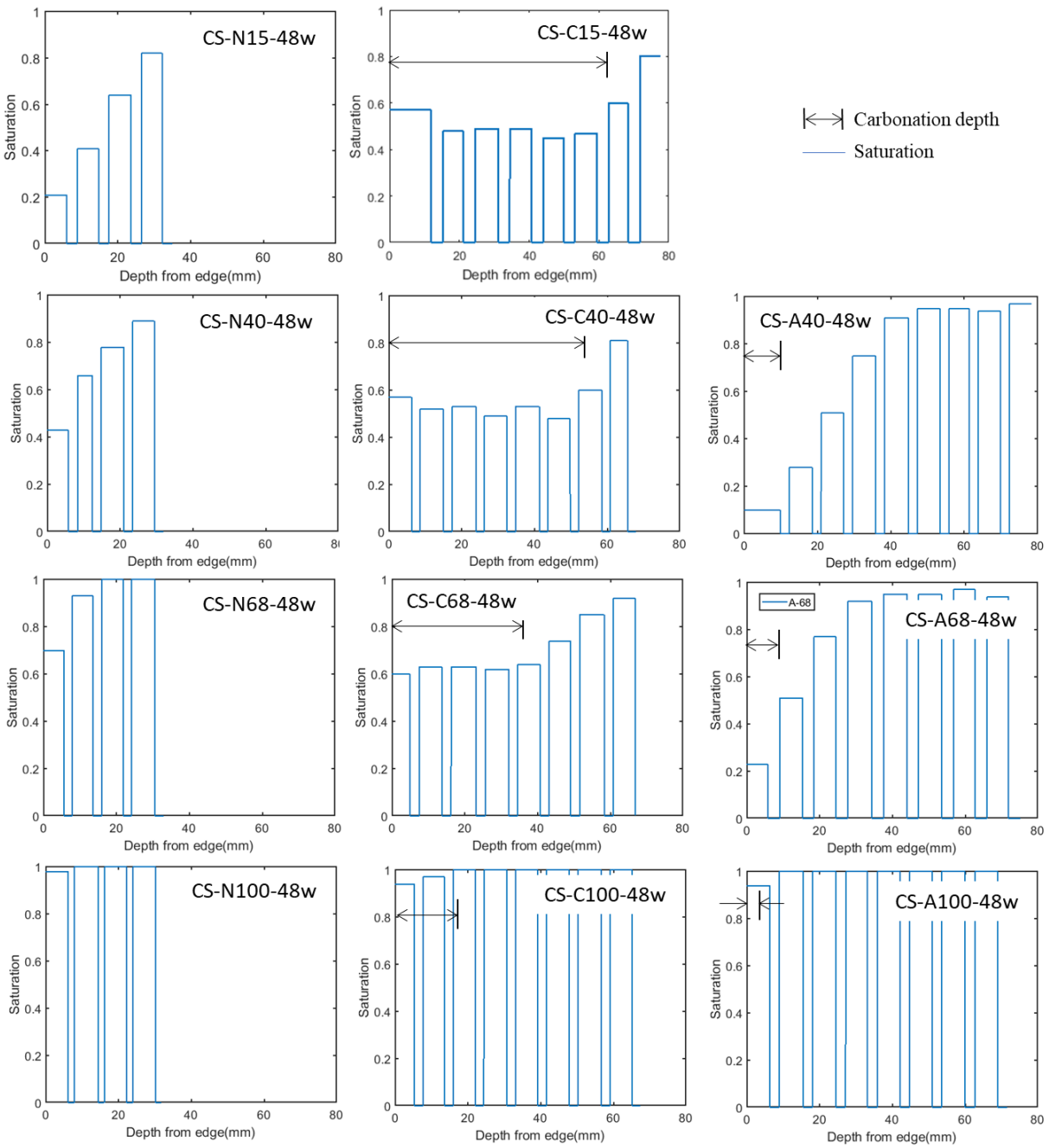

Figure C2 Saturation profile measured from slices cut from Cast Stone samples aged for 48 weeks (saturation profile in CS-A15-48w was not measured because sample breaks apart during the process of slicing).

C-II Determination of mean pore diameter as function of saturation

Mean pore diameter (d_{50}) as a function of saturation is derived from the pore size distribution. The pore size distribution in Cast Stone was characterized by a combination of nitrogen adsorption/desorption (N_2 sorption) and mercury intrusion porosimetry (MIP) to account for different optimum measurement ranges of the test methods. Mesopore structure was determined by N_2 sorption conducted at 77.2 K using a Micromeritics 2020 Accelerated Surface Area and Porosimetry System. The pore size distribution between 1.7 and 30 nm diameter was derived assuming cylindrical pores using the Barrett, Joyner, and Halenda (BJH) model. Macroscale pore structure to a minimum pore diameter of 3 nm was determined by MIP using a Micromertics AutoPore V9600 porosimeter up to a maximum pressure of 430 MPa. The representative pore size radius as a function of water saturation (Figure C3) was derived by fitting the combined results of pore size distribution from nitrogen sorption (pore diameter less than 30nm) and MIP (pore diameter between 30 nm and 340 μm), assuming drying in the pores occur progressively from largest pores to the smaller pores without hysteresis. The mean pore diameter of gas filled pores (d_{50}) at a certain saturation state is derived from the average between the minimum gas filled pore diameter at the specific saturation value and the largest pore size measured (Figure C4). There is only negligible difference in d_{50} at S<0.9 because the minimum gas filled pore size in this range is around 5 orders of magnitude lower than the largest pore size.

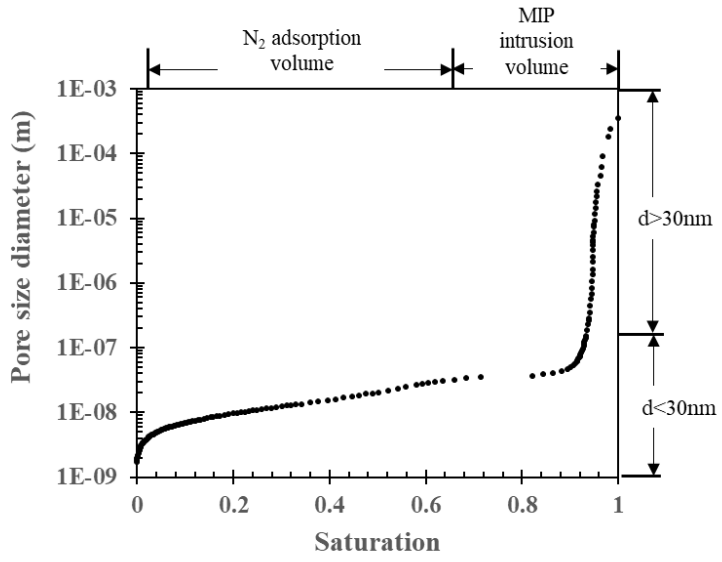

Figure C3 Representative pore diameter as a function of water saturation of Cast Stone.

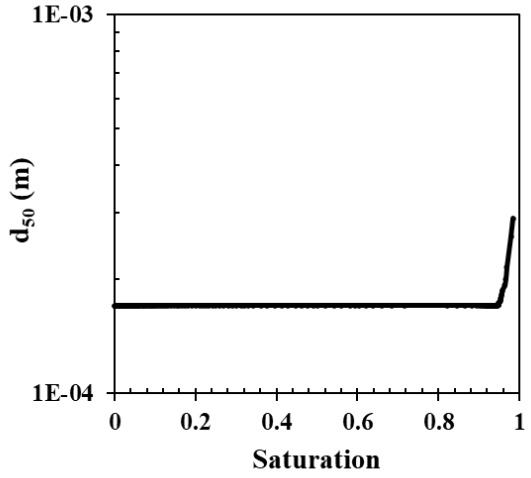

Figure C4 Mean gas filled pore diameter as a function of water saturation of Cast Stone.

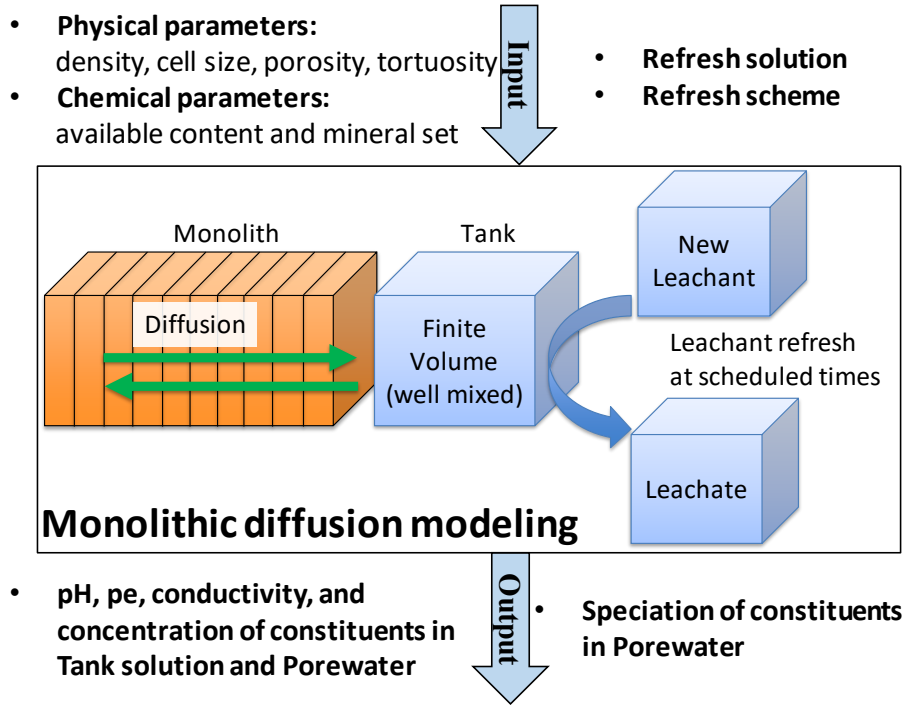

Figure D1 Conceptual illustration of the monolithic diffusion model.

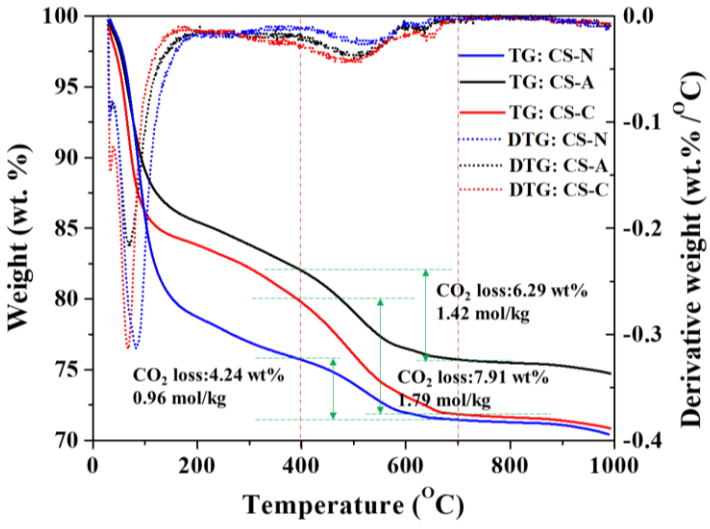

Figure D2 Carbonate content from thermogravimetric analysis of CS-N, CS-A, and CS-C.

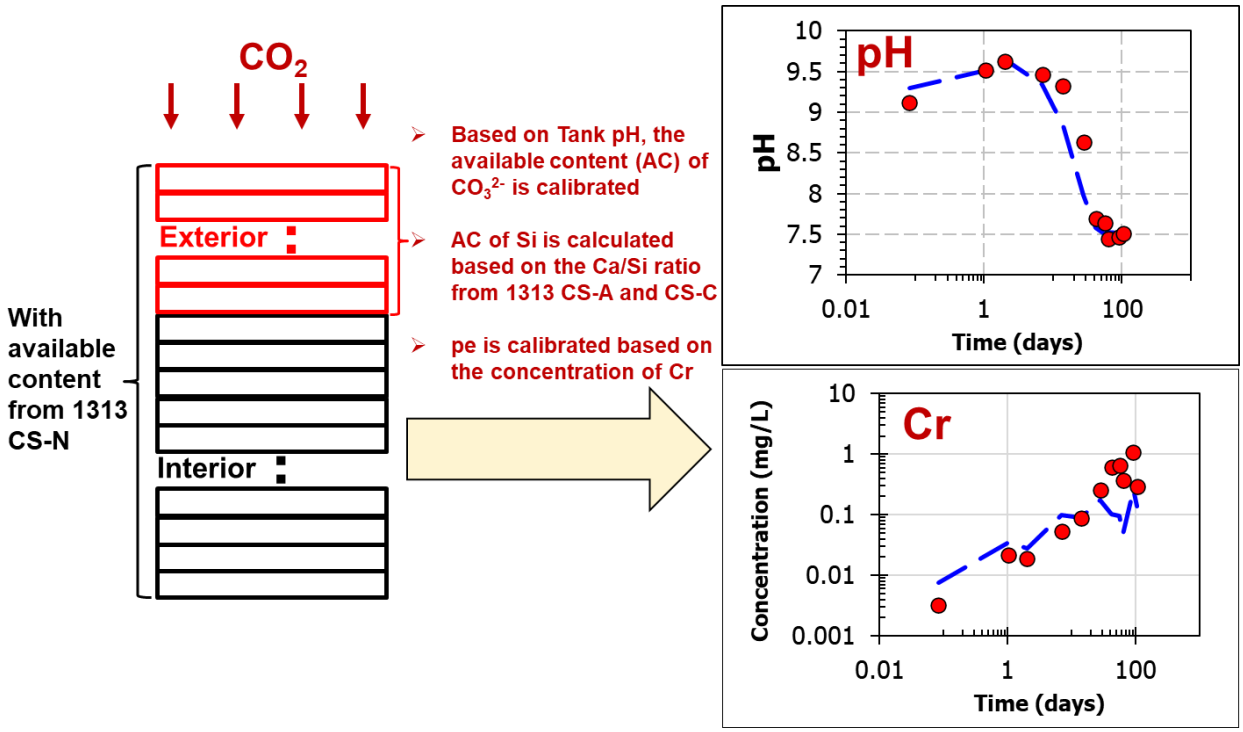

Figure D3 Illustration of the settings of pe and available content of carbonate in carbonated samples (CS-A-48w and CS-C-48w).

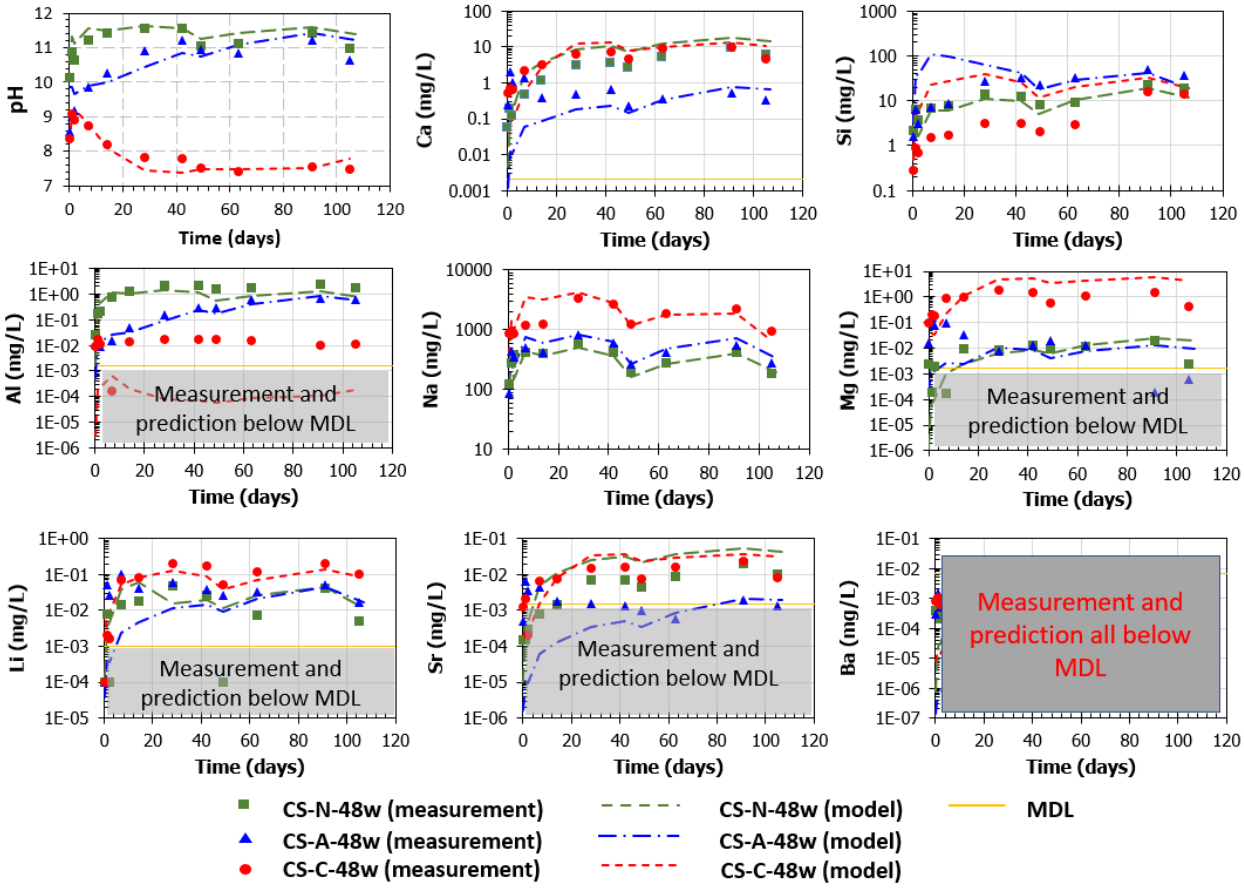

Figure D4 Experimental measurements and reactive transport modeling results of diffusion-controlled leaching concentrations of major constituents and carbonation sensitive constituents in CS-N-48w, CS-A-48w, and CS-C-48w.

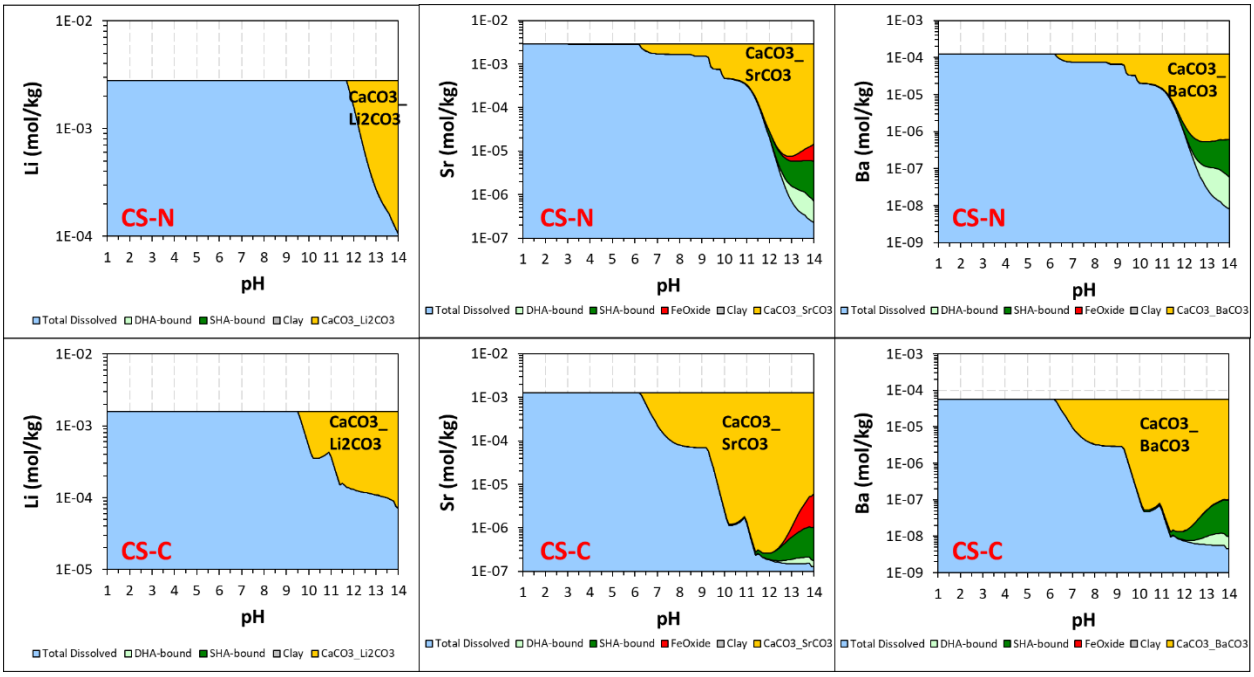

Figure D5 Geochemical speciation modeling results of carbonation sensitive constituents (Li, Sr, Ba) for CS-N and CS-C.

Table D1 Calibrated eluate pe for Cast Stone materials from pH dependent leaching.

CS-N		CS-A		CS-C	
pH	**pe**	**pH**	**pe**	**pH**	**pe**
12.6*	2.1*	12.9	1.8	13.1	1.1
11.9	3.3	12.1*	3.2*	12.5	2.1
10.6	5.5	10.6	5.6	10.9	4.6
9.0	7.9	9.5	7.3	9.9*	6.3*
8.2	9.1	8.6	8.7	8.3	9.0
7.2	10.9	7.1	11.2	7.3	10.5
6.3	12.4	5.6	13.4	5.7	12.5
5.5	13.6	4.5	14.8	4.5	14.7
4.4	15.0	3.1	17.0	3.1	17.0
3.0	16.6	1.6	19.1	1.1	19.7

*natural pH and natural pe

APPENDIX E: SUPPLEMENTARY INFORMATION FOR CHATPER 5

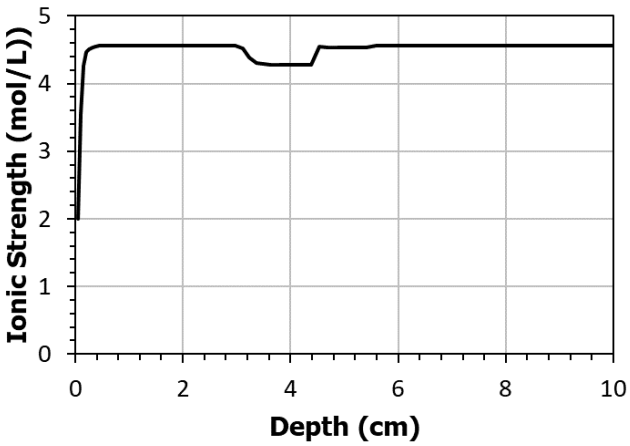

Figure E1 Initial ionic strength profile in CS-C68-48w sample from diffusion-controlled leaching simulation.

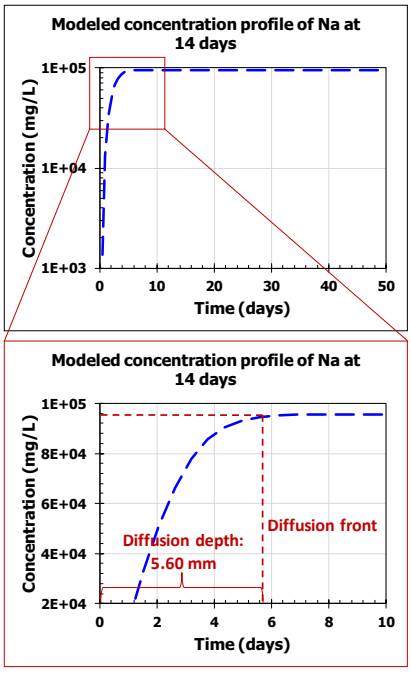

Cell number	Depth (mm)	Concentration (mg/L)
1	0.5	1355
2	1.0125	13249
3	1.5378	33215
4	2.0763	51328
5	2.6282	66360
6	3.1939	77738
7	3.7737	85564
8	4.3681	90441
9	4.9773	93187
10	**5.6017**	**94582**
11	6.2417	95219
12	6.8978	95482
13	7.5702	95579
14	8.2595	95611
15	8.966	95621
16	9.6901	95623
17	10.432	95624
18	11.193	95624
19	11.973	95624
...	...	...
48	45.43	95624
49	47.066	95624
50	49	95624

Figure E2 Illustration of diffusion depth of Na at a certain time (i.e., 14 days) based on the concentration profile of Na in the pore water of monolith [173].

The diffusion front of Na is defined as the deepest cell with concentration of Na lower than 99 % of the initial Na concentration in the pore water. At the leaching time of 14 days, cell No. 10 (depth = 5.60 mm)

is the deepest cell with concentration of Na lower than 99 % of initial Na concentration in the pore water, so the diffusion front of Na at 14 days is at cell No. 10 and the leaching depth of Na is 5.60 mm.

E-I. Carbonation model

A reactive transport model was used for predicting carbonation front ingress in Cast Stone under drying conditions (Figure E3). A parsimonious mineral set (Table E1) was used for describing the Cast Stone matrix. The moisture transport model introduced in Chapter 2 was embedded to calculate the liquid flow and vapor diffusion as a function of external relative humidity. Effective diffusivities ($D_{e,G}$) of CO_2 were calculated from free diffusivity ($D_{0,G}$), porosity (ε), gas phase tortuosity (τ_G), and saturation (S). The exponent of *(1-S)* is calibrated based on the moisture profile in the monolith, which is different from the conditions used for the disk drying experiment (Eq. 2-9).

$$D_{e,G} = \frac{D_{0,G}}{{\tau_G}^2}(1-S)^{4/3} \cdot \varepsilon^{4/3} \tag{E-1}$$

Tortuosity factors in the initial material were derived by the calibration against saturation profile measured on Cast Stone monolith dried under inert conditions (N_2). The tortuosity factor in the carbonated region was calibrated against the carbonation depth from measurement. The carbonated region was defined as the cells in which CNASH content was less than 1E-9 mol/kg. From the predicted pore solution profile, the lowest depth with pH greater than 9 was considered as the carbonation depth.

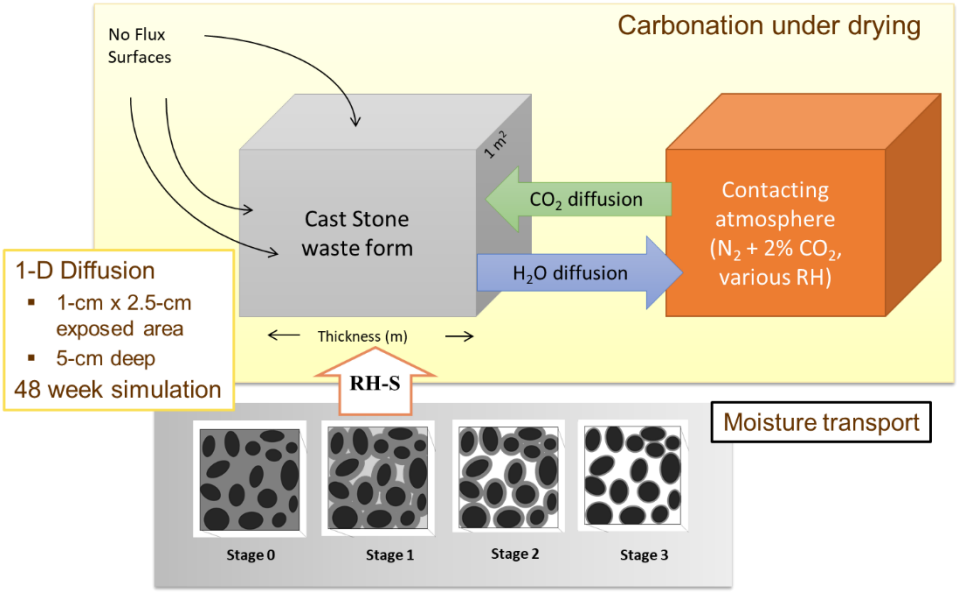

Figure E3 Conceptual model of carbonation under drying.

Table E1 Parsimonious mineral set of Cast Stone used in carbonation modeling.

Notation	*Formula*	*Log(K)*[a]	*Reaction*
CEM18_INFCNA_CNASHss [b]	$16CaO{\cdot}5.5Na_2O{\cdot}2.5Al_2O_3{\cdot}19SiO_2{\cdot}21H_2O$	-9.836	CEM18_INFCNA + 0.5 H_2O -> 0.3125 $Al[OH]_4^-$ + 1 CEM18_CNASH_ss + 1 Ca^{+2} + 1.1875 $H_2SiO_4^{-2}$ + 0.6875 Na^+
CEM18_T2C_CNASHss [b]	$3CaO{\cdot}2SiO_2{\cdot}5H_2O$	2.982	CEM18_T2C_CNASHss + 1 H^+ -> 1 CEM18_CNASH_ss + 1.5 Ca^{+2} + 2 H_2O + 1 $H_2SiO_4^{-2}$
CEM18_TobH_CNASHss [b]	$2CaO{\cdot}3SiO_2{\cdot}5H_2O$	-21.51	CEM18_TobH_CNASHss -> 1.5 CEM18_CNASH_ss + 1 Ca^{+2} + 1 H^+ + 0.5 H_2O + 1.5 $H_2SiO_4^{-2}$
CEM18_Amor_Sl [b]	SiO_2	-25.72	CEM18_Amor_Sl + 2 H_2O -> 2 H^+ + 1 $H_2SiO_4^{-2}$
CEM18_Brc [b]	$Mg(OH)_2$	17.18	CEM18_Brc + 2 H^+ -> 2 H_2O + 1 Mg^{+2}
CEM18_C3S [b]	Ca_3SiO_5	51.63	CEM18_C3S + 4 H^+ -> 3 Ca^{+2} + 1 H_2O + 1 $H_2SiO_4^{-2}$
CEM18_Cal [b]	$CaCO_3$	-8.45	CEM18_Cal -> 1 CO_3^{-2} + 1 Ca^{+2}
CEM18_hemicarbonate [b]	$Ca_4Al_2(CO_3)_{0.5}(OH)_{13}{\cdot}5.5H_2O$	40.93	CEM18_hemicarbonate + 5 H^+ -> 2 $Al[OH]_4^-$ + 0.5 CO_3^{-2} + 4 Ca^{+2} + 10.5 H_2O
CEM18_monocarbonate [b]	$Ca_4Al_2(CO_3)(OH)_{12}{\cdot}5H_2O$	24.38	CEM18_monocarbonate + 4 H^+ -> 2 $Al[OH]_4^-$ + 1 CO_3^{-2} + 4 Ca^{+2} + 9 H_2O
CEM18_Ord_Dol [b]	$CaMg(CO_3)_2$	-16.99	CEM18_Ord_Dol -> 2 CO_3^{-2} + 1 Ca^{+2} + 1 Mg^{+2}
CEM18_Portlandite [b]	$Ca(OH)_2$	23.19	CEM18_Portlandite + 2 H^+ -> 1 Ca^{+2} + 2 H_2O
Ferrihydrite [c]	$Fe_2O_3{\cdot}3H_2O$	-18.18	Ferrihydrite + 1 H_2O -> 1 $Fe[OH]_4^-$ + 1 H^+
Gaylussite [d]	$Na_2Ca(CO_3)_2{\cdot}5H_2O$	-9.516	Gaylussite -> 2 CO_3^{-2} + 1 Ca^{+2} + 5 H_2O + 2 Na^+
Gibbsite [d]	$Al(OH)_3$	7.7	$Al(OH)_3$ +3H^+ = Al^{3+} + 3H_2O
Nahcolite [d]	$NaHCO_3$	-10.79	Nahcolite -> 1 CO_3^{-2} + 1 H^+ + 1 Na^+
Natron [c]	$Na_2CO_3{\cdot}10H_2O$	-1.508	Natron -> 1 CO_3^{-2} + 10 H_2O + 2 Na^+
Nitratine[e]	NaNO3	1.70	$NaNO_3$ -> Na^+ + NO_3^-

[a] *formation reaction constant;*
[b] *mineral from CEMDATA18 database* [87]*;*
[c] *mineral from Minteq. V4 database* [156]*;*
[d] *mineral from LLNL database* [88]*;*
[e] *G. Faure, 1991* [89].

APPENDIX F: SUPPLEMENTARY INFORMATION FOR CHATPER 6

Table F1 Summary of models and key input parameters in the dissertation.

Model–function	Key input parameters	
	Physical parameters	Chemical parameters
Moisture transport model – drying simulation	Porosity; pore size distribution; free water diffusivity in air; gas phase tortuosity factor*; mass transfer coefficient of water; saturated hydraulic conductivity; van Genuchten parameters.	Surface tension and water activity of pore solution as a function of saturation.
Reactive transport model – simulation of carbonation under drying	Porosity; pore size distribution; free water diffusivity in air; adaptive gas phase tortuosity factor*; mass transfer coefficient of water and CO_2; saturated hydraulic conductivity; van Genuchten parameters.	Mineral assemblage*; available content; surface tension and water activity of pore solution as a function of saturation.
Geochemical speciation model – pH dependent leaching simulation	—	Liquid to solid ratio; mineral assemblage*; available content[1]; pe*.
Reactive transport model – diffusion controlled mass transport leaching simulation	Porosity; free ionic diffusivity; profile of liquid phase tortuosity factor*; saturation.	Tank solution refresh scheme; mineral assemblage[2]; initial profile of available content[3]; initial profile of pe*.

* Parameters derived from calibration.
[1] Available content of CO_3^{2-} and Si from calibration, otherwise from Method 1313 results.
[2] Same mineral assemblage as developed from geochemical speciation model.
[3] Available content of CO_3^{2-} from calibration.